

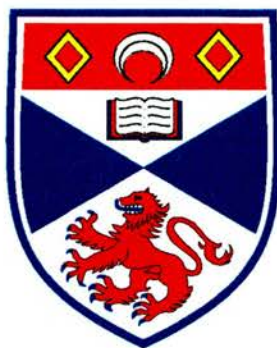
University of St Andrews



Full metadata for this thesis is available in
St Andrews Research Repository
at:

<http://research-repository.st-andrews.ac.uk/>

This thesis is protected by original copyright



The University of St Andrews

Investigations of a Model Enantioselective
Heterogeneous Catalyst:
(R,R)-Tartaric Acid and
Methyl Acetoacetate on Ni{111}.

Thesis submitted in accordance with the
requirements of the University of St Andrews
for the degree of Doctor of Philosophy

Timothy Edward Jones

August 2002



TK E 290

Abstract

The asymmetric hydrogenation of methyl acetoacetate over (R,R)-tartaric acid modified Ni catalysts is a rare example of a heterogeneously catalysed enantioselective process. Little is understood on a fundamental level about the surface of the Ni nanoparticles after adsorption of the chiral modifier and the interaction of the reactant molecule with the clean and chirally modified metal surface. Using a variety of surface analytical techniques, adsorption of (R,R)-tartaric acid and methyl acetoacetate on Ni{111} is investigated in order to elucidate the nature of the chirally modified surfaces and the creation of enantioselective sites.

The adsorption of (R,R)-tartaric acid on Ni{111} results in the formation of two distinct ordered adlayer structures whose stability is dependent on adsorption temperature, the rate of arrival of the modifiers at the surface and the presence or absence of co-adsorbed CO. The adsorption of methyl acetoacetate only occurs in regions of low (R,R)-tartaric acid coverage and results in the local rearrangement of tartrate modifiers to produce a two-dimensional co-crystal consisting of a single adsorbed orientation of reactant molecules. The relevance of this work to enantioselective heterogeneous catalysis is discussed.

The design and construction of a reaction cell attached to a UHV system is discussed with the aim of investigating the liquid phase hydrogenation of methyl acetoacetate over tartrate modified Ni{111}. Initial results achieved using this system are presented.

Finally, a medium energy ion scattering investigation of the tartaric acid adsorption on Cu{110} probes whether monolayer formation involves the chiral redistribution of surface Cu atoms. This study models the initial stages of corrosive chemisorption by the modifier, thought to be an important parameter in the preparation of chirally modified Ni catalysts.

Declarations

I, Timothy Edward Jones, hereby certify that this thesis, which is approximately 52,000 words in length, has been written by me, that it is the record of work carried out by me and that it has not been submitted in any previous application for a higher degree.

Date: 27-8-02

Signature of candidate:

I was admitted as a research student in November, 1998 and as a candidate for the degree of PhD in August, 2002; the higher study for which this is a record was carried out in the University of St Andrews between 1998 and 2001.

Date: 22-8-02

Signature of candidate:

I hereby certify that the candidate has fulfilled the conditions of the Resolution and Regulations appropriate for the degree of PhD in the University of St Andrews and that the candidate is qualified to submit this thesis in application for that degree.

Date: 22 August 2002

Signature of supervisor:

In submitting this thesis to the University of St Andrews I understand that I am giving permission for it to be made available for use in accordance with the regulations of the University Library for the time being in force, subject to any copyright vested in the work not being affected thereby. I also understand that the title and abstract will be published, and that a copy of the work may be made and supplied to any *bona fide* library or research worker.

Date: 27-8-02

Signature of candidate:

List of Publications

TE Jones and CJ Baddeley; "A RAIRS, STM and TPD study of the Ni{111}/*R,R*-tartaric acid system: Modelling the chiral modification of Ni nanoparticles." *Surface Science*. **513** (2002) 453

TE Jones and CJ Baddeley; "Direct STM evidence of a surface interaction between chiral modifier and pro-chiral reagent: Methyl acetoacetate on *R,R*-tartaric acid modified Ni{111}." *Surface Science*. **519** (2002) 237

TE Jones, TCQ Noakes, P Bailey and CJ Baddeley; "Structural and compositional analysis of two ordered surface alloys produced by adsorption and thermal decomposition of Mo(CO)₆ on Ni{111}." *Surface Science*. **523** (2003) 12

TE Jones, TCQ Noakes, P Bailey and CJ Baddeley; "MEIS investigations of adsorbate induced formation of chiral Cu arrangements in the Cu{110}-*R,R*-tartaric acid and *S,S*-tartaric acid systems." To be submitted to *Surface and Interface Analysis*.

TE Jones, TCQ Noakes, P Bailey and CJ Baddeley; "Determination of the layer by layer composition of surface alloys in the Ni{111}/Au system." In preparation.

RJ Pearson, JJF Belch, F Khan, DJ Newton, TE Jones, CJ Baddeley and AR Butler; "Elucidating the mechanism by which transdermally delivered *S*-nitrosothiol sugars enhance peripheral blood flow." In preparation.

Glossary

AES	Auger electron spectroscopy
AFM	Atomic force microscopy
amu	Atomic mass unit
CSD	Crystallite size distribution
DFT	Density functional theory
eda	Enantio-differentiating ability
ee	Enantiomeric excess
fcc	Face centred cubic
FID	Flame ionisation detector
GC	Gas chromatography
hcp	Hexagonal close packed
HTA	Bitartrate
H ₂ TA	Tartaric acid (molecular)
IMFP	Inelastic mean free path
IR	Infrared
L	Langmuir
LEED	Low energy electron diffraction
MAA	Methyl acetoacetate
MCT	Mercury cadmium telluride
MEIS	Medium energy ion scattering
MHB	Methyl 3-hydroxybutyrate
MIDAS	Multi instance data acquisition system
MNi	Modified nickel
ML	Monolayer
MRNi	Modified Raney nickel
OY	Optical yield
PM	Photoelastic modulation
ppm	Parts per million
PTFE	Polytetrafluoroethane (Teflon)
QMS	Quadrupole mass spectrometer
RAIRS	Reflection absorption infrared spectroscopy

RFA	Retarding field analysis
RGA	Residual gas analyser
RNi	Raney nickel
STM	Scanning tunnelling microscopy
TA	Monotartrate
TEA	Toroidal electrostatic detector
THF	Tetrahydrofuran
TPD	Temperature programmed desorption
UHV	Ultra high vacuum
XPS	X-ray photoelectron diffraction

Acknowledgements

I would like to start by acknowledging my supervisor, Dr Chris Baddeley, for whom I cannot thank enough for his endless help, patience and encouragement, without which I would never have been able to complete a year, let alone three. Also for the huge amount of help I have received in improving my written English skills, especially reducing my tendency to use a comma rather than a full stop. The Zywiec are on me.

Special thanks goes to Dr Steve Francis for all his help with UHV equipment and technical guidance in many aspects of surface chemistry. I would also like to express my immense gratitude for the trouncing I regularly received at his hands on the squash court, not to mention facial injuries. I'm sure I'm a better person for it! I would like to thank all the members of the surface chemistry group, in particular Prof. Neville Richardson for the use of the STM, Dr Qiao Chen for his assistance and advice and (lab) Emma for putting up with my chat and disruptive mates. A big thanks also goes to technical support staff in St Andrews, especially Bobby, Brian and Colin and to the MEIS facility staff of Tim, Paul and Brian in Daresbury.

I would like to express a *qualiti maximi* to Iborg, Pauline and HP for the many memorable nights out and football scenario's, mostly. Huge thanks go to (my) Emma for her understanding, patience and encouragement, especially during this last year when time has been a little scarce.

Finally, I cannot thank my parents enough for all their support, encouragement and significant financial assistance throughout my entire time at university.

Table of Contents

Chapter One: Background	1
1.1 Introduction	1
1.2 Enantioselective Catalysis	4
1.3 Heterogeneous Enantioselective Catalysis	6
1.3.1 Hydrogenation of β -keto Esters over Modified Nickel Catalysts	8
1.3.2 System Variables	21
1.4 Aims and Objectives	27
1.5 References	30
Chapter Two: Experimental	33
2.1 Introduction	33
2.1.1 Electron Spectroscopies	35
2.2 Surface Spectroscopic Techniques	37
2.2.1 Low Energy Electron Diffraction (LEED)	39
2.2.2 Auger Electron Spectroscopy (AES)	42
2.2.3 Infrared Spectroscopy (IR)	45
2.2.4 Scanning Tunnelling Microscopy (STM)	49
2.2.5 Temperature Programmed Desorption (TPD)	52
2.2.6 Gas Chromatography (GC)	55
2.2.7 Medium Energy Ion Scattering (MEIS)	57
2.3 References	58

Chapter Three: Adsorption of (R,R)-Tartaric Acid on

Ni{111}	60
3.1 Introduction	60
3.2 Experimental	67
3.3 Results and Discussion	70
3.3.1 LEED and AES Studies	70
3.3.2 RAIRS Studies	73
3.3.3 TPD Studies	86
3.3.4 STM Studies	100
3.4 Summary	120
3.5 References	124

Chapter Four: Adsorption of Methyl Acetoacetate on Ni{111}

and (R,R)-Tartaric Acid Modified Ni{111}	126
4.1 Introduction	126
4.1.1 Proposed Models	128
4.2 Experimental	135
4.3 Results and Discussion	135
4.3.1 MAA Adsorption on Ni{111}	136
4.3.1.1 RAIRS Studies	136
4.3.1.2 TPD Studies	138
4.3.1.3 STM Studies	141
4.3.1.4 Summary	142
4.3.2 MAA Adsorption on R,R-H ₂ TA Modified Ni{111}	143
4.3.2.1 RAIRS Studies	144
4.3.2.2 TPD Studies	148
4.3.2.3 STM Studies of Ordered Structures	154
4.4 Summary	162
4.5 References	164

Chapter Five: Hydrogenation of Methyl Acetoacetate on (R,R)- Tartaric Acid Modified Ni{111}	166
5.1 Introduction	166
5.2 Enantioselective Catalysis	169
5.3 Chamber Design	172
5.3.1 Sample Transfer Procedure	174
5.3.2 Reaction Cell	175
5.3.3 Purification and Transfer of the Reaction Components	177
5.3.4 Theoretical Hydrogenation Activity	178
5.4 Experimental	179
5.5 Results and Discussion	181
5.5.1 Hydrogenation Reaction in the Absence of Ni{111}	183
5.5.2 Hydrogenation Reaction in the Presence of Ni{111}	186
5.5.3 Hydrogenation Reaction in the Presence of Modified Ni{111}	189
5.5.4 Hydrogenation Reaction using THF as a Solvent	191
5.6 Future Work	195
5.7 References	196

Chapter Six: A Medium Energy Ion Scattering Study of (R,R)- Tartaric Acid Modified Cu{110} Surfaces	198
6.1 Medium Energy Ion Scattering	198
6.1.1 Ion Scattering	203
6.1.2 Facility Setup	207
6.1.3 Data Analysis	210
6.2 Introduction	218

6.3 Experimental	224
6.3.1 VEGAS Simulations	228
6.4 Results and Discussion	235
6.4.1 Structural Analysis of Cu{110}	237
6.4.2 Structural Analysis of R,R-H ₂ TA Modified Cu{110}	240
6.4.3 Structural Analysis of S,S-H ₂ TA Modified Cu{110}	243
6.4.4 Quantitative Elemental Analysis	246
6.5 Summary	249
6.6 References	252
Chapter Seven: Summary	254
7.1 Summary of Results	254
7.2 Additional Experiments	256
7.3 References	258

Chapter One

Background

1.1 Introduction

Just by looking at one's own hands it would seem surprising to say that a particular feature of them is seen as a research and discussion point for scientists. It is not the hands we are specifically interested in but the type of symmetry that they possess. They are mirror images of one another. In nature, most biological molecules possess this type of symmetry and these molecules have structures that are not superimposable on each other, just as the left hand is not superimposable on the right hand. Molecules that are not superimposable on their mirror image are called chiral and the two mirror image forms are called optical isomers or enantiomers. Chiral molecules can exist naturally either as a specific enantiomer or where both enantiomers occur, they often have different biological and physical properties ^[1].

Enantiomers are referred to as either right handed (denoted S or D) or left handed (R or L). The simplest example of a pair of enantiomers is a carbon atom surrounded by four different substituent groups, as in figure 1.1.

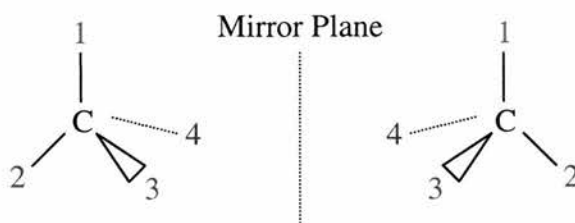


Figure 1.1. A chiral molecule forming a pair of enantiomers.

The notation given to the enantiomers is determined by priority that is dependent on the atomic number of the individual substituent groups present, e.g. the lowest atomic number having the lowest priority. In this example, the priority decreases with $4 > 3 > 2 > 1$. Looking along the C-1 bond in the molecule on the left, with atom 1 being furthest away, the priority decreases in an anti-clockwise direction and is known as the (S)-enantiomer. In the case of the molecule on the right, its priority decreases in a clockwise direction, hence the (R)-enantiomer.

Many compounds associated with living organisms are chiral, for example DNA, enzymes, antibodies and hormones ^[2]. Enantiomers also play an important role in many industrial processes including the production of drugs, insecticides, herbicides, flavour and aroma compounds where the enantiomers of the produced compounds may have distinctly different biological activities ^[3]. Nature is very sensitive to chirality, for example the two naturally occurring enantiomers of limonene smell differently. (S)-limonene smells of lemons while the mirror image compound (R)-limonene smells of oranges ^[2]. We are able to identify the contrast in smells between the enantiomers because our nasal receptors are also made up of chiral molecules that can distinguish the difference ^[2].

The activity of drugs may also be highly dependent on which enantiomer is used. In the 1960s, a drug called thalidomide was prescribed to pregnant women to alleviate the symptoms of morning sickness. Thalidomide occurs as a 50:50 (racemic) mixture of the (R) and (S)-enantiomers. The (R)-enantiomer is responsible for its anti-inflammatory properties whilst the (S)-enantiomer is responsible for its teratogenic properties ^[4]. However, it has since be found that purification of the racemic mixture into its two

enantiomers and prescribing the patient only the (R)-enantiomer is also not the answer since the liver contains an enzyme that interconvert the two enantiomers in the body ^[4].

The importance of enantioselective or asymmetric catalysis, the industrial process by which one enantiomer is produced in excess, is emphasised by the award of the 2001 Nobel Prize for Chemistry to three scientists; Knowles, Noyori and Sharpless, for their research in the area of homogeneous chiral catalysis ^[2]. Knowles and colleagues at Monsanto developed the first industrial asymmetric synthesis using a Rh based catalyst and the diphosphine ligand DiPAMP that was capable of making (L)-dopa (3,4-dihydroxy-phenylalanine) using a prochiral olefin hydrogenation process ^[1]. This drug has been used in the treatment of Parkinson's disease. The mirror image compound, (D)-dopa was found to be inactive in the treatment.

The current industrial routes used for enantioselective catalysis are homogeneous catalysis and organic synthesis. These routes are widely used and are well understood ^[5-6]. However organic synthetic routes often give very low yields and, in homogeneous catalysis, problems can arise due to the difficulty in separating the products from the catalyst greatly affecting the costs. Economic and social factors alone dictate the need to develop routes that give the product in high yield but at a low cost.

It is known that heterogeneous catalysis fulfils these requirements well. At present about 90% of the world's petrochemicals are produced by heterogeneous catalytic routes. However, the products formed tend to be relatively simple, e.g. ethanol, ethylene oxide etc ^[7]. The formation of one chiral molecule at the expense of the other has proved beyond heterogeneous catalysis in all but a small number of cases ^{[5][8-9]}. Therefore

enantioselective heterogeneous catalysts are rare but their potential importance is huge [10].

In a biological system, when a chiral compound is consumed and produced, it will consist of a single enantiomer and show optical activity. However, when the same compound is produced in a laboratory it usually consists of a racemic mixture of the two enantiomers and therefore shows no overall optical activity [5].

1.2 Enantioselective Catalysis

The basis of enantioselective catalysis is that the catalyst may differentiate the stereo structure of a reagent in a reaction and generate one enantiomer in excess [5]. An example of this type of catalysis is the enantio-face differentiating reactions. When a prochiral reactant molecule is introduced into a catalyst system possessing a chiral environment the two faces of a reagent molecule may interact differently with the catalyst and a subsequent reaction may result in the production of two different molecules. This can be illustrated for a hydrogenation reaction in figure 1.2.

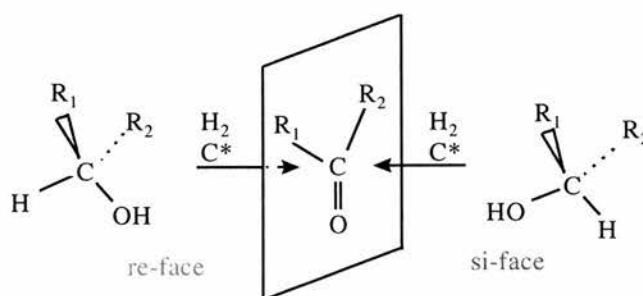


Figure 1.2. Mode of reaction employed in enantio-face differentiation.

The two faces of the reactant molecule are denoted re or si by a similar 'priority' rule to that used to determine the absolute configuration of a chiral molecule. If R₂ is given a

higher priority than R_1 and as oxygen is the highest priority, attack from the left hand side results in a decreasing priority in a clockwise direction, i.e. the re-face of the reactant molecule. Likewise, decreasing priority is in the anti-clockwise direction if the attack is from the right hand side and therefore the reactant molecule face is denoted si. Attack from the re-face therefore yield the (S)-enantiomer whilst attack attack from the si-face yield the (R)-enantiomer. When the catalyst can differentiate between the two types of interaction the product is optically active, i.e. differentiation of the two enantiofaces can generate optically active products. It is well known that these reactions can produce a large amount of optically active material for catalytic amounts of an optically active reagent. The two faces of the reagent are referred to as enantiofaces and the reaction is often known as an enantioselective reaction ^[5].

The ability of a catalyst to provide the required products with high selectivity is of the highest importance and often the ultimate guide by which catalyst performance is measured and is subsequently the aspect of catalysis that has received most attention ^[8]. Its selectivity can also give information about reaction mechanism and surface conditions of the catalyst ^[9].

The effectiveness of differentiating reactions can be expressed in terms of optical yield or enantiomeric excess (ee), also known as enantioselective ability or more commonly enantioselectivity. Optical yield is the degree to which optical purity is achieved and is determined from measurements of optical rotation as optically active species rotate the plane of polarisation of plane-polarised light. This arises due to the difference in the refractive indices for right and left circularly polarised light ^[10A]. The degree of polarisation can easily be measured and calculated using the equation:

$$\text{O.Y.} = \frac{[\alpha]_{\text{D}}^{\text{T}}}{[\alpha]_0^{\text{T}}} = \frac{100\alpha}{[\alpha]_0^{\text{T}}lc}$$

where $[\alpha]_{\text{D}}^{\text{T}}$ is the specific rotation of the product measured at the sodium D-line and 293 ± 3 K, $[\alpha]_0^{\text{T}}$ is the specific rotation of the pure enantiomer under the same conditions, α is the measured optical rotation, l the path length of the cell and c is the solute concentration ^[11]. An enantiomeric pair rotate the plane of polarised light in equal but opposite directions resulting in a net zero rotation of light ^[10B]. Enantiomeric excess is expressed using the concentration of the two enantiomers and is defined as:

$$\%ee = 100 \frac{[(\text{R})\text{-enantiomer}] - [(\text{S})\text{-enantiomer}]}{[(\text{R})\text{-enantiomer}] + [(\text{S})\text{-enantiomer}]} \quad [11]$$

1.3 Heterogeneous Enantioselective Catalysis

Supported metal catalysts possess no inherent chirality and in a reaction they are unselective and generate a racemic product. For metal catalysed enantioselectivity to be achieved, the reaction must take place in a chiral environment. Such an environment can be achieved by either supporting the metallic active phase on a chiral support or adsorbing a chiral molecule (modifier) onto the active phase of a metal catalyst ^[8].

Studies into liquid phase heterogeneous enantioselective catalysis have shown the existence of two main types of reaction, using platinum and nickel based catalysts ^[8].

These are illustrated in figure 1.3.

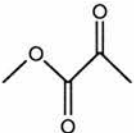
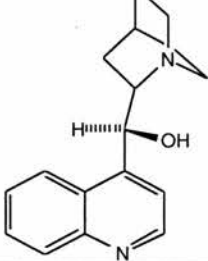
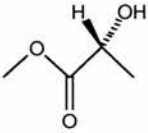
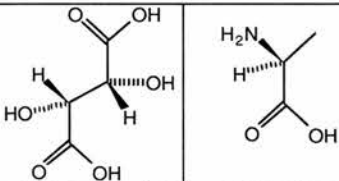
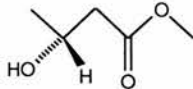
catalyst	reactant	modifier	product
EuroPt			
	methyl pyruvate	cinchonidine	R-methyl lactate
Raney Ni or Ni/SiO ₂			
	methyl acetoacetate	R,R-tartaric acid	S-alanine
			R-methyl-3-hydroxybutyrate

Figure 1.3. Two most common heterogeneous enantioselective catalyst systems ^[8].

In the case of platinum based catalysts, the hydrogenation of the α -keto ester, methyl pyruvate yields a racemic methyl lactate product. However, hydrogenation of methyl pyruvate over the platinum catalyst modified with cinchona alkaloids, such as the chiral molecule cinchonidine, yields R-methyl lactate as the dominant product ^[8].

In the case of nickel catalysed hydrogenation of the β -keto ester, methyl acetoacetate (MAA), modification with α -hydroxy acids (e.g. (R,R)-tartaric acid) or α -amino acids (e.g. (S)-alanine) yields R-methyl-3-hydroxybutyrate ((R)-MHB) in excess ^[8]. The product, (R)-MHB is an important intermediate in the synthesis of a carbonic anhydrase inhibitor MK-0507 used in the treatment of glaucoma ^[13].

Despite extensive research and the fact that the catalytic systems provide high optical yields, the principles that govern enantioselectivity at the solid surface are not established.

1.3.1 Hydrogenation of β -keto Esters over Modified Nickel Catalysts

A vast number of research papers have been published in this field since the 1970's. Most of this research has been based on Raney nickel (RNi) and powdered nickel catalysts using a variety of modifiers and only a relatively small number of studies have been completed on supported nickel catalysts^[8].

RNi is prepared from a nickel/aluminium alloy suspended in a basic solution consisting of 20% aqueous sodium hydroxide at 100°C for 1 hour followed by successive washings with water to leave a porous (Raney) nickel structure. The RNi is then modified with an aqueous modifying solution at specific temperature and pH and separated by decanting and washing with solvent^[9]. It has been shown that MRNi (modified) catalysts with a high Al content is unfavourable for enantioselective catalysis^{[14][36]}. Therefore the preparation of the RNi catalysts is highly dependent on its preparation method.

Hoek *et al*^[14] have shown that unsupported and supported silica nickel catalysts also exhibit comparably high levels of enantioselectivity to that of MRNi, although the use of alumina as a support significantly lowers the optical yield^[14]. As the results obtained for MRNi are also comparable with those of the nickel catalysts, MNi shall from here onwards denote all types of modified Ni catalysts.

A variety of different modified catalysts have been studied using activated metals other than Ni, such as Raney -Co, -Fe, -Cu and -Ru in enantioselective hydrogenation

reactions of several similar reactants, however MNi was found to possess the greatest enantio-differentiating ability (eda) ^[5].

The enantioselective hydrogenation reactions have been studied over nickel catalysts using many different modifiers and it is well established that modification of Ni with optically pure isomers of α -amino or α -hydroxy acid yield catalysts with the greatest ee of ~95% ^{[5][8-9]}. Experimental rules have been established with respect to the structure of the modifying reagent and the enantioselectivity of MNi ^[9]. These are:

1. The preferred structure of the modifying reagent is R-CHX-COOH (where X=NH₂ or OH) and the presence of any substituent on C-2, N or O decrease enantioselectivity.
2. The direction of enantioselectivity ((R) or (S) product) is dependent on two factors, the configuration of chiral compound and the nature of X.
3. The degree of optical purity is governed by the nature of substituent R, increased bulkiness of R increases the optical purity of the amino acid-MNi but decreases that of hydroxy acid-MNi. An increase (decrease) in electron density at the chiral centre increases (decrease) optical purity of amino acid-MNi and decreases (increases) in that of hydroxy acid-MNi.
4. In all cases, when acidic modifying reagents are used, modification at or near pH 5.0 gives the modified catalyst with the highest enantioselectivity.
5. If the modifying reagent has two chiral centres, the configuration of the second chiral centre greatly affects the enantioselectivity of MNi.

These findings, as well as economic implications suggest that tartaric acid and its derivatives were the best modifying reagents^[9]. Such modifications are highly specific in that the nickel catalyst is selective for asymmetric hydrogenation of β -keto derivatives rather than α -keto compounds and the direction of enantioselectivity is usually dependent upon the catalyst modifier^[8]. Modification with the α -hydroxy acid, (R,R)-tartaric acid (R,R-H₂TA) was found to yield the highest enantioselectivity in the hydrogenation of MAA over MNi catalysts^[8].

Despite the huge number of studies reported and the large amount of information that have accumulated, there is little consensus of opinion regarding the nature of enantioselective site(s) and the interactions between the surface, modifier and reactant molecules^[15]. Knowledge of the modifier stereochemistry is insufficient to conclude the causes of enantioselectivity as modification using amino acids and hydroxy acids of different absolute configuration can display the same sign of enantioselectivity, e.g. R,R-H₂TA and (S)-alanine both produce (R)-methyl 3-hydroxybutyrate^[16]. There are however general agreements in that the achievement of enantiomeric excess is reflected to some extent by the nature of the modified (selective site) and bare nickel (non-selective) metal sites^{[15][17]}. Also, the enantioface of the ketone is differentiated during the adsorption of the reactant by the R,R-H₂TA on the catalyst and the hydrogenation step is the rate-determining step^[17].

Therefore, the main points of debate in enantioselective hydrogenation are:

1. the nature of modified surface and complexes produced by the acid modification,

2. the nature of the modifier-reactant interaction on the surface,
3. the possible role of corrosive chemisorption of the acid modifier in the creation of active sites and the role of complexes resulting from the leaching of nickel during modification ^[8].

One of the major difficulties, noted by several different workers ^[8], has been the attainment of reproducible reaction rates and optical yields. The catalyst preparation and modification procedures strongly affect enantioselectivity whilst reaction variables also play an important part ^[9]. Quantitative analysis of the results obtained from studies concerning enantioselective system, are difficult due to the vast range of experimental conditions that apply. Enantioselectivity is dependent on virtually every parameter related to catalyst preparation and modification ^[38]. Consequently very small changes in catalyst preparation, activation and modification often have drastic effects on the reaction rates and optical yields and the reproducibility of this system is made even more complicated by the corrosive interaction of the modifier with the catalyst surface ^[38].

1.3.1.1 Nature of the Surface Complexes

The nature of modified surface complex(es), in terms of their structure, conformation and local order is potentially influential in determining the interaction of incoming species. This is because functional groups that are involved in interaction of the molecule to the surface cannot be available for coupling to further species ^[8]. R,R-H₂TA can exist in at least three different forms and is one of the most studied α -hydroxy acids. The three forms known to exist are those of the neutral bi-acid form, the monotartrate and the bitartrate form as illustrated in figure 1.4.

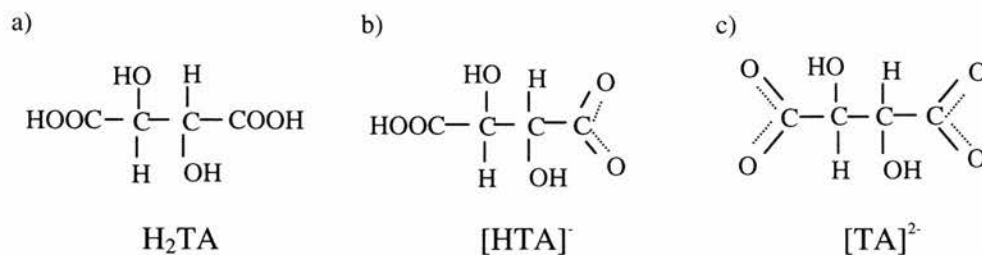


Figure 1.4. Three forms of tartaric acid, a) neutral bi-acid, b) mono-tartrate and c) bi-tartrate form ^[18].

Adsorption modes of the tartaric acid molecules are further complicated as they can form intermolecular hydrogen bonds between adjacent molecules and one or both of the hydroxy groups ^[19].

Early spectroscopic studies helped develop a model that suggested that α -hydroxy acids were adsorbed as a surface carboxylate ^{[16][21][28]}. Carboxylates are well studied as they are regarded as common intermediates in many catalytic reactions such as water gas shift reaction, methanol synthesis and selective oxidation on surfaces of metal oxides ^{[16][20]}.

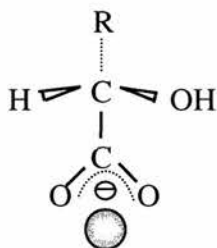


Figure 1.5. Proposed adsorption mode of a carboxylic acid with the surface, via a carboxylate.

The molecule sits upright with respect to the surface and, as illustrated in figure 1.5, it is possible to see that the α -hydroxy group is available for hydrogen bonding with adjacent surface molecules. It would therefore appear feasible to create surface ordering involving two or more molecules ^{[5][9]}. Tartaric acid, however, possesses two terminal

carboxylate groups and two hydroxy groups. This brings into question the behaviour of the second carboxylic acid group. The adsorbed species can attach via both of the carboxylates or perhaps one or both of the carboxylic acid groups are involved in interactions with adjacent molecules.

The adsorption of amino acids contrast to that of α -hydroxy acids as they form chelate structures and therefore it is clear that hydroxy acids and amino acids of identical absolute configuration form chemisorption complexes that differ strongly in structure and reactivity ^[22]. The chelate adsorption structure of α -amino acids on a metal surface is illustrated in figure 1.6.

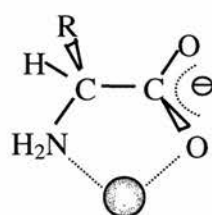


Figure 1.6. The chelate form of a α -amino acid ^[8]. When R= H; Glycine and R=CH₃; Alanine.

It is of importance to note that whilst hydroxy acids contain hydroxyl groups that are capable of forming hydrogen bonds with adjacent molecules, the amino group of the adsorbed amino acid can be involved in bonding to the surface ^[22].

Glycine is a very well studied α -amino acid and it is known that in a solution containing metal ions and glycine, metal-glycino complexes are formed. A metal ion interacts with two anionic glycine molecules to form a chelate structure ^{[3][23-26]}.

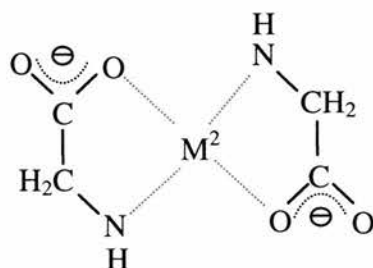


Figure 1.7. Adsorption mode of glycine in a solution containing metal ions.

This brings into question the interaction of the reactant MAA with the surface. The adsorption structure of MAA on supported catalyst particles has also been shown to be similar to that of the corresponding metal chelate and kinetic data have indicated that it is in the physisorbed enol form of MAA ^[16].

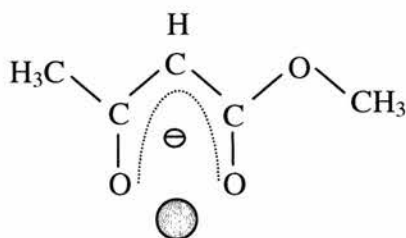


Figure 1.8. Adsorption mode of MAA via the enol form.

The resulting hydrogen atom on carbon-3 is acidic and it has been postulated that it can undergo hydrogen bonding ^[16]. Therefore this suggests that a hydrogen bonding interaction may also be important in formation the modifier/reactant interaction or perhaps with the metal surface. Groenewegen *et al* ^[16] have subsequently suggested a possible surface structure, as shown in figure 1.9.

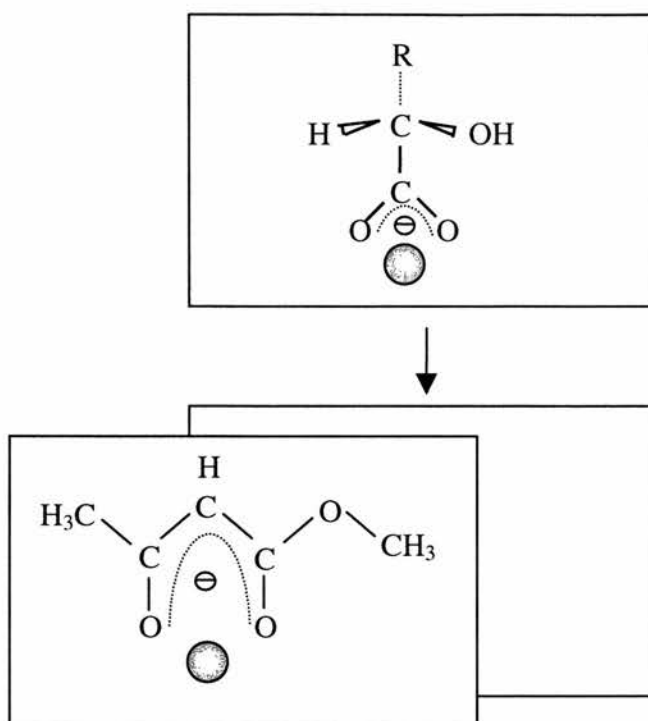


Figure 1.9. Proposed coadsorption of MAA and an α -hydroxy acid^[9]. The actual position of the α -hydroxy acid is represented by the blank rectangle but has been moved up for clarity.

Two rules have been suggested to explain the interaction of the modifier, reagent and surface in the generation of enantioselective sites, illustrated in figure 1.9. Firstly, the observed enantioselectivity results from the adsorption on adjacent nickel sites of MAA and the modifier, R,R-H₂TA. They interact with each other but not with other surface atoms. Secondly, their preferred configuration is characterised by the position of the methoxy group of the MAA and the hydroxy group of the modifier. When these are on the same side hydrogen bonding interactions may occur. Therefore two transition states arise from the interaction of a hydrogen atom with the β -carbon of the MAA chelate, having different free energies^[5].

Similar rules apply for the use of α -amino acids as modifiers but since they form chelates rather than carboxylates, their configuration will be different ^[5].

The above model is just one of many different models proposed for this system. It must be stressed that these models are speculative and no direct evidence for their presence exists. It is therefore important to understand the manner and conditions that species bind to the metal surface, as they will lead to a better understanding of the modification and reaction steps.

1.3.1.2 Corrosive Chemisorption

Evidence suggests that the modification process of the metal catalyst is a corrosive one resulting in the abstraction of the metal from the metal lattice and the leaching into the modifier solution ^[27]. Observations of the modification solution turning green have been rationalised by the presence of nickel tartrate complexes being present in solution indicating that the acid modification procedure was a corrosive process ^[14]. This may be important in the formation of enantioselective sites as it has been suggested the nickel tartrate complexes adhere to the surface and may serve as enantioselective sites. Hoek *et al* ^[14] have proposed that since pure nickel tartrate is unable to catalyse hydrogenation in the absence of metallic nickel, a dual site mechanism is present. Hydrogen is dissociated on the surface of nickel particles, followed by migration of hydrogen atoms to the tartrate complex, where they become attached to the adsorbed reactant molecule in two steps ^[27]. This model suggests that nickel atoms in the nickel tartrate complex serving as enantioselective sites have two vacant ligand positions available for adsorbed hydrogen and the reagent ^[27].

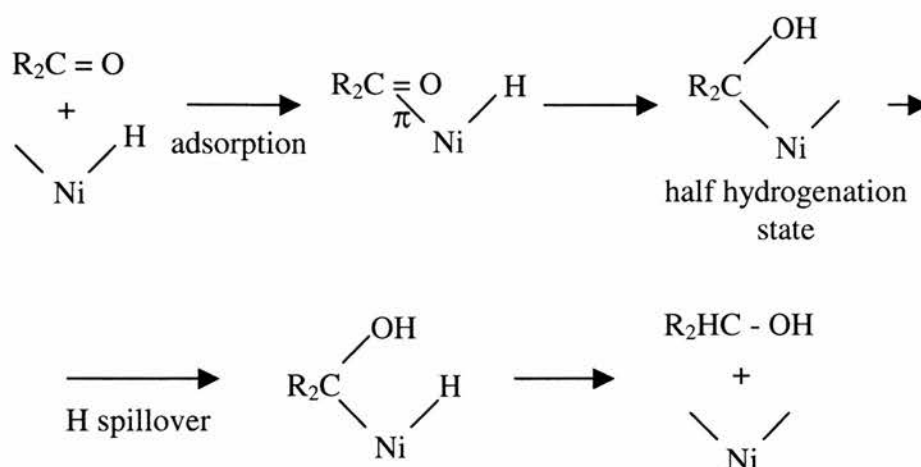


Figure 1.10. Scheme of hydrogenation at the Ni atom with two available coordination sites ^[14].

However, Keane *et al* ^[37] have reported that nickel tartrate leached out during the modification procedure is also optically selective and without any pretreatment acts as an enantioselective catalyst. They therefore conclude that, in contrast to reports by Hoek, metallic nickel is not an essential component of the enantioselective catalyst but suggest that some of the corroded NiTA will remain on the silica support to form a selective site whilst some diffuse into solution ^[37].

Typical results for adsorption of tartaric acid on Ni/SiO₂ catalysts have shown that, depending on modification conditions, the amount of nickel leached into the modification solution can be up to 60% of nickel initially present on the catalyst ^[8]. Since the catalyst is considerably corroded during modification the particle size of the catalyst is expected to change during the modification procedure. Nickel leaching results in selective dissolution of small (<2nm) particles from the catalysts and since it has been reported that larger crystallite catalysts gave higher enantioselectivity ^{[9][28-29]}, this raises the question of what possible role does corrosive chemisorption by the modifier have in creating enantioselective sites?

However, it has also been observed that catalysts with higher enantioselectivities often have a lower hydrogenation activity, perhaps due to the catalysts with larger metal crystallite sizes generally having lower specific surface area ^[15]. Therefore, the enantioselectivity of a modified catalyst is dependent on the crystallite size distribution (CSD) of the nickel particles and catalysts containing around 10nm crystallite with narrow CSD gave the best results ^[9].

1.3.1.3 Secondary Modifiers

There have been many studies into the affects of adding secondary promoters to the catalysts. On addition of the additives to the modifier solution it was noted that there was a remarkable enhancement of enantioselectivity but studies have not determined the precise source of enantiocontrol ^[9]. The best additives, discovered serendipitously by the addition of ‘dirty’ water, are those of the alkali metal halides.

Second modifying reagent (NaX) (g)	Optical yield (%)
None	39.2
Na ₂ SO ₄ (10)	56.5
NaCl (10)	72.1
NaBr (10)	83.1

Table 1.1. Effect of second modifying reagent on the enantioselectivity of R,R-H₂TA-NaX-MNi under identical modification and reaction conditions ^[9].

Sodium bromide has been found to be the most effective secondary modifying reagent even though it has no enantioselectivity of its own ^{[9][30]}. The degree of

enantioselectivity is of debate but general consensus exists that there is some benefit whilst it is observed that the high hydrogenation activity observed for the original modified catalyst decreases after addition of the secondary modifier^[9]. Sodium bromide is thought to block potential tartaric acid adsorption sites and the subsequent decrease in the amount of nickel leached into solution indicates a stabilisation of the surface metal/modifier component^[30]. Enhancement of enantioselectivity cannot be attributed merely to a poisoning of the unselective sites, while the role of NaBr modifying the stereochemistry of the selective sites cannot be ruled out. The variation in tartrate surface coverage might have a greater bearing on enantioselectivity^[30].

It is interesting to consider the possible inter-linking between corrosive chemisorption and addition of metal adatoms in the MNi systems and the role they may play in determining the structure of possible enantioselective sites. Surface science model studies have investigated benzoic acid adsorbed on Cu{110} and {111} surface and it has been observed that the addition of sodium can affect the molecular orientation of an adsorbate. Perry *et al*^[31] have shown that upon adsorption of benzoic acid on Cu{110} the benzoic acid deprotonates and the benzoate is bound to the surface via two equivalent oxygen atoms along the close-packed <110> azimuth^[32], as illustrated in figure 1.11.

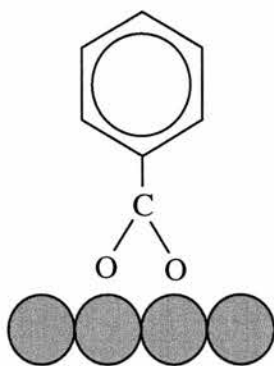


Figure 1.11. Benzoate adsorption along the <110> azimuth on Cu{110}.

At low coverages the benzoate species lie flat and parallel to the surface, attributed to maximising the surface to molecule bond via both the carboxylate and π -electron system of the phenyl ring. The RAIR spectrum has confirmed that at low coverage the surface is dominated by flat lying benzoate species which form the 'template' for a second upright species which inserts between four of the flat lying molecules ^[31]. As the coverage increases to saturation the flat lying species reorientates perpendicular to the surface ^[31]. In contrast to this, benzoic acid adsorbs to the Cu{111} surface only in an upright orientation for all coverages. The formation of the flat lying species has been attributed to a higher equilibrium concentration of Cu adatoms on the surface. The {110} face possesses a higher surface energy and therefore greater Cu mass transport from step and kink sites occurs during adsorption of the carboxylate ^[31].

When Na is pre-dosed onto the Cu{111} surface (<0.04ML) and then an increasing coverage of benzoic acid is coadsorbed, Na being sufficiently mobile at room temperature to avoid being trapped at step edges, the RAIRS data indicate that the surface is dominated by flat lying species at low benzoate coverage. As the benzoate coverage increases the IR bands associated with a flat orientation are attenuated and replaced by bands for the upright species ^[31]. This behaviour is identical to that observed on Cu{110}. Since Na is not known to induce surface reconstruction on Cu{110} and as Cu{111} is the most thermodynamically stable face the similarity of the molecular reorientation behaviour indicates that it is the metal adatoms that are required for the formation of the flat lying species ^[31].

In terms of the relevance to catalysis, what possible relationship exists between the effects of corrosive chemisorption and the addition of the secondary modifiers? These two ‘processes’ do not appear to complement one another. A catalyst consisting of larger nickel particles possesses a higher enantioselectivity and the effect of corrosive chemisorption removes the smaller nickel particles. So why does the enantioselectivity then increase when a secondary modifier is added that reduces the extent of corrosive adsorption whilst still increasing the enantioselectivity? Perhaps the non-selective sites exist on the smaller nickel particles and, as stated in the literature^{[5][9]}, the addition of Na then blocks these unselective sites. It would then appear that Na may also function as a stabiliser for these smaller Ni particles and reduce the amount of Ni leached into the modification solution.

1.3.2 System Variables

The three main points of debate may be directly related to each other but it is the preparation and reaction conditions that ultimately determine the properties that the catalysts possess. Small changes in one factor of the modification and reaction process often means there is a snowball type effect with several other important factors changing greatly. This explains why there are many conflicting reports in the literature with apparently similar experiments giving very different results^[30]. For this reason a summary of the different factors and how they affect the catalyst properties shall be given.

1.3.2.1 Modification Variables

It is well documented that variation of modification time, temperature, concentration and pH of the modification solution have an important influence on enantioselectivity of the modified nickel catalyst, including its direction and the amount of adsorbed modifier on the catalyst ^{[9] [30]}.

1.3.2.1.1 Modification Time

The uptake of tartaric acid has been shown to be time dependent and characterised by an initial rapid uptake followed by a slow attainment to the final level of adsorption ^[30]. Treatment times vary depending on the study with times of 10 to 60 minutes needed to achieve equilibrium level of adsorption on their supported catalysts ^{[30][33]}. However, the time required for the tartaric acid adsorption to reach a maximum decreases with increasing modification temperature ^[33] whilst the modification time in the absence of agitation has been shown to require a 5-fold increase to achieve the same adsorption of modifier with agitation ^[30].

At lower modification times, catalysts containing higher tartaric acid concentrations have been shown to both pass through a maximum ^[33] and have no effect on enantioselectivity ^[34]. In contrast, Fu and co workers ^[35] have shown that longer modification times result in catalysts with higher enantioselectivity.

1.3.2.1.2 Modification Temperature

Modification temperature has produced varying accounts in optimum selectivity with values ranging from 323K, 328-333K and 343-353K ^[30]. In some special cases, such as the modification at different temperature with (S)-glutamic acid, two kinds of MNi

catalyst are prepared. (S)-Glu-MNi modified below 353K produces (R)-MHB, whilst above 373K (S)-MHB is produced. This indicated the possibility that there are two kinds of differentiating sites functioning in opposite directions on the surface of the catalyst. If the proportion of this site is temperature dependent then the overall optical yield and direction of enantioselectivity may significantly change from one direction to the other. The ratio of these two sites is said to be an important factor in deciding the degree of enantioselectivity on MNi^[9].

1.3.2.1.3 Modification pH

Studies show a rather complex dependence on enantioselectivity suggesting that there exist optimum modifying pH at 3.0, 5.0, 5-9 and 10 for obtaining an effective catalyst when modified with an optically active acid, depending on the report^[9]. One hydroxy acid containing a phenyl group gave two kinds of MNi with different directions of enantioselectivity by modifying below and above pH 10.5. This indicated enantioselectivity depends on the density of differentiating sites and on the ratio of two kinds of differentiating sites^[9].

1.3.2.1.4 Modifier Solvent

The solvent used also plays an important role in determining the amount of modifier adsorbed on the metal surface. Alcoholic solvents with a lower polarity, gave an observed increase in modifier adsorption^[30]. However, this is in contrast with the solubility of tartaric acid, which decreases in alcoholic solvents with a lower polarity and therefore aqueous solvents give tartaric acid greater solubility. In other words, the lower the solubility of tartaric acid in the chosen solvent, the greater adsorption of tartaric acid onto the supported metal and hence increase in the number of adsorbed

tartaric acid molecules ^[30]. The degree of enantioselectivity also decreases with increasing polarity of the alcohol, so the greater solvation strength of the more polar alcohols must therefore interfere with the modifier/reactant interaction that determines enantiocontrol ^[30].

1.3.2.1.5 Modifier Concentration

There are many differences in the results that have been obtained for the modifier concentration and several studies have proposed that the enantioselectivity reaches a plateau and upon further increase of concentration, the enantioselectivity is unaffected ^[30]. However, Keane *et al* ^[33] have reported that the number of adsorbed tartaric acid molecules decreases with higher tartaric acid concentration resulting in a reduction in the enantioselectivity. This observation has been attributed to the greater degree of nickel leaching as tartaric acid concentration increases.

1.3.2.1.6 Corrosive Adsorption

From testing the nickel content in the “post-modifier” it was observed that leaching into solution occurs to a lesser extent in alcoholic media and is suppressed by less polar alcoholic solvents. The effect of alcoholic solvents as modifying medium can be said to stabilise the surface Ni-tartaric acid formation and generate greater concentration of supported enantioselective sites ^[30].

In a study with modifying conditions of $t_{\text{mod}}=2\text{h}$, $T_{\text{mod}}=323\text{K}$ and $[\text{tartaric acid}]=0.03\text{M}$ a loss of ~30% of the initial metal loading recorded with aqueous treatment compared to ~3% in the case of ethanolic treatment. The metallic dispersion, expressed as $(\text{Ni}_{\text{surface}}/\text{Ni}_{\text{total}})\times 100\%$, initially measured as 33% for the freshly reduced catalyst

dropped to 23% and 31% after treatment in aqueous and ethanolic solvent respectively. This represented a shift in average surface weighted particle size from 3.1 to 4.4 nm as a result of aqueous treatment, supporting the suggestion that smaller nickel crystallites are preferentially leached from the catalyst ^[30].

1.3.2.2 Reaction Variables

Reaction temperature was found not only to change the optical yield but also the configuration of the predominant product. These findings indicate the possibility that two enantioselective reactions, producing the (R)- and (S)- products, were carried out side by side in the reaction system. The change of configuration of the predominant product could be due to the change in surface metal which generates a higher functionalised coverage of the remaining metal particles by the modifier ^[9].

1.3.2.2.1 Reaction Temperature

The optical yield and product configuration is strongly dependent on the reaction temperature suggesting the possibility that two enantioselective reactions may be carried out side by side ^[9]. The change of configuration may also be attributed to a change in the nature of the interaction between the modifier and reactant ^[9].

Changing the reaction temperature from 333K to 373K in a high pressure liquid phase hydrogenation did not strongly affect the optical yield. On the other hand, when the reaction was carried out at ambient pressure and the temperature altered, complex changes in optical yield were observed ^[5]. Ozaki ^[39] has proposed that the choice of modifier is highly specific in the determination of both the yield and product configuration. In the case of R,R-H₂TA, the optical yield passed through a maximum at

~50°C for hydrogenation at atmospheric pressure and dropped rapidly either side of this maximum ^[39].

1.3.2.2.2 Hydrogen Pressure

The effect of hydrogen pressure on the optical yield of enantioselective hydrogenation of MAA, found that the optical yield decreases with increasing pressure of hydrogen up to 10^6 Pa ^[28] and optical yield is expected to be insensitive to hydrogen pressure from 2.5×10^6 to 10^7 Pa. In the range 10^5 to 3×10^6 Pa complicated changes in the optical yield were observed ^{[5][28]}. However, once again other reports give conflicting results. One such report claims that the asymmetric process is independent of the hydrogen pressure ^[5] whilst hydrogenation of unmodified nickel catalysts at atmospheric pressure has been shown not to proceed in the liquid phase because of corrosion of the catalyst ^[9].

The combination of bubbling hydrogen at a fixed rate through the catalyst/substrate suspension under constant agitation resulted in conversions and enantioselectivities that were reproducible to $\pm 2\%$ and $\pm 4\%$ respectively. At low hydrogen flow rates and/or agitation reaction time required to convert MAA to the same level of MHB was up to 80 hours ^[30]. The apparent reaction rate was found to be independent of stirring speeds between 600-800rpm but below 600rpm, reaction rates showed a marked decrease, due to diffusion limitations ^[30].

1.3.2.2.3 Reaction Solvent

The reaction solvent has been shown to both influence and have no effect on reaction rate and selectivity ^[30]. The rate of hydrogenation was found to be dependent on the dielectric constant of the solution. The best rates were observed in alcoholic media

followed by semipolar solvents such as methyl propionate, ethyl acetate and tetrahydrofuran (THF) [30]. Orito *et al* have shown that the semipolar solvents of ethyl acetate and THF gave the highest optical yields whilst methanol and ethanol gave poor result [5].

Transesterification of the β -keto ester has been observed at higher reaction temperatures [30], therefore the choice of solvent is significant in the formation of the required products.

1.4 Aims and Objectives

The industrial application of catalysis is a multi-billion dollar industry involving a massive number of processes, many of which are well understood. However, with the ever increasing need for the production of optically pure compounds, the understanding of the subtle interactions that are required for the development of heterogeneous enantioselective catalysts have proved beyond the limits of heterogeneous catalysis.

At present, the heterogeneous catalytic studies in this system are confusing with very little coherence between studies for just about every factor that determines the enantioselectivity. It would therefore appear that a more fundamental study of this system is required to establish some light on the genuine influence of each of the preparation, modification and reaction variables.

The aim of this research is therefore to use surface science in order to investigate the interactions of R,R-H₂TA on Ni{111} by dosing R,R-H₂TA under controlled conditions

onto a model catalyst surface. These well defined catalyst surfaces can then be tested for activity and selectivity in the liquid phase hydrogenation of MAA with a fewer number of experimental variables and hence more reliable information. Testing each of the different parameters independently and combining the results may yield information that aids the design of a catalyst with better activities and selectivities.

In chapter 2, a discussion of the principles behind the use of ultra high vacuum (UHV) conditions along with a summary of the techniques that are to be employed in this study will be given. Chapter 3 consists of the study of the interaction of R,R-H₂TA with the metal surface in terms of the molecular orientation and 2D packing on the surface that may determine the formation of the enantioselective sites. Chapter 4 shall follow on from the study in chapter 3 by observing the behaviour of the reactant molecule MAA on the metal surface. The interaction of MAA with that of the modified surface has also been studied in order to determine the modifier-reactant orientation and interactions that may form the sites for the hydrogenation of MAA to (R)-MHB. The design and building of the liquid/high pressure cell and vacuum chamber shall be discussed in chapter 5. Liquid phase hydrogenation reaction are reported on Ni{111} and R,R-H₂TA modified Ni{111} that have been prepared in the UHV chamber then transferred into the liquid/high pressure cell. The activity and selectivity of the reactions shall be monitored by gas chromatography (GC) fitted with a chiral separating column. In chapter 6, discussion of the employment of medium energy ion scattering (MEIS) to establish the possible effects of corrosive leaching of metal atoms by the modifier R,R-H₂TA in the Cu{110} system shall be given. Chapter 7 shall conclude this PhD thesis by summarising the previous 4 chapters the combination of which may yield information that has direct relevance and implications to the catalytic hydrogenation reaction. A

brief discussion into future experiments and experiments already completed that have a relevance to this study shall also be presented.

1.5 References

- [1] R Stevenson; *Chem. Br.* **37**, 11 (2001) 24
- [2] www.nobel.se/chemistry/laureates/2001/chemadv.pdf
- [3] SM Barlow, KJ Kitching, S Haq and NV Richardson; *Surf. Sci.* **401** (1998) 322
- [4] TD Stephens; *Chem. Br.* **37**, 11 (2001) 38
- [5] A Tai and T Harada; *Tailored Metal Catalysts*, Y Isawawa (ed.), D Reidel Publishing Company, 1986. 265
- [6] HU Blaser, F Spindler and M Studer; *Appl. Catal. A.* **221** (2001) 119
- [7] GC Bond; *Heterogeneous Catalysis – Principles and Applications*. 2nd Edition, PW Atkins, JSE Holker and AK Holliday (eds.), Oxford Science Publications, 1987. 86
- [8] G Webb and PB Wells; *Cat. Today* **12** (1992) 319
- [9] Y Izumi; *Adv. Cat.* **32** (1983) 215
- [10] PW Atkins; *Physical Chemistry*. Fifth edition, Oxford University Press, 1994. A) 761, B) 517
- [11] MA Keane; *Can. J. Chem.* **72** (1994) 372
- [12] M Bowker, E Rowbotham, FM Leibsle and S Haq; *Surf. Sci.* **349** (1996) 97
- [13] MA Keane; *J. Chem. Soc. Faraday Trans.* **93**, 10 (1997) 2001
- [14] A Hoek and WMH Sachtler; *J. Catal.* **58** (1979) 276
- [15] MA Keane. *Langmuir* **10** (1994) 4560
- [16] JA Groenewegen and WMH Sachtler; *J. Catal* **38** (1975) 501
- [17] S Nakagawa, A Tai, T Okuyama and T Sugimura; *Topics in Catalysis.* **13** (2000) 187
- [18] MO Lorenzo, S Haq, T Bertrams, P Murray, R Raval and CJ Baddeley; *J. Phys. Chem. B.* **103** (1999) 10661

- [19] MO Lorenzo, CJ Baddeley, C Muryn and R Raval; *Nature*. **404** (2000) 376
- [20] A Bandara, J Kubota, A Wada, K Domen and C Hirose; *J. Phys. Chem. B*. **101** (1997) 361
- [21] M Bowker, S Haq, R Holroyd, PM Parlett, S Poulston and N Richardson; *J. Chem. Soc. Faraday Trans.* **92**, 23 (1996) 4683
- [22] JA Groenewegen and WMH Sachtler; *J. Catal.* **33** (1974) 176
- [23] J Hasselstrom, O Haris, M Weinelt, N Wassdahl, A Nilsson, M Nyberg, LGM Pettersson, MG Samant and J Stohr; *Surf. Sci.* **407** (1998) 221
- [24] A Ihs, B Liedburg, K Udval, C Tornkvist, P Bodo and I Lundstrum; *J. Colloid Int. Sci.* **140** (1990) 192
- [25] NA Booth, DP Woodruff, O Schaff, T Giessel, R Lindsay, P Baumgartel and AM Bradshaw; *Surf. Sci.* **397** (1998) 258
- [26] J Williams, S Haq and R Raval; *Surf. Sci.* **368** (1996) 303
- [27] LJ Bostelaar, RAD der Graaff, F B Hulsbergen, and J Reedijk; *Inorg. Chem.* **23** (1984) 2294
- [28] Y Nitta, F Sekine, J Sasaki, T Imanaka and S Teranishi; *Chem. Let.* (1981) 541
- [29] Y Nitta, F Sekine, T Imanaka and S Teranishi; *Bull. Chem. Soc. Jpn.* **54** (1981) 980
- [30] MA Keane; *Langmuir* **13** (1997) 41
- [31] CC Perry, S Haq, BG Frederick, Q Chen and NV Richardson; *Surf. Sci.* **409**, 3 (1998) 512
- [32] PDA Pudney, BG Frederick and NV Richardson; *Surf. Sci.* **307-309** (1994) 46
- [33] MA Keane and G Webb; *J. Catal.* **136** (1992) 1
- [34] S Tatsumi; *Bull. Chem. Soc. Jpn.* **41** (1968) 408
- [35] L Fu, HH Fung and WMH Sachtler; *J. Mol. Catal.* **42** (1987) 29
- [36] T Harada, M Yamamoto, S Onaka, M Imaida, H Ozaki, A Tai and Y Izumi; *Bull.*

Chem. Soc. Jpn. **54** (1981) 2323

[37] MA Keane and G Webb; *J. Chem. Soc. Chem. Commun.* (1991) 1619

[38] KE Simons, PA Meheux, SP Griffiths, IM Sunderland, P Johnston, PB Wells, AF Carley, MK Rajumon, MW Roberts and A Ibbotson; *Recl. Trav. Chim. Pays-Bas* **113** (1994) 465

[39] H Ozaki; *Bull. Chem. Soc. Jpn.* **51**, 1 (1978) 257

Chapter Two

Experimental Techniques

2.1. Introduction

Catalytic properties of surfaces are influenced by the composition and structure on the atomic scale. It is therefore essential to understand the complex structure of the metal surface in order to predict and design, better and cheaper catalysts with specific functions ^{[1A][2A]}.

A typical heterogeneous catalyst consists of small metal particles dispersed on high surface area/porous supports such as silica or alumina ^[1A] with each of the metal particles displaying different crystallographic planes or faces with structural defects and of indeterminate chemical composition ^[3A]. Each of the crystal faces have different atomic arrangements and overall this results in a large number of different available adsorption sites. In a fundamental study of surface structure it is far too complicated to study interactions of an adsorbate with all possible exposed crystal faces, therefore to simplify the problem it is common to look at one particular face using a single crystal. This limits the number of adsorption sites making data interpretation simpler and also by selecting specific crystal faces we are able to study the interactions on the faces that are catalytically relevant.

It is known that for fcc metals the equilibrium shape of the metal particles or clusters (the sizes of the clusters relevant in catalysis are >1nm) is that of a truncated

octahedron, figure 2.1 b ^[4]. This has also been supported from observations of supported metal clusters using electron microscopy and physisorption of gas molecules indicated that the metal clusters adopt this lowest surface energy shape ^[4-6].

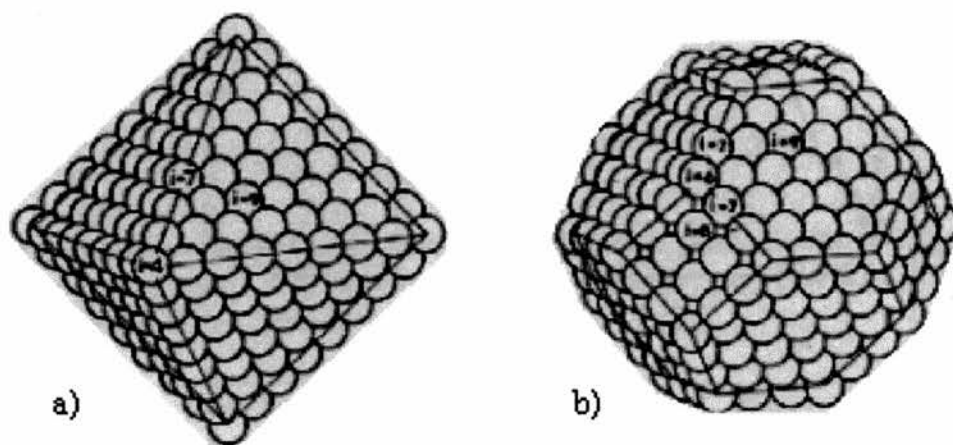


Figure 2.1. Regular fcc polyhedral metal clusters, a) octahedron, b) truncated octahedron ^[4].

The truncated octahedron shape may initially be formed from an octahedron with the faces being the $\{111\}$ crystal face (figure 2.1 a). However the low co-ordination corner atoms of the octahedron have a low stability, therefore the corners are ‘knocked off’ increasing the co-ordination number and introducing $\{100\}$ facets giving the overall more stable truncated octahedron (figure 2.1 b) ^[4]. Although not all particles have this shape, from a catalytic point of view, it seems more relevant that the crystal faces to study should either that of the $\{111\}$ or $\{100\}$ faces.

Traditionally surface science experiments are carried out in stainless steel vacuum chambers under ultra high vacuum (UHV) conditions to probe surface interactions at well defined single crystal surfaces using free particles such as electrons or ions. UHV conditions need to be employed because these particles can only be used at pressures of about 10^{-4} torr or lower otherwise their mean free path in the gas phase would be too

small ^[3A] and also because of contamination to the atomically clean surface. Under normal high vacuum conditions ($\sim 10^{-6}$ torr) a clean surface would become covered with a monolayer of contaminants, from the residual gas atmosphere, in ~ 1 s. In order to obtain a clean surface for the duration of an experiment, i.e. times of at least one hour, the base pressure of the chamber realistically needs to be in the order of 10^{-10} torr or lower ^{[3A][7]}. Also, many of the techniques employed for characterising the surface involve emitting and detecting electrons. Residual gas particles present in a vacuum chamber with a 'poor' base pressure would mean a higher probability that the electrons would be involved in collisions with residual gas particles and inhibit the electrons from reaching the sample and/or returning to the detector. The lower the quantity of gaseous particles in the residual gas, the greater the number of electrons that can reach the target and return to the detector increasing the quality and reliability of the information obtained. Therefore UHV conditions are essential for this type of fundamental study.

2.1.1 Electron Spectroscopies

Electrons strongly interact with matter. A monoenergetic beam of electrons with a kinetic energy, E_p , incident upon a solid surface will undergo either elastic or inelastic collision processes. Some of the electrons are scattered without energy loss (elastic scattering) but the majority interact with the surface and lose energy (inelastic scattering) ^[8A]. This energy loss is in a series of discrete (or sometimes continuous) loss events resulting in a broad spectrum of kinetic energies between zero and E_p ^[8A]. The intensity of electrons with well defined energies diminish as a function of distance into the solid and this decay follows the exponential first-order law:

$$I(d) = I_0 \exp \left(\frac{-d}{\lambda(E)} \right)$$

Where $I(d)$ is the measured intensity of the electron beam that has travelled through a distance d , I_0 is the initial intensity of the electron beam and $\lambda(E)$ is the inelastic mean free path (IMFP) of an electron at energy E as it passes through the material ^[8A]. The IMFP is defined as the distance an electron beam can travel before its intensity decays to $1/e$ of its original value and is therefore an average of how far an electron can travel before losing its energy ^[9A]. Electrons with an IMFP of 5 \AA that manage to escape into the vacuum must have originated from the first few surface layers and they are therefore highly surface sensitive as the IMFP is only weakly dependent on the material it is passing through but highly dependent on kinetic energy. This dependence can be illustrated using the 'universal curve' for metals ^[7B-8A] illustrated in figure 2.2.

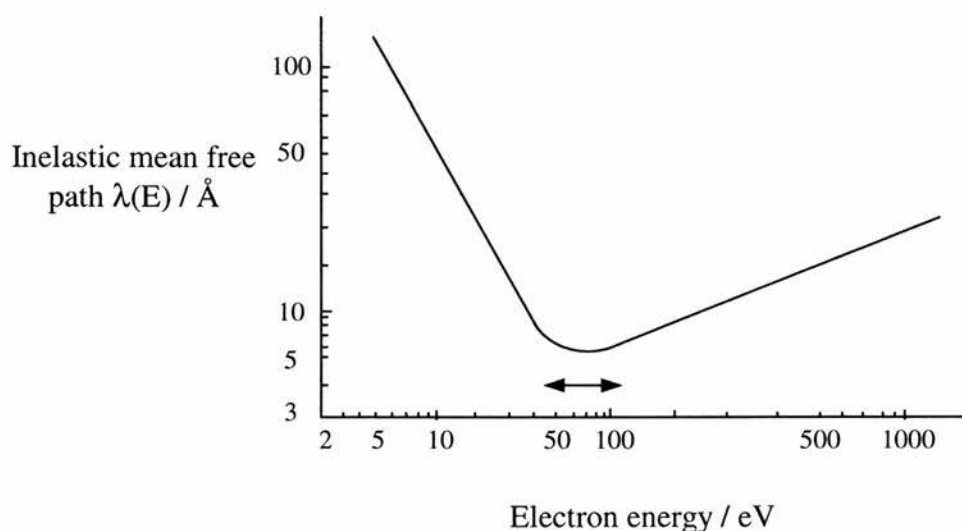


Figure 2.2. 'Universal curve' relating IMFP with electron energy ^{[2A][8A]}.

The shape of the curve, rationalised by differences in electron velocity and removal of energy loss processes, means that electrons with kinetic energies that are covered by the double headed arrow are the most surface sensitive ^{[2A][8A]}.

The requirement for UHV conditions for many surface analytical techniques prevents the application of these methods in the pressure conditions typically employed in heterogeneous catalysis, which are often at atmospheric pressure or higher and elevated temperature. There are several ways that the so called ‘pressure and structure gap’ that exists between surface science and catalysis can start to be bridged ^[10]. The study of metal nanoparticles deposited onto planar oxide surfaces using surface science techniques may help to bridge the structure gap as the surface structure is more similar to catalyst particles than the single crystal. Likewise, to bridge the pressure gap, various techniques have been developed to monitor surfaces at the gas/solid or liquid/solid interface, e.g. photoelastic modulation reflection adsorption infrared spectroscopy (PM-RAIRS), scanning tunnelling microscopy (STM) and atomic force microscopy (AFM) ^[10-11].

2.2 Surface Spectroscopic Techniques

Classical thermodynamic and kinetic methods for characterising catalyst surfaces yield data giving an ‘average’ understanding of the system properties rather than atomic/molecular specificity ^[8B]. A comprehensive understanding of the surface properties requires the surface phenomena to be probed on a molecular level, using surface science techniques.

The generic surface science experiment is one that uses electrons, photons, ions or helium atoms in order to probe the surface which can give valuable information on the properties of the surface.

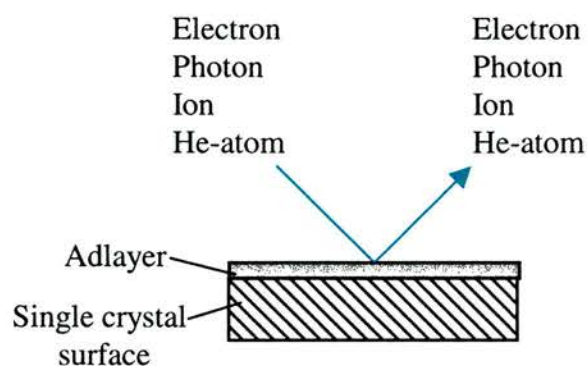


Figure 2.3. Generic surface science experiment.

Many spectroscopies are based on either some sort of excitation or scattering process that occurs inside the surface region or the bulk. For a technique to be called surface sensitive it must yield particles or radiation that has evolved or been scattered from the outermost layers of the sample ^[1A].

To characterise the surface fully, there are several questions that need to be answered.

1. What atoms are present on the surface and in what concentration?
2. Precisely where are these atoms/molecules located and what orientation do they possess?
3. How strongly do the atoms/molecules interact with the surface and each other?
4. How does the nature of their interaction affect the surface in terms of reactivity and selectivity? [8B]

No single spectroscopic technique is capable of answering all of these questions fully, therefore in surface science a multi-technique approach is used in which a range of surface sensitive probes are used to gain complementary information into the surface properties.

The surface chemical composition can be examined using AES techniques whilst the surface structure can be studied using LEED and STM. Investigations into molecular orientation and bond strengths can be elucidated using IR and TPD spectroscopies.

2.2.1 Low Energy Electron Diffraction (LEED)

LEED is one of the most important and commonly used techniques for the determination of the long range ordering of periodic surface structures ^[3A]. The technique uses a beam of monoenergetic low energy electrons, in the range of 20-200eV, emitted from a filament. These electrons are accelerated into a drift tube enclosed within an electron gun towards an earthed single crystal sample with a well-ordered surface structure. Electrons in this energy range possess an inelastic mean free path of between about 5 and 10 Å and hence a high surface sensitivity ^[1C]. The beam of electrons may also be regarded as a series of electron waves, a consequence of wave-particle duality ^[9B]. In this energy range, they possess de Broglie wavelengths of the same order of magnitude as atomic spacings that enables diffraction with the periodic array of surface atoms ^[8C-9B]. The typical experiment is displayed in figure 2.4.

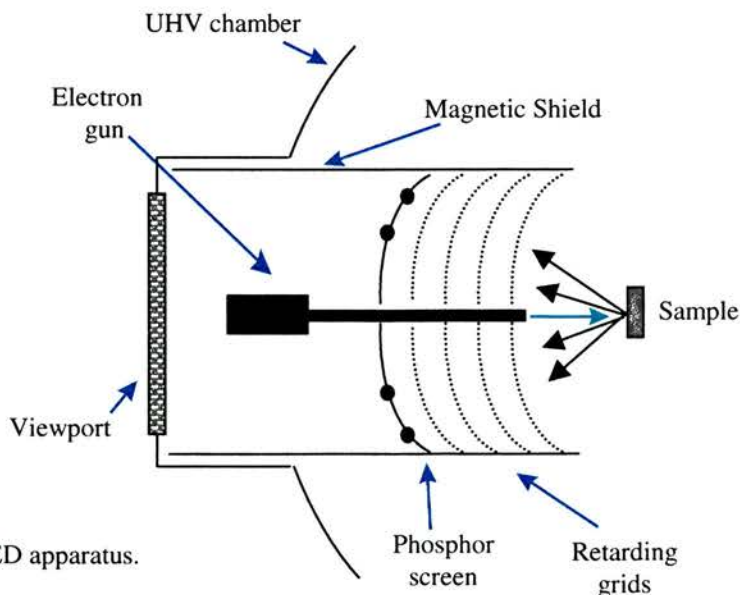


Figure 2.4. LEED apparatus.

The electron beam that has undergone diffraction with the surface travel towards a series of concentric retarding grids. The two outer of the four retarding grids are biased to ground potential to ensure the electrons travel in a 'field free' region ^[8A]. The inner two are negatively biased at ~97% of the incident energy and then finally the electrons are accelerated to a phosphor screen that is biased to ~5-6KeV. The retarding grids ensure that only electrons that meet Bragg's condition and undergo constructive interference can pass through towards the screen ^[3D] whilst the screen is biased to accelerate the transmitted electrons with sufficient kinetic energy to stimulate emission of visible photons from the phosphor screen. On the screen, diffraction 'spots' can then be observed. The observed LEED pattern gives information on shape, size and symmetry of the 2D unit cell and variations in unit cell induced by absorption ^[3C].

2.2.1.1 Theory

The principle behind LEED can be illustrated by electron diffraction from a 1D periodic chain of atoms.

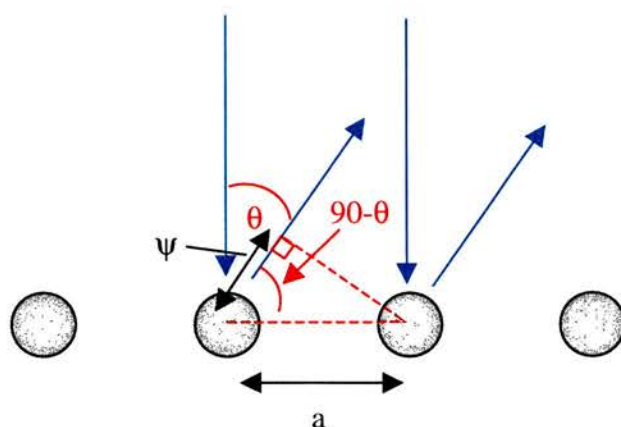


Figure 2.5. Illustration of electron diffraction in the LEED technique.

An incident electron beam that is scattered by a row of atoms, periodically spaced with a separation a , and scattered at an angle θ , will undergo constructive interference if the scattered electron waves from neighbouring atoms have a path difference ψ , that are multiples of the de Broglie wavelength, $\psi = n\lambda$ ^[3C]. When this occurs, the Bragg condition has been met and the path difference is given by:

$$n\lambda = a \sin \theta$$

where λ is the de Broglie wavelength of the electron and is constant for fixed incident electron kinetic energy. Rearranging the equation we obtain the expression:

$$\sin \theta = \frac{n\lambda}{a}$$

This expression states that for a fixed wavelength and lattice spacing, only well defined values of θ are allowed for constructive interference to be observed ^[8C]. Therefore, this expression illustrates that discrete diffracted beams will be observed at specific angles and that the angle of the observed diffraction 'spot', $\sin \theta$, is inversely proportional to the lattice spacing, a . The observed diffraction feature is therefore the reciprocal space view of the real space structure and a large separation between the spots on the LEED pattern indicates a small inter-atomic distance and visa versa ^[1C]. Similarly, if the lattice constant, a , is fixed and the kinetic energy of the electrons is increased (a decrease in λ) then θ will increase and the diffracted beams will move closer together ^[8C]. This concept plays an important part in interpreting diffraction data.

For a satisfactory LEED pattern to be obtained, the domains of ordered structure need to be uniform over about 50\AA or more on the surface. The longer range the order of the surface overlayer or the more ordered domains with a size $>50\text{\AA}$, the better the observed

LEED pattern is in terms of sharp bright diffraction features and a lower background intensity.

All LEED experiments were carried out using Omicron SpectraLEED optics and the electron beam was produced by thermionic emission from an LaB₆ filament.

2.2.2 Auger Electron Spectroscopy (AES)

This technique, that takes its name from Pierre Auger who first reported this effect, provides a highly surface sensitive elemental analysis of the sample. The basis of this technique is to bombard an earthed surface with an electron beam possessing a kinetic energy in the range of 1 to 10 keV ^[1D]. The first of the three step processes is to create a core hole or electron vacancy in atoms of the sample. The excited atoms relax by an electron from a higher shell (an electron level of lower binding energy), known as the down electron filling the vacant hole ^{[1D][8D]}. A quantum of energy (equal to the difference in binding energy between the core hole and down electron) is emitted. This quantum of energy either escapes into the vacuum as an X-ray photon (X-ray fluorescence) or in an Auger transition by the emission of a second (Auger) electron ^[8D].

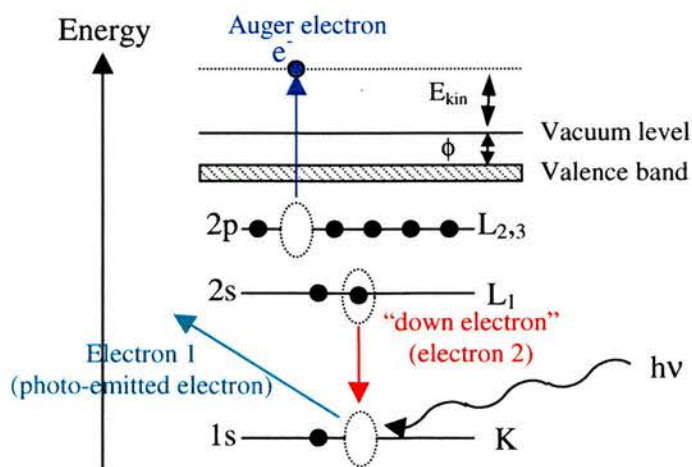


Figure 2.6. Energetics of the Auger process ^[8D].

It is these secondary electrons that are detected and the kinetic energy of the electron, E_{kin} , is entirely determined by the energy levels associated with the emission and not by the energy of the primary electrons ^[1D].

The kinetic energy of the Auger electron can be given by the expression ^[8D]:

$$E_{kin} = \boxed{E_K - E_{L1}} - \boxed{E_{L2,3} - \phi}$$

Energy available to the Auger electron from the 'down' electron

Energy required to overcome barrier to emission from within atom

where ϕ is the work function of the solid, that is the minimum energy required to remove an electron from the highest occupied energy level in the solid to the 'vacuum level' ^[8B]. It can be seen from this equation that the kinetic energy of an Auger electron is characteristic solely of the binding energies within the specific atoms and their detection can be used as a means of elemental analysis. Most elements have Auger electron transitions in the energy range $0 < E < 1000\text{eV}$, such as C and O that have Auger electron energies of $\sim 270\text{eV}$ and $\sim 520\text{eV}$. The IMFP for these elements is $\sim 10\text{\AA}$ or less so detection of these elements must have originated from the near surface region.

The most common type of AES spectrometer and the type that is used in this study is the Retarding Field Analyser (RFA), a reason for this is because RFAs can also be used for LEED measurements ^[2C]. As with LEED the sample sits at the centre of the concentric spherical centre grids. The first grid, nearest the sample is set at ground potential to ensure the electrons leaving the sample travel in a field free region ^[2C]. In LEED the diffracted beams are observed on the fluorescent screen but in AES the screen acts as a

collector of electrons. The grids in front of the screen are set at a potential, V_0 , corresponding to a minimum pass energy of

$$E_0 = eV_0$$

so only electrons possessing energies greater E_0 are able to reach the screen and counted whilst all electrons with a lower energy are retarded. The electrons that reach the screen must therefore have a kinetic energy between that of the retarding voltage V_0 and the primary beam energy E_p . Therefore the current arriving at the detector is given by

$$\int_{E_0}^{E_p} N(E) dE$$

where $N(E)$ is the number of electron states having an energy, E . If this current is differentiated it is therefore possible to obtain the desired energy distribution of the different electron energies. This is achieved by applying an additional small modulation voltage, $\Delta V \sin \omega t$, to the retarding voltage, V . Therefore the current arriving at the detector is given by

$$\int_{E_0}^{E_p + \Delta E} N(E) dE$$

and results in an energy distribution $N(E_0)\Delta E$. Therefore the number of electrons possessing a particular kinetic energy can be counted ^[2C].

This type of modulation leads to problems, as the Auger peaks are small and superimposed on a large secondary electron background. It is therefore necessary to display the electron energy distribution as a derivative to yield a $dN(E)/dE$ curve ^[8D]. This can be achieved electronically as the current arriving at the detector is expressed as a sum of harmonics in which the amplitude of the second harmonic ($\sin 2\omega t$) is proportional to $dN(E)/dE$ ^[2D]. Therefore, measurement of the second harmonic by the

use of a phase sensitive detector results in a plot of $dN(E)/dE$ ^[3D]. To a first approximation, the peak to peak height for individual Auger peaks on the $dN(E)/dE$ spectrum is proportional to the surface concentration of an element ^[8D].

All AES experiments were carried out using Omicron RFA SpectraLEED optics with the electron beam produced by thermionic emission from a LaB₆ filament. The optics are interfaced to a PC and analysed using DAT 100 software.

2.2.3 Infrared Spectroscopy (IR)

Infrared spectroscopy is the most common form of vibrational spectroscopy and is often considered the first and most important of the modern spectroscopic techniques that has found general acceptance in catalysis ^[1B]. Infrared provides specific information on the type of bonds present in a molecule or adsorbed species in terms of their identity and the way in which they chemisorb on the surface of the catalyst ^[8E]. One of the greatest advantages of this technique is that it yields the information in a non-destructive way and doesn't require UHV conditions therefore the technique is very versatile ^[1B].

Molecules possess discrete levels of rotational and vibrational energy and transitions between vibrational levels can occur by adsorption of infrared photons. However, as a rule the only allowed transitions are those where the vibrational quantum number changes, Δv , by ± 1 ^[9C].

The number of fundamental vibrations is given by the formula:

$$3N-6 \text{ (for non-linear molecules)}$$

$3N-5$ (for linear molecules)

where N is the number of atoms ^[9C]. There are four types of vibrations that can occur in a molecule:

1. Stretching vibrations (ν) – changing of the bond length;
2. Bending vibrations in one plane (δ) – changing of bond angles whilst the bond length remains the same;
3. Bending vibrations out of plane (γ) – one atom oscillates through a plane defined by at least three neighbouring atoms;
4. Torsion vibrations (τ) – the angle between two planes changes. ^[1B]

The frequencies of these vibrations decrease in the order $\nu > \delta > \gamma > \tau$ ^[1B]. Stretching vibrations also tend to be split into symmetric (ν_{sym}) and asymmetric (ν_{asym}) stretches that are independent of each other, i.e. excitation of one does not induce excitation of the other ^[9C] and ν_{asym} occurs at higher frequency than ν_{sym} . The observed vibrational frequencies tend to increase with increasing bond strength and with decreasing mass of the vibrating atoms ^[1B].

Infrared spectroscopy is most commonly used in the transmission mode, i.e. the infrared beam passes through the sample and the beam intensity analysed as a function of frequency. However it is quite frequent for the sample to be opaque to infrared radiation, so the technique can be used in reflection mode. Reflection absorption infrared spectroscopy (RAIRS) is carried out on flat surfaces, in this case a single crystal in UHV ^[8E].

In RAIRS the incident infrared beam (I_0) is aligned at a grazing angle with respect to the surface, typically $\sim 3^\circ$. During reflection the p-component of the IR light, i.e. the component perpendicular to the surface, excites those vibrations of the chemisorbed molecule for which the component of the dipole perpendicular to the surface changes. The reflected beam (I) is detected for the losses due to the molecular vibrations.

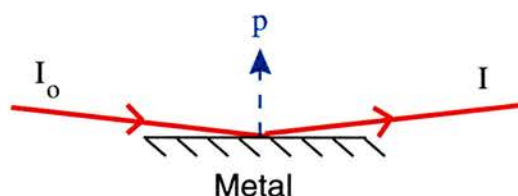


Figure 2.7. Illustration of the IR beam alignment with respect to the surface in the RAIRS technique.

In order for a vibration to be infrared active there must be an accompanying change in the electric dipole moment. Surface dipole selection rules dictate that the vibrations will only be observed if the dipole change has a component which is perpendicular to the surface ^{[1B][8E]}. This can be illustrated in figure 2.8.

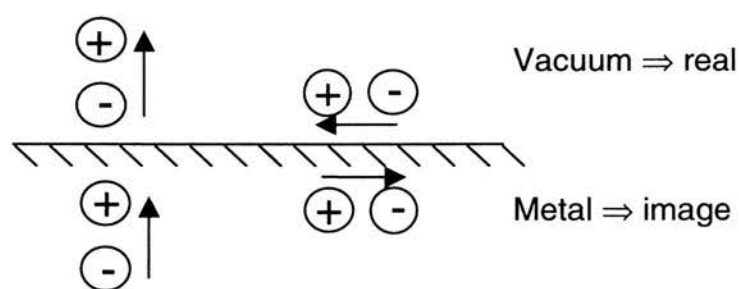


Figure 2.8. Illustration of the surface dipole selection rule ^[8E].

If the change in dipole moment is parallel to the surface, i.e. possess no p-component, then the image dipole will cancel out the actual dipole and the vibration will not be observed. However, if the dipole change does have a component perpendicular to the surface then the image dipole will reinforce the actual dipole and will be observed. This

is an important aspect of this technique as it enables the determination of molecular orientation.

The infrared beam is analysed by means of a Michelson interferometer and the resulting signal obtained from the detector is known as an interferogram^[13A]. The interferogram is a scan of the sum of all the information required to produce the spectrum and specific information, such as the wavelength can be obtained via the mathematical process called Fourier transformation to acquire a spectrum of intensity vs wavelength^[13A]. The Fourier transformed spectrum contains all vibrational information including the vibrations of the surface species and impurities on the mirrors and in the detector chamber. The unwanted vibrations can be removed by first running a ‘background spectrum’ of the pre-dosed surface, subsequent spectra can be reprocessed against the background and should leave a spectrum of only the vibrations associated with the adsorbed species. The path of the IR beam external to the UHV system is also purged with dry air to minimise the adsorption bands of gas phase water molecules and CO₂. A problem with infrared techniques is that in a single monolayer film, there are typically less than 10¹⁵ molecules cm⁻² and owing to the small number of absorbing molecules, only 2-3% of the beam is absorbed. Therefore the small signal from the absorbing molecules is hidden within the large reflected beam and can reduce the signal to noise ratio^[8E]. Any molecules on the surface which obey the selection rule will absorb a specific amount energy from the beam and excite vibration modes, which are characteristic of the specific bond vibration mode. It is common in spectroscopy to specify the wavelength of the radiation as a closely related quantity, the wavenumber $\bar{\nu}$, where $\bar{\nu}$ is given by

$$\bar{\nu} = \frac{1}{\lambda}$$

and has units of cm^{-1} .

The RAIRS experiments were carried out in an Omicron UHV system with a base pressure of 1×10^{-10} torr using a Nicolet Magna-IR 860 spectrometer equipped with a mercury cadmium telluride (MCT) detector interfaced to a PC and analysed using Omnic ESP software.

2.2.4 Scanning Tunnelling Microscopy (STM)

STM has become a powerful tool for imaging the local surface topography of a planar conducting sample with atomic resolution using a tip of molecular dimensions since the early 1980's [1E]. The technique is very versatile and can be used for imaging in a variety of different environments ranging from UHV to the liquid-solid interface and at temperatures of liquid helium to considerably above room temperature, e.g. 1000K.

The principle behind this technique is that if two conductors are brought extremely close to each other but are not physically touching each other, a current will flow between them if a potential difference is applied. This is because the electron wavefunctions at the Fermi level are not entirely confined to their potential wells but extend into the vacuum with a characteristic exponential inverse decay length K . This is given by:

$$K = \left(\frac{2\pi}{h} \right) (2m\phi)^{1/2}$$

where h is Planck's constant, m is the electron mass and ϕ is the effective local work function. Taking a typical value of ϕ of 4 eV, K can be calculated to be about 1 \AA [9D]. This means that the wavefunction decays to $1/e$ of their amplitude within 1 \AA of the

surface. Therefore if the two conductors are brought sufficiently close together, to within a few Ångströms, the electron wavefunctions start to overlap and quantum mechanical tunnelling occurs and a current will flow across the gap. The tunnelling current is in the range of pA or nA and varies exponentially with distance ^[1E].

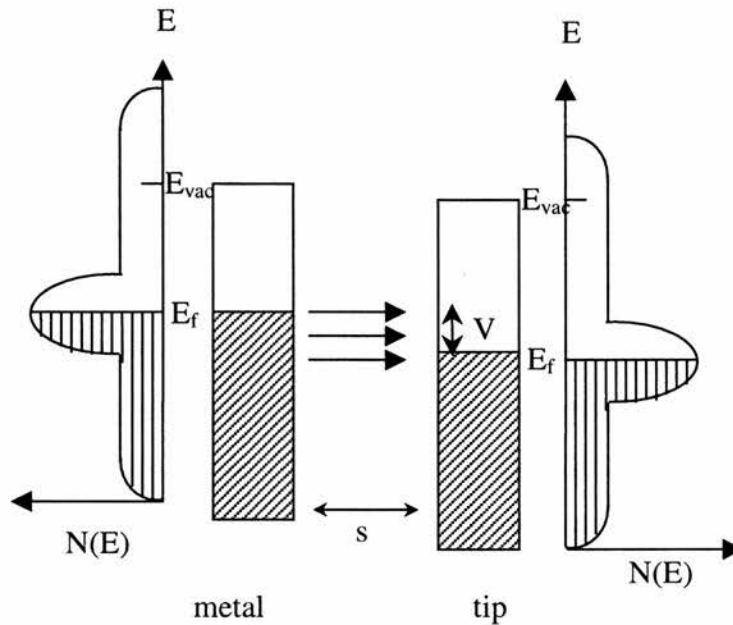


Figure 2.9. Principle behind tunneling between a metals surface and STM tip ^[1E].

In STM, an atomically sharp tip approaches the surface of a planar conductor, in this case a single crystal. The diagram above shows how when a small positive potential, V , is applied to the tip, a measurable tunnelling current is induced flowing from the occupied states of the metal into the unoccupied states of the tip. The voltage V , shifts the position of the electrons in the metal up with respect to those of the tip. If the separation s is small enough electrons can tunnel and the STM images the density of occupied states. Changing the bias on the tip to a small negative value, the current flows in the reverse direction and the unoccupied density of states are imaged. The scanning tunnelling microscope is illustrated in figure 2.10.

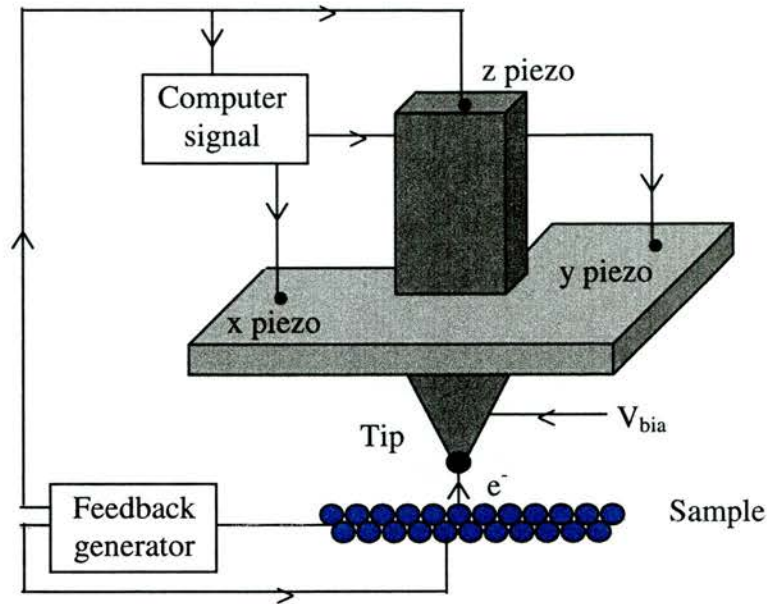


Figure 2.10. Experimental apparatus used in STM ^[8E].

The STM tip ideally contains of a single atom at its apex and can easily be prepared by cutting or electrochemical etching in aqueous solution. The tip is mounted on the STM head that is controlled by piezoelectric crystals that expand and contract by $\sim 1\text{\AA}$ per millivolt enabling precision control over the tip ^[8E].

Vibrations, thermal drift and electronic noise are three main factors that limit the ability of the control of the tip and to acquire a good resolution in the image. This means that the STM is operated in a quiet, air conditioned room to avoid acoustic room vibrations and reduce thermal drift. The STM head is also mounted on an assembly that consists of soft springs or using eddy currents to damp unwanted vibrations ^[8E].

There are two basic modes of operation, constant current or constant height modes. In constant current mode, the tip is brought to the surface until a required tunnelling current is measured. The tip then rasters across the surface and a feedback network

ensures that the current between the tip and surface remains the constant. This means that if there are atoms or molecules in the path of the lateral movement then the tip must move up to avoid hitting it. This displacement is then measured and a plot of displacement versus the x and y coordinates can be obtained ^[8E-9D]. In constant height mode, the tip is held at a constant height above the surface whilst measuring the current. Tip current is now plotted against the x and y coordinates and provides surface topography ^[9D].

The STM experiments were carried out in constant current mode on an Omicron UHV system with an etched W tip and interfaced to a PC and analysed using Scala Pro 2.5 software. The base pressure of the UHV system is 1×10^{-10} torr.

2.2.5 Temperature Programmed Desorption (TPD)

The desorption of adsorbed atoms and molecules is one of the most fundamental elementary surface kinetic processes and provides information on the strength of the interactions between the surface and adsorbed species ^[8G]. Since the adsorption on a clean metal surface is generally a non-activated process the desorption activation energy is approximately equal to the differential heat of adsorption ^[13]. Information on the adsorbed species comes about from the knowledge that any species adsorbed to a surface must be bound to the surface by a specific amount of energy. The adsorbate desorbs from the surface at a rate that is determined by the Boltzmann factor, the desorption rate increasing upon heating the surface ^[2B].

The technique at first sight is therefore the simplest method by which the bond energy in adsorption can be measured and in favourable circumstances the reaction order can be determined and hence provide information to the dissociative or non-dissociative state of the adsorbate ^[12].

Experimentally, a linear temperature ramp under vacuum, typically $\sim 5\text{Ks}^{-1}$, is applied to the sample after adsorption of the adsorbate and the rate of desorption is followed by monitoring the amount of adsorbate desorbed as a function of temperature. Using a quadrupole mass spectrometer it is possible to detect a whole range of masses in the same experiment giving information on the range of desorption products ^[8G].

The concept is very simple, as the temperature of the sample increases it will eventually reach a point where the available thermal energy is sufficient to overcome the desorption activation barrier, the adsorbate-surface bond breaks and desorption is observed ^[2B]. For the simplest case where the activation energy for desorption is constant for all coverages a single desorption peak is observed and the temperature at which the maximum desorption occurs, corresponds to the maximum desorption rate ^[8G]. The activation energy of desorption, E_{des} , can therefore be given by the Redhead method:

$$E_{\text{des}} = RT_{\text{max}} \left[\ln \left(\frac{\nu T_{\text{max}}}{\beta} \right) \times 3.64 \right] \quad [2B]$$

where R is the gas constant, T_{max} is the peak maximum temperature, ν is the pre-exponential factor and β is the heating rate (dT/dt) ^[2B]. This expression is approximately

correct for first-order desorption ^[1F], i.e. the temperature of T_{\max} is independent of coverage.

Analysis of TPD spectra is fraught with difficulties that can invalidate quantitative and qualitative conclusions ^[2B]. Problems arise due to temperature inhomogeneity across the sample as it is heated, desorption from the support rods and reversible adsorption-desorption effects occurring on the vessel wall. These all tend to lead to line broadening of the desorption trace halfwidths and render lineshape analysis hazardous ^[12]. Further problems arise from interconversion from one state of the adsorbate to another during the heating and this means that the desorbing species may be different to that present on the surface before the heating commenced. Complex desorption traces consisting of multiple peaks have been attributed to the individual desorption states, each due to desorption from a physically and chemically distinct binding states having different desorption activation energies. Multiple peaks on polycrystalline adsorbents have often been attributed to desorption from different crystal faces but even on single crystals the presence of multiple peaks are more common than not. These complex traces may have arisen because of repulsive lateral interactions between the adsorbed species on the surface where the entire adsorbed layer is homogeneous ^[12]. The two different models require different analytical procedures however, within this work, TPD shall not be used for extensive interpretation of desorption behaviour but as a technique to identify desorption features that indicate how strongly bound the adlayer was to the surface.

All TPD experiments were carried out with a temperature ramp of $\sim 2\text{Ks}^{-1}$ and the desorbing species monitored using a Spectra Microvision Plus MS interfaced to a PC and analysed using Spectra RGA software for windows.

2.2.6 Gas Chromatography (GC)

Gas chromatography is the separation of a mixture of compounds (solute) into its separate constituent components. Separating the solute into its components makes it easier to identify and measure the amount of the individual component ^[13B]. To be suitable for GC analysis, the solute must have sufficient volatility and thermal stability. If all or some of its components are in the gas or vapour phase at the maximum temperature defined by the column, then it is likely that they can be analysed by GC.

The principle of the technique is that the solute is introduced into a mobile phase, i.e. the carrier gas and is carried along through a column containing a distributed stationary phase ^[13B]. The species in the sample undergo multiple interactions with the stationary phase as it moves through the column in the mobile phase. The individual components emerge at the end of the process in order of their interaction with the stationary phase. That is, the components that reach the end of the column first are those that have undergone least interaction with the stationary phase and likewise, the components that are undergo many interactions with the stationary phase will emerge from the column after the longest time ^[13B]. It is essential to carefully choose the type of column for the type of compound that are being analysed as the choice of materials for the stationary and mobile phases determine the retention time of the individual components. With careful choice it is possible to separate molecules that differ only slightly in their physical and chemical properties, even two enantiomers of the same molecule can be separated.

In this study, the GC is fitted with a Restek Rt- γ DEXsa chiral capillary column that is capable of excellent chiral selectivity for R- and S-MHB^[14]. The stationary phase in the column consists of 14% cyanopropylphenyl and 86% dimethyl polysiloxane that is doped with 2,3-di-acetoxy-6-O-tert-butyl dimethylsilyl gamma cyclodextrin. The modified cyclodextrin enables enantiomeric separation to be obtained and also show enhanced lifetime, with almost no loss in resolution after many injections compared to column made with pure cyclodextrin.

The basic GC apparatus setup as illustrated below.

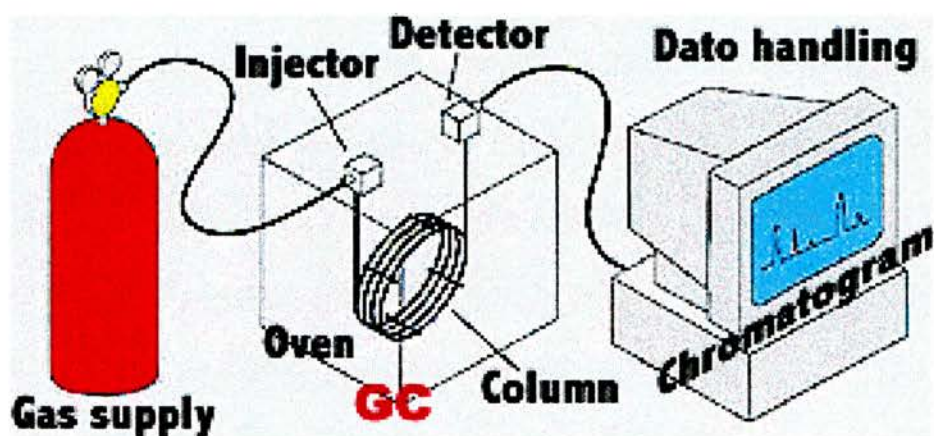


Figure 2.11. Illustration of GC apparatus^[15].

At the heart of the GC is the capillary column, where the separation occurs and is situated inside a temperature controlled oven. A dry, oxygen free carrier gas such as helium is purged through the injector and into the column. The solute is injected into the injector that is heated to about 230°C via a 1 μ L syringe and is vaporised. The solute vapour is transported into and through the column by the carrier gas at a rate determined by the physical properties, temperature and composition of the column. The fastest moving solutes exits the column first followed by the remaining solute in corresponding

order and enters a heated flame ionisation detector (FID). Inside the FID, the compounds are burned in a hydrogen-air flame and carbon containing compounds are attracted towards a collector. The number of ions hitting the collector is counted and a signal is generated. The size of the signal is recorded by a computer and plotted against time.

The GC experiments were carried using an Agilent 6850 GC system interfaced to a PC and analysed using the 6850GC software.

2.2.7 Medium Energy Ion Scattering (MEIS)

MEIS is a technique that allows quantitative and qualitative analysis of the atomic mass, depth profile and surface structure of a surface. A full description of this technique however, shall be given in chapter 6.

2.3 References

- [1] JW Nienmantsverdriet; *Spectroscopy in Catalysis – An Introduction*. VCH, Weinheim, 1993. A) 2-4, B) 193-213, C) 146-150, D) 68-72, E) 175-186, F) 24-36
- [2] DP Woodruff and TA Delchar; *Modern Techniques of Surface Science*. 2nd Edition. EA Davis, IM Ward and DR Clarke (eds), Cambridge University Press. A) 2, B) 356-409, C) 112-117, D) 84-85
- [3] G Ertl and J Küppers; *Low Energy Electrons and Surface Chemistry*. VCH, Weinheim, 1985. A) 1, B) 6-7, C) 201-266, D) 9-11
- [4] CR Henry, C Chapon, S Giorgio and C Goyhenex; *Chemisorption and Reactivity on Supported Clusters and Thin Films*. RM Lambert and G Pacchioni (eds.), Kluwer Academic Publishers, 1997. 117
- [5] JPK Doye and DJ Wales; *Z. Phys. D-Atoms Mol. Clusters*. **40**, 1-4 (1997) 194
- [6] EK Parks, GC Nieman, KP Kerns and SJ Riley; *J. Chem. Phys.* **107**, 6 (1997) 1861
- [7] A Chambers, RK Fitch and BS Halliday; *Basic Vacuum Technology*. Institute of Physic Publishing Ltd, 1989. 2-3
- [8] G Attard and CJ Barnes; *Surfaces*. Oxford Chemistry Primers-59, Oxford Science Publications, 1998. A) 24-27, B) 37-38, C) 47-57, D) 43-47, E) 79-80, F) 57-62, G) 71-75.
- [9] PW Atkins; *Physical Chemistry*. 5th Edition, Oxford University Press, 1994. A) 40, B) 8-9, C) 570-581, D) 449-454
- [10] DW Goodman; *Surf. Sci.* **299/300** (1994) 837
- [11] GA Somorjai; *Surf. Sci.* **299/300** (1994) 849
- [12] DA King; *Surf. Sci.* **47** (1975) 384
- [13] HH Willard, LL Merritt, JA Dean and FA Settle; *Instrumental Methods of*

Analysis. 7th Edition, Wadsworth Publishing Company, California, 1988. A) 302,

B) 540-579

[14] <http://www.restekcorp.com/advntage/figa98-6.htm>

[15] http://gc.discussing.info/gs/a_introduction/whatisgc2.html#GCrunning

Chapter Three

Adsorption of (R,R)-Tartaric Acid on Ni{111}.

3.1 Introduction

The only comprehensive study of the adsorption of tartaric acid on single crystal surfaces to date has come from studies by Lorenzo *et al* on Cu{110}^[1-2]. Using STM, LEED and RAIRS techniques they have investigated the molecular packing and molecular orientation of both R,R and S,S-H₂TA on Cu{110} at a range of modifier coverages and substrate temperatures.

405 K	Bitartrate (9 0) (1 2)		High coverage monotartrate monolayer (4 1) (2 5)	
350 K	Monotartrate (4 0) (2 3) Bitartrate (9 0) (1 2)	Slow change ↓ over time.	High coverage monotartrate monolayer	
300 K	Low coverage monotartrate monolayer	(4 0) (2 3)	(4 1) (2 3)	Bi-acid multilayer
83 K	Weakly perturbed neutral bi-acid molecules			

Increasing coverage \longrightarrow

Figure 3.1. The adsorption phase diagram of R,R-H₂TA on Cu{110} ^[1].

The adsorption phase diagram, figure 3.1, illustrates how coverage, temperature and adsorption time results in a variety of ordered overlayer structures ^[1]. Their studies suggested that, depending on the adsorption conditions, tartaric acid overlayers existed in three different structural forms. In the sub-monolayer regime, at low temperature, adsorption was in the molecular bi-acid form, H₂TA. At room temperature and above, adsorption was either as a monotartrate, HTA, whereby one of the carboxylic acid terminal groups is deprotonated or as a bitartrate, TA, whereby both carboxylic acid groups are deprotonated. Adsorption of tartaric acid in the multilayer regime exists only as H₂TA ^[1].

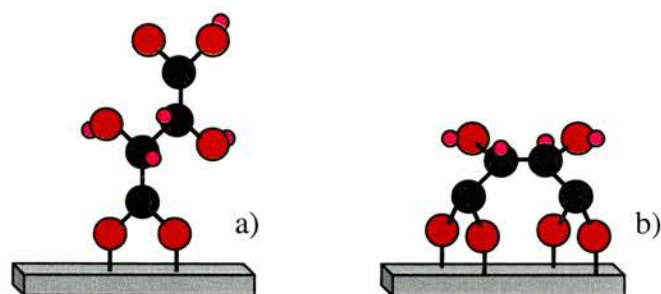


Figure 3.2. Molecular orientation of a) monotartrate and b) bitartrate species on Cu{110}.

The growth of R,R-H₂TA on Cu{110} at 300K is observed by STM.

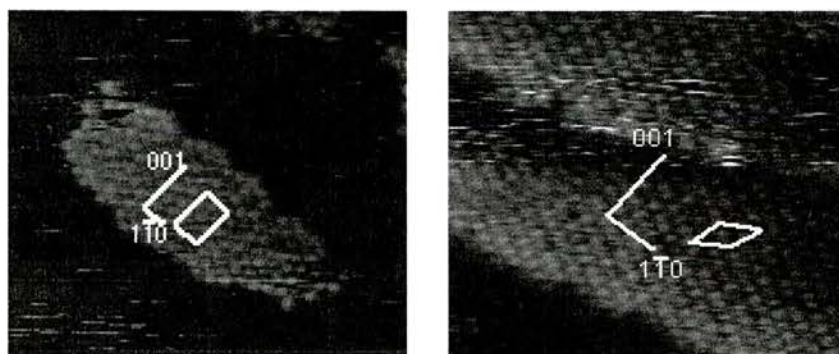


Figure 3.3. STM images of R,R-HTA adsorbed on Cu{110} at 300K corresponding to a low coverage (40 23) structure and a high coverage (41 23) structure, from left to right ^[3].

The STM images (figure 3.3) show the nucleation of R,R-H₂TA into small islands at low coverage with a unit cell (40 23) and at high coverage a unit cell (41 23)^{[1][3]}. (The matrix is presented, for convenience, as (M₁₁ M₁₂, M₂₁ M₂₂) throughout this thesis.

IR data indicate that each of the features observed in the STM are in the monotartrate form due to the presence of both $\nu(\text{C}=\text{O})^{\text{acid}}$ and $\nu_{\text{sym}}(\text{OCO}^-)$ IR bands. Therefore, it was determined that tartaric acid dissociatively adsorbs to the surface via one of the carboxylate groups^[1]. Analysis of TPD data also backed up the existence of the monotartrate by the presence of a single desorption from the surface at 483K, a desorption temperature much higher than that of the molecular bi-acid species (250K) formed on the surface when the adsorption is carried out at 83K^[1]. The higher desorption temperature was rationalised by strong anchoring of the tartrate species via the carboxylate groups to the Cu surface and possibly stabilised by strong intermolecular hydrogen bonding^{[1][3]}. Increasing the coverage leads to a steady growth of these islands until the entire surface is effectively covered. Further adsorption leads to the creation of a new higher coverage phase, also consisting of monotartrate species but with a more densely packed unit cell, (41 23) and a unit cell corresponds to a local coverage of 0.3ML^{[1][3]}.

A very important observation by Lorenzo *et al* resulted from adsorption of R,R-H₂TA at 405K that gave rise to a modified surface in which ordered chiral arrays of bitartrate species were observed^[1-3]. These were found to adopt a (90 12) adlayer unit cell. The adsorption of S,S-H₂TA under the same conditions gave a LEED pattern which corresponded to a (90 -12) unit cell. The observed STM images are displayed in figure 3.4.

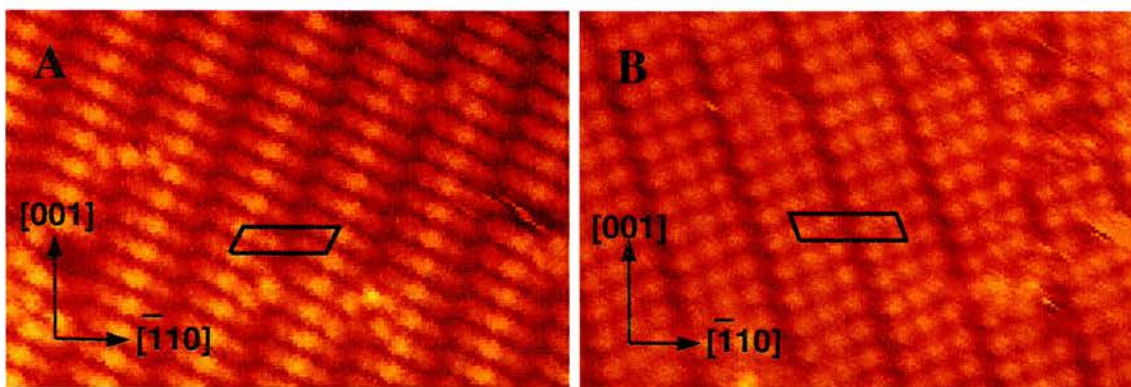


Figure 3.4. STM images showing chiral surfaces created by dosing of a) R,R-H₂TA and b) S,S-H₂TA on Cu{110} at 405K ^[2].

It can be easily seen that the two structures are mirror images of one another. Only when R,R-H₂TA was dosed onto the surface was the (90 12) structure observed and the (90 -12) structure was only observed when dosing with S,S-H₂TA. The STM image of this phase exhibited repeating units of three features and these units appear to have a chain-like growth along particular directions. In the case of R,R-H₂TA the growth is along the <-114> direction whilst with S,S-H₂TA the chain growth is in the <1-14> direction ^[2] which corresponds to growth in the mirror image direction to the <-114>. In this case the <001> is the azimuthal direction where the mirror plane cuts the surface. The authors explained the observed ordered arrays in terms of their molecular structure with the α -hydroxy groups directing the chain growth via an extended hydrogen bonding network of neighbouring tartrate molecules, as illustrated in figure 3.5.

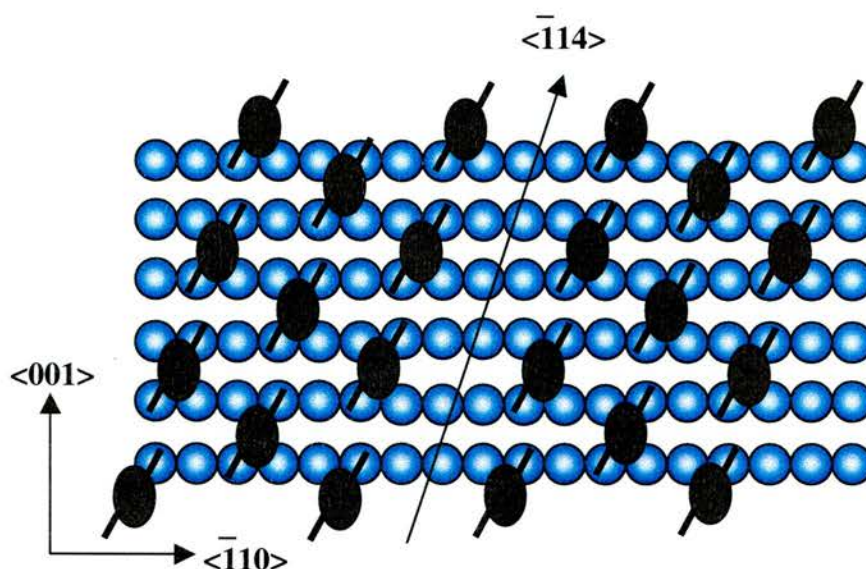


Figure 3.5. Diagram of R,R-H₂TA covered Cu{110} showing how the α -hydroxy groups interact via H-bonding, directing the chain growth along the $\langle \bar{1}14 \rangle$ direction ^[2].

The authors suggested that this structure might be important in rationalising the enantioselective catalysis over MNi surfaces. In particular it was suggested that the channels between the chains of bitartrate molecules may be important docking points for the reactant MAA molecules and subsequent hydrogenation ^[2]. Unfortunately, there is no discussion as to the reasons for the formation of bare Cu channels. The distance between neighbouring tartrate molecules also appears to be too large for significant hydrogen bonding interactions to occur between them. In water, the O-H-O bond length has been quoted as being between 2.7 and 3.1 Å ^[5] which is significantly smaller than the distance of at least 4 Å observed between the neighbouring molecules.

The presence of intermolecular hydrogen bonding to explain the bitartrate molecules aligning along the $\langle \bar{1}14 \rangle$ direction has since been discounted from Density Functional Theory (DFT) calculations ^[6]. Antonio *et al* suggested that rather than intermolecular hydrogen bonding existing, the formation of strong intramolecular hydrogen bonding between the α -hydroxy groups and the carboxy groups arise, as illustrated in figure 3.6.

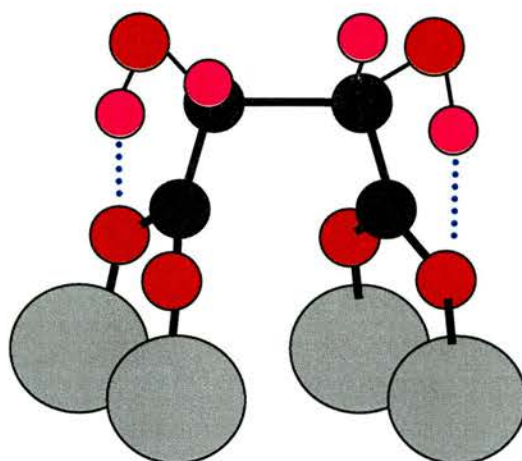


Figure 3.6. Model proposed by Antonio *et al* ^[6] illustrating intramolecular hydrogen bonding in R,R-H₂TA.

The authors calculations also suggested that these hydrogen bonds cause structural distortion of the molecule via two types of distortion. The first involves deformation of the carbon backbone and the other modifies the carboxy plane from the $\langle -110 \rangle$ direction effectively twisting the molecule by 6.2° clockwise ^[6]. The $\langle -114 \rangle$ direction that the bitartrate molecules appear to line up along when R,R-H₂TA is adsorbed has been partially attributed to these distortions. It is also of interest to note that Antonio *et al* have stated that both of these distortions are present, although with a smaller magnitude, in the succinate molecule under the same domain ^[6]. The main difference between tartaric and succinic acids is the absence of the α -hydroxy groups in succinic acid which means that the latter molecule cannot experience inter nor intra-molecular hydrogen bonding ^[6]. Therefore, there must be some ‘extra’ interplay between the molecule and the surface to account for some of the distortion.

The DFT studies investigated the effect of chemisorption of the molecule on the Cu atoms. The calculations suggest that there is an expansion of the Cu-Cu nearest neighbour spacing along the $\langle -110 \rangle$ direction upon adsorption. Therefore the surface

Cu atoms are subjected to a compression stress and the existence of bare Cu channels may be areas that possibly allow for relaxation and release of this stress ^[6]. Although the DFT model presents explanations for the observed orientation and ordered phase of bitartrate molecules along with the formation of channels of bare Cu, the model relies on all the bitartrate molecules being in identical adsorption sites. Just from observation of the STM image it appears as though the centre feature of the unit of three is brighter than the outer two. This may be an indication that the centre feature is a bitartrate molecule in a different orientation or perhaps in a different adsorption site. Therefore it does appear as though further and more detailed studies on this phase need to be completed to obtain a more precise model.

A recent study of the R,R-H₂TA adsorption on Ni{110} at 300K by Humblot *et al* ^[7] has shown that bitartrate species are found to be dominant at low coverage whilst no long range order structure are observed, in contrast to that observed on Cu{110}. The authors have observed that adsorption results in repulsive interactions between the α -hydroxy groups of the bitartrate and the metal atoms forming a severely strained adsorption induced stress on the surface Ni atoms ^[7]. It has been proposed that the subsequent stress is alleviated by significant relaxation of the surface metal atoms resulting in the bonding Ni atoms resembling a ‘chiral footprint’ ^[7]. DFT calculations have shown that only one chiral footprint is favoured by R,R-H₂TA and the authors have interpreted these observations by suggesting that the chiral footprint can be sustained over 90% of the system, leading to an overall highly chiral metal surface ^[7].

Studies involving adsorption of R,R-H₂TA under UHV condition have concentrated on Cu. The use of Cu as a hydrogenation catalyst in a catalytic reaction has been studied by

Klabunovskii^[8] and it was found not to be a good hydrogenation catalyst for this type of reaction. His studies indicated that hydrogenation of MAA using nickel catalysts yielded the greatest activity and enantioselectivity, therefore whilst studying the interactions on Cu has a degree of relevance, catalytically it seem more appropriate to study the adsorption of R,R-H₂TA (and S,S-H₂TA) on nickel surfaces. The {111} surface, in particular, is the most thermodynamically stable and hence likely to predominate on the exposed facets of Ni nanoparticles. Therefore in this chapter we will discuss the interaction of R,R-H₂TA with the Ni{111} single crystal surface.

3.2 Experimental

The Ni{111} single crystal was mounted onto the manipulator via Ta wire spot welded to the Mo power feed-through. The Mo power feed-through was connected to the Cu power feed-through by stainless steel barrel connectors. The C-type, tungsten-rhenium thermocouple was also spot welded to the back of the sample to ensure a good thermal contact was obtained.

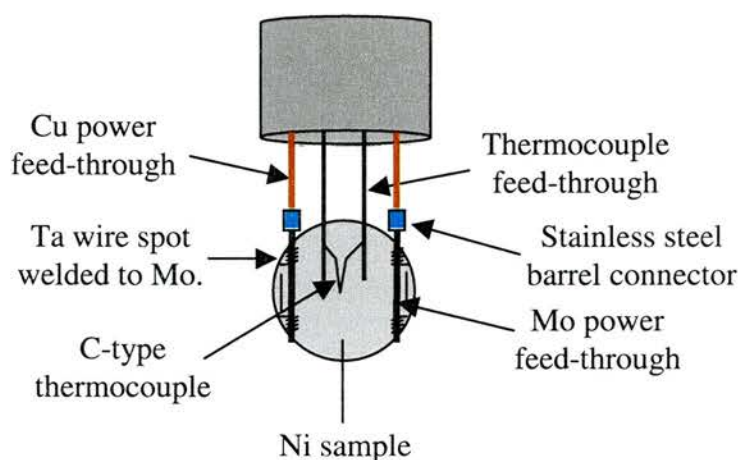


Figure 3.7. Illustration of the method used to mount the sample on the manipulator.

The system was pumped down and baked overnight to obtain UHV conditions and all the filaments were outgassed whilst the chamber was still warm. The base pressure of the system was 3×10^{-10} torr.

The Ni{111} sample was cleaned by cycles of Ar^+ ion sputtering with a beam energy of 1.5kV and annealing to 900K. This process is utilised to physically remove surface material by breaking bonds between surface atoms and the single crystal surface. To restore the surface structure the surface is annealed to facilitate surface diffusion and remove defect sites formed during the sputtering process and desorb embedded argon ions ^[9]. The cycles were continued until no impurities were visible in the AES and a sharp (1x1) LEED pattern was observed, characteristic of the clean and well ordered surface.

The tartaric acid sublimation doser consists of a 70mm (outside diameter) electrical feed-through flange with two power electrodes and two thermocouple electrodes.

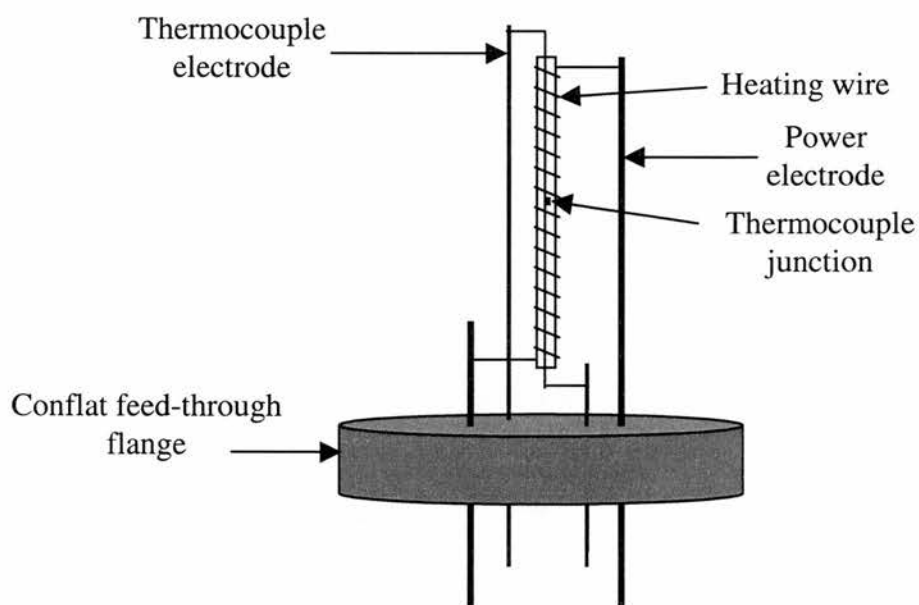


Figure 3.8. Illustration of the tartaric acid sublimation doser.

The open ended glass tube has a K-type, alumel-chromel thermocouple junction running through its centre and Ta heating wire is wrapped round the outside of the glass tube. The tube is filled with R,R-H₂TA then mounted to the feed-through flange, as in figure 3.8. The feed-through flange is attached to the UHV chamber, pumped using a turbomolecular pump and the dosing line baked overnight. The R,R-H₂TA source was outgassed at 373K for about an hour before dosing. The base pressure of the dosing line was 5×10^{-9} torr.

R,R-H₂TA was dosed onto Ni{111} as a function of incident flux, time and substrate temperature. It was difficult to determine quantitatively the dose of R,R-H₂TA that Ni{111} was exposed to as similar dosing conditions resulted in slightly different dosing pressures of R,R-H₂TA and different intensities of IR bands. The reason for this is even though the temperature of the R,R-H₂TA source is accurately known there is likely to be a temperature gradient across the source. Therefore the amount of R,R-H₂TA sublimed into the vacuum chamber is likely to be different for apparently identical source temperatures. Consideration of the Langmuir exposure (1×10^{-6} torr s⁻¹ = 1L) was also employed but again the consistency between different doses was not as reliable as that of the dosing time. Two different UHV chambers were also employed for the STM/RAIRS and TPD experiments, which also introduced a slight problem with correlation of the dose between the chambers. Therefore it was decided that the dosing conditions would simply be described as increasing coverage for the RAIRS data whilst the dosing time was the most consistent for R,R-H₂TA TPD experiments.

3.3 Results and Discussion

3.3.1 LEED and AES studies

Adsorption of R,R-H₂TA onto the clean Ni{111} surface yielded unexpected results from AES and LEED experiments. The adsorption of a molecule containing hydrogen, carbon and oxygen atoms would be expected to show the presence of both carbon and oxygen in the Auger spectrum. Adsorption of R,R-H₂TA at 300 K for 30 minutes, as an example, did indeed show the presence of both oxygen and carbon on the surface. As the surface was annealed, the peak-to-peak intensity of the oxygen AES feature decreases with increasing temperature until the level of oxygen present is beyond the detection limit of the detector at a temperature of about 473 K. The intensity of the carbon feature remains roughly constant until an annealing temperature of about 543 K after which this feature slowly decreases to zero at around 823 K. The intensity of these features and the temperature at which the carbon and oxygen features desorb are dependent, to some extent, on the R,R-H₂TA dose and the stated temperature should be taken as an average for all coverages.

When analysing the variety of R,R-H₂TA coverages using LEED, a complex LEED pattern was instantaneously formed that sharpened as the surface was annealed and was most intense at 473 K. The LEED pattern is displayed in figure 3.9.

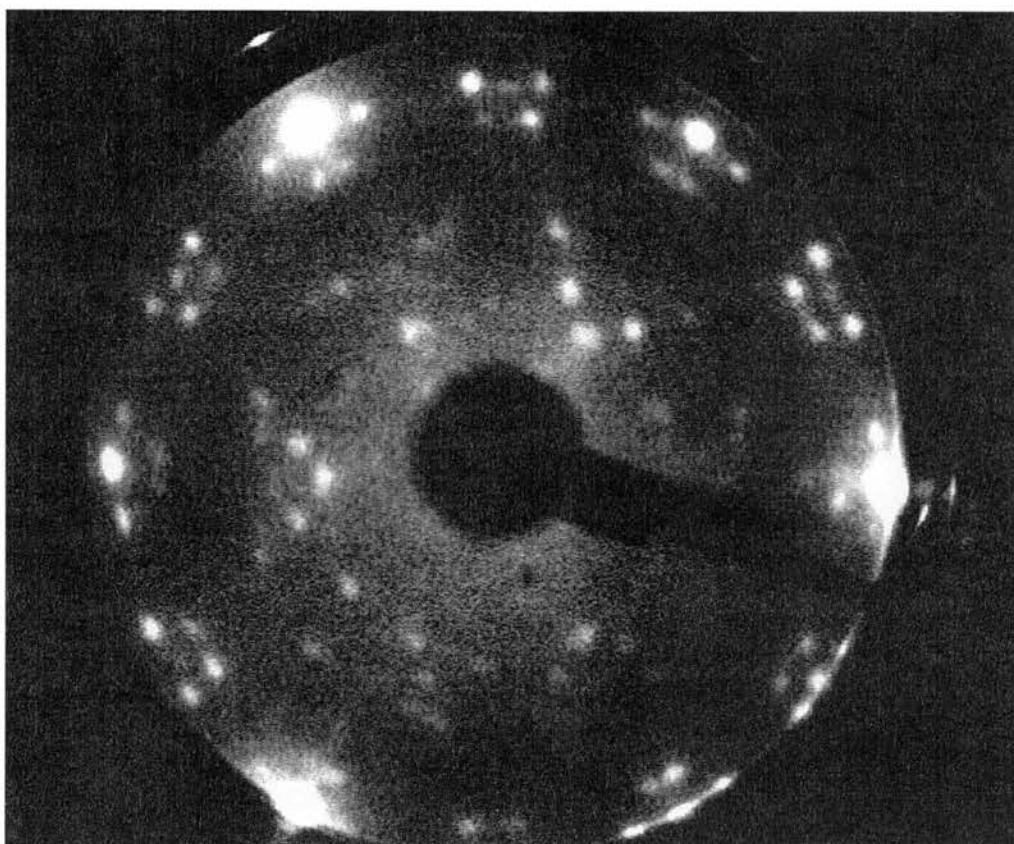


Figure 3.9. The $(\sqrt{39} \times \sqrt{39})R16.1^\circ$ LEED pattern taken with a beam energy of 61.7eV. R,R-H₂TA dosed on Ni{111} at 300K for 30 minutes and annealed to 473K.

Upon further annealing the sharpness of the image decreases until only the integer order beams are visible at a temperature of about 823 K. The LEED pattern in figure 3.9 coincides with an Auger spectrum containing only carbon and nickel features.

Careful analysis of the LEED pattern suggest that it corresponds to two mirror equivalent domains of a $(\sqrt{39} \times \sqrt{39})R16.1^\circ$ structure. A segment of the reciprocal net lattice that describes the observed complex LEED image is displayed in figure 3.10.

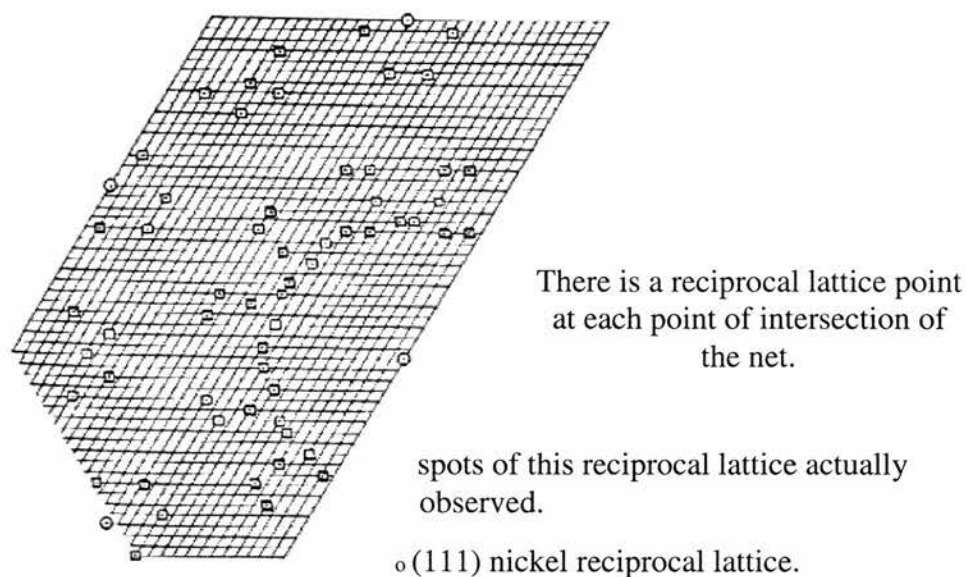


Figure 3.10. A segment of the $C(\sqrt{39} \times \sqrt{39})R16.1^\circ$ reciprocal net lattice which describes the complex pattern in figure 9^[10].

Such structures have been observed following CO adsorption on Ni{111}^[11-12] and S on Ni{111}^[13]. The absence of S in the AES spectrum suggests that the structure is most likely due to a C overlayer. This can either be caused by electron beam decomposition^[14] or dissociation of R,R-H₂TA on Ni{111}. It is therefore important to know at what stage the R,R-H₂TA molecule dissociates. Is the decomposition due to the reactivity of Ni{111} adsorption sites, a result of the electron beam or even a consequence of sublimation dosing?

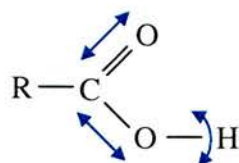
It is known that Ni is more reactive than Cu and it may be possible that decomposition could occur on the {111} terrace. However, in the catalytic reaction it has been quoted that a catalyst with larger Ni particles sizes result in a greater enantioselectivity^[15]. Bigger Ni particles indicate larger Ni{111} facets therefore suggesting that the {111} face is fundamental to a catalyst with good enantioselectivity. If decomposition occurs when the R,R-H₂TA is heated in the sublimation doser, i.e. before the molecule is in contact with the metal surface, this would require an alternative dosing method.

However, this sublimation method has been used successfully in previous studies^[1-2] and it appears unlikely to be the cause.

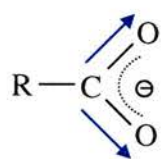
The most likely reason is a result of the electron beam utilised in the LEED and AES techniques that may be stimulating decomposition of the molecule, a mechanism observed in several different systems^[16-18]. A simple test for this is to look at the prepared sample with the STM before and after using the LEED and AES electron beam. A difference in the appearance of the surface is a good indication that the electron beam is damaging the overlayer. The outcome was that the surface was different in appearance before and after exposure to the electron beam. Subsequently, it was attempted to obtain LEED images using a low filament emission and also moving the sample so different areas of the surface were in the LEED beam, however the $\sqrt{3}\times\sqrt{3}$ structure was instantaneously observed on all occasions. Therefore electron beam stimulating decomposition of the R,R-H₂TA molecule appears most likely. Subsequently in this study, the use of AES or LEED were not able to assist the elucidation of the nature of the surfaces dosed with R,R-H₂TA.

3.3.2 RAIRS Studies

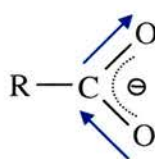
The growth of R,R-H₂TA was established using RAIRS. The RAIRS chamber was attached to the STM system and meant that the surfaces could be prepared under UHV in the RAIRS chamber and the sample transferred into the STM. This enables direct correlation of the molecular orientation of the dosed species with the obtained STM images. A particular advantage of using RAIRS is that molecular orientation can be determined, with molecules consisting of different functional groups being distinguishable. R,R-H₂TA possesses two carboxylic acid groups.



Three particularly characteristic IR vibrations that are associated with this functional group are those of $\nu(\text{C}=\text{O})$, $\nu(\text{C}-\text{O})$ and $\delta(\text{O}-\text{H})$ at $\sim 1750\text{cm}^{-1}$, 1380cm^{-1} and 1130cm^{-1} respectively ^[1]. Deprotonation of the carboxylic acid protons yields a carboxylate group.



Symmetric Stretch



Asymmetric Stretch

Two important IR vibrations that are characteristic to this functional group are those of $\nu_{\text{asym}}(\text{OCO}^-)$ and $\nu_{\text{sym}}(\text{OCO}^-)$ at $\sim 1600\text{cm}^{-1}$ and 1400cm^{-1} respectively ^[1]. These assignments are very important as they give an indication as to how the R,R-H₂TA binds to the surface.

With the R,R-H₂TA molecule, there is also a strong possibility of intermolecular hydrogen bonding between adjacent molecules. RAIRS can detect the presence of hydrogen bonding interactions of the carboxylic acid groups as they lead to direct perturbations of the molecular vibrations, generally lowering the $\nu(\text{C}=\text{O})$ vibration and increasing the $\nu(\text{C}-\text{O})$ vibration ^[1].

Adsorption of R,R-H₂TA on Ni{111} over a range of temperatures and coverages has been studied and leads to the formation of a phase diagram that is summarised in figure 3.11.

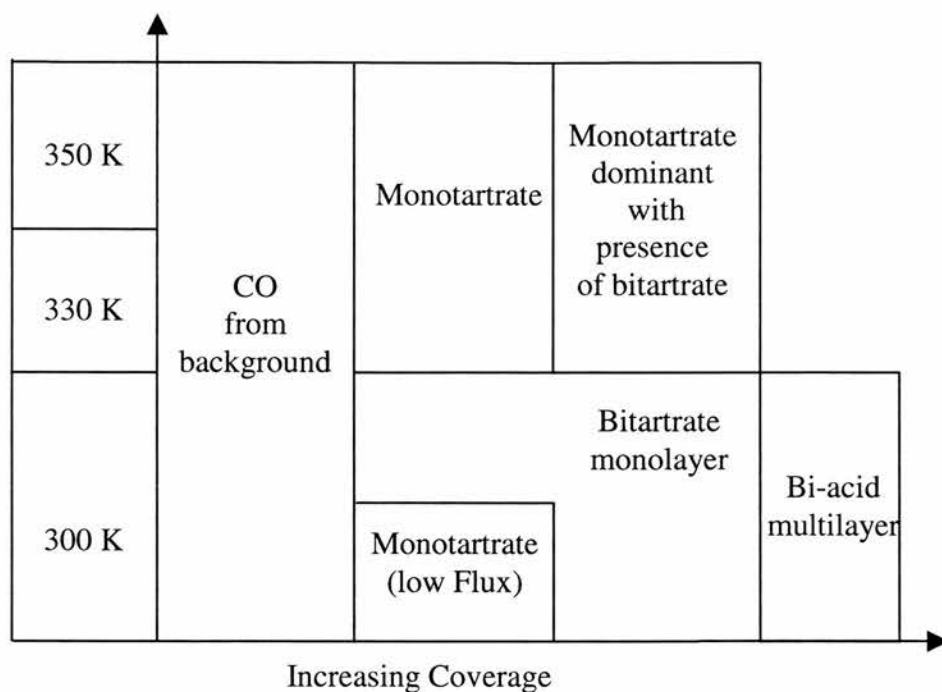


Figure 3.11. The adsorption phase diagram of R,R-H₂TA on Ni{111}.

The IR assignments for all observed R,R-H₂TA features have been previously studied in detail ^[1] and they required a small revision for this study ^[19] and is summarised in table 3.1.

Assignment	300 K		330 K	350 K	Ordered Phases	
	Low Flux	High Flux			300 K	350 K
$\nu(\text{CO})^{\text{atop}}$				2024		
$\nu(\text{CO})^{\text{3 fold-bridge}}$	1868 1826 1813	1857 1852 1834	1834	1849	1830	1826
$\nu(\text{C=O})^{\text{acid}}$	1761	1762		1774	1773	1761
$\nu(\text{C=O})^{\text{hydrogen bonded}}$	1656		1651	1651		
$\nu_{\text{asym}}(\text{OCO}^-)$			1602	1618 1590		
$\nu_{\text{sym}}(\text{OCO}^-)$	1428 1419	1428	1424	1431	1428	1419
$\nu(\text{C-O})^{\text{acid}}$	1397	1395	1390	1397	1396	1397
$\delta(\text{O-H})^{\text{alc}}$	1380	1364	1372	1375	1380	
$\delta(\text{C-H})$	1307 1212 1194 1189	1189 1176	1326 1298 1192 1177	1310 1185	1309 1194	1212 1189
$\delta(\text{O-H})^{\text{acid}}$	1123	1136				1123
$\nu(\text{C-O})^{\text{alc}}$	1113 1112	1113 1104 1070	1109 1061	1111	1113	
$\nu(\text{C-C})$		959	959			944

Table 3.1. Assignments of observed IR bands in RAIRS experiments for the adsorption of R,R-H₂TA on Ni{111}.

3.3.2.1 Adsorption at 300K

Adsorption of R,R-H₂TA at room temperature is subtly dependent on the flux emitted from the R,R-H₂TA source. Alteration of the source flux may be thought to be analogous to a difference in concentration of the modification solution in the catalytic reaction. Figures 3.12 and 3.14 show the RAIR spectra obtained with increasing exposure for low flux and high flux dosing respectively, where the temperature of the source is 410 K for low flux and 420 K for high flux.

3.3.2.1.1 Low Flux Adsorption

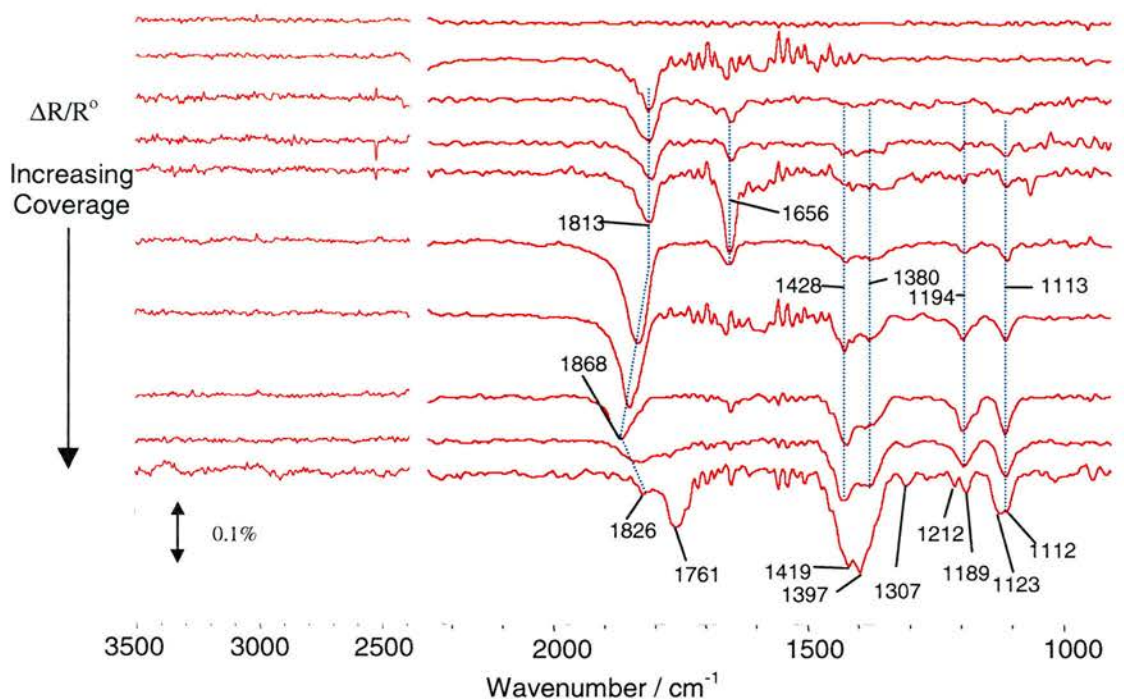


Figure 3.12. RAIR spectrum of the sequential, low flux dosing of R,R-H₂TA on Ni{111} at 300 K.

Upon initial dosing of R,R-H₂TA, the RAIR spectra are dominated by the features at 1813cm⁻¹ and 1852cm⁻¹ for the low (figure 3.12) and high (figure 3.14) flux doses respectively. These two features have been assigned in this thesis to CO sitting in 3-fold hollow sites and the difference in frequency is associated to their relative coverage^[20-21]. Although there have been many IR studies into the adsorption sites of CO on Ni{111} there is still much debate as to the actual assignment of the vibration bands arising between about 1860cm⁻¹ and 1800cm⁻¹^[21-25]. Literature values of features in this range have been assigned to stretching modes of CO in hcp, fcc and bridging sites. The amount of CO present on the surface, in this thesis, is much less than a monolayer and at most the IR signal is about 0.1%. Therefore the IR bands in this range have been assigned to CO in 3-fold hollow sites, whether hcp or fcc sites. The presence of CO

suggests that either CO is adsorbing from the background or R,R-H₂TA is decomposing upon initial adsorption or a combination of both. This observation is in direct contrast to that observed for Cu{110} where CO (or H₂) does not adsorb at 300 K. One possible method to differentiate between these two effects would be to use ¹³C isotopically labelled R,R-H₂TA, however this has not been attempted in this thesis.

After the initial dose of R,R-H₂TA there is growth of a feature at 1656cm⁻¹ along with the presence of CO. This has been assigned to a ν(C=O), strongly downshifted from the stretching frequency of the carbonyl group of the free carboxylic acid indicating that this carbonyl group is involved in some sort of interaction either with another molecule or the Ni surface. A band of similar frequency has been observed in the studies by Lorenzo *et al* of R,R-H₂TA on Cu{110} ^[1] and was assigned to a carbonyl group involved in hydrogen bonding, in the form of a cyclic dimer (figure 3.13a). The cyclic dimer is created by hydrogen bonding between two adjacent carboxylic acid groups of monotartrate molecules forming a ring type structure. This band however, may also be assigned to a monodentate carboxylate group where one of its oxygen atoms is bound to the surface and the other away from the surface, figure 13b. This is similar to a phase observed for adsorption of formic acid at 200K ^[26] and a room temperature saturation coverage of glycine ^[27] on Cu{110}.

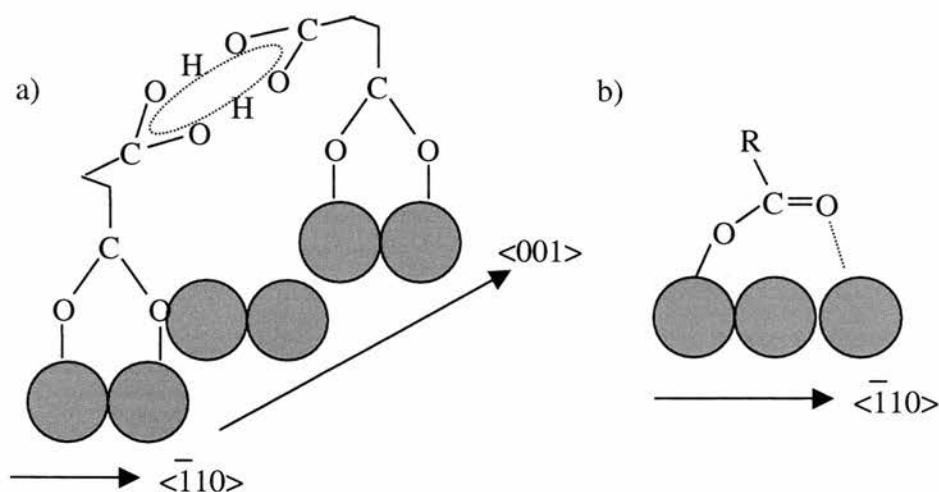


Figure 3.13. Possible molecular orientation giving rise to the IR band at $\sim 1650\text{cm}^{-1}$ on a Cu{110} surface. a) hydrogen bonded carboxylate groups forming an intermolecular cyclic acid dimer and b) a monodentate carboxylic acid group.

The presence of this band therefore suggests there may be three types of species present. The first, one of the carboxylic acid groups of the R,R-H₂TA might be interacting with neighbouring tartrate molecules and forming the hydrogen bonded cyclic dimer. Alternatively, the carboxylic acid group may be bound to the surface as a monodentate species and stabilised by hydrogen bonding interactions between carboxylic acid groups of neighbouring tartrate molecules. Also, this frequency may be attributed to a carboxylic acid group where the carbonyl group is weakly interacting with the surface, similar to that suggested by Bowker *et al* ^[26] for formic acid adsorption on Cu{110}. These two types of orientation may occur to one or both of the carboxylic acid groups of the R,R-H₂TA by molecular adsorption, possibly at step edges allowing some of the carboxylic acid groups of the tartaric acid to adopt the monodentate orientation. However, due to the application of the IR metal surface selection rule it is impossible to differentiate between the two.

Along with the carbonyl stretching bands, the growth of features at 1428cm^{-1} , 1380cm^{-1} , 1194cm^{-1} and 1113cm^{-1} assigned to $\nu_{\text{sym}}(\text{OCO}^-)$, $\delta(\text{O-H})_{\text{alc}}$, $\delta(\text{C-H})$ and $\nu(\text{C-O})^{\text{alc}}$ respectively, indicating that R,R-H₂TA is bound to the surface via at least one carboxylate group. The disappearance of the feature at 1656cm^{-1} coincides with the growth of the $\nu_{\text{sym}}(\text{OCO}^-)$ feature at 1428cm^{-1} and the continued growth of the other features that is characteristic of a tartrate species. At higher dose the tartrate features increase and CO eventually decreases to be replaced by the feature at 1761cm^{-1} . This new feature is associated with $\nu(\text{C=O})^{\text{acid}}$ and is coupled to the growth of two features at 1397cm^{-1} and 1123cm^{-1} assigned to $\nu(\text{C-O})^{\text{acid}}$ and $\delta(\text{O-H})^{\text{acid}}$ respectively. This is indicative of the formation of the multilayer, whereby both of the carboxylic acid groups of the R,R-H₂TA species remain protonated.

It is of interest to note that we do not observe any features in the range 2500cm^{-1} to 3500cm^{-1} , the range in which it would be expected to observe stretching vibrations associated with the carboxylic acid O-H groups and C-H groups. This may indicate that at all coverages, the C-H vibrations of the R,R-H₂TA and tartrate backbone may be close to parallel to the surface as do those for the carboxylic acid protons in the multilayer but as C-H vibrations are relatively weak in IR, in comparison to carbonyl vibrations they may be masked by the background signal.

The low flux RAIRS data is therefore indicative of two phases in the sub-monolayer regime. The first phase, at low coverage may possibly contain a hydrogen bonded carboxylic acid cyclic dimer suggesting that the surface is dominated by monotartrate species. However, the IR data may also indicate the formation of bitartrate species bound to the surface via only one oxygen atom of the carboxyl group and the other

oxygen remaining as part of a carbonyl functionality. At an intermediate coverage IR data is indicative of a carboxyl group bound with both oxygen atoms equidistant to the surface and therefore suggesting a bitartrate surface species. At high coverage the observed IR bands are consistent with physisorbed bi-acid multilayers. It is important to point out that a mixture of species may be present due to the inhomogeneity of the surface as the STM images show the presence of ordered regions interspersed with disordered regions. The presence of bitartrate species from the RAIR spectra could also invoke the presence of a monotartrate with the carbonyl band of the carboxylic acid group being parallel to the surface due to the surface dipole selection rule.

3.3.2.1.2 High Flux Adsorption

The deposition of R,R-H₂TA with a higher flux, displayed in figure 3.14, follows a similar pattern to that of the low flux dose.

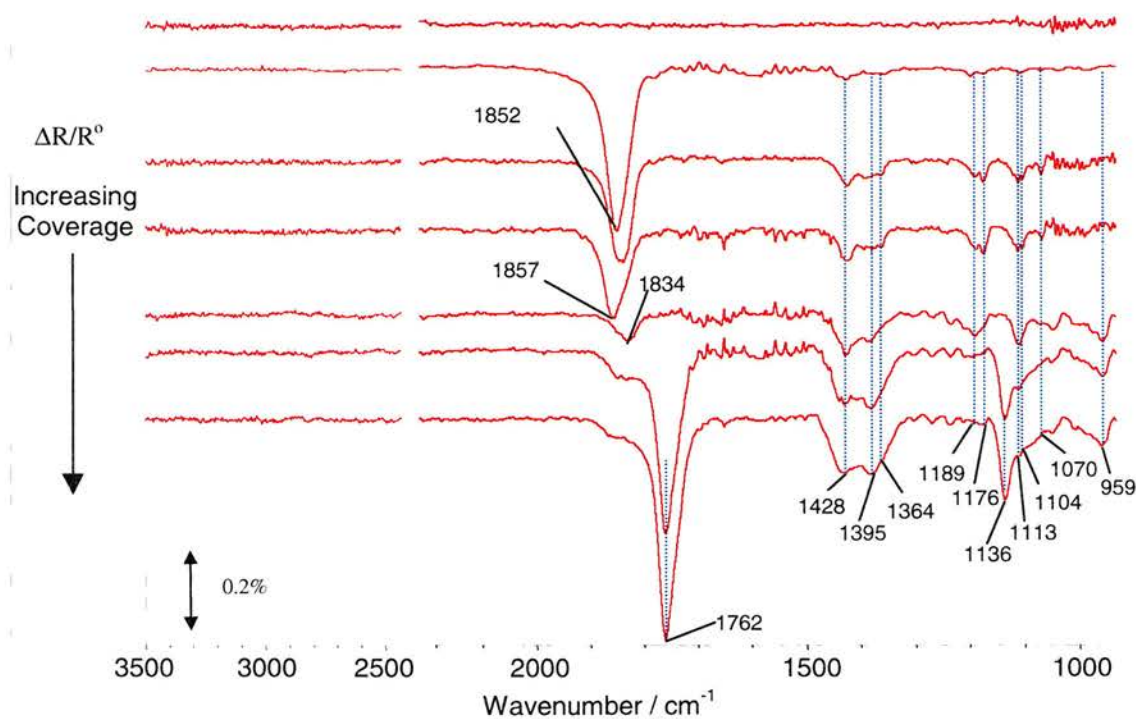


Figure 3.14. RAIR spectrum of the sequential, high flux dosing of R,R-H₂TA on Ni{111} at 300 K.

The difference in the RAIR spectrum following the high flux dose compared to the corresponding spectrum of the low flux is the absence of the feature at $\sim 1650\text{cm}^{-1}$. As with the low flux dosing, CO is the dominant surface species at low coverage. The most prominent peaks at low coverage are those at 1428cm^{-1} , 1364cm^{-1} , 1189cm^{-1} and 1113cm^{-1} associated with $\nu_{\text{sym}}(\text{OCO}^-)$, $\delta(\text{O-H})^{\text{alc}}$, δCH and $\nu(\text{C-O})^{\text{alc}}$ features suggesting the presence of bitartrate surface species. As the coverage increases so do the features associated with the bitartrate species and simultaneously the intensity of the CO starts to decrease and eventually almost disappears. On formation of the multilayer, we once again get a ‘switching’ in intensities so the features associated with $\nu(\text{C-O})^{\text{acid}}$ and $\delta(\text{O-H})^{\text{acid}}$ at 1396cm^{-1} and 1136cm^{-1} become more dominant and a new feature, that is also the most dominant, grows at 1762cm^{-1} associated with $\nu(\text{C=O})^{\text{acid}}$ is consistent with the formation of the multilayer.

High flux dosing at 300 K therefore results in a single bitartrate phase at all sub-monolayer coverages and the formation of the bi-acid at the multilayer.

3.3.2.2 Adsorption at 330K

The RAIR spectrum for R,R-H₂TA adsorption at 330K, with a source flux equivalent to the high flux (420 K) in the room temperature dose, is displayed in figure 3.15.

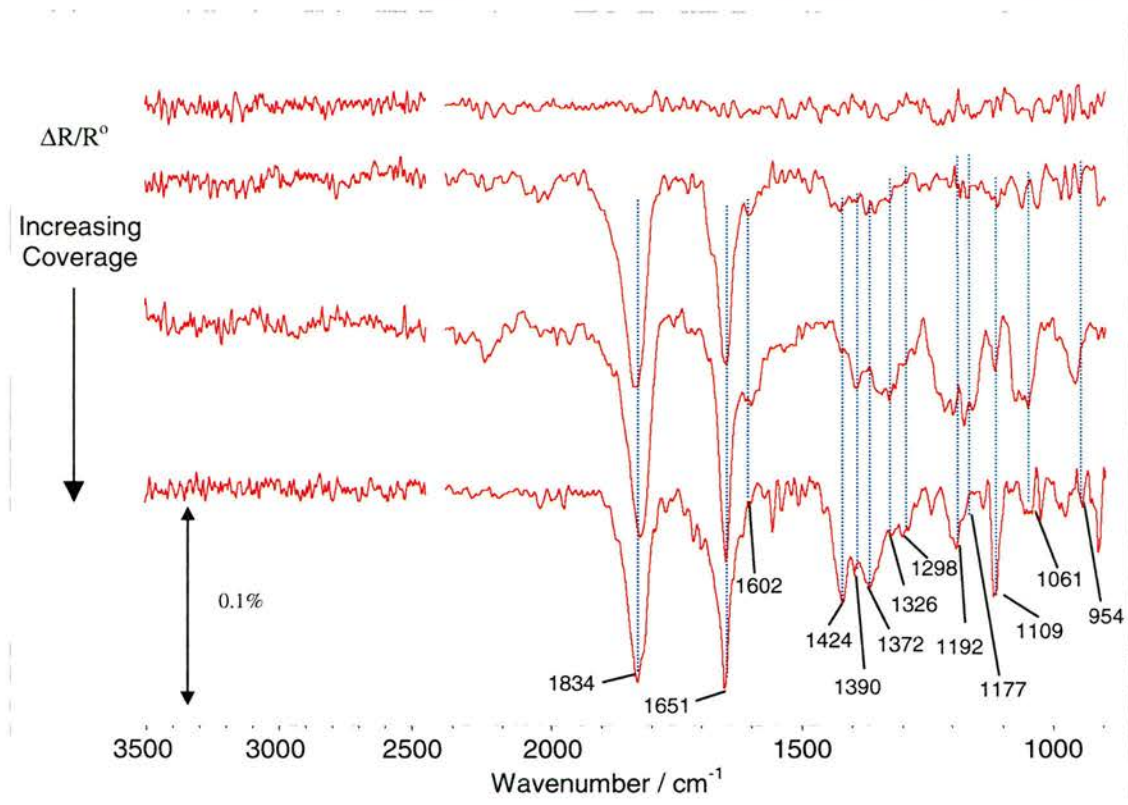


Figure 3.15. RAIR spectrum of the sequential dosing of R,R-H₂TA on Ni{111} at 330K.

The initial dose in the RAIR spectrum is dominated by the presence of CO at 1834cm⁻¹ and a feature at 1651cm⁻¹ consistent with a hydrogen bonded carbonyl group. There is also growth of carboxylate groups characterised by the $\nu_{\text{sym}}(\text{OCO}^-)$ band at 1422cm⁻¹ and the growth of α -hydroxy groups by the $\delta(\text{O-H})^{\text{alc}}$ band at 1372cm⁻¹ indicating the presence of bitartrate or monotartrate species. The small $\nu_{\text{asym}}(\text{OCO}^-)$ feature at 1602cm⁻¹ imply some of the carboxyl groups may not be bound symmetrically to the surface. Further dosing results in the CO and hydrogen bonded carbonyl bands having a constant intensity whilst the $\nu_{\text{asym}}(\text{OCO}^-)$ feature increases slightly along with growth of 1390cm⁻¹, 1326cm⁻¹, 1192cm⁻¹, 1177cm⁻¹, 1061cm⁻¹ and 954cm⁻¹. These latter features are assigned to $\nu(\text{C-O})^{\text{acid}}$, $\delta(\text{C-H})$, $\nu(\text{C-O})^{\text{alc}}$ and $\nu(\text{C-C})$. After the final R,R-H₂TA dose, the RAIR spectrum is still dominated by CO and carbonyl bands along with the presence of $\nu_{\text{sym}}(\text{OCO}^-)$, $\delta(\text{O-H})^{\text{alc}}$, $\delta(\text{C-H})$ and $\nu(\text{C-O})^{\text{alc}}$.

At 330K, dosing as a function of time suggests the surface may consist of species similar to that observed at 300K for the low flux dose. The adlayer may be that of a monotartrate phase where neighbouring molecules interact in the form of a cyclic dimer. These IR bands may also be characteristic of a bitartrate phase where one or both of the carboxylic acid functionalities are bound in a monodentate fashion whilst the other oxygen remains part of the carbonyl group. The existence of small $\nu_{\text{asym}}(\text{OCO}^-)$ features suggest a proportion of surface species must consist of asymmetrically bound carboxyl groups but at higher coverage the surface is almost entirely covered by symmetrically bound carboxyl groups.

3.3.2.3 Adsorption at 350 K

The RAIR spectra for R,R-H₂TA dosing at 350K is shown in figure 3.16.

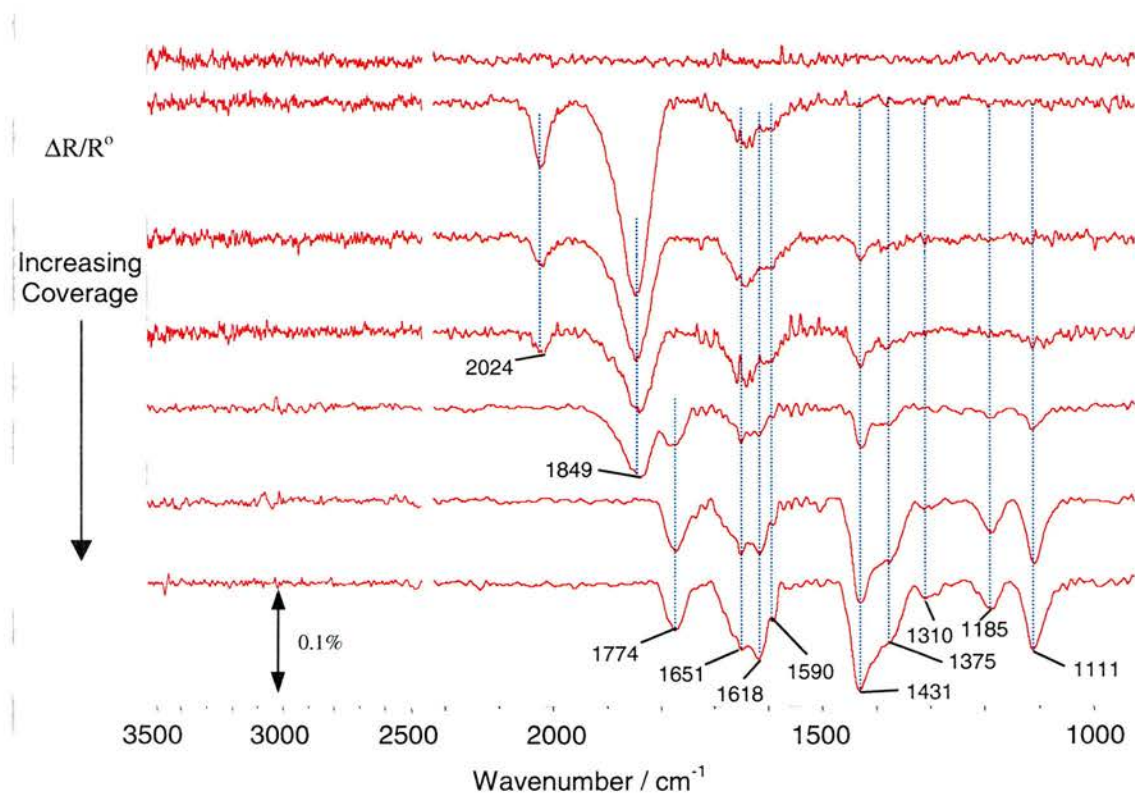


Figure 3.16. RAIR spectrum of the sequential dosing of R,R-H₂TA on Ni{111} at 350 K.

Upon initial adsorption the spectrum is again dominated by the CO stretch at 1849cm^{-1} , a lower intensity feature at 2024cm^{-1} associated with CO sitting in atop nickel sites ^[16] and a broad feature at 1651cm^{-1} corresponding to a hydrogen bonded carbonyl species with a small shoulder at 1590cm^{-1} of a $\nu_{\text{asym}}(\text{OCO}^-)$ band. With increasing dose, we observe the growth of $\nu_{\text{sym}}(\text{OCO}^-)$ bands at 1431cm^{-1} , $\nu_{\text{asym}}(\text{OCO}^-)$ band at 1618cm^{-1} and a decrease in the intensity of the atop CO at 2024cm^{-1} and the CO in the 3 fold hollow site at 1849cm^{-1} . With increasing coverage, features associated with atop CO disappear and the growth of features associated with R,R-H₂TA at 1375cm^{-1} , 1310cm^{-1} , 1185cm^{-1} , 1111cm^{-1} and also the increase in intensity of the $\nu_{\text{sym}}(\text{OCO}^-)$ at 1431cm^{-1} is observed. Along with these IR bands we also observe the presence of a feature at 1774cm^{-1} normally associated with carboxylic acid functional groups. The multilayer is unstable at temperatures $>300\text{K}$ and it would be predicted that there would be no formation of the multilayer at this temperature. However, after the final dose the acquisition of IR data was continued and the three molecular R,R-H₂TA IR bands were seen to decrease in intensity until they disappeared. This suggests that the multilayer is only formed due to the high R,R-H₂TA flux that continues to supply R,R-H₂TA to the surface after the monolayer coverage has been achieved. Unfortunately, the quality of this data was impaired by bands associated with water miscancellation appearing due to the time difference between taking the background spectra and latter ‘no dose’ acquisitions. Therefore this data has been omitted from the spectrum in figure 3.16.

Adsorption of R,R-H₂TA at 350K appears similar to adsorption at 330K and at 300K at low coverage with a low flux dose. The surface is initially dominated by the presence of CO and carbonyl groups either interacting with adjacent molecules or with the surface.

As the coverage increases, CO appears to be displaced from the surface and is accompanied by the growth of bands associated with monotartrate or bitartrate species. At all coverages the presence of asymmetric carboxylate stretches suggest that both oxygen atoms are bound to the surface but are not quite equidistant with the surface.

3.3.3 TPD Studies

The appearance of several possible adsorbed phases in the RAIR spectra means it may be possible to identify these phases by the temperature they desorb from the surface. Gas phase R,R-H₂TA shows the presence of masses at 2 (H₂), 18 (H₂O), 28 (CO), 44 (CO₂) and 150 (H₂TA) amu, amongst others. However in this study, a desorption experiment of R,R-H₂TA on Ni{111} does not show the presence of mass 150 amu corresponding to molecular R,R-H₂TA and therefore suggests that adsorbed R,R-H₂TA decomposes into fragments on the surface as a result of increasing surface temperature. IR data also suggest the formation of the bi-acid multilayer at saturation coverage. However features corresponding to the multilayer disappear after the surface has been left for several minutes with no further dose between acquiring IR spectra. The lack of molecular R,R-H₂TA TPD features also indicates that the multilayer is not stable above 300K and molecular R,R-H₂TA readily desorbs before the TPD experiment can be initiated.

3.3.3.1 Adsorption at 300K

3.3.3.1.1 Temperature Programmed Desorption of Low Flux R,R-H₂TA Dose

The CO TPD spectra for an increasing coverage of R,R-H₂TA with a low flux dose is illustrated in figure 3.17.

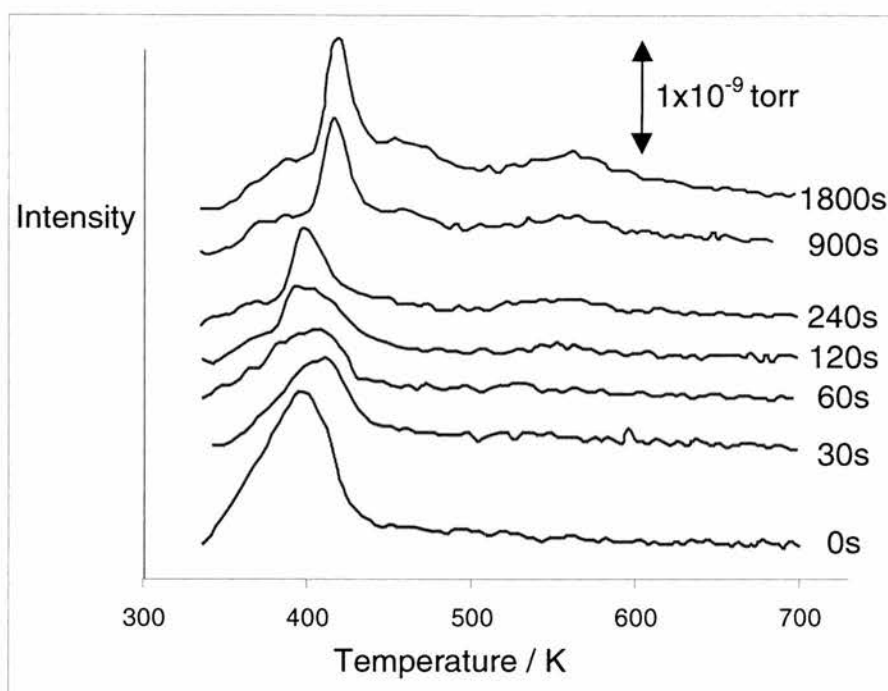


Figure 3.17. CO TPD spectra of an increasing, low flux dose of R,R-H₂TA on Ni{111} at 300 K.

The CO TPD from a nominally ‘clean’ Ni{111} surface yields a single asymmetric desorption feature with a T_{\max} of $\sim 400\text{K}$ and suggest that CO accumulates on the surface whilst the sample cools following cleaning. This desorption temperature is in good agreement with values stated in literature for low coverage CO on Ni{111} ^{[23][28]}. With increasing dose this feature decreases in intensity and after a 240s dose, has been replaced by a higher temperature CO feature at $\sim 420\text{K}$ and accompanied by the growth of two smaller features with a T_{\max} $\sim 460\text{K}$ and 560K . The presence of at least one small feature is observed with a T_{\max} $\sim 360\text{K}$, consistent with desorption of a higher surface coverage of CO ^[23] which may have originated from CO sitting in less favourable Ni sites. This presumably arises from CO displaced from the 3 fold hollow sites to atop sites by the increasing R,R-H₂TA coverage.

The initial decrease in the CO peak area following R,R-H₂TA adsorption and the growth of a new feature at ~420K with an increase in dosing time indicates that R,R-H₂TA adsorption displaces adventitious CO from the surface. The appearance of the desorption feature at higher T_{max} suggests once the coverage of CO is below a critical value, the formation of a more stable surface species is instigated. It therefore appears as though the presence of CO on the surface may destabilise the tartrate overlayer perhaps by inhibiting hydrogen bonding between adjacent molecules.

The feature at 420K is assigned to the decomposition of the stabilised surface tartrate species whilst the lower intensity feature at 460K is assigned to decomposition of another, even more stable species. This second species is believed to form during the first decomposition/desorption process at 420K that effectively creates space for neighbouring tartrate species to adopt another configuration of higher stability. The feature at ~560K is assigned to C_(ads) and O_(ads) recombination process of decomposed material.

The presence of CO₂ desorption features in the TPD spectra is a good indicator of the stability of tartrate species on the metal surface. Each R,R-H₂TA molecule possesses two carboxylic acid functional groups that are known to interact with the surface in the form of a carboxylate. The presence of CO₂ in the desorption spectra must therefore have originated from R,R-H₂TA as CO₂ present in the vacuum chamber as residual gas does not adsorb on Ni{111} at room temperature^[29] unlike CO. The CO₂ TPD for increasing low flux dose at 300K is illustrated in figure 3.18.

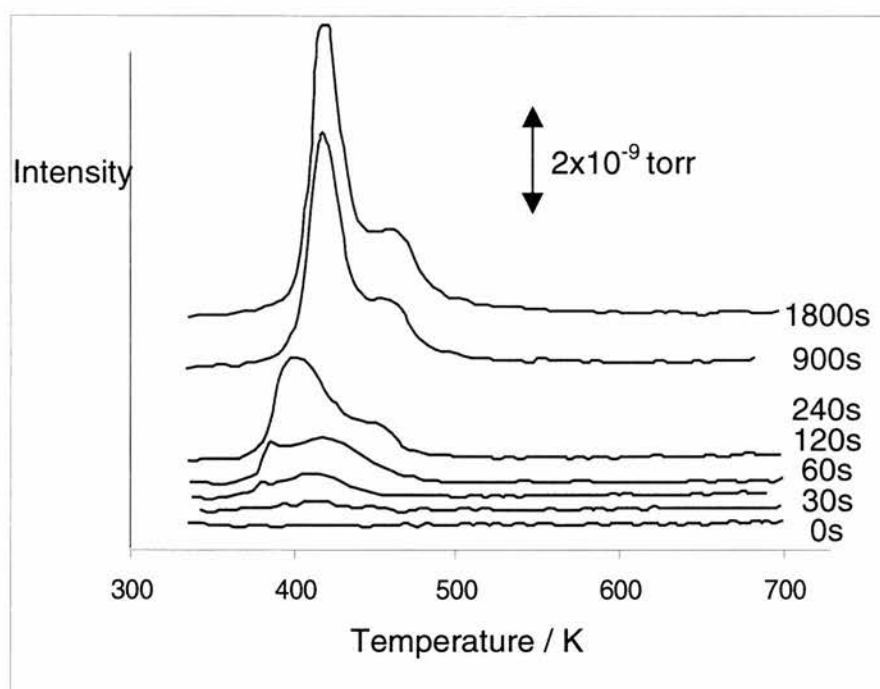


Figure 3.18. CO₂ TPD spectra of an increasing, low flux dosing of R,R-H₂TA on Ni{111} at 300 K.

The lack of features from the clean Ni{111} surface confirms that no CO₂ is initially present. Upon adsorption of R,R-H₂TA, a small broad feature is visible with a T_{\max} of ~ 410 K. With increasing R,R-H₂TA coverage, this feature shifts slightly to higher temperature (~ 425 K) and is accompanied by a small lower temperature feature with a T_{\max} of ~ 380 K. After a 240s dose, these two features have grown into a more intense feature at 400K and a second lower intensity feature with T_{\max} of ~ 450 K. Further dosing causes these desorption peak areas to increase and shift to higher temperature where they have T_{\max} values of ~ 420 K and ~ 460 K respectively, indicating a stabilisation of the surface species. These two features behave similarly to those in the CO TPD for comparable doses and this coincident desorption suggests that the desorption features in CO and CO₂ originate from the same process.

The TPD data suggest the presence of a two step decomposition pathway, the first is the decomposition of tartrate species to a more stable surface species but with a lower

coverage. This lower coverage surface species then decomposes at $\sim 460\text{K}$ and the lack of any further CO_2 desorption features indicates that the high temperature CO desorption feature result from the recombination of $\text{C}_{(\text{ads})}$ and $\text{O}_{(\text{ads})}$ of the remaining R,R- H_2TA decomposition products.

The presence of H_2 in the TPD spectra can also help to confirm the decomposition pathway and for this dose, the H_2 TPD spectra are illustrated in figure 3.19.

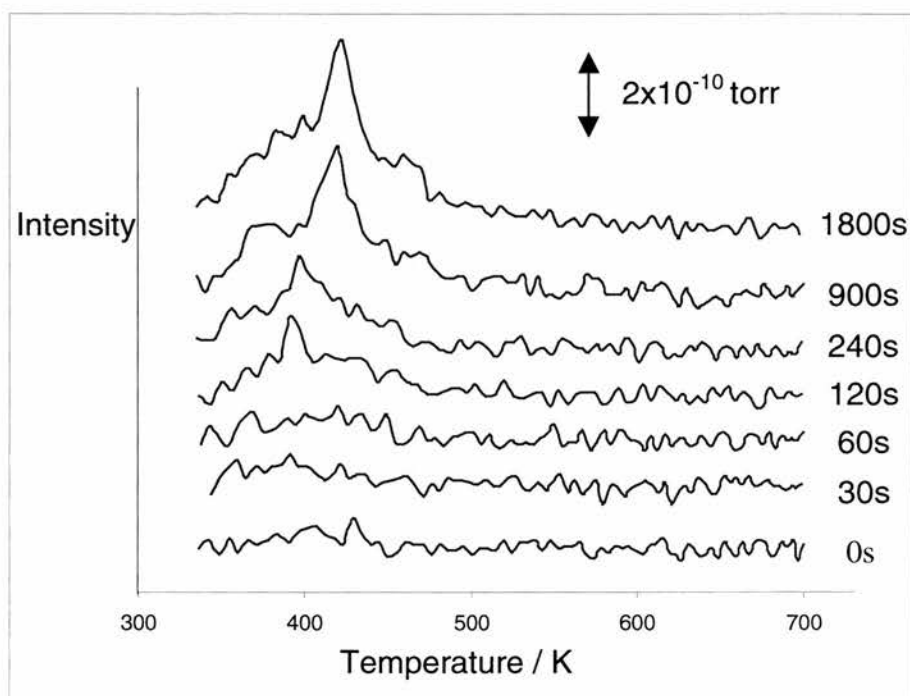


Figure 3.19. H_2 TPD spectra of an increasing, low flux dosing of R,R- H_2TA on Ni{111} at 300 K.

Figure 3.19 illustrates the presence of desorption features that increase in intensity with dose, the main feature having a T_{max} of $\sim 400\text{K}$ at low coverage. After a dose of 240s, the most intense feature is shifted to a higher temperature, $T_{\text{max}} \sim 420\text{K}$ and a shoulder with $T_{\text{max}} \sim 460\text{K}$ is also present. The broadness of the desorption features is formed by $\text{H}_{(\text{ads})}$ recombination derived at lower temperature from deprotonation of the carboxylic acid functionality and a result of tartaric acid decomposition at higher temperatures.

These desorption temperatures are again coincident with the features observed for CO and CO₂.

The H₂O TPD spectra gives further insight into the adsorption and decomposition pathways of the adsorbed R,R-H₂TA and is illustrated in figure 3.20.

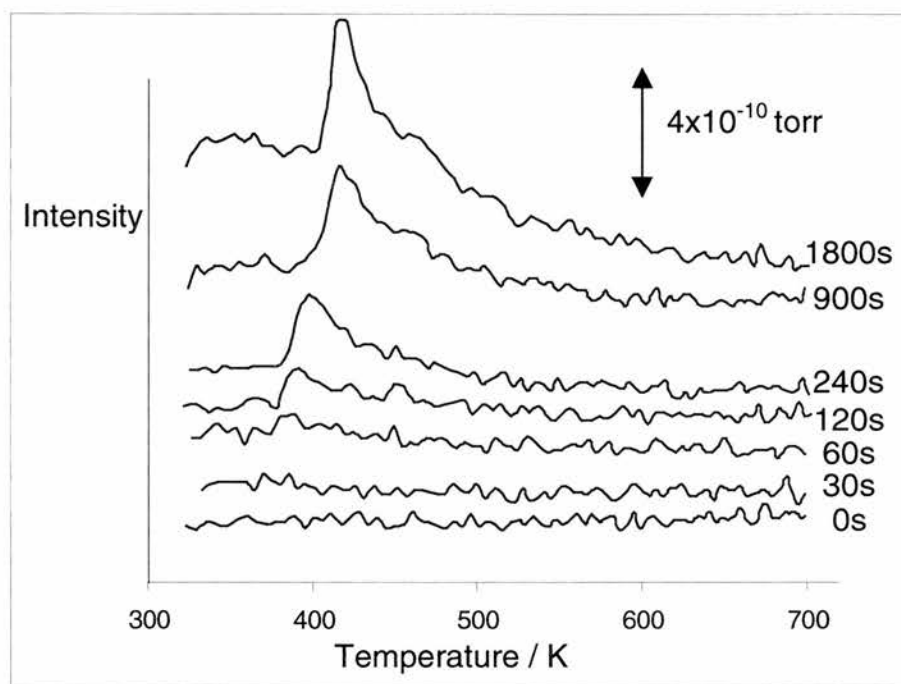


Figure 3.20. H₂O TPD spectra of an increasing, low flux dosing of R,R-H₂TA on Ni{111} at 300 K.

There is again the presence of two distinct types of desorption features. The first, at lower coverage with a $T_{\max} \sim 400\text{K}$ and the second occurring at higher coverage associated with the formation of the stabilised tartrate species, having a $T_{\max} \sim 420\text{K}$ and shoulder at $\sim 460\text{K}$. The sloping backgrounds of the desorption traces at the higher temperature side of the T_{\max} are probably a result of the slow pumping speed of H₂O, formed by the recombination of H_(ads) and O_(ads) or OH_(ads) and H_(ads) facilitated by the initial decomposition of R,R-H₂TA.

3.3.3.1.2 Temperature Programmed Desorption of High Flux R,R-H₂TA Dose

The CO and CO₂ TPD spectra with increasing coverage for a high flux dose are illustrated in figures 3.21 and 3.22 and appear to be almost identical to that observed for the low flux dose.

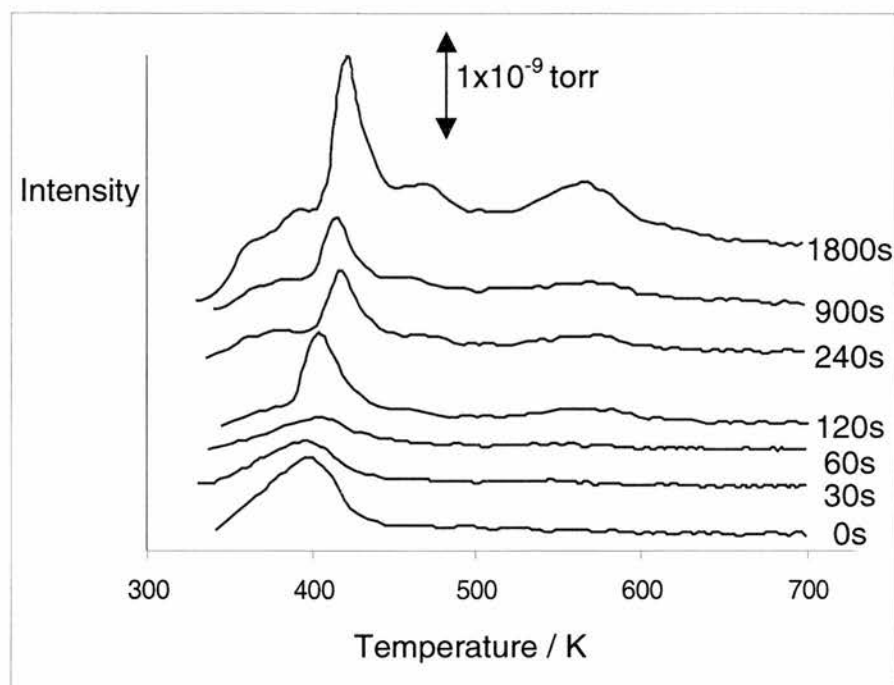


Figure 3.21. CO TPD spectra of an increasing, higher flux dosing of R,R-H₂TA on Ni{111} at 300 K.

The clean surface again has an asymmetric CO desorption feature with a T_{\max} of about 400K arising from CO adsorbed from the background. Its peak area decreases as R,R-H₂TA is dosed onto the clean surface indicating the displacement of CO from the surface. A second feature with a T_{\max} of ~405K grows in intensity until it is the dominant feature at 120s and is accompanied by the growth of a small feature with T_{\max} ~570K. The desorption feature at 405K presumably originates from the growth of surface tartrate species whilst the higher temperature desorption feature is the result of C_(ads) and O_(ads) recombination. After a 240s dose the feature at 405K has shifted to a higher desorption temperature of ~420K and also visible is the presence of a small

shoulder at $\sim 470\text{K}$. These features, along with the higher temperature desorption feature continue to increase in intensity with increasing dose. The intensity of these features do not appear to saturate suggesting that there may be some second layer growth. However, the lack of a multilayer desorption feature indicates that these species may interact with the first tartrate layer via a stronger chemical bond rather than a weak, Van der Waals interaction. The shift in desorption temperature from 405K to 420K is assigned to the formation of a more stable tartrate species initiated by the displacement of CO present prior to the dosing of R,R-H₂TA. The shoulder at 470K is attributed to desorption of a tartrate species of higher stability.

The CO₂ TPD confirm the presence of a two step decomposition pathway.

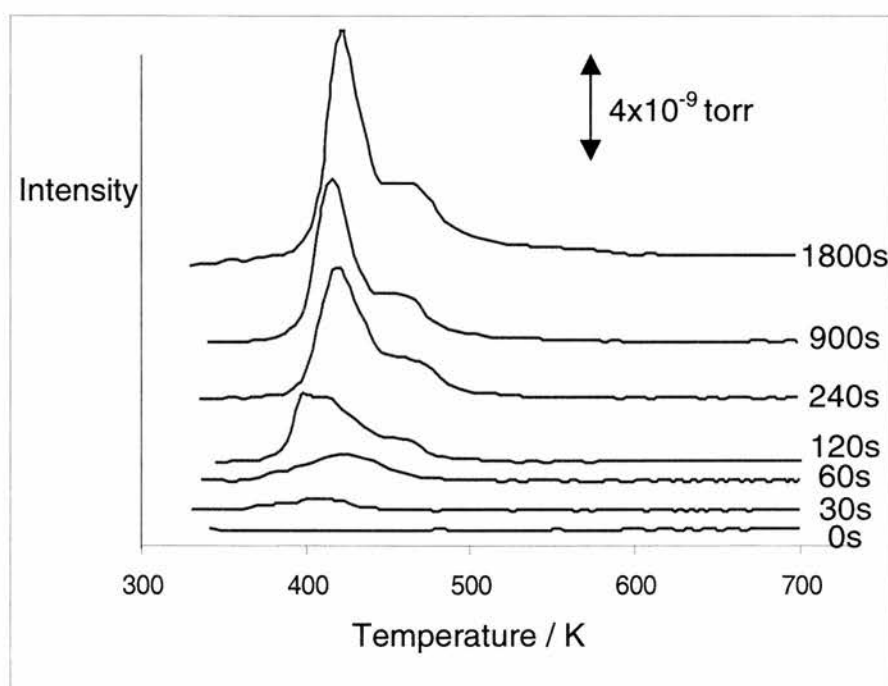


Figure 3.22. CO₂ TPD spectra of an increasing, higher flux dosing of R,R-H₂TA on Ni{111} at 300 K.

The desorption plot is characterised by the growth of two CO₂ features at $\sim 400\text{K}$ and 460K whilst the clean surface is initially free of CO₂. After 240s dose the most intense feature has shifted from $\sim 400\text{K}$ to 420K whilst the smaller feature has remained at

~460K. The CO₂ desorption features are again concomitant with two of the CO desorption features suggesting that they occur from the same decomposition process on the surface.

The H₂ TPD spectra, for the higher flux dose is illustrated in figure 3.23.

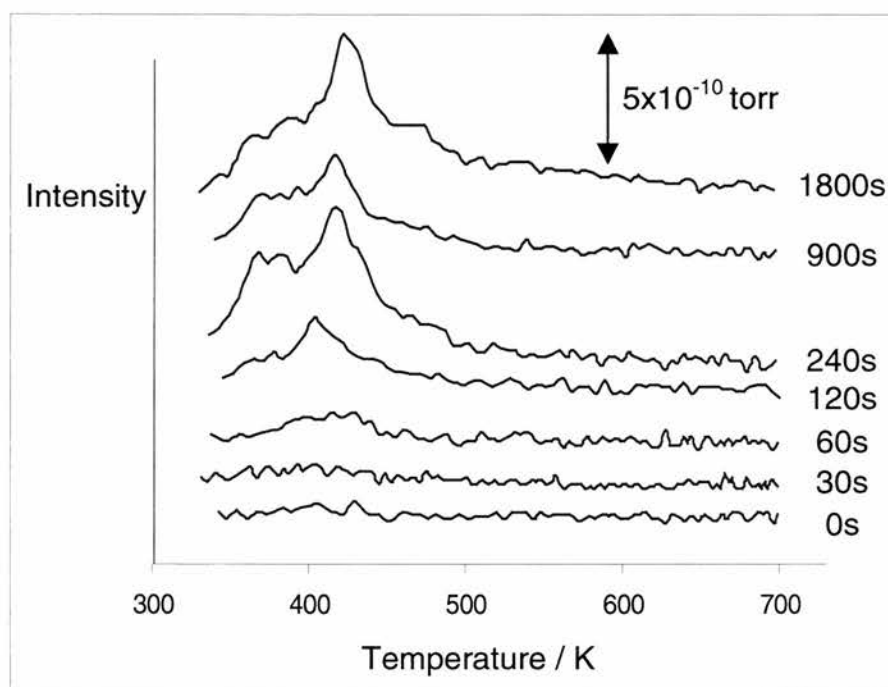


Figure 3.23. H₂ TPD spectra of an increasing, higher flux dosing of R,R-H₂TA on Ni{111} at 300 K.

The growth of the desorption features is characterised by a dominant feature with T_{\max} ~400K that shifts to ~420K and is accompanied by the growth of a shoulder at ~460K after a 240s dose. The growth is very similar to that observed for the lower flux dose and the appearance of features below 400K is probably due to the recombination of H_(ads) arising from the deprotonation of R,R-H₂TA when forming the carboxylate. The 420K desorption feature also coincides with the desorption of a CO and CO₂ feature.

The H₂O TPD spectra, for the high flux dose is illustrated in figure 3.24.

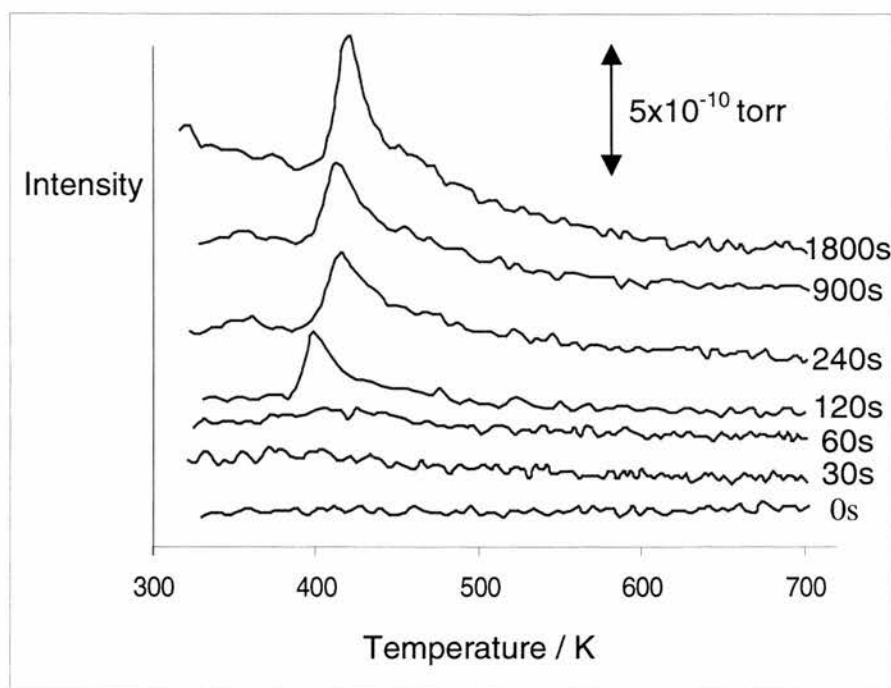


Figure 3.24. H₂O TPD spectra of an increasing, higher flux dosing of R,R-H₂TA on Ni{111} at 300 K.

The H₂O TPD again confirms the formation of a more stable tartrate species with increasing R,R-H₂TA coverage. This is indicated by the shift in temperature of the H₂O desorption feature from a T_{\max} of $\sim 400\text{K}$ to $\sim 420\text{K}$ between a dose of 120s and 240s.

Comparison of the low and high flux doses at 300K indicate the presence of one main difference. The onset of the adlayer stabilisation occurs after 240s for a low flux dose whilst this shift in T_{\max} occurs after 120s with a higher flux dose. This observation can be explained in terms of the higher tartrate coverage for the higher flux dose which displaces CO_(ads) more rapidly.

3.3.3.2 Temperature Programmed Desorption of R,R-H₂TA Dose at 350K

The CO and CO₂ TPD spectra for dosing at 350 K with a source temperature equivalent to the high flux dose are illustrated in figures 3.25 and 3.26.

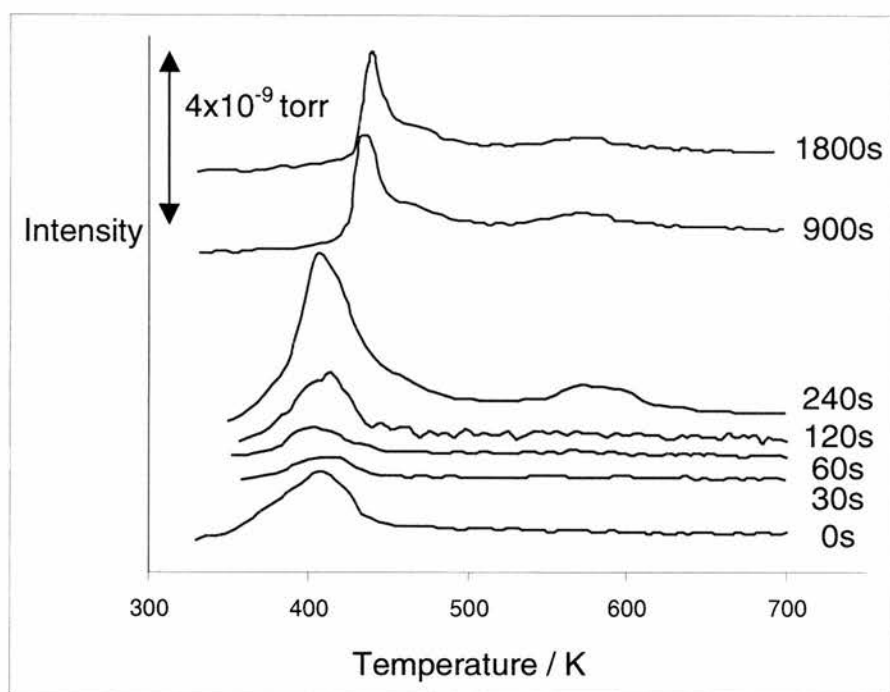


Figure 3.25. CO TPD spectra of an increasing dose of R,R-H₂TA on Ni{111} at 350 K.

The CO TPD shows the presence of adventitious CO adsorption with T_{\max} of ~400K and upon dosing R,R-H₂TA there is a dramatic decrease in the peak area. This feature then starts to increase in intensity up to a 240s dose at which point there is growth of a small shoulder at ~470K along with the feature with T_{\max} of 580K due to C_(ads) and O_(ads) recombination. The area of the 400K feature is largest after a 240s dose and the largest of all individual features, in comparison to the dosing at 300K. Further dosing shows the feature shifts to a higher temperature of ~440K along with the presence of the 470K feature after further increase in dose.

The CO₂ TPD spectra for the dosed at 350K is illustrated in figure 3.26.

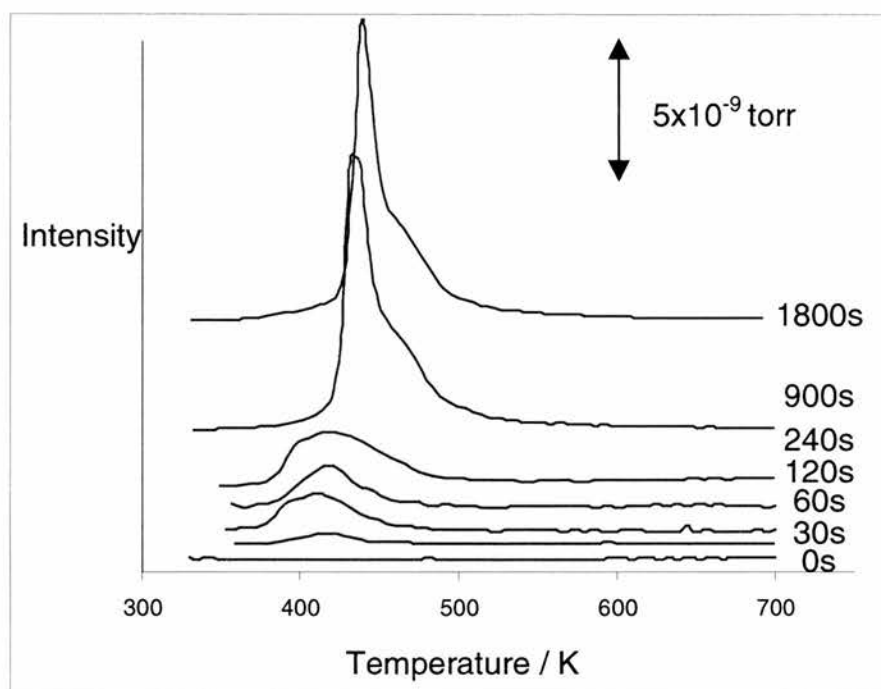


Figure 3.26. CO₂ TPD spectra of an increasing dose of R,R-H₂TA on Ni{111} at 350 K

The CO₂ desorption spectra is characterised by the growth of a feature at ~420K and as the coverage increases the initial feature is accompanied by the growth of a second feature at ~400K. After a 900s dose, there is the shift to higher temperature associated with the formation of the more stable tartrate species. The largest feature after this dose has a T_{\max} of ~440K and the smaller shoulder feature is observed with a T_{\max} ~465K.

The H₂ TPD desorption spectra is illustrated in figure 3.27.

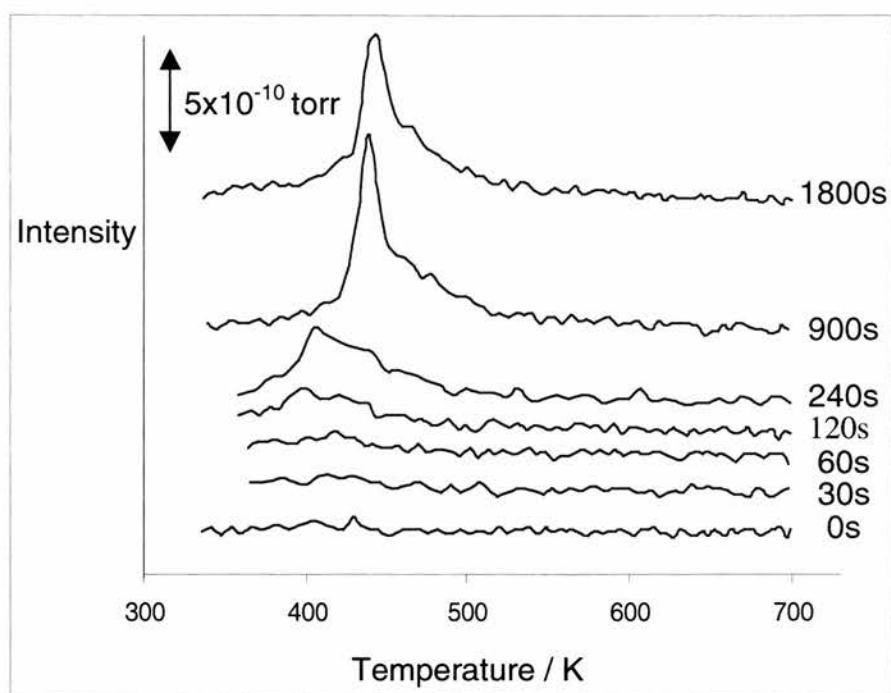


Figure 3.27. H₂ TPD spectra of an increasing, higher flux dosing of R,R-H₂TA on Ni{111} at 350 K.

With increasing dose, the growth of the desorption feature with $T_{\max} \sim 400\text{K}$ is observed up to a dose of 240s of R,R-H₂TA. After a 900s dose, the temperature of the feature again shifts to $\sim 440\text{K}$ with a shoulder having a $T_{\max} \sim 470\text{K}$, consistent with the CO and CO₂ TPD spectra and the formation of a more stable surface species.

The H₂O TPD plot is illustrated in figure 3.28.

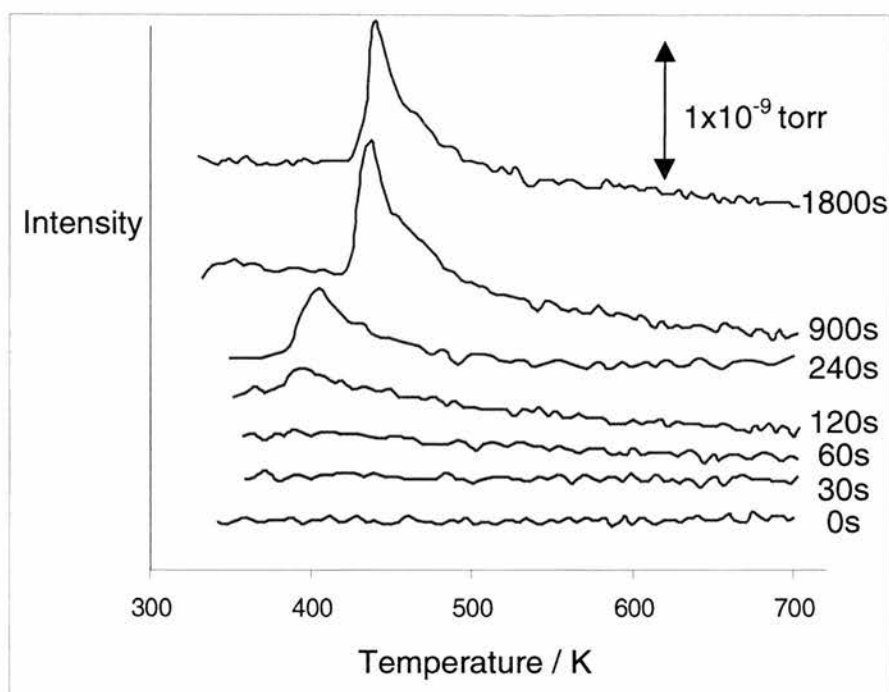


Figure 3.28. H₂O TPD spectra of an increasing, higher flux dosing of R,R-H₂TA on Ni{111} at 300 K.

The growth of a feature with $T_{\max} \sim 400\text{K}$ is observed as a function of increasing R,R-H₂TA dose, up to a dose of 240s. Following a 900s dose, this feature has shifted to $\sim 440\text{K}$ and there is also the growth of a shoulder at $\sim 470\text{K}$, consistent with the shifting in temperature observed for the CO, CO₂ and H₂ TPD.

Comparison of the TPD spectra for the low and high flux dosing at 300K indicate that the decomposition is very similar with the presence of CO_(ads) inhibiting the formation of a stabilised surface tartrate species. Once the coverage of CO_(ads) is below a critical level the surface species become more thermally stable, implicated by a 20K increase in desorption temperature. The attainment of the stabilised surface species is quicker for the higher flux dose due to the higher coverage of tartate species present after equivalent doses, hence a faster displacement of CO_(ads). This stabilised surface species then decomposes at $\sim 460\text{K}$ and the only further desorption process is that associated with

CO. AES spectra taken after the TPD runs revealed a relatively small amount of C (<0.1ML) remains on the surface but no O. It is therefore apparent that the presence and/or absence of CO_(ads) plays an extremely important role in the formation of the tartrate adlayer.

Comparison of the TPD spectra for R,R-H₂TA dosing at 350K with that at 300K indicates a number of significant differences. When dosing at 350K at higher coverage, the T_{max} of the main desorption feature is ~20K higher than the equivalent feature observed following R,R-H₂TA exposure at 300K. This indicates that the tartrate species formed on the surface at 350K are more stable than those dosed at 300K and results in the higher temperature desorption feature appearing as a shoulder on the main desorption peak rather than a separate feature. This observation may be very important as the optimum modification conditions are thought to be around 350K ^{[8][31]} and this study has shown that the surface species present at 350K are different to those at 300K.

The difference in the adsorbed species at 350K to that at 300K is also illustrated in the H₂ TPD spectra which indicates that the surface has a lower coverage of H_(ads) compared to that dosed at 300K as there is no low temperature shoulder to the main desorption peak. Also, the CO TPD indicate that the lower temperature shoulder is absent, probably a result of the lower sticking probability at elevated temperatures and consequently the creation of a high coverage of CO is much more difficult at 350K than at 300K.

3.3.4 STM Studies

Liquid phase catalytic reactions involving Ni based catalysts modified with R,R-H₂TA are known to be a corrosive process as analysis of the reaction mixture, post-reaction

indicates the presence of dissolved Ni ^{[8][31]}. The adsorption and examination of R,R-H₂TA on Ni{111} using an STM also gives rise to images where there is some evidence of ‘corrosion’ at the step edges leaving an observed serrated step edge, displayed in figure 3.29, rather than a regular straight step edge. This effect was not observed when analysing the clean surface.

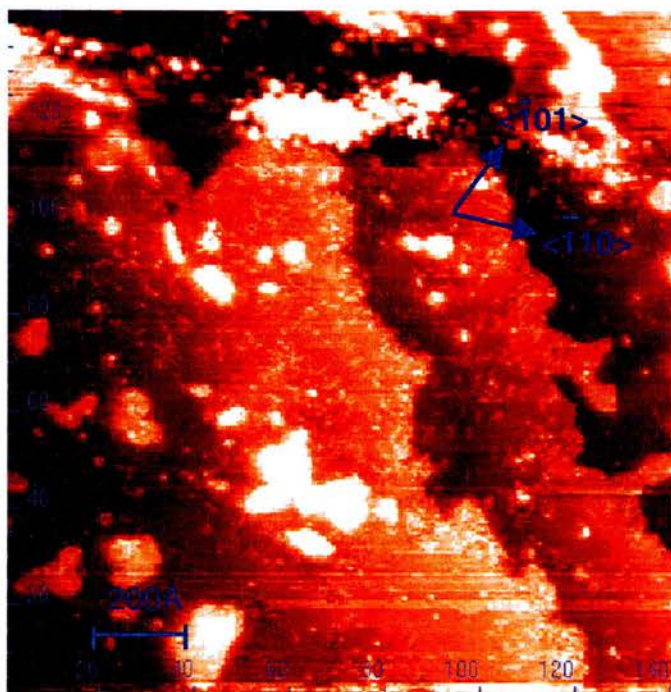


Figure 3.29. STM image illustrating corrosion of the step edges by the acid modifier, $V_{tip} = -0.302V$; $I_{tip} = 0.309nA$.

It is well known for surface diffusion to occur for atoms and molecules on a surface to enable them to reach their minimum free energy state. The diffusion rate is dependent on the crystallographic direction of diffusion, absolute temperature and surface coverage of the adsorbate ^[9]. It is very common for an adsorbate to collide with the surface and make thousands of atomic hops before it sticks to the surface with the activation energy for diffusion dependent on, amongst many factors, the roughness of the surface. The {111} face of an fcc surface has a relatively low roughness and

therefore the diffusion coefficient is likely to be relatively large. Step edges are areas with low diffusion coefficients as they are rougher, therefore an adsorbate colliding with the {111} face within a critical distance of the step edge has a high probability of binding to the surface at step edge sites ^[32].

It has been suggested that corrosive adsorption of R,R-H₂TA is important in formation of enantioselective sites as it has been suggested that abstracted nickel ions may form some sort of nickel tartrate complex adhering to the surface. It has been proposed that such complexes may serve as enantioselective sites ^{[8][31]}. Therefore the observation of images, such as in figure 3.29, might be important because if this effect is corrosion of the step edge, it would be interesting to determine the ultimate fate of the corroded Ni atoms. Perhaps they just lead to a higher proportion of metal adatoms on the terraces or move to other areas on the step edge. An exciting proposition would be if they were forming part of a nickel tartrate complex, however this is pure speculation and this study has not provided any evidence to suggest that this is the case.

It is therefore important to understand how the R,R-H₂TA interacts and grows on the surface to try and help answer these questions and others that have been discussed in previous chapters.

3.3.4.1 Adsorption at 300K

R,R-H₂TA is seen to congregate at step edges upon initial contact with the clean metal surface, illustrated in the STM image in figure 3.30A.

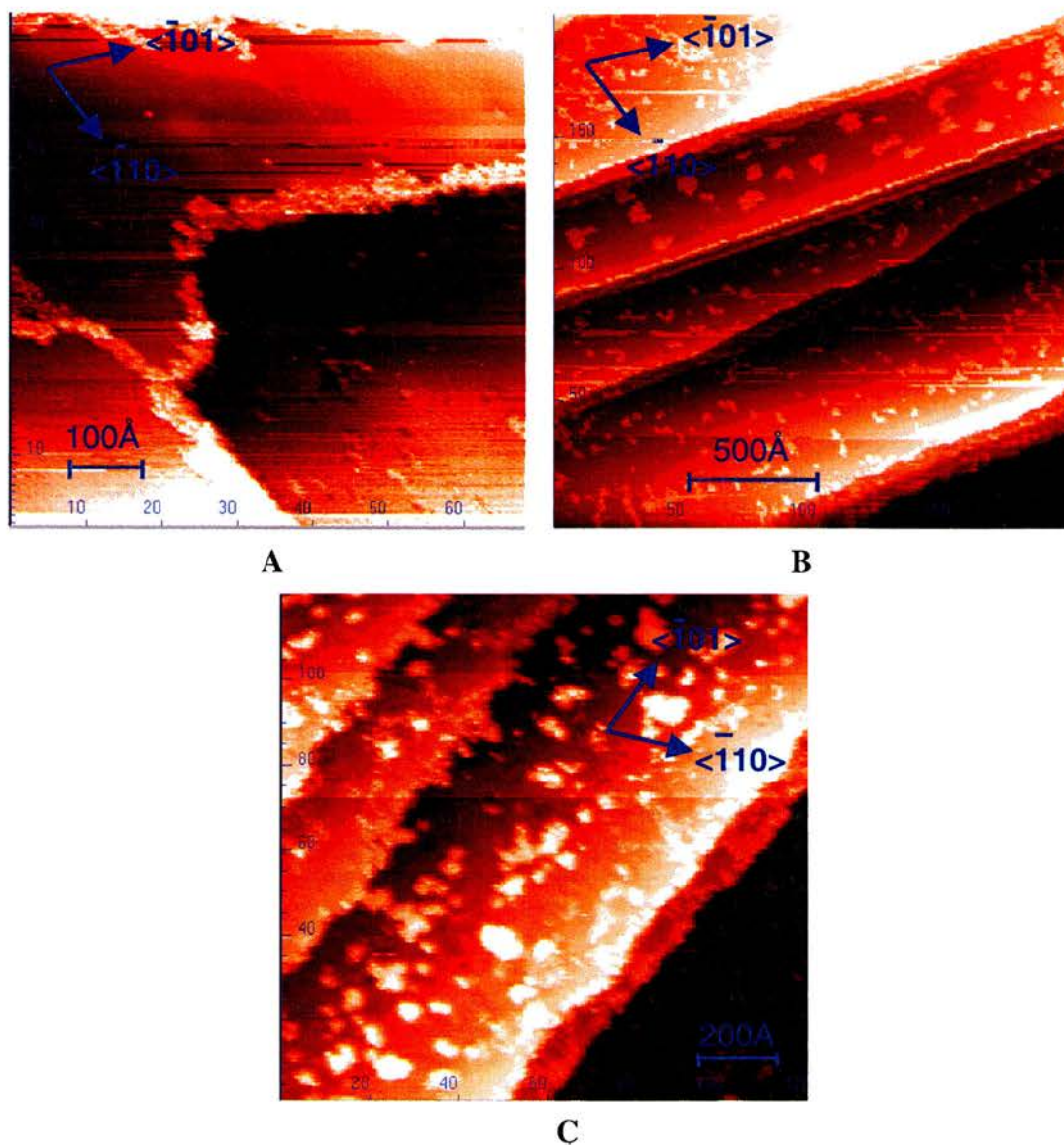


Figure 3.30. STM images showing the growth of R,R-H₂TA dosed at 300K, a) $V_{tip} = -0.426V$; $I_{tip} = 0.420nA$; b) $V_{tip} = -0.409V$; $I_{tip} = 0.535nA$ and c) $V_{tip} = -0.590V$; $I_{tip} = 0.240nA$.

In the submonolayer regime, the surface is generally disordered with fairly large clean terraces visible. Upon further dosing, figure 3.30B, there is evidence of overlayer growth on the terrace by the existence of small islands ‘dotted’ about the terrace. These small islands having an average size of $\sim 50\text{\AA}$ and appear to consist of disordered tartrate species. A closer examination of the step edges, figure 3.30C, clearly shows the presence of material decorating the step edge whilst island growth is dominant on the terraces.

As the coverage increases, the small disordered islands grow in size until large areas of the surface become covered. As the coverage approaches the monolayer regime, small areas of ordered structure are observed covering ~50% of the {111} terrace whilst the remainder of the terrace retains its disorder, as is illustrated in figure 3.31A.

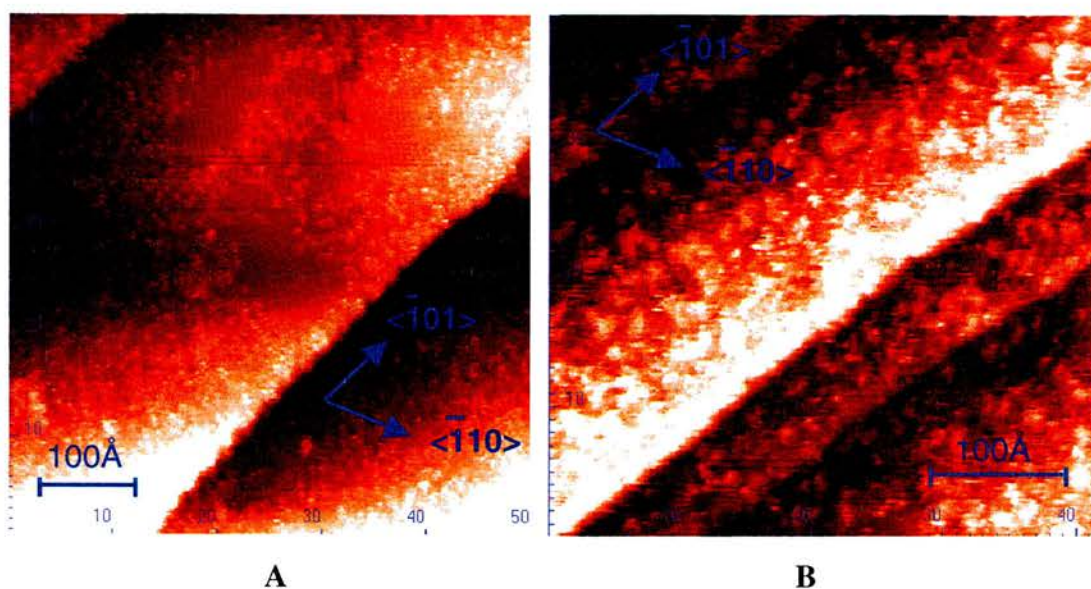


Figure 3.31. STM images showing the growth of R,R-H₂TA dosed at 300K, a) $V_{tip} = -0.308V$; $I_{tip} = 0.372nA$ and b) $V_{tip} = -0.284V$; $I_{tip} = 0.158nA$.

Further dosing results in totally disordered STM images, figure 3.31B. Either the ordered structures exist beneath the subsequent adsorbed layers or the higher coverage destroys the surface ordering.

Many different areas on the surface show the existence of ordered structures, however analysis has determined that there are just two different ordered structures observed for all coverages at 300K. These appear to be restricted to relatively small areas of ~100Å.

3.3.4.2 Adsorption at 330K

Adsorption of R,R-H₂TA at 330K occurs in a similar way to that at room temperature with initial adsorption sites existing at the step edge. The STM also indicates that growth on the terraces occur in small islands that increase in size until the whole terrace is effectively covered. No ordered structures have been observed from dosing at this 330K.

3.3.4.3 Adsorption at 350K

Adsorption of R,R-H₂TA at 350K again occurs in a similar way to that at 300K and 330K. The STM images show the presence of material decorating the step edges but where terrace growth is observed, it appears to be via long thin islands parallel to the step edge, illustrated in figure 3.32A.

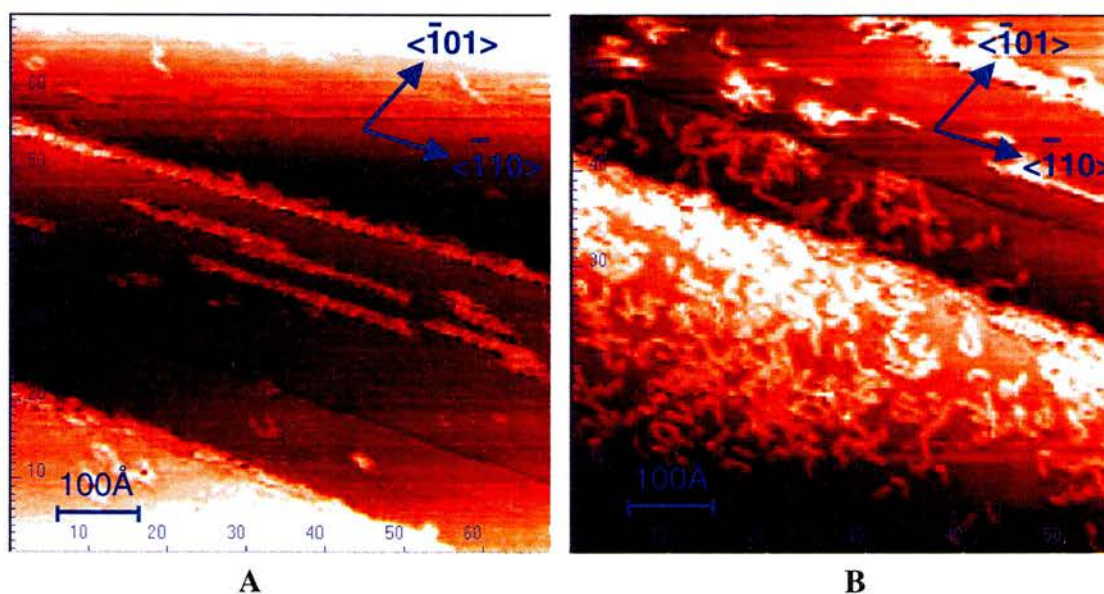


Figure 3.32. STM images showing the growth of R,R-H₂TA at 350K, a) $V_{tip} = -0.357V$; $I_{tip} = 0.327nA$ and b) $V_{tip} = -0.357V$; $I_{tip} = 0.327nA$.

For a slightly higher coverage the growth becomes dendritic with preferential growth being observed along the three close packed directions, illustrated in figure 3.32B. This is in contrast to what is observed for adsorption of R,R-H₂TA at 300K and 330K where

more rounded islands are observed. However, the appearance of this dendritic growth is similar to the polymeric structures observed in studies by Bonello *et al* ^[33] of methyl pyruvate adsorption on Pt{111}. Further dosing results in the formation of an ordered adlayer that also covers ~50% of the terrace.

3.3.4.4 Ordered Phases

Whilst analysing the STM data it became clear that an unambiguous model for the ordered species was not possible due to the lack of a LEED pattern. As stated previously, upon exposure of the electron beam with the R,R-H₂TA covered surface, the beam induced decomposition of the tartrate species. Therefore it is not possible to be absolutely certain how the overlayer structure relates to the underlying {111} surface. However, the LEED pattern of the clean surface has been recorded using a CCD camera to capture the diffraction pattern of the clean Ni{111} surface and hence determine the close packed direction to within $\pm 2^\circ$. The STM image has the same orientation as in the diffraction experiment and therefore it is possible to relate the orientation of the overlayer structure with respect to the close packed directions of the metal substrate. Subsequently it has been possible to obtain an accurate model for the observed ordered structures and the absence of a LEED pattern for the ordered overlayer is only a minor inconvenience.

The STM images were analysed by visually determining the overlayer unit cell and confirming by measurement of the proposed unit cell dimension. The unit cell was superimposed upon a hexagonal mesh, representing the {111} face, in the same orientation as that observed from the LEED pattern. Distances and angles between

individual features were also measured to aid the analysis and these were also placed on the substrate mesh and have led to the production of realistic models.

3.3.4.4.1 Adsorption of R,R-H₂TA at 300K

Adsorption of R,R-H₂TA at room temperature (6×10^{-8} torr of R,R-H₂TA for 120s) gave rise to two different ordered structures observed in STM images. Both of the ordered arrays corresponded to a slightly different local coverage of R,R-H₂TA and are distinguished by their unit cell matrix. The RAIR spectrum of this dose is illustrated in figure 3.33.

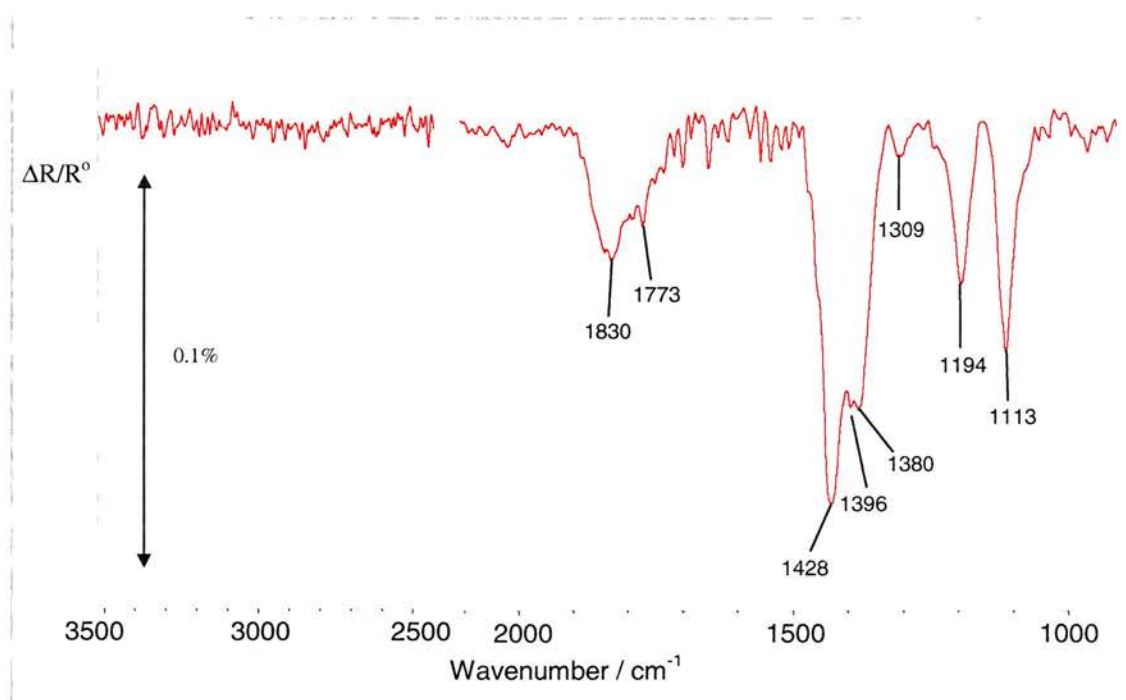


Figure 3.33. RAIR spectrum of R,R-H₂TA on Ni{111} at 300 K resulting in ordered STM images.

The RAIR spectrum exhibits typical bands observed for R,R-H₂TA on Ni{111}. Strong features at 1428cm⁻¹, 1380cm⁻¹, 1309cm⁻¹, 1194cm⁻¹ and 1113cm⁻¹ are associated with various stretching and bending modes of the R,R-H₂TA binding through at least one of its carboxylate groups. The presence of a band at 1830cm⁻¹ indicated CO in a 3 fold hollow site and the small shoulder at 1773cm⁻¹ indicates the possible presence of

carboxylic acid functionalities. The size of the $\nu_{\text{sym}}(\text{OCO}^-)$ suggests that the majority of the surface species may be bitartrate whilst the presence of smaller $\nu(\text{C}=\text{O})$ and $\nu(\text{C}-\text{O})$ at 1773cm^{-1} and 1396cm^{-1} suggests that a smaller amount of the surface may be covered in monotartrate species. However, these two bands are most likely associated with the initial formation of the multilayer due to the relatively large dose of R,R-H₂TA because the higher frequency band was never observed as high as 1760cm^{-1} for the monotartrate in the Cu{110} study [1-3]. The RAIRS data therefore suggests that the surface is covered by a majority of bitartrate species.

3.3.4.4.1.1 The (50 12) Phase

The first of the observed ordered STM images is illustrated in figure 3.34.

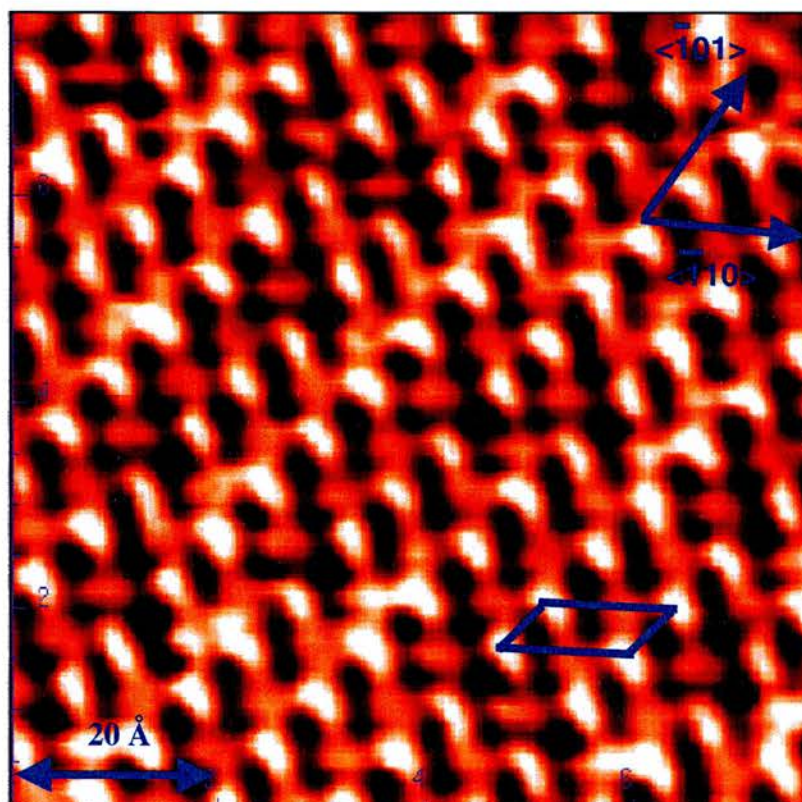


Figure 3.34. STM image of ordered adlayer obtained after dosing at 300K, $V_{\text{tip}} = -0.501\text{V}$; $I_{\text{tip}} = 0.514\text{nA}$.

The unit cell for the image in figure 3.34 is easily determined and the long side of the unit cell has been measured at 12.3Å (4.9 Ni-Ni spacings) and the short side measured at 7.0Å (2.8 Ni-Ni spacings), with internal angles of 44.7° and 135.3°.

It is well documented that thermal drift causes slight distortion to the STM image in the vertical direction. The amount of time taken to scan the full image is dependent on the scan speed and the area that is being scanned but in our studies, it is common that the time taken to scan a full image is in the order of 4 minutes. This is several orders of magnitude longer than it takes to scan a single line, in the x scan direction. This means that thermal drift, in an extreme case can be in the range of 20%^[34] and could result in a small elongation or contraction of the STM image at ambient conditions. For this reason, scanning of the surface using the STM was only commenced once the sample had been allowed to cool to room temperature for several hours. Also, measurements of the image perpendicular to the scan direction are not as accurate in comparison to measurements in the horizontal scan direction, which are very accurate. The small differences in the measured distances and angles between the model structures and STM images are therefore rationalised by this phenomenon.

The proposed unit cell structure for the appearance of the STM image in figure 3.34 is illustrated in figure 3.35.

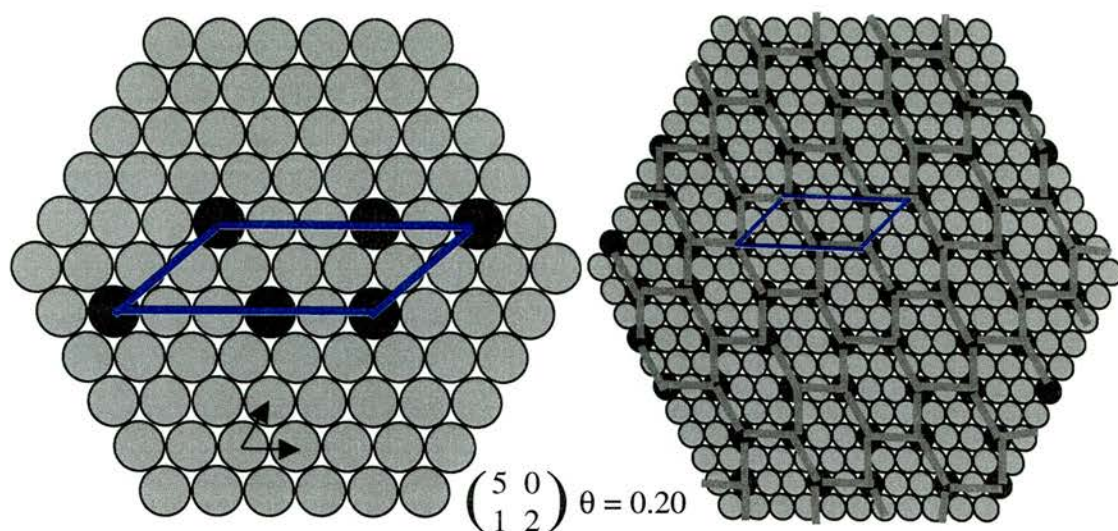


Figure 3.35. Possible model for the unit cell and overlayer structure with the striping observed in the STM image illustrated in figure 3.34.

It can be determined confidently that the longest side of the unit cell lies along the close packed direction as the features in the STM show this distance to be almost exactly 5 Ni-Ni spacings apart. The dimensions of the unit cell in the model are 12.5\AA (5 Ni-Ni spacings) and 7.0\AA (2.8 Ni-Ni spacings) and having internal angles measured as 40° and 140° . These values are in close agreement with those measured from the STM image, with the very small differences being due to thermal drift in the vertical, y direction.

The individual features in the STM image are separated by about 7.2\AA (2.9 Ni-Ni spacings) and 5.2\AA (2.1 Ni-Ni spacings) along the horizontal (5, 0) direction. The maximum length associated with R,R-H₂TA species bound as a monotartrate is about 5\AA ^[1] and therefore suggest that the features separated by 5.2\AA and 7.15\AA are individual molecules. The presence of stripes in the STM image between the features separated by 5.2\AA may also be an indication of hydrogen bonding, a similar effect was observed with R,R-H₂TA on Cu{110}^{[1][3]}. However, the related RAIR spectra in figure 33 does not show the presence of IR bands around 1650cm^{-1} corresponding to a carboxylic acid

carbonyl group involved in hydrogen bonding. The lack of an IR band can be explained in terms of the metal surface dipole selection rule. If the change in dipole moment for the carbonyl stretch of the carboxylic acid are parallel to the surface then this vibration would not be observed. Therefore this suggests that the two features separated by 5.2Å are two monotartrate species that are interacting via hydrogen bonding between the carboxylic acid groups and this interaction is parallel to the surface and the vibration is not observed because of the metal-surface selection rule.

There are also stripes present with a component in the y direction, from the corner feature of the lower section of the unit cell to the central feature in the upper section, along the (-1, 2) direction in the model. This distance has also been measured from the STM image to be about 5Å. It appears very unlikely that these two features are two ends of the same molecule and the striping is therefore associated with hydrogen bonding interactions. Each feature has three connecting stripes that have been assigned to hydrogen bonding interactions. An R,R-H₂TA molecule possesses two carboxylic acid and two α-hydroxy functional groups, all of which can be involved in hydrogen bonding. As the molecule has to interact with the surface via at least one of the carboxylic acid groups, this therefore leaves only three possible groups per molecule to interact with neighbouring molecules. This therefore discounts the presence of the structure consisting of bitartrate species as they only have two α-hydroxy groups that are capable of hydrogen bonding. For this reason the stripes in the vertical direction have been assigned to hydrogen bonding interactions with the α-hydroxy groups of a monotartrate molecule. The monotartrate species are stabilised by three hydrogen bonding interactions involving the three functional groups able to form hydrogen bonds

and results in a structure containing two molecules per unit cell with a local coverage of 0.20ML.

The proposed structure of the monotartrate, cyclic dimer overlayer is illustrated in figure 3.36.

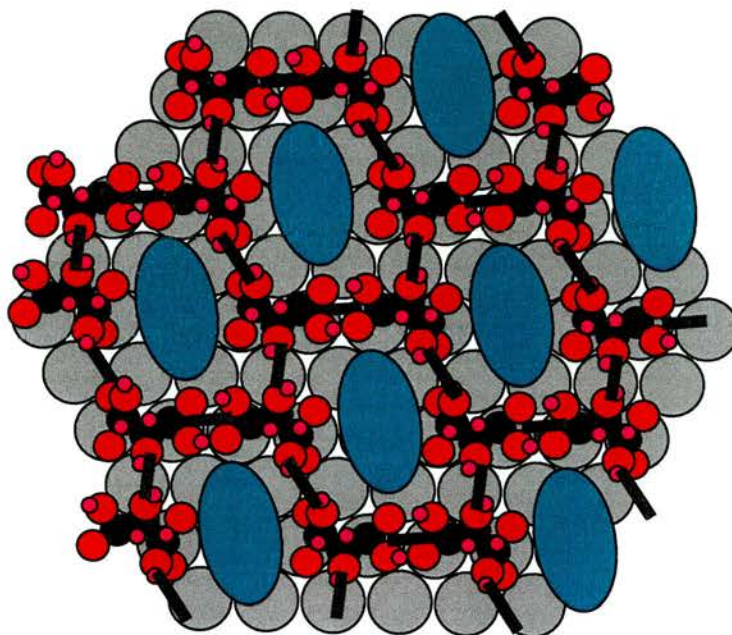


Figure 3.36. Proposed structure for the observed STM image in figure 3.34.

The green lobes show areas of bare Ni surface and their average size, as measured from the STM image is $\sim 8\text{\AA}$. An MAA molecule has a length measured at $\sim 7\text{\AA}$ and it therefore appears feasible for an incoming MAA molecule to attach to the surface at the sites denoted by the green lobes. The addition of an MAA molecule brings into consideration the possible effect it would have on the ordered surface in terms of the possible MAA orientation, whether one particular orientation is favoured or perhaps inducing restructuring of the overlayer.

3.3.4.4.1.2 The (4-1 -13) Phase

The second ordered STM structure observed after adsorption at 300 K is of a distinctive L shaped overlayer and is displayed in figure 3.37.

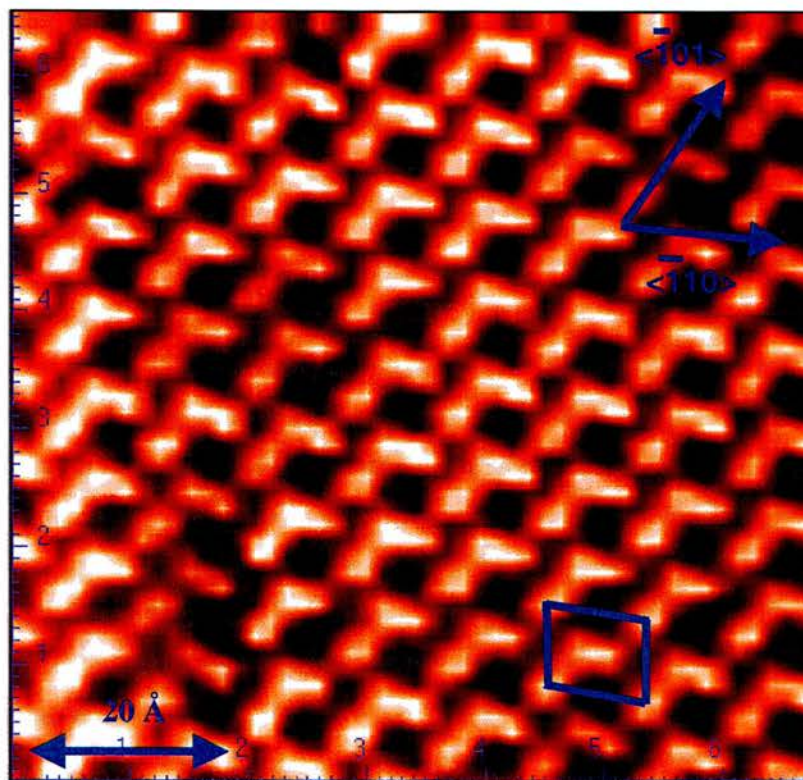


Figure 3.37. STM image of ordered adlayer obtained after dosing at 300K, $V_{tip} = -0.501V$; $I_{tip} = 0.514nA$.

The unit cell is easily visually determined. The vertical, shortest side of the unit cell is measured with a distance of 7.2\AA (2.9 Ni-Ni spacings) and the longest side measured as 10.0\AA (4 Ni-Ni spacings) with internal angles measured as about 79° and 101° from the STM image. Using the same methodology, as used in the analysis of the image in figure 3.34 to determine the unit cell and hence obtain a model of the overlayer, a model for the second of the STM images is illustrated in figure 3.38.

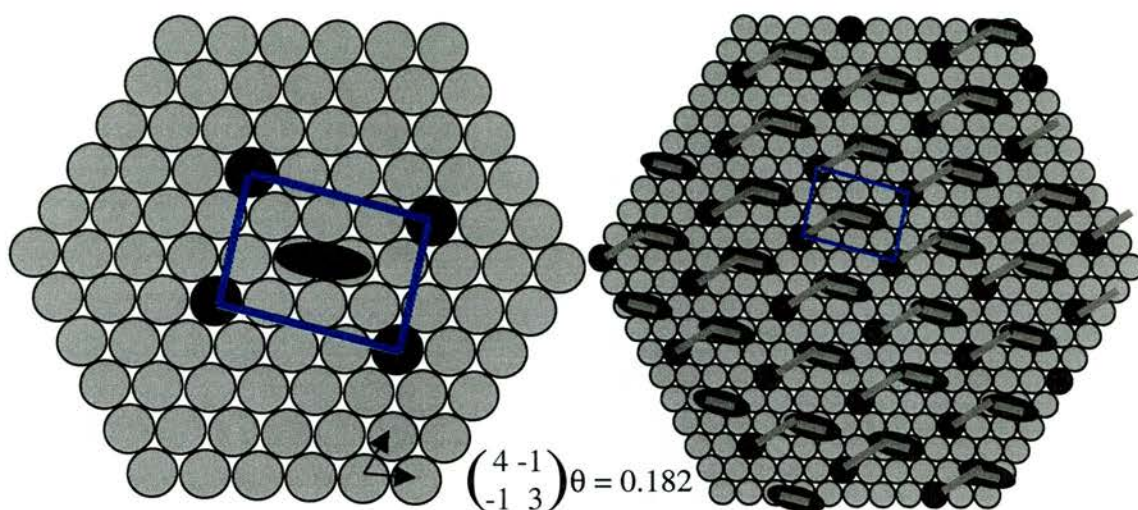


Figure 3.38. Possible model for the unit cell and overlayer structure observed in the STM image illustrated in figure 3.37.

The long vector of the unit cell is measured with a distance of 9.2\AA (3.7 Ni-Ni spacings) and the shorter vector has been measured with a distance of 6.7\AA (2.7 Ni-Ni spacings). The internal angles of the model unit cell are measured as 85° and 95° . The model that has been proposed is again consistent with the measured parameters in the STM images with small differences being accounted for by thermal drift during data collection.

There appear to be two types of features present in the STM image. The first is a long thin feature with a measured length of about 6\AA and a smaller, more circular feature with a diameter of about 3\AA . However, in the STM images there appears to be a small area in the bottom left hand corner that shows the presence of two separate features with the same distinctive L shape. This is probably due to a defect in the ordered structure and may give an important insight into the formation of this ordered adlayer. These features have been measured with a length of $\sim 4\text{\AA}$, which is consistent with the length of a monotartrate molecule. If this is the case, then the stripes in the STM image that exists between most of these features may again be consistent with intermolecular hydrogen bonding between neighbouring species with the dipole change of the

carboxylic acid groups being perpendicular to the surface. Therefore, assuming the L shaped features are composed of two features, there are two molecules per unit cell resulting in a local coverage of 0.182ML.

The proposed overlayer structure consists of monotartrate molecules interacting via hydrogen bonding as to form the cyclic dimer and is illustrated in figure 3.39.

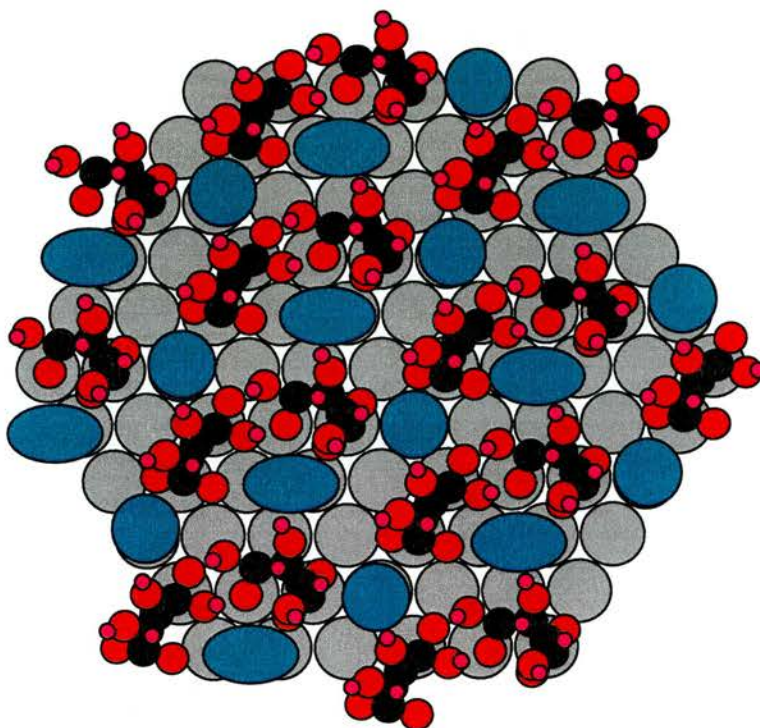


Figure 3.39. Proposed overlayer structure for the observed STM image in figure 3.37.

The L shaped features are clearly visible in the model above and the green lobes again depict clean areas on the Ni surface. There are two different sizes of clean metal in this model, which on close inspection of the STM image are also present. The size of the larger area of clean surface has been measured as $\sim 4.0\text{\AA}$. This space is probably too small from an incoming MAA molecule to attach to the surface however the possibility of the MAA molecule reconstructing the overlayer cannot be discounted.

3.3.4.4.2 Adsorption of R,R-H₂TA at 350 K

Adsorption of R,R-H₂TA at 350 K (2×10^{-8} torr of R,R-H₂TA for 150s) also gave rise to a different ordered structure as observed from the STM. The RAIR spectrum of this dose is illustrated in figure 3.40.

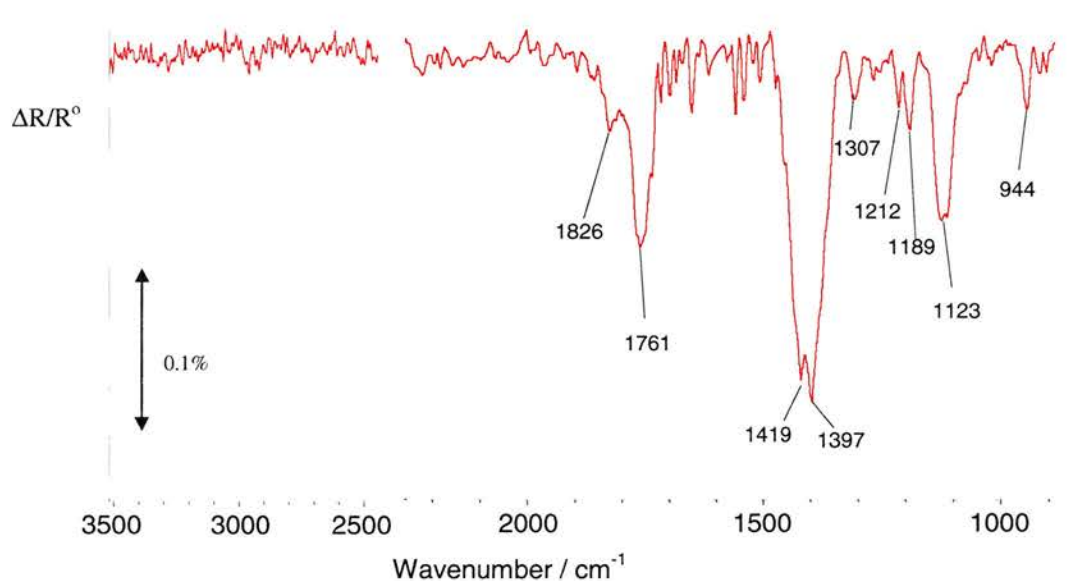


Figure 3.40. RAIR spectrum of the sequential dosing of R,R-H₂TA on Ni{111} at 350 K resulting in ordered STM images.

The exposure of R,R-H₂TA in the RAIR spectra at 350K show adsorption bands consistent with the presence of bitartrate species and the initial formation of the multilayer. The observed ordered STM image observed after dosing R,R-H₂TA at 350K is illustrated in figure 3.41.

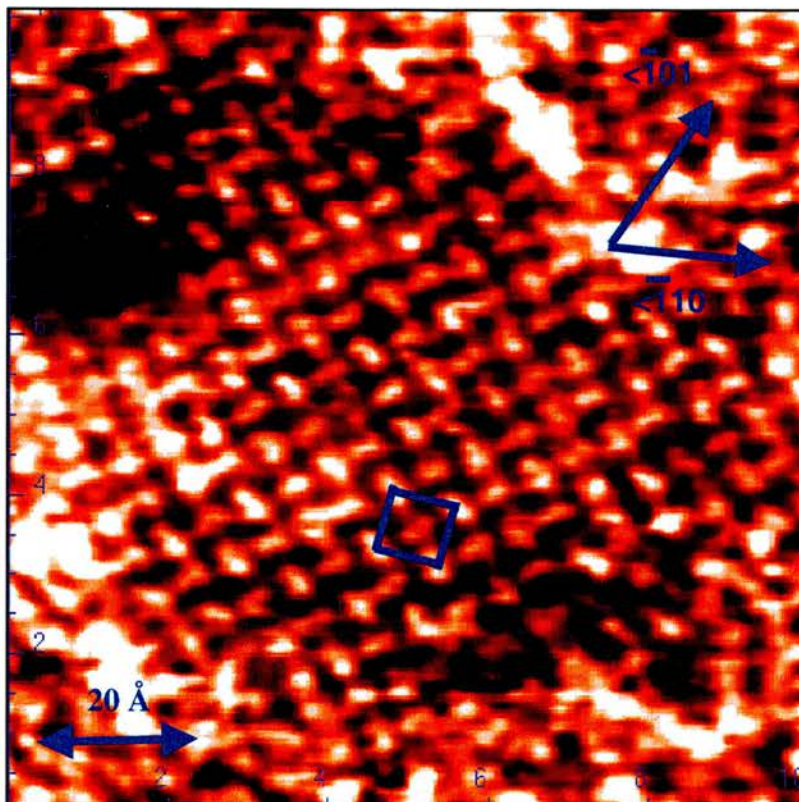


Figure 3.41. STM image of ordered adlayer obtained after dosing at 350K, $V_{tip} = -0.501V$; $I_{tip} = 0.343nA$.

The STM image above indicates that the unit cell is nearly rectangular with dimensions of 7.6 \AA (3.1 Ni-Ni spacings) and 8.3 \AA (3.3 Ni-Ni spacings) and the internal angles measured as 91.5° and 88.5° . The proposed model for the adsorbed phase is illustrated in figure 3.42.

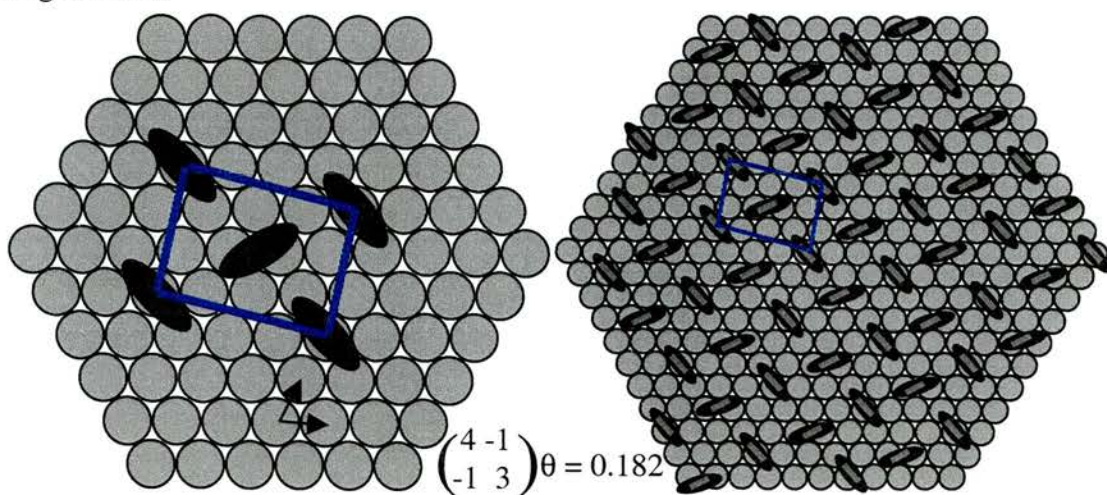


Figure 3.42. Possible model for the unit cell and overlayer structure observed in the STM image illustrated in figure 3.41.

The model unit cell has dimensions of 6.7 Å (2.7 Ni-Ni spacings) and 9.2 Å (3.7 Ni-Ni spacings) with internal angles of 94° and 86°. Again this model matches the observed STM image accurately. The individual features in the STM image have a length of approximately 4.5 Å and the unit cell is characterised by adjacent features that appear to be rotated by about 90° with respect to each another. The length of these features is consistent with that of a monotartrate however, depending on the contrast of the image or which part of the molecule is being imaged, the presence of a bitartrate species cannot be discounted.

The unit cell for the dose at 350K is identical to that of one of the ordered structure observed for the dose at 300K (figure 3.37). In fact, the area associated with defects of the adlayer in the 300K structure look very similar to that of the observed STM image in figure 3.41. On a close inspection of this STM image, in certain areas it is apparent that individual features appear to be composed to two separate features that is possible to be the image, possibly those of the terminal carboxylate groups or the α -hydroxy groups. The unit cell in this case could be illustrated as in figure 3.43.

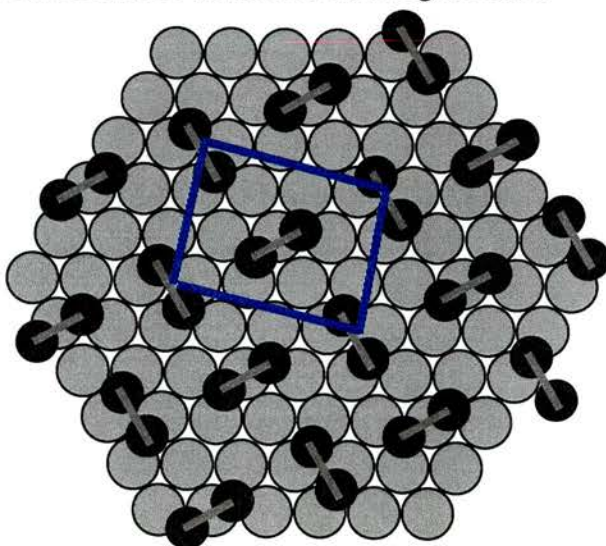


Figure 3.43. Possible unit cell for the overlayer structure observed in figure 3.41.

This observation therefore suggests that the features are those of the bitartrate species and assuming two molecules per unit cell, the local coverage of this structure is 0.182ML. The proposed overlayer structure is illustrated in figure 3.44.

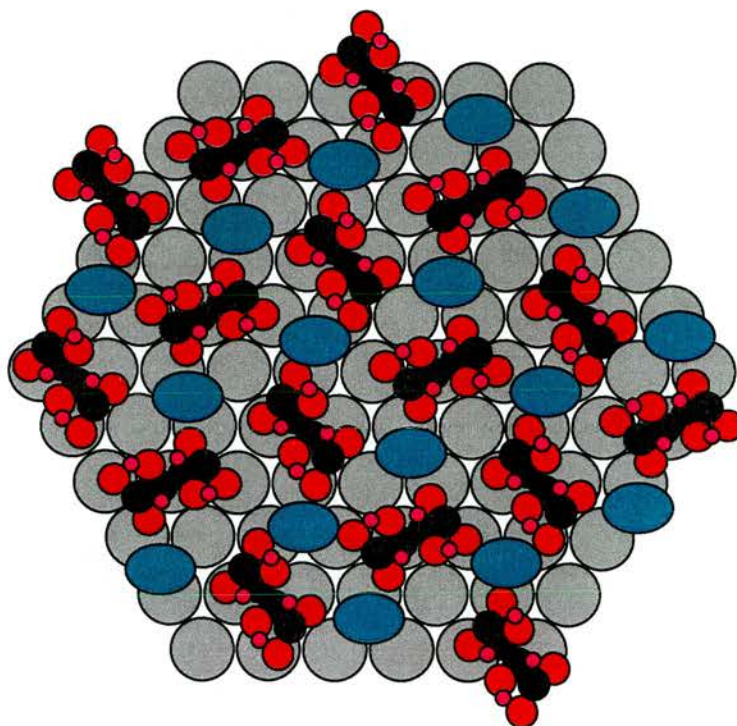


Figure 3.44. Proposed overlayer structure for the observed STM image in figure 3.41.

The green lobed areas again denote areas of clean surface and their average size is approximately 3\AA . This is again probably too small to allow an incoming MAA molecule to bind with the surface and although the local coverage of this ordered overlayer is identical to an ordered overlayer observed after deposition of R,R-H₂TA at 300K the area of clean Ni surface is smaller for the 350K case. Therefore, it would appear very unlikely that this ordered structure contain the site(s) responsible for the enantioselective hydrogenation.

At present, theoretical calculations are underway to determine if these models are realistic and help pin the molecules into their respective adsorption sites. However the calculations are currently incomplete and have subsequently been omitted from this thesis.

3.4 Summary

The growth of R,R-H₂TA on Ni{111} is dependent on both the incident flux and the adsorption temperature and shows certain similarities with the growth reported on Cu{110} with both monotartrate and bitartrate species observed [1-3]. However, the presence of CO on the surface is in contrast to that observed for Cu{110} and appears to play an important role in the construction of stable surface species.

With the exception of features due to CO_(ads), adsorption at 300K with a low incident flux is dominated by the presence of IR bands at ~1650cm⁻¹ at low coverage whilst at higher coverage the band at about 1430cm⁻¹ is dominant. The former band has been assigned to a carbonyl stretch that has been strongly downshifted from its analogous frequency in the free molecule indicating that it is involved in some sort of interaction with either the Ni surface or another molecule. The latter band is associated with a symmetric carboxylate stretch. This growth is similar to that of adsorption at 330 K and 350K except once the 1650cm⁻¹ band has reached saturation this band disappears for adsorption at 300K. TPD indicate that the main difference between two these surfaces is that at 350K there is a much lower coverage of H_(ads) indicated by the lack of a low temperature shoulder observed when dosing at 350K. This presumably results in sufficient H_(ads) present to protonate the carboxylate at one end of the R,R-H₂TA molecule at 300K and suggesting the presence of a phase change from a bitartrate to a

monotartrate species, a similar effect has also been observed for Cu{110} [1-3]. Therefore the most likely explanation for the low coverage, low incident flux adsorbate at 300K is that of a bitartrate where one of the carboxylate groups is bound monodentate to the surface and at high coverage the surface species are bidentate bitartrate. At 300K with a high incident flux and at 350K with increasing coverage the surface is dominated by the bidentate carboxylate functionality.

The TPD and STM data indicate two distinct ordered surface structures exist whose stability is dependent on the adsorption temperature. These ordered structures are only observed for sub-monolayer coverages and are confined to relatively small areas of the surface in contrast to the larger extent of ordering on Cu{110}.

Adsorption at 300K results in the formation of two structures, the first having a (50 12) unit cell and the second a (4-1 -13) unit cell. Adsorption at 350K has been observed to produce a single ordered structure, also with a (4-1 -13) unit cell. The (50 12) structure, observed to be the majority surface species, is stabilised by a hydrogen bonding network shown by each feature having three links. This suggests that three of the four functional groups on each molecule are involved in lateral interactions with neighbouring molecules whilst the fourth being the carboxylate functionality that binds the molecule to the surface. Our model therefore suggests the formation of back-to-back monotartrate species linked in the form of a cyclic dimer and further hydrogen bonding occurring between α -hydroxy groups of adjacent molecules. The (4-1 -13) structure observed at 300K consist of paired features and suggests the formation monotartrate dimers whilst there is no apparent interaction between individual dimers. These models are consistent with the IR data in that if the carboxylic acid functionality is parallel to the surface then

employment of the surface dipole selection rule would ensure this IR band is not observed.

The RAIR spectra for adsorption at 350K shows the presence of symmetric carboxylate stretching however the lack of carboxylic acid functionality indicates that the surface species could be bitartrate or monotartrate with the ‘free’ carboxylic acid group parallel to the Ni surface. TPD and STM data also indicate that the surface species are different to that at 300K as the initiation of desorption occurs at ~ 20K higher after adsorption at 350K. The only ordered STM structure observed after adsorption at 350K has the same unit cell as the minority ordered structure observed at 300K however this ordered phase is different and characterised by features alternating by 90°. This structure has been assigned to bitartrate species that are also known to be the most thermally stable tartrate phase on Cu{110} [1-3].

All RAIR spectra are characterised by the initial presence of surface CO adsorbed onto the surface whilst the sample was cooling to 300K, 330K and 350K. The IR bands associated with CO decreased with increasing R,R-H₂TA coverage suggesting that CO is displaced from the surface by R,R-H₂TA. TPD experiments indicate the important role adventitious CO has in the formation of stabilised tartrate species. When the level of CO displaced from the surface has decreased below a critical level there is a shift to a higher desorption temperature for features observed in the CO, CO₂, H₂O and H₂ TPD spectra. This suggests that CO disrupts intermolecular interactions between the tartrate species and it is only when the amount of CO is below a certain point that the surface species are stabilised. The presence of a stepwise desorption/decomposition process is easily seen and it is possible that the loss of tartrate species in the large feature at lower

temperature creates space for neighbouring molecules to adopt a more stable configuration resulting in the second, smaller feature at higher desorption temperature. The lack of further features in the CO₂, H₂ and H₂O TPD spectra and the presence of a small high temperature desorption feature in the CO TPD indicate that the tartrate species have either desorbed as fragments or have decomposed to O_(ads) and C_(ads) that then recombine and desorb at the higher temperature.

3.5 References

- [1] MO Lorenzo, S Haq, T Bertrams, P Murray, R Raval and CJ Baddeley; *J. Phys. Chem. B* **103** (1999) 10661
- [2] MO Lorenzo, CJ Baddeley, C Muryn and R Raval; *Nature*. **404** (2000) 376
- [3] MO Lorenzo; PhD thesis. University of Liverpool. 1999. Chapter 3, 68-144.
- [4] T Harada, Y Hiraki, Y Izumi, J Muraoka, H Ozaki and A Tai; *Proc. 6th Int. Congr. Catal.* (London, 1976) 1204
- [5] www.biologie.uni-hamburg.de/b-online/e18/18c.html
- [6] L Antonio, MM Barbosa and P Sautet; *J. Am. Chem. Soc.* **123** (2001) 6639
- [7] V Humblot, S Haq, C Muryn, WA Hofer and R Raval; *J. Am. Chem. Soc.* **123**, 3 (2002) 503
- [8] A Tai and T Harada; *Tailored Metal Catalysts*. Y Isawawa (ed.), D Reidel Publishing Company, 1986. 265
- [9] G Attard and CJ Barns; *Surfaces*. Oxford Chemistry Primers-59, Oxford Science Publications, 1998. 23-30.
- [10] T Edmonds and P Pitkethly; *Surf. Sci.* **15** (1969) 137
- [11] GA Somorjai; *Introduction to Surface Chemistry and Catalysis*. John Wiley and Sons Inc, 1994. 143
- [12] H Nakano and J Nakamura; *Surf. Sci.* **482-485** (2001) 341
- [13] V Maurice, N Kitakatsu, M Siegers and P Marcus; *Surf. Sci.* **373** (1997) 307
- [14] G Ertl and J Küppers; *Low Energy Electrons and Surface Chemistry*. VCH, Weinheim, 1985. 335
- [15] Y Nuriko, F Sekine, T Imanaka and S.Teranishi; *Bull. Chem. Soc. Jpn.* **54**, 4 (1981) 980
- [16] C Bater, M Sanders and JH Craig; *Surf. Sci.* **451**, 1-3 (2000) 226

- [17] www.cem.msu.edu/~cem924sg/kaiShen.dpd
- [18] S Mezhenny, I Lyubinetsky, WJ Choyke and JT Yates; *J. Appl. Phys.* **85**, 6 (1999) 3368
- [19] DH Williams and I Fleming; *Spectroscopic Methods in Organic Chemistry*. Third Edition. McGraw-Hill Book Company (UK) Ltd. Chapter 2, 35-73.
- [20] JC Campuzano and RG Greenler; *Surf. Sci.* **83** (1979) 310
- [21] KS Smirnov and G Raseev; *Surf. Sci.* **384** (1997) L875
- [22] N Ikemiya, T Suzuki and M Ito; *Surf. Sci.* **466** (2000) 119
- [23] G Held, J Schuler, W Sklarek and HP Steinrück; *Surf. Sci.* **398** (1998) 154
- [24] M Trenary, KJ Uram, F Bozso and JT Yates; *Surf. Sci.* **146** (1984) 269
- [25] H Conrad, G Ertl, J Küppers and EE Latta; *Surf. Sci.* **57** (1976) 475
- [26] M Bowker, S Haq, R Holroyd, PM Parlett, S Poulston and NV Richardson; *J. Chem. Soc., Faraday Trans.* **92**, 23 (1996) 4683
- [27] SM Barlow, KJ Kitching, S Haq and NV Richardson; *Surf. Sci.* **401** (1998) 322
- [28] FT Netzer and TE Madey; *J. Chem. Phys.* **76** (1982) 710
- [29] HJ Freund and MW Roberts; *Surf. Sci. Rep.* **25** (1996) 225
- [30] K Christmann, RJ Behm and G Ertl; *J. Chem. Phys.* **70** (1979) 4168
- [31] Y Izumi; *Adv. Cat.* **32** (1983) 215
- [32] JH Ferris, JG Kushmerick, JA Johnson and PS Weiss; *Surf. Sci.* **446**, 1-2 (2000) 112
- [33] JM Bonello, FJ Williams, AK Santra and RM Lambert; *J. Phys. Chem. B.* **104** (2000) 9696
- [34] Personal communication with Q Chen.

Chapter Four

Adsorption of Methyl Acetoacetate on Ni{111} and (R,R)-Tartaric Acid Modified Ni{111}.

4.1 Introduction

The adsorption geometry of MAA on clean, unmodified Ni{111} is of great importance as to understand the modifier-reactant interaction on the Ni{111} surface, the behaviour of MAA on Ni{111} must be known. With an awareness of the individual behaviour of modifier and reactant on the surface it may be possible to gain an insight into the mechanism for the possible formation of the enantioselective sites.

To our knowledge, the only report of MAA adsorption on a single crystal metal surface is the PhD thesis of Lorenzo ^[1] where MAA was studied on Cu{110}. In its natural form, MAA exists as a liquid in two tautomeric forms, the diketone or enol with the keto form dominant however in the presence of various solvents the equilibrium position is known to shift. Lorenzo's studies have indicated that at 300K, MAA adsorbs on Cu{110} in its enol form and orientates with the molecular plane roughly perpendicular to the surface, illustrated in figure 4.1, indicated by strong $\nu(\text{C}=\text{O})$ bands and weaker $\nu(\text{C}-\text{O})^{\text{ester}}$ and $\nu(\text{C}=\text{C})$ bands in the IR spectra.

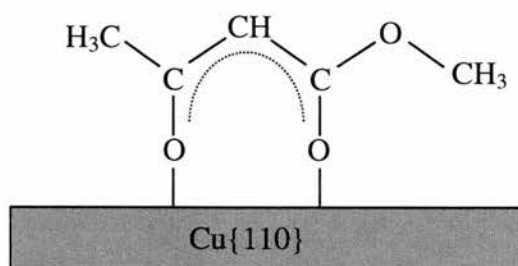


Figure 4.1. Illustration of the bonding and orientation of MAA on Cu{110} at 300 K^[1].

Its molecular orientation remains unchanged as a function of coverage and TPD data indicate it is thermally stable on the surface until 470K. No multilayer growth was observed^[1].

Lorenzo also studied the adsorption of MAA on ordered R,R-H₂TA phases on Cu{110}^[1]. IR data indicate that MAA only adsorbs on surfaces consisting of a low tartrate coverage, reinforcing catalytic data suggesting that free metal sites are required for hydrogenation to occur^{[2][3][4]}. In the low coverage regime, Lorenzo observed adsorption of MAA to a Cu{110} surface covered with both monotartrate and bitartrate phases. However, when the surface is covered in a monotartrate phase, STM data indicate that the MAA molecules do not interact with the ordered tartrate overlayer. In contrast, when the ordered phase is that of the bitartrate there is an observed interaction between MAA molecules and the tartrate islands, resulting in small changes in the ordered (90 12) structure. Extra bands are also observed in the RAIR spectra that suggests a slight change in MAA orientation has occurred whereby the molecules are now only bound to the surface via the ester carbonyl group. This ‘new’ overlayer structure is reported to be stabilised by the α -hydroxy groups of the bitartrate molecules^[1].

These observations have been rationalised by the amount of ‘free’ space surrounding individual tartrate molecules. The monotartrate adlayer is much more closely packed and subsequently there is insufficient room for a MAA molecule to attach within the ordered structure whilst the presence of bare channels observed for the bitartrate structure allow the MAA molecules to bind within the surface and interact with the R,R-H₂TA molecules ^[1]. Although a tilted MAA orientation is proposed for this observation, a specific model describing the interaction between MAA, bitartrate molecules and the Cu surface has not been proposed.

4.1.1 Proposed Models

4.1.1.1 Modifier-Reactant 1:1 Interaction

The enantioselective sites of the modified nickel catalyst are dual functional. They possess the ability to differentiate the enantiofaces of the reactant molecule and hydrogenate the specific face to yield one enantiomer in excess ^[5]. There have been many suggested models for the possible enantioselective sites that give rise to this dual functionality, involving the interaction between MAA and R,R-H₂TA and also with the metal surface ^[6-7]. However all of these models are based on the kinetic and catalytic data ^[6] and do not take into account the actual modified surface. Of all the models proposed the most accepted are at best speculative as there is very little spectroscopic data to back up the models. An example of one of these models is illustrated in figure 4.2.

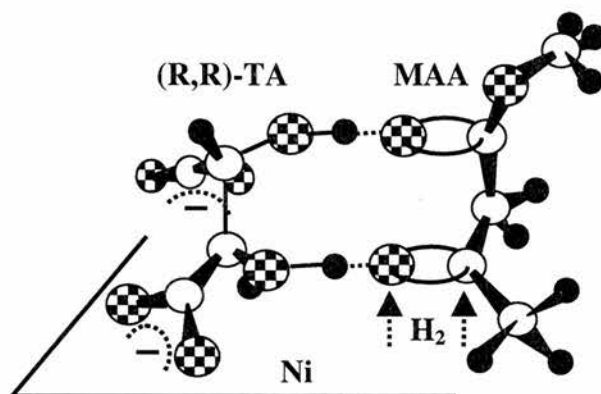


Figure 4.2. A proposed adsorption mode of R,R-H₂TA and MAA on the nickel surface^[6-8].

In this model the R,R-H₂TA molecule is interacting with the surface as a bitartrate and the reactant molecule interacts with the modifier molecule via a hydrogen bonding system between the hydroxy groups of the modifier and the ketone and ester carbonyl groups of the reactant. The hydrogen bond coupling between the modifier and the reactant molecules suggests a 1:1 interaction and if hydrogenation occurs from the surface side of the carbonyl bond, it is possible to visualise that a solitary MAA molecule will yield a single enantiomer. For one product to dominate in the catalytic reaction there must be a difference in adsorption energy of the two faces. However, there appears to be nothing in this model to hinder an incoming MAA molecule rotated by 180°, with respect to the MAA orientation in figure 2.2, hydrogenating the opposite face of the molecule. Therefore, this maybe good as a model for the hydrogenation of the reactant molecule but may not be an accurate description of the enantioselective site.

The structures of the adsorption complexes on supported nickel catalysts have been determined by infrared spectroscopies^[7] and the proposed models come about on the assumption based of the hydrogen bonding ability of the two hydroxy groups of tartaric acid and the two carbonyl groups of MAA. Catalytic data suggests that all four

functional groups of tartaric acid appear to be essential to perform effective enantioselective hydrogenation. Upon removing one of the four functional groups of tartaric acid it was observed that the enantioselectivity over the Ni catalyst halved and when two were removed, the enantioselectivity of the catalyst was almost lost ^[6].

It has also been suggested that another compound, other than MAA, containing an oxygen atom bound to the β -carbon of the prochiral carbonyl group and having two hydrogen bond acceptors arranged about 2.5Å apart should be hydrogenated over tartaric acid modified Ni catalysts with high optical yields ^[7]. Table 4.1, is an illustration of how the enantioselectivities vary with reactant structure.

Reagent	Optical yield (%)	Predominant configuration
$\begin{array}{c} \text{CH}_3 - \text{C} - \text{C} - \text{O} - \text{CH}_3 \\ \parallel \quad \parallel \\ \text{O} \quad \text{O} \\ \text{Methyl pyruvate} \end{array}$	2.0	R
$\begin{array}{c} \text{CH}_3 - \text{C} - \text{CH}_2 - \text{C} - \text{O} - \text{CH}_3 \\ \parallel \quad \quad \parallel \\ \text{O} \quad \quad \text{O} \\ \text{Methyl acetoacetate} \end{array}$	86	R
$\begin{array}{c} \text{CH}_3 - \text{C} - (\text{CH}_2)_2 - \text{C} - \text{O} - \text{CH}_3 \\ \parallel \quad \quad \quad \parallel \\ \text{O} \quad \quad \quad \text{O} \\ \text{Methyl 4-oxopentanoate} \end{array}$	38	R
$\begin{array}{c} \text{CH}_3 - \text{C} - (\text{CH}_2)_3 - \text{C} - \text{O} - \text{CH}_3 \\ \parallel \quad \quad \quad \parallel \\ \text{O} \quad \quad \quad \text{O} \\ \text{Methyl 5-oxohexanoate} \end{array}$	0	-

Table 4.1. Enantioselective hydrogenation of prochiral ketones with R,R-H₂TA-MNi ^[7].

The α -ketoester, methyl pyruvate, a hydrogenation reagent used in the enantioselective heterogeneous reaction over modified platinum catalysts has a structure that does not allow a close fitting interaction with R,R-H₂TA and a slow hydrogenation and a poor

optical yield are observed. With the γ -ketoester, methyl 4-oxopentanoate, the distance is somewhat greater and close fitting interaction is not possible, however the flexible nature of carbon chain allows the substrate to achieve a two-site interaction with tartaric acid to a certain extent, with a moderate optical yield^[9]. With the δ -ketoester, methyl 5-oxohexanoate, either the ester carbonyl behaves as a hydrogen bond acceptor or hydrophobic alkyl chain with virtually negligible optical yield arising from existence of the two countering adsorption modes. The enhancement of the optical yield and the hydrogenation rate of β -ketoester over R,R-H₂TA-MNi has been proposed to originate from the hydrogen bonding between the modifying reagent and the reactant on the metal surface^[7]. However, the catalytic data has not taken into account the physical size of the reactant molecules. As indicated in the work by Lorenzo *et al*^[10-11] and discussed in chapter 3 of this study, the size of the areas of 'clean' surface may also play an important part in determining the enantioselective sites. The three different ordered structures we observed in chapter 3 possess areas of clean surface of particular dimensions and adsorption of molecules into these areas of bare metal would encounter steric hindrance if adsorbate dimensions are too big and these sites would therefore be unfavourable.

Other mechanisms speculated involve the modifier-reactant interaction occurring at step edges where by one of the carbonyl groups of the reactant molecule interacts with metal atoms at the step edge and the other with one of the hydroxy groups of R,R-H₂TA. However, this appears unlikely as catalysts with larger Ni particles generate a greater optical yield^[12] and larger particles are dominated by the {111} face that possess fewer step and kink sites^[13]. One particular model, that appears feasible is the possibility that R,R-H₂TA forms some sort of nickel tartrate complex, perhaps created as a result of

acid modification ^[6]. Such a model was proposed by Hoek *et al* ^[14] for nickel catalysts modified with nickel tartrate, illustrated in figure 4.3, with each nickel atom being tetra-coordinated.

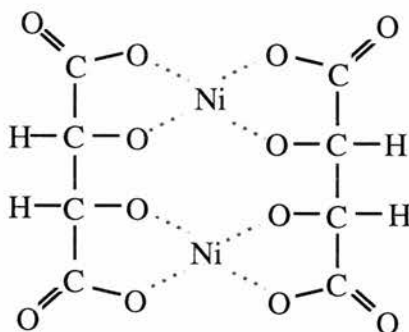


Figure 4.3. Proposed binuclear nickel tartrate complex ^[14].

It was proposed that one of the remaining two coordination states of nickel participates in hydrogenation of the reactant molecule. The structure of the nickel tartrate complex acts as a template whereby the specific reactant enantioface can be hydrogenated and hydrogen is supplied from metallic nickel to the hydrogenation site of the complex by a spill over transport via the tartaric ligand ^[6].

4.1.1.2 Template Model

This ‘Template Model’ was initially proposed by Webb *et al* ^[8] to explain the behaviour of the Pt/cinchonidine system, the second of the two main liquid phase heterogeneous enantioselective hydrogenation reactions. The hydrogenation of the α -keto ester, methyl pyruvate over alkaloid modified platinum catalysts, cinchonidine is used as the chiral modifier.

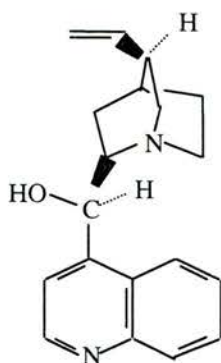


Figure 4.4. Cinchonidine - chiral modifier for hydrogenation of α -keto esters over Euro Pt-1 catalysts.

The authors ^[8] proposed a model in which cinchonidine is chemisorbed to surface Pt atoms via the π -electron system of the quinoline moiety giving an L shaped footprint on the surface to produce a 2-D array on the Pt surface, illustrated in figure 4.5. Their studies revealed that two molecules interact via hydrogen bonding of the quinuclidine N and the keto oxygen of the reactant molecule, whilst the hydrogen is supplied from the acidic media ^{[8][15]}.

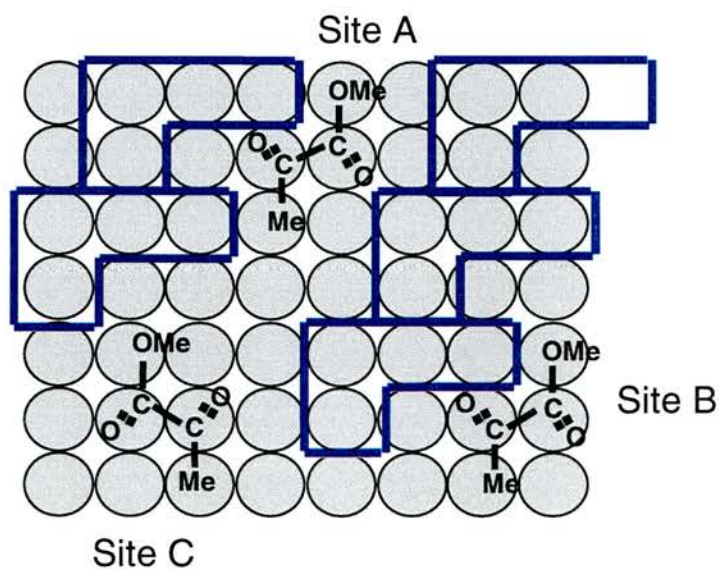


Figure 4.5. A proposed scheme for the adsorption sites in Euro Pt-1 system ^[8].

The modifier molecules were proposed to order up over the surface in groups of 2 or 3 leaving exposed shaped ensembles of Pt atoms for the pyruvate adsorption. The

modifier overlayer acts as a template for the incoming reactant molecules directing the adsorption to one face only and hence introducing enantioselectivity to the system ^[8]. These type of sites are those such as sites A and B. Burgi *et al* ^[15] has suggested a 1:1 interaction model in which the modifier and reactant molecules interact at the edge of the modifier islands. In the model illustrated in figure 4.5, there are also bare metal sites that yield the racemic product such as at site C.

It is stressed in the report ^[8] that the model is ‘only a model’ and there are many assumptions made in explaining the adsorption states, hence the template model has since been questioned. Catalytic experiments and modelling ^[15-16] suggest the 1:1 interaction is all that is required for enantioselective catalysis in this system whilst surface science experiments throw doubt on the existence of ordered arrays consisting of 2 or 3 molecules ^[16]. No adsorbate induced LEED patterns were obtained discounting the possibility of long range ordering and the rotational flexibility in the modifier permits the 1:1 interaction to be achieved to a maximum effect ^[16]. Studies by Lorenzo *et al* of MAA adsorption on R,R-H₂TA modified Cu{110} ^[10-11] have also suggest a template type model which may be important in explaining the role of the modified Ni-based catalysis. However their studies were reported using Cu, which is known to be a poor hydrogenation catalyst ^[7] and subsequently no direct evidence exists for the presence of these interactions in the Ni system ^[6-8]. Therefore, in this chapter the adsorption of MAA on Ni{111} and R,R-H₂TA modified Ni{111} has been investigated to shed light on the molecular mechanisms underlying the enantioselective catalysis.

4.2 Experimental

The Ni{111} single crystal was cleaned by cycles of Ar⁺ ion bombardment at 1.5keV and annealing to 900K. LEED and AES were employed to determine surface structure and the level of surface contamination respectively.

MAA was dosed onto the Ni{111} surface at 300K. At room temperature, MAA is a liquid and has a vapour pressure of about 1 torr. Therefore MAA can be purified by cycles of freeze-pump-thaw using a turbomolecular pump. After purification, the MAA vapour was then dosed into the UHV chamber containing the Ni{111} single crystal via a leak valve to the desired pressure and time.

The prepared surfaces were characterised by RAIR and TPD spectroscopies and STM was used to observe any 2-D topological features.

4.3 Results and Discussion

Adsorption of MAA on Ni{111} and on R,R-H₂TA modified Ni{111} at 300K as a function of increasing dose has been studied using IR spectroscopy. The assignments for the observed IR bands have been based on those obtained for R,R-H₂TA and MAA on Cu{110}^[10] and they required a small revision for this study^[17] and are summarised in table 4.2.

Assignment	MAA + Ni{111}	MAA + R,R-H ₂ TA /Ni{111}
$\nu(\text{C-H})^{\text{enol}}$ on C=C	3017	
$\nu_{\text{asym}}(\text{CH}_3)$	2958	2963
$\nu(\text{CO})^3$ fold-bridge	1789	
$\nu(\text{C=O})$	1726	
β -keto, H-bonded to ester or surface interaction ^(enol)	1653	
$\nu(\text{C=C})^{\text{enol}} + \nu(\text{C=O})^{\text{enol}}$	1610 1587	1591
$\nu(\text{C} \cdots \text{C})^{\text{enol}}$	1558	
$\delta_{\text{asym}}(\text{CH}_3)$	1452 1435	1448
$\delta_{\text{sym}}(\text{CH}_3)$	1363	1365
$\gamma(\text{C-H})^{\text{enol}}$	1301	1312
$\nu(\text{C-O})^{\text{ester}}$	1277	1285 1265
$\nu(\text{C-C})$	1207	

Table 4.2. IR assignments observed in the adsorption of MAA on Ni{111} and on R,R-H₂TA/Ni{111}.

4.3.1 MAA Adsorption on Ni{111}

4.3.1.1 RAIRS Studies

The adsorption of MAA on Ni{111} at 300K as a function of increasing coverage is illustrated in figure 4.6.

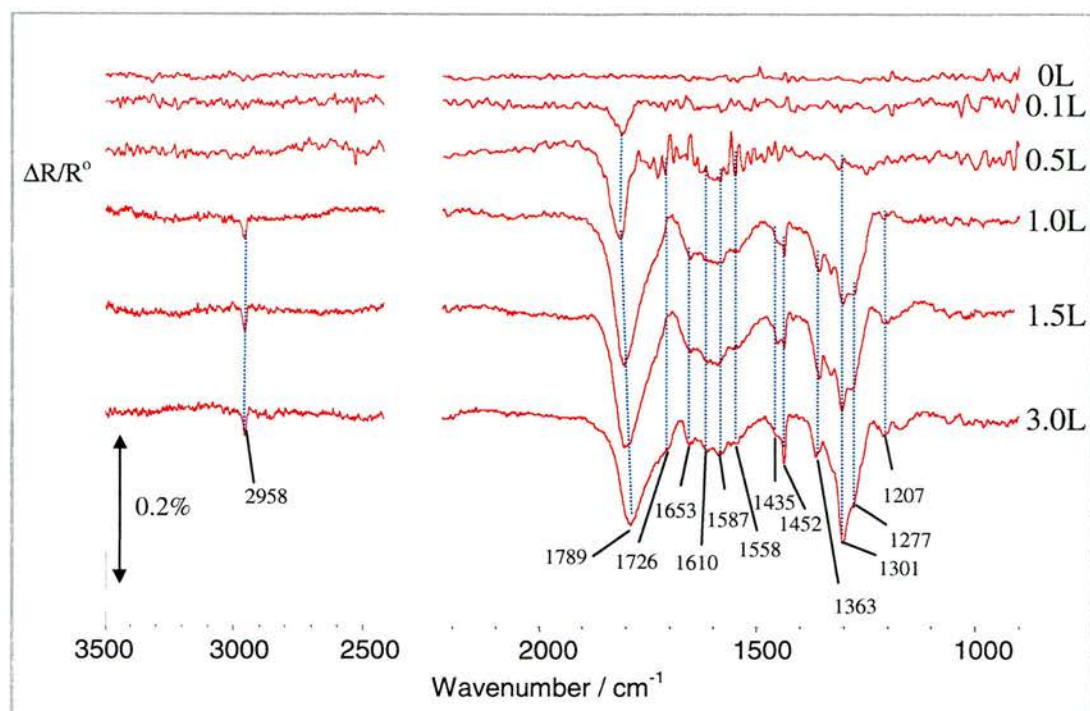


Figure 4.6. RAIR spectrum of the sequential dosing of MAA on Ni{111} at 300 K.

Upon initial adsorption of MAA the RAIRS spectrum is dominated by a single band at about 1800cm^{-1} assigned to the $\nu(\text{CO})$ in 3 fold bridge sites^[18]. Again the presence of a low CO coverage after the initial dose suggests that either CO is adsorbed from the background or MAA is decomposing at low coverage. With increasing dose, IR bands associated with the MAA molecule are observed and these bands increase in intensity until the monolayer is saturated. It appears that the bands do not shift in frequency and no new bands arise as a function of coverage suggesting that a single MAA phase adsorbs at low coverage and this phase dominates to the monolayer coverage with no change in molecular orientation.

The IR bands are very interesting as they give a vital indication into the orientation of the MAA molecules. The strongest bands appear to be those associated with $\text{CO}_{(\text{ads})}$ and

CH out of plane bending modes of the MAA molecule. With the growth of the feature at $\sim 1300\text{cm}^{-1}$ there is a shoulder at the low frequency side of the $\text{CO}_{(\text{ads})}$ band assigned to $\nu(\text{C}=\text{O})$. This feature is much weaker than that observed for MAA on Cu{110} whilst the CH out of plane mode in the nickel work is much more intense. These observations alone suggest that the MAA molecule in the nickel work is orientated close to parallel to the surface at low MAA coverage and with increasing dose the molecule becomes slightly tilted with respect to the surface. This is also confirmed by the presence of weak $\nu(\text{C}-\text{O})^{\text{ester}}$ features, in this work at about 1280cm^{-1} , whilst on Cu, this feature is strong^[1]. The IR spectra also exhibit the bands associated with symmetric and asymmetric bending modes associated with the methyl groups in the frequency range $1450\text{-}1300\text{cm}^{-1}$. Although the molecule is orientated parallel to the surface it appears to be in the enol form illustrated by the bands in the range $1560\text{-}1660\text{cm}^{-1}$ associated with the presence of $\nu(\text{C}=\text{C})$ and $\nu(\text{C}=\text{O})$ combination bands. No IR bands are observed that are associated with multilayer growth suggesting that MAA molecules only adsorb at available metal sites.

4.3.1.2 TPD Studies

Desorption studies of MAA on Ni{111} indicate that there is no molecular desorption of the MAA molecule and therefore any desorption pathway must be via a decomposition mechanism. This observation is in agreement with studies by Zahidi *et al*^[21] in which the molecular desorption of methyl formate, ethyl formate and methyl acetate from Ni{111} only occurred below 300K and that above 300K the desorption products consisted entirely of CO and H₂. In contrast to desorption of R,R-H₂TA, MAA contains no carboxylic acid functional groups or similar groups containing a CO₂ moiety and therefore no desorption features were observed associated with a mass of 44

for CO₂. The only features that were observed are those of mass 28 (CO) and 2 (H₂) for all coverage ranges.

The CO TPD is illustrated in figure 4.7.

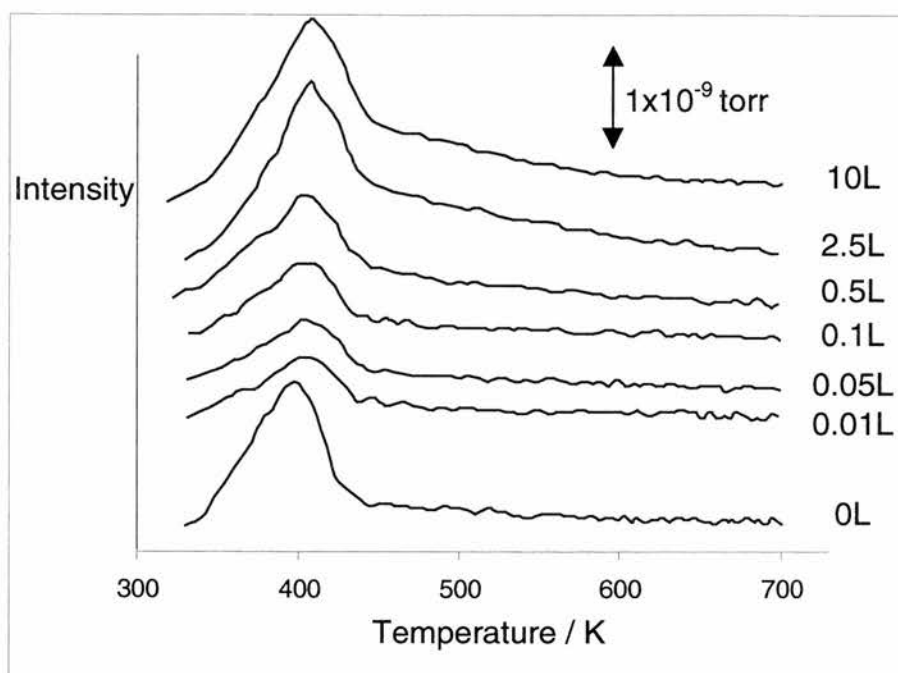


Figure 4.7. CO TPD for increasing coverage of MAA on Ni{111} dosed at 300K.

A single desorption feature is observed for all coverages. Prior to adsorption the TPD spectra is dominated by a feature with a T_{\max} of ~ 400 K associated with CO sitting in 3 fold hollow sites on the Ni{111} surface ^[19]. After adsorption, there is a decrease in the intensity of the CO desorption feature and the T_{\max} of the feature has also shifted to a slightly higher temperature of about 405K. With further dosing the peak at 405K does not shift in temperature but increases in intensity.

The initial decrease in intensity may be indicative of a displacement of CO from the pre-dosed surface upon adsorption of MAA, as observed for tartaric acid in chapter 3. Adsorption of MAA on Ni{111} occurs with a relatively high sticking probability and

the surface appears to have been saturated after a 2.5L dose. Desorption from the surface is initiated at about 350K. This may indicate CO desorption from $\text{CO}_{(\text{ads})}$, possibly as a result of MAA forcing $\text{CO}_{(\text{ads})}$ into atop or bridge sites however, this may also suggest decomposition of MAA revealing that the MAA species are relatively thermally unstable. The single desorption feature observed for the MAA covered surface suggests that there is a single MAA phase present for all coverages and its stability is not temperature dependent. There are no features at higher temperature associated with the recombination of $\text{C}_{(\text{ads})}$ and $\text{O}_{(\text{ads})}$ that was observed for the CO TPD of R,R-H₂TA on Ni{111} suggesting that MAA decomposes and all oxygen atoms are lost in the single CO desorption features. However, the CO desorption spectra in this experiment does show a sloping background on the high temperature side of the desorption peak that may be attributed to this recombination process.

The H₂ desorption plot is illustrated figure 4.8.

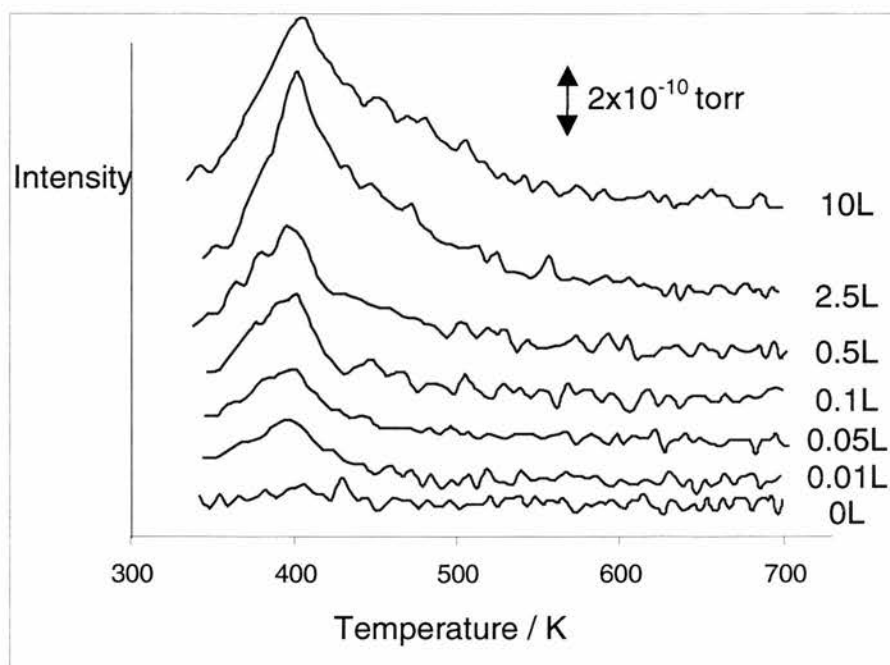


Figure 4.8. H₂ TPD for increasing coverage of MAA on Ni{111} dosed at 300K.

It can be seen in the plot in figure 4.8 that at all MAA coverages, the appearance of H₂ desorption features have a T_{max} very similar to that of CO at about 400K. These features are observed following a low MAA dose and reinforce the observations in the IR data whereby it is evident that MAA has a relatively high sticking probability on a Ni{111} surface. The desorption features increases in intensity until there is no further increase suggesting that the monolayer coverage has been attained after ~2.5L. A broad shoulder is also evident at the high temperature side of the desorption feature and this may indicate the desorption of recombined H_(ads) on the surface as the temperature increases, possibly from H adsorbed at step edge or defect sites.

The TPD data therefore suggests that molecular MAA adsorbs to the surface and decomposes at relatively low temperature to leave the surface covered with CO_(ads) and CH_{x(ads)} as a function of increasing temperature. At a temperature of ~400K, the temperature of maximum desorption for H₂ occurs presumably via a recombination of H_(ad) after decomposition of CH_{x(ads)}. At a temperature of ~405K, CO is observed to decompose from the surface. It would therefore be expect that C_(ads) remains on the surface after the TPD procedure, an assumption that was confirmed by the presence of C along with Ni and no O in the Auger spectrum that was taken after the completion of the TPD.

4.3.1.3 STM Studies

STM has been employed in studying the surface covered by MAA. Unfortunately it was not possible to obtain any images of reasonable quality and no ordered images were

observed, most likely because either MAA is too mobile or MAA molecules have no tendency to order.

4.3.1.4 Summary

MAA adsorbs to the Ni{111} surface mainly in its enol form and at low coverage the plane of the MAA molecule is roughly parallel orientation. As the coverage increases the presence of weak carbonyl and (C-O)^{ester} vibrations suggest that the molecule has slightly tilted with respect to the surface. TPD and IR data confirm the presence of a little adventitious CO adsorbed whilst the sample was cooling to room temperature and upon MAA dose the CO was seen to be displaced from the surface. However, in contrast to the behaviour of R,R-H₂TA and CO on Ni{111} and even though TPD data indicate that some CO is displaced, IR suggest that CO exists on the surface for all MAA coverages. The frequency of the observed IR band assigned to CO suggests that it is the most strongly bound CO sitting in 3-fold hollow sites^[18] and therefore it is quite likely that MAA is unable to displace the small amount of CO that is present. The existence of CO may explain why no ordered structures are observed in the STM and why the IR and TPD data indicate the presence of a single MAA phase possibly resulting from CO disrupting any lateral stabilisation between MAA molecules.

The onset of MAA decomposition occurs at ~350K to yield CO_(ads) and CH_{x(ads)} surface species and results in the desorption of CO and H₂ whilst C_(ads) remains present on the surface.

4.3.2 MAA Adsorption on R,R-H₂TA Modified Ni{111}

In chapter 3 it was shown that STM images of ordered structures were observed for relatively low coverages of R,R-H₂TA on Ni{111}. One of the three observed ordered overlayer structures may be important in terms of possessing possible adsorption sites for MAA as it contains areas of clean nickel within its structures that appear big enough to accommodate the reactant molecule. These areas of clean metal may be important as it has been shown in the study of MAA on R,R-H₂TA modified Cu{110} that MAA only adsorbs where clean Cu{110} sites are available ^[1]. Also catalyst data has shown that when the concentration of R,R-H₂TA in the modification solution gets beyond a limiting value the catalytic activity rapidly decreases until the catalyst becomes completely inactive ^[6-7]. However, catalytic data has also shown that a range of β -keto esters containing bulky substituents on both the ester functionality and acyl side of the molecule can be hydrogenated with R,R-H₂TA modified Ni{111} ^[20]. This indicates that the areas of clean Ni, within the ordered R,R-H₂TA islands may not be involved in the differentiation and hydrogenation processes of the reactant molecule as more bulky molecules would not be able to fit in these areas without a substantial rearrangement of the local R,R-H₂TA structure.

For these reasons it becomes very important to determine how the reactant interacts with the modified surface. Several questions need to be answered. Does the adsorption occur via the areas of clean metal within the ordered structure or at the edge of the ordered islands, as has been suggested for the case of hydrogenation of methyl pyruvate by cinchonidine modified Euro Pt-1 and Pt/SiO₂ catalysts ^{[8][15]}. Therefore adsorption of MAA to various coverages of R,R-H₂TA modified Ni{111} will be studied.

4.3.2.1 RAIRS Studies

4.3.2.1.1 MAA Adsorption on Ni{111} Modified with a Low Coverage of R,R-H₂TA

Adsorption of R,R-H₂TA at room temperature (1×10^{-8} torr of R,R-H₂TA for 60s) gave rise to the RAIR spectrum is illustrated in figure 4.9.

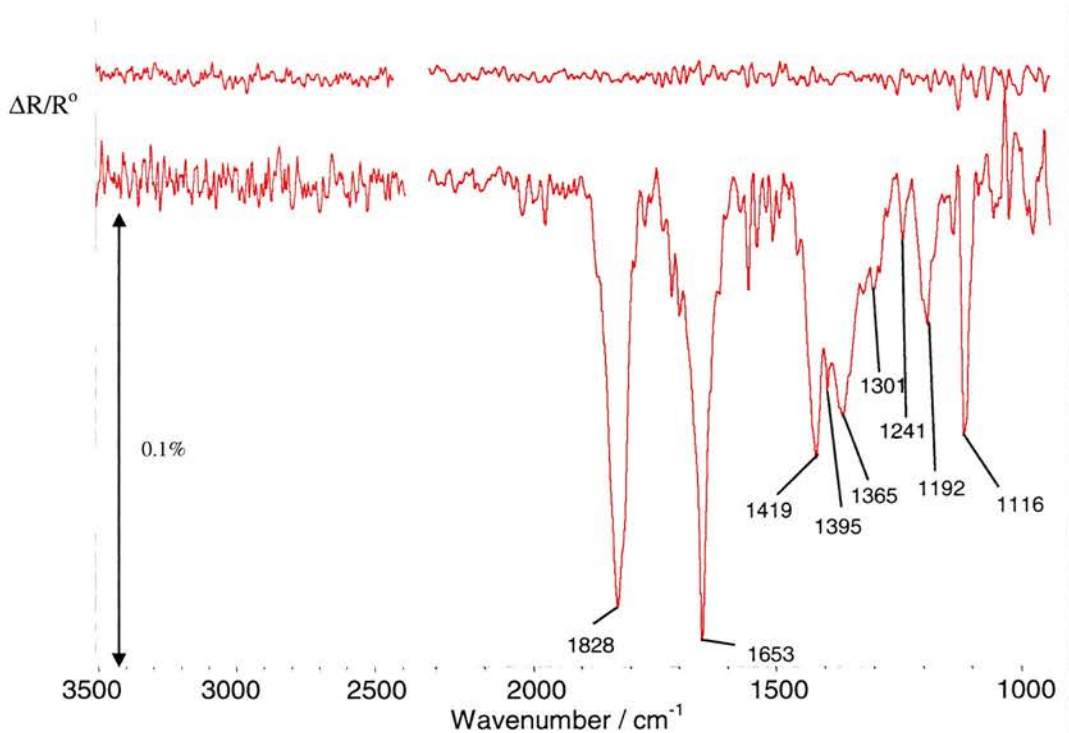


Figure 4.9. RAIR spectrum of a low coverage of R,R-H₂TA on Ni{111} at 300K.

The IR spectrum shows the characteristic features associated with R,R-H₂TA either in the form of a bitartrate where one of the carboxylate groups is monodentate or as a monotartrate species in which neighbouring molecules interact in the form of a cyclic dimer. It is also possible that there is some lateral stabilising with hydrogen bonding interactions between neighbouring molecules.

Adsorption of MAA to this surface resulted in the corresponding RAIR spectrum illustrated in figure 4.10.

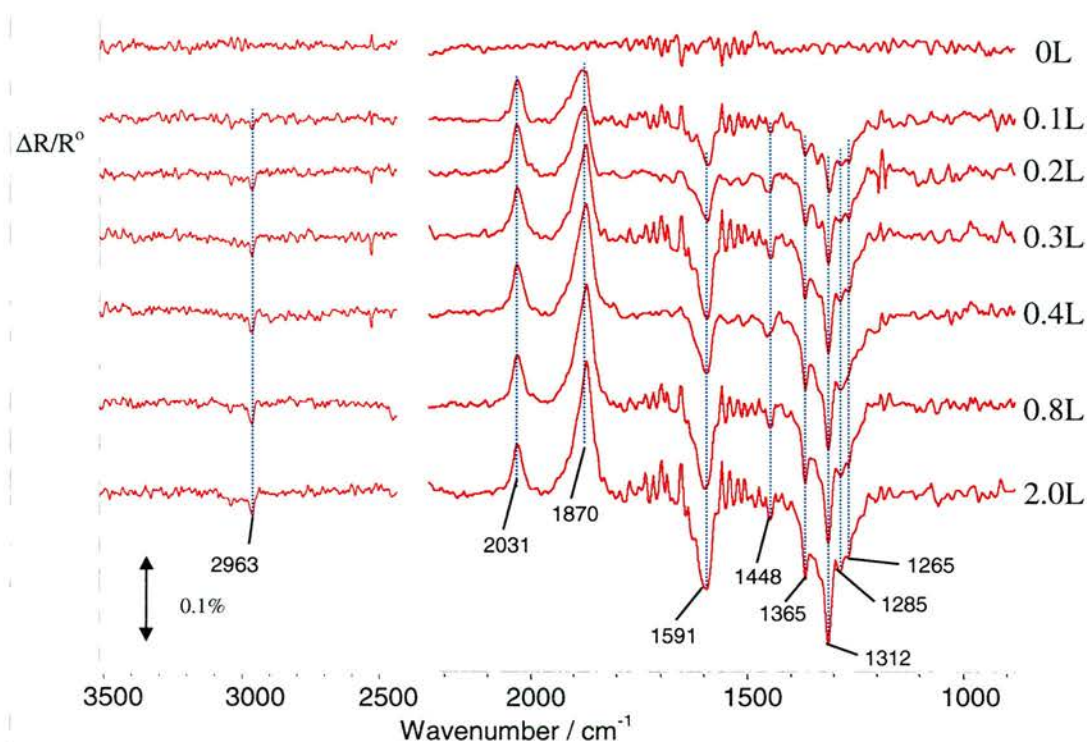


Figure 4.10. RAIR spectrum of MAA dosed onto a low coverage R,R-H₂TA modified Ni{111} at 300K, relative to a R,R-H₂TA/Ni{111} background.

Upon initial dosing of MAA it can be seen that there is the growth of features associated with MAA. At lower MAA coverage the CH out of plane mode at 1312cm⁻¹ is dominant with the symmetric and asymmetric $\nu(\text{CH}_3)$ features at 1365cm⁻¹ and 1448 cm⁻¹ respectively also observed along with weak features at 1285cm⁻¹ and 1265cm⁻¹ associated with $\nu(\text{C-O})^{\text{ester}}$. There is also a relatively strong feature at 1591cm⁻¹ associated with the combination band of $\nu(\text{C=C})^{\text{enol}}$ and $\nu(\text{C=O})^{\text{enol}}$ whilst there are negative features at 1870cm⁻¹ and 2031cm⁻¹ associated with loss of CO from 3 fold bridge and atop nickel sites respectively. This RAIR spectra therefore shows that the adsorption of MAA on R,R-H₂TA modified Ni{111} is very similar to that observed on clean Ni{111}. The exception is the lack of carbonyl features expected at about 1730cm⁻¹. This indicates the MAA molecule is orientated close to parallel to the surface

by applying the surface dipole selection rule. It is also interesting to note that the MAA orientation may be similar to that observed on tartrate modified Cu{110} surfaces in that the ester carbonyl may be interacting with the surface whilst the carbonyl on the keto group is involved in an interaction with tartrate species.

The observation of strong positive bands associated with desorption of CO in 3-fold and atop sites initially appears odd as only CO bands associated the 3-fold bridge sites are observed for the adsorption of R,R-H₂TA and the frequency of the desorption band is ~40cm⁻¹ higher than would be expected. However the explanation for these observations is that between the dosing of R,R-H₂TA and MAA the sample had been analysed in the STM chamber and the time difference between the doses was approximately four and half hours. This therefore leaves sufficient time for additional CO to adsorb from the residual gas background and this would therefore result in extra features being observed in the IR spectrum.

Adsorption of MAA on the modified surface is accompanied by the displacement of CO from the surface and the MAA interacts with the surface solely in the enol form with the plane of the molecule being roughly parallel to the surface. The presence of the enol combination bands also suggests that the molecule is twisted so that the ester carbonyl is tilted with respect to the surface.

4.3.2.1.2 MAA Adsorption on Ni{111} Modified with a High Coverage of R,R-H₂TA

Adsorption of R,R-H₂TA at room temperature (6x10⁻⁸ torr of R,R-H₂TA for 900s) gave rise to the RAIR spectrum is illustrated in figure 4.11 consistent with a high coverage dose of R,R-H₂TA.

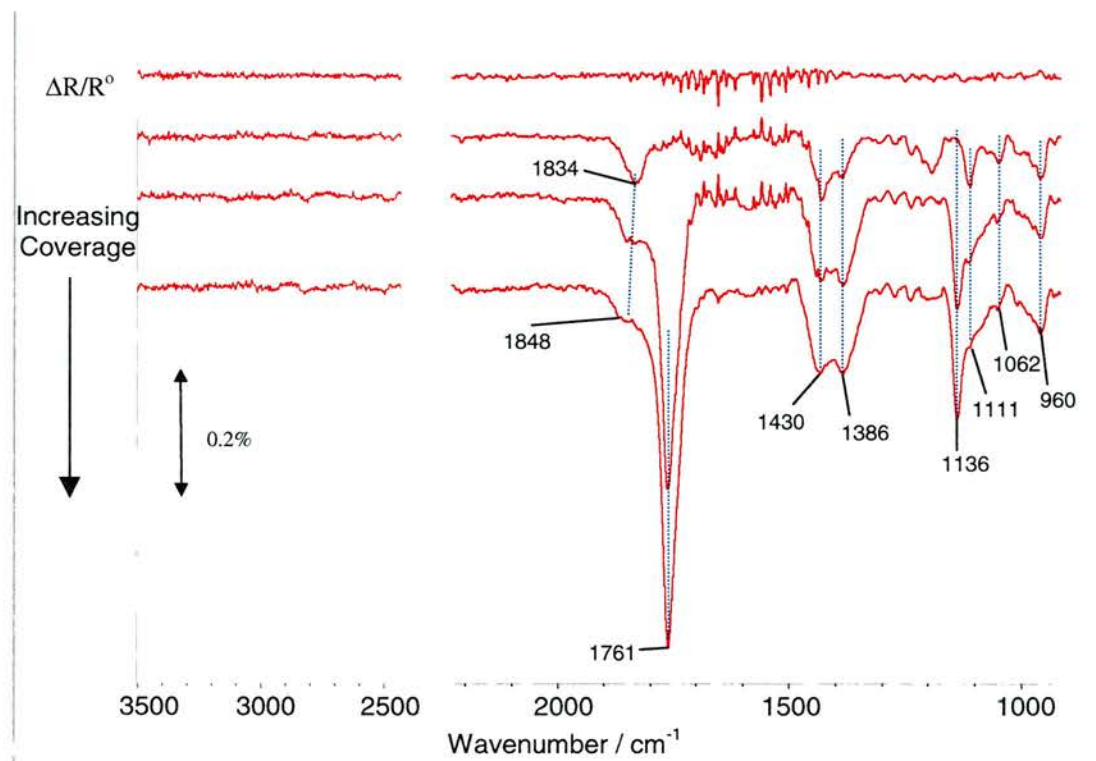


Figure 4.11. RAIR spectrum of a high coverage of R,R-H₂TA on Ni{111} at 300K.

Adsorption of a high coverage of R,R-H₂TA on Ni{111} is again characterised by IR bands associated with tartaric acid molecules in a multilayer coverage. These multilayer features disappear when no more R,R-H₂TA is dose due to desorption of the unstable multilayer.

Adsorption of MAA to this surface is characterised by the RAIR spectra illustrated in figure 4.12.

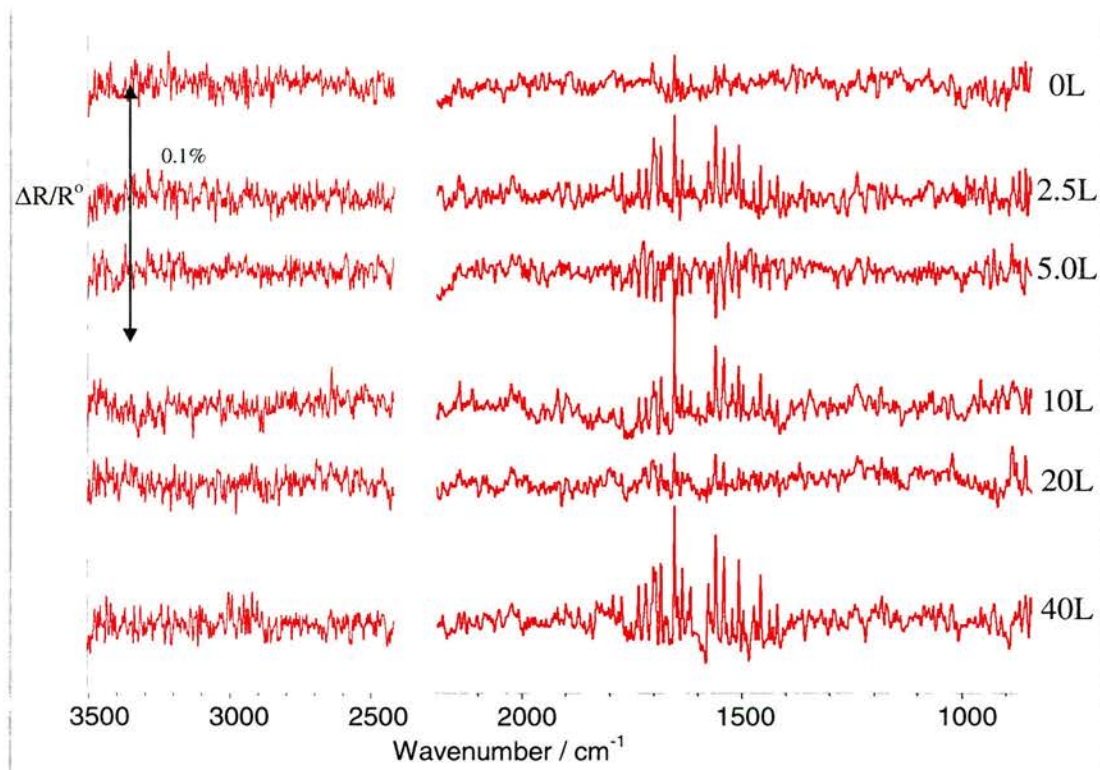


Figure 4.12. RAIR spectrum of MAA dosed onto a high coverage R,R-H₂TA modified Ni{111} at 300K, relative to a R,R-H₂TA/Ni{111} background.

It can be clearly seen that adsorption of MAA on a R,R-H₂TA saturated Ni{111} surface shows no new features in the RAIR spectrum and the only noticeable features are those of water miscancellation from the background spectrum. This result is conclusive evidence that no MAA adsorbs to Ni{111} surface under UHV conditions when no free metal sites are available to the reactant molecule.

4.3.2.2 TPD Studies

All TPD studies for the adsorption of MAA onto R,R-H₂TA modified Ni{111} were carried out by initially subjecting the Ni{111} surface to a specified dose of R,R-H₂TA. After each specific R,R-H₂TA dose, a 5L dose of MAA (5×10^{-8} torr for 100s) was introduced into the UHV chamber. Dosing of MAA onto the modified Ni{111} was

conducted once the chamber pressure had recovered to at least 3×10^{-9} torr, generally in the time scale of seconds to several minutes depending on the dosing time of R,R-H₂TA.

The CO TPD spectra for an increasing dose of R,R-H₂TA and then a 5L dose of MAA at 300K is illustrated in figure 4.13.

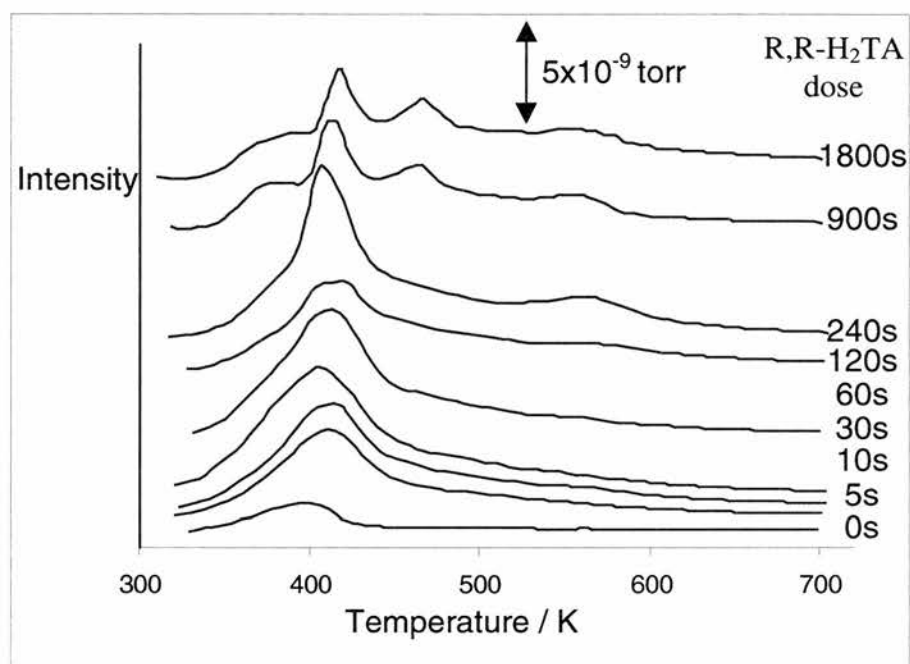


Figure 4.13. CO TPD for a 5L dose of MAA on an increasing dose of R,R-H₂TA modified Ni{111} surface at 300K.

The CO TPD for just a 5L MAA dose is consistent with that observed previously in this chapter for MAA on Ni{111} and has a T_{\max} of ~ 405 K. When R,R-H₂TA and MAA coexist on the surface it is apparent that there is a single desorption feature with a T_{\max} ~ 410 K and this feature is present at all coverages with increasing intensity up to a dose of 240s. After a 900s dose the intensity of this feature decreases slightly and is accompanied by an increase in T_{\max} to ~ 420 K. The change in this feature also occurs with the presence of extra features with T_{\max} of ~ 380 K, ~ 460 K and ~ 560 K. The CO

TPD spectra after a 900s dose is very similar to the higher coverage CO TPD spectra observed for R,R-H₂TA dosing at 300K and therefore indicates that at a saturation coverage of R,R-H₂TA the sticking probability of MAA is very small.

The presence of MAA on the modified surface results in CO TPD spectra that are strikingly different to that of just R,R-H₂TA on Ni{111}. The difference in the spectra at sub-monolayer R,R-H₂TA coverages is good evidence to suggest that when MAA is present on the surface there is some sort of interaction between the two different species. The similarity between the TPD spectra at higher R,R-H₂TA coverage also confirm this interaction.

The CO₂ desorption spectra are illustrated in figure 4.14.

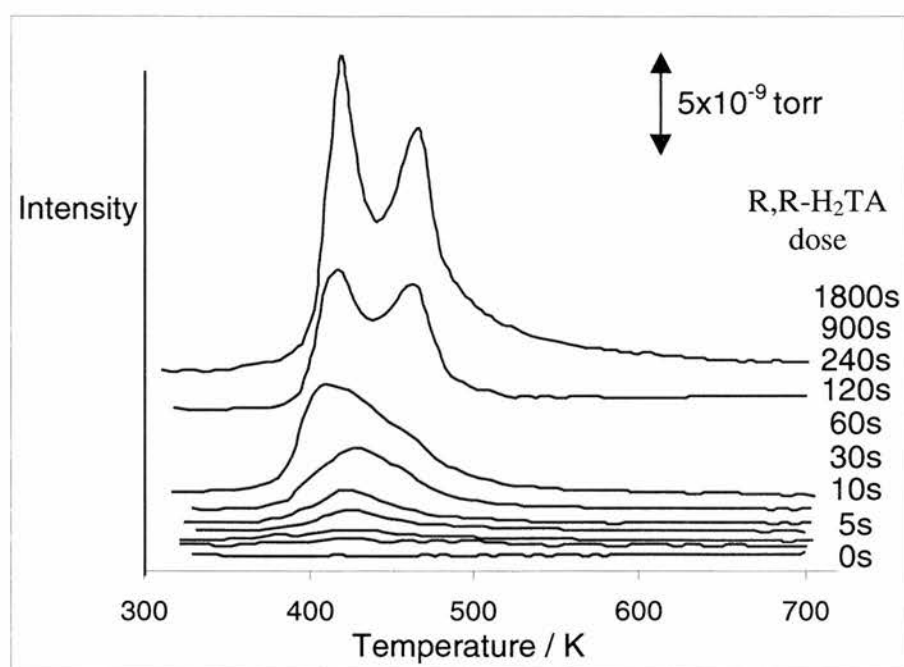


Figure 4.14. CO₂ TPD for a 5L dose of MAA on an increasing dose of R,R-H₂TA modified Ni{111} surface at 300K.

The CO₂ TPD is characterised by the growth of a single broad desorption feature with a T_{max} of 420K. After a 60s dose of R,R-H₂TA and 5L dose of MAA the T_{max} increases to ~430K then decreases to ~410K and a growth of a shoulder at ~460K. After a dose of 900s two features of approximately equal intensity are observed with T_{max} ~420K and 460K. The change in shape of the desorption spectra coincides with that in the CO TPD spectra and the shape is consistent with the desorption of an R,R-H₂TA overlayer with the exception of the intensity of the 460K feature. There are two possible reasons to explain this difference, either MAA has induced some sort of reorganisation of the tartrate species or the growth of the R,R-H₂TA phase associated with the peak at 460K is time dependent and increases with increasing time. After a high dose of R,R-H₂TA the chamber pressure takes more time to ‘recover’ and subsequently the 460K phases has more time to grow before dosing the MAA and it is this extra time that may account for the increase in intensity. As no MAA is observed to stick at R,R-H₂TA saturation coverage, the most reasonable explanation is that the nature of the R,R-H₂TA overlayer species is time dependent, a effect has also be reported in the study of R,R-H₂TA on Cu{110} ^{[1][10-11]}.

This effect was confirmed by completing a TPD experiment in which the surface was left for 30 minutes after a 300s R,R-H₂TA dose. The TPD spectrum is illustrated in figure 4.15.

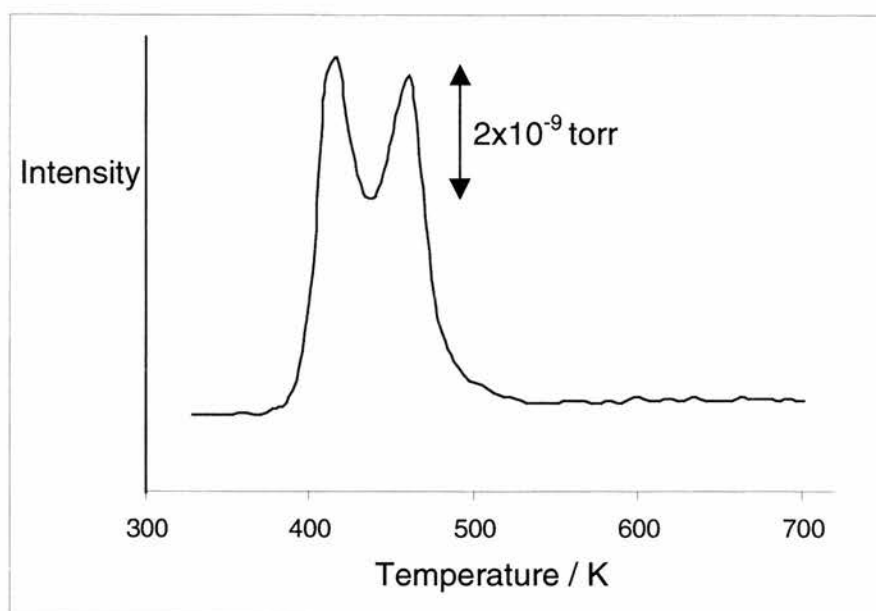


Figure 4.15. CO₂ TPD for a 300s R,R-H₂TA dose on Ni{111} at 300K.

It is clear to see that the desorption features at ~410 and 460K are of roughly equal in intensity. This therefore backs up the suggestion that the growth of the 460K tartrate species is time dependent.

The CO₂ desorption spectra indicates that co-adsorption of MAA and R,R-H₂TA result in a surface that is different from that of R,R-H₂TA covered Ni{111} at sub-monolayer coverages indicating that MAA interacts with the tartrate species. After a 900s R,R-H₂TA dose, the TPD spectra correspond to that of the surface dosed with R,R-H₂TA indicating that at higher R,R-H₂TA coverage no MAA adsorbs to the surface.

The H₂ TPD spectrum is illustrated in figure 4.16.

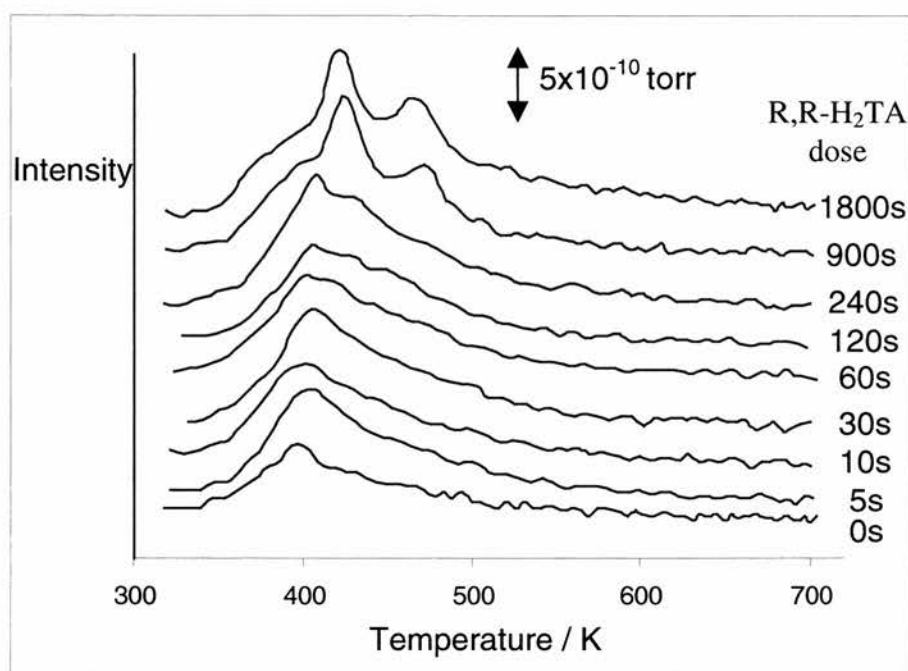


Figure 4.16. H₂ TPD for a 5L dose of MAA on an increasing dose of R,R-H₂TA modified Ni{111} surface at 300K.

The TPD plot shows the presence of a broad feature with a T_{\max} of about 400K that increases slightly in intensity with increasing coverage. After a dose of 900s the shape of the desorption features change and become much more reminiscent of the high coverage H₂ TPD of R,R-H₂TA on Ni{111}. Upon the formation of the ‘new’ desorption features, the dominant peak has increased in temperature and possesses a T_{\max} of about 420K. Additional peaks are observed at 460K and at the lower temperature side of the main peak. The main difference between the higher R,R-H₂TA coverage on Ni{111} and the co-adsorption doses is the intensity of the 460K feature, that can be rationalised by the time dependency observed for the formation of the higher temperature tartrate species. Again the TPD spectra indicate that after a dose of 900s, MAA no longer adsorbs and the resulting spectra are more similar to those observed for R,R-H₂TA on Ni{111} alone.

The H₂O TPD spectra, illustrated in figure 4.17 also indicates the presence of a single desorption spectra with a T_{\max} of $\sim 400\text{K}$ for a dosing up to 240s.

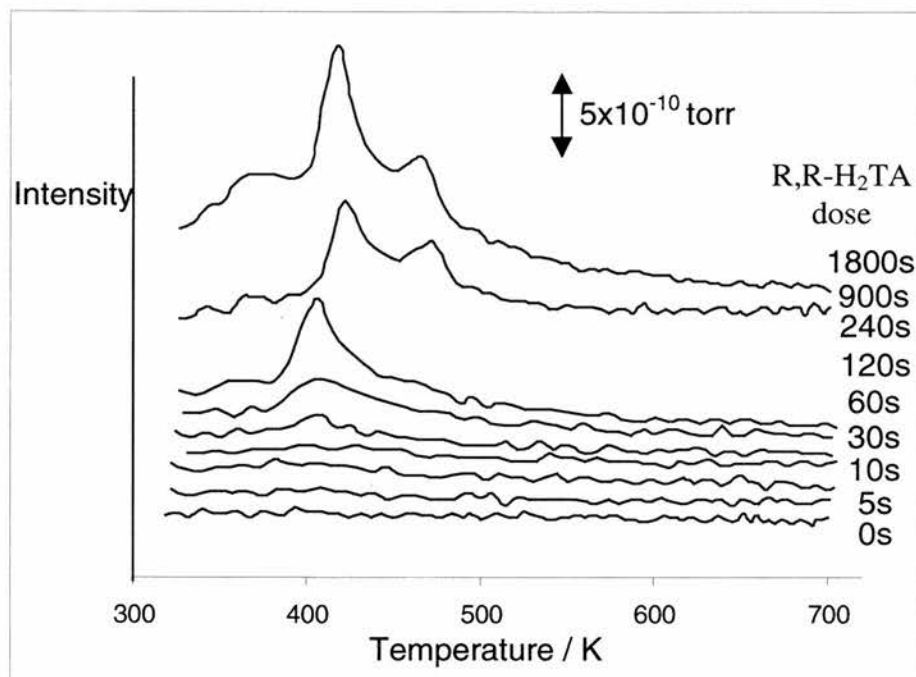


Figure 4.17. H₂O TPD for a 5L dose of MAA on an increasing dose of R,R-H₂TA modified Ni{111} surface at 300K.

The H₂O TPD indicate the formation of a majority species that desorbs with $T_{\max} \sim 410\text{K}$. The sloping behaviour around 460K also suggests the formation of a minor species that is also more stable. After 900s, there is a change in shape of the desorption spectra consistent with the desorption of R,R-H₂TA and indicating that no MAA is adsorbed to the surface.

4.3.2.3 STM Studies of Ordered Phases

STM studies on the modified surface dosed with MAA indicated the presence of two similar ordered phases, neither of which have been observed for dosing R,R-H₂TA or MAA alone on Ni{111}. Due to this fact and that both RAIRS and TPD indicate that there is some interaction between the R,R-H₂TA and MAA molecules leads to the

possibility that these ordered phases consist of co-adsorbed species. The first image was observed after dosing R,R-H₂TA and then exposing to $\sim 1 \times 10^{-9}$ torr background of MAA and is illustrated in figure 4.18. The RAIRS spectra giving rise to these images is illustrated in figures 4.9 and 4.10.

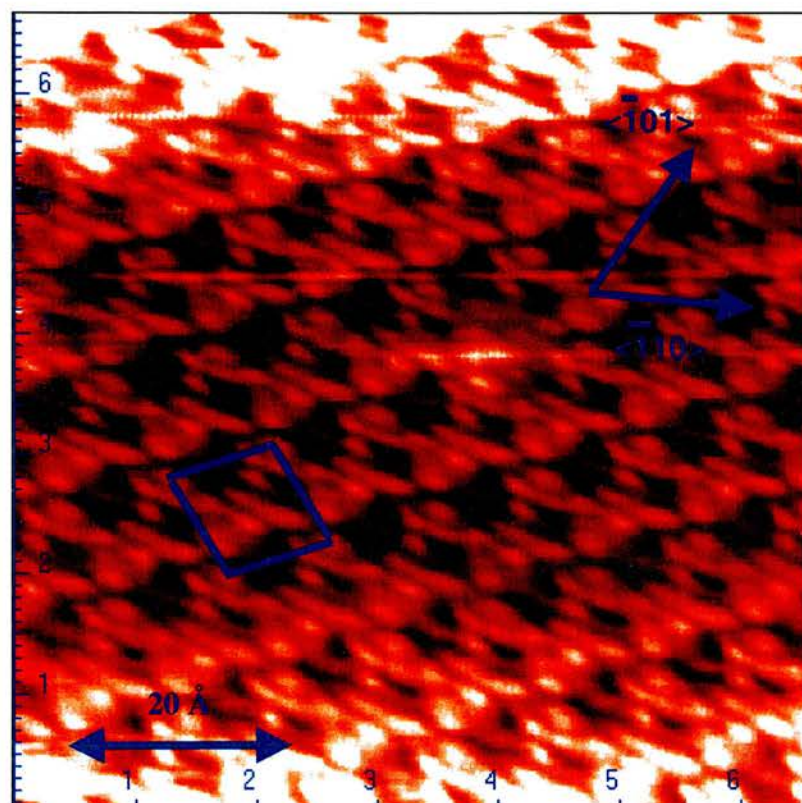


Figure 4.18. High resolution STM image showing an ordered overlayer structure obtained after co-dosing R,R-H₂TA and MAA on Ni{111} at 300K, $V_{tip} = -1.0V$; $I_{tip} = 0.985nA$.

The image in figure 4.18 shows a very high resolution structure. This is initially present on the surface in a relatively small area, covering $\sim 40\%$ of the terrace. With increasing scan time, this structure appeared to grow on the terraces until the majority of the terrace was seen to be covered by this ordered adlayer, although large areas of the surface remain disordered. On closer analysis of this image it is apparent that the image contains structure that is visually similar to that of MAA molecules. This is easily illustrated in a close up view of the image.

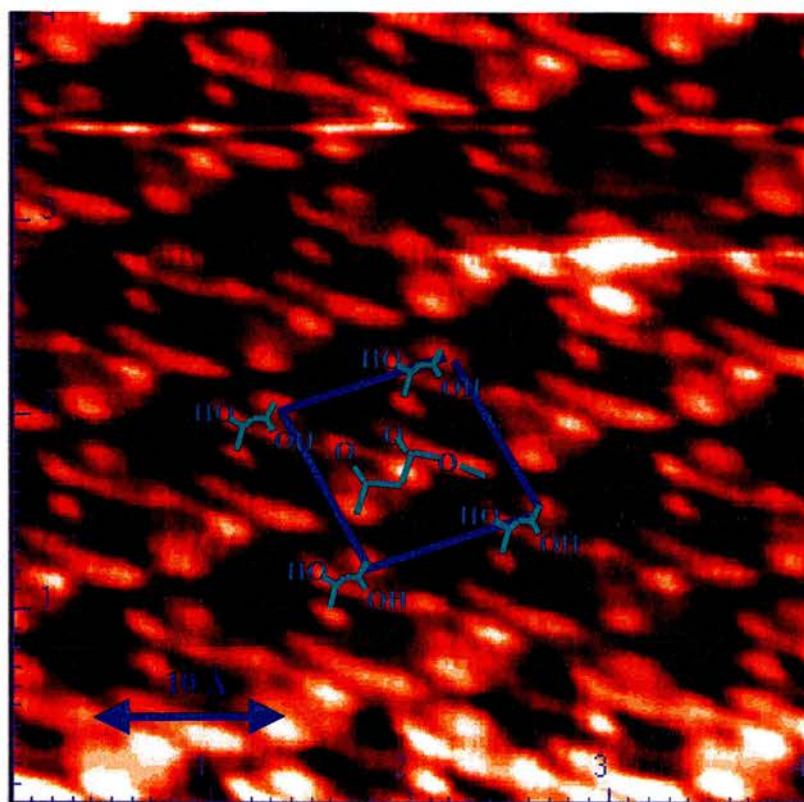


Figure 4.19. A close-up view of the STM image illustrated in figure 4.18.

It is the feature in the centre of the unit cell that looks remarkably similar to an MAA molecule that has a flat lying orientation whilst the measured length of this is $\sim 7\text{\AA}$, similar to that of an MAA molecule and too long to be a surface bound tartrate species. The methoxy groups of the MAA molecules are in the trans conformation, in contrast to that of the stable gas phase configuration of a similar molecule, methyl acetate in which the cis form is dominant ^[21]. Zahidi *et al* ^[21] have reported that this surface induced rotational isomerisation occurs at low acetate coverages for the adsorption of methyl acetate on Ni{111} and have attributed this observation to steric repulsion as the packing density of the adsorbed ester increases beyond a critical level ^[21]. It has also been proposed that these low coverages are expected to be easily achieved under typical conditions for heterogeneous catalysis and therefore may be significant in developing

mechanistic schemes to describe these reaction. However, it should also be pointed out that their studies have also shown that the adsorption of methyl acetate on Ni{111} is roughly perpendicular to the surface, in contrast to our studies of MAA ^[21].

The corners of the unit cell consist of bitartrate molecules and there appears to be hydrogen bonding interaction between one of the α -hydroxy groups of the R,R-H₂TA and the β -keto carbonyl of the MAA molecule. This model is consistent with the observed RAIR spectra of MAA with the molecules being orientated parallel to the surface. The dimension of the unit cell in figures 4.18 and 4.19 has been measured as 9.3 Å (3.7 Ni-Ni spacings) and 8.9 Å (3.6 Ni-Ni spacings) and has internal angles of 101° and 79°. A possible model for the observed STM overlayer structure is illustrated in figure 4.20.

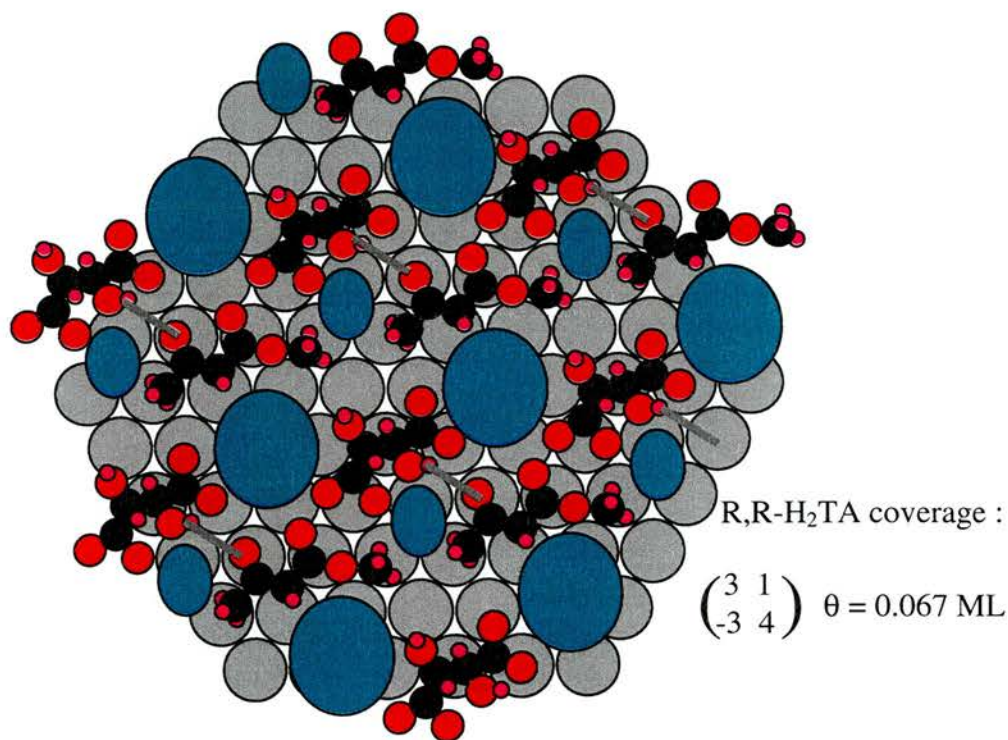


Figure 4.20. Possible model for the observed STM image of co-existing R,R-H₂TA and MAA molecules.

The dimensions of the unit cell in the model are 9.0Å (3.6 Ni-Ni spacings) and 9.0Å (3.6 Ni-Ni spacings) and with internal angles of 93° and 87°, very similar to that observed for the STM image. Therefore, the unit cell consist of one MAA and one bidentate bitartrate molecule giving a local coverage of 0.133ML and a local R,R-H₂TA coverage of 0.067ML. The lowest tartrate coverage observed for the adsorption of R,R-H₂TA on Ni{111} was 0.182ML. This suggests that the formation of these co-adsorbed structures is most likely achieved by displacement of CO from disordered regions of the surface consisting of co-adsorbed R,R-H₂TA and CO.

The STM image also indicate that all the MAA molecules have the same orientation indicating that the structure is able to differentiate the enantioface of the MAA molecule. It is also interesting to note that hydrogenation of these species by attack by H_(ads) would yield R-MHB as the product and therefore is direct evidence for the observation of enantioselective sites formed upon modification of the Ni{111} surface by R,R-H₂TA. The most plausible reason for enantioface differentiation in this structure is due to the hydrogen bonding interactions being much more likely to occur between the α-hydroxy groups of R,R-H₂TA and the ketone functional group than the ester carbonyl group of the MAA molecule.

As the coverage of MAA increases a second ordered adlayer is observed and again this structure is only when both MAA and R,R-H₂TA are co-adsorbed on the Ni{111} surface. The ordered structure consists of groups of three features however this structure has only been observed on small areas of the surface, unlike that of the structure in figure 4.18. The STM image is illustrated in figure 4.21 and the dose corresponds to the RAIR spectra displayed in figures 4.9 and 4.10.

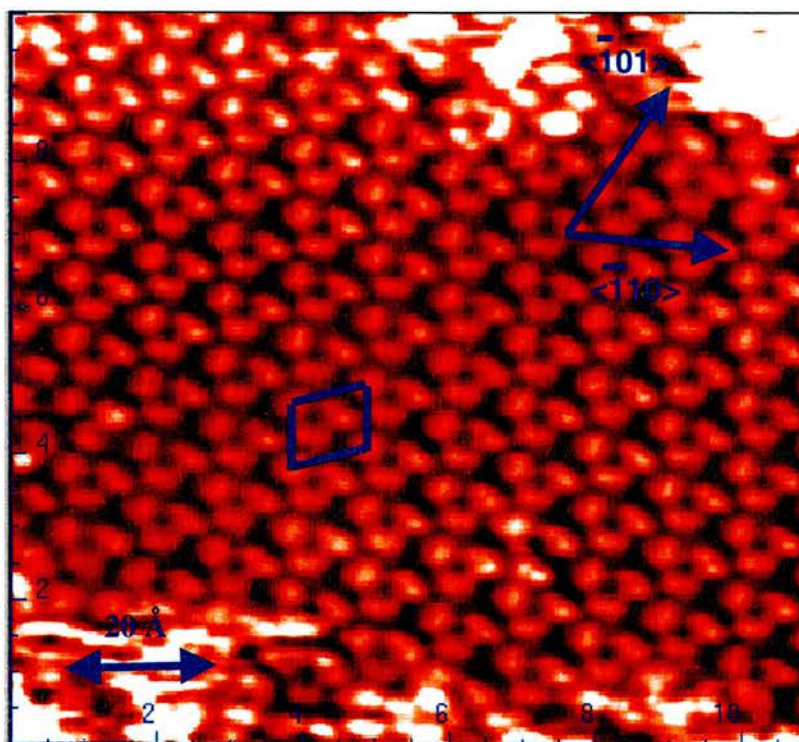


Figure 4.21. STM image of ordered molecules obtained after co-dosing of R,R-H₂TA and MAA at 300K, $V_{\text{tip}} = -1.0\text{V}$; $I_{\text{tip}} = 0.985\text{nA}$.

This image shows three features that congregate into a triangular structure and has unit cell dimensions measured from the STM image as 11.1 \AA (4.5 Ni-Ni spacings) and 8.9 \AA (3.6 Ni-Ni spacings) with internal angles measured as 109° and 71° . This unit cell is larger than that observed in the image containing sub-molecular resolution and the size of the three features appear to be similar to one another. A possible model for this ordered overlayer is illustrated in figure 4.22.

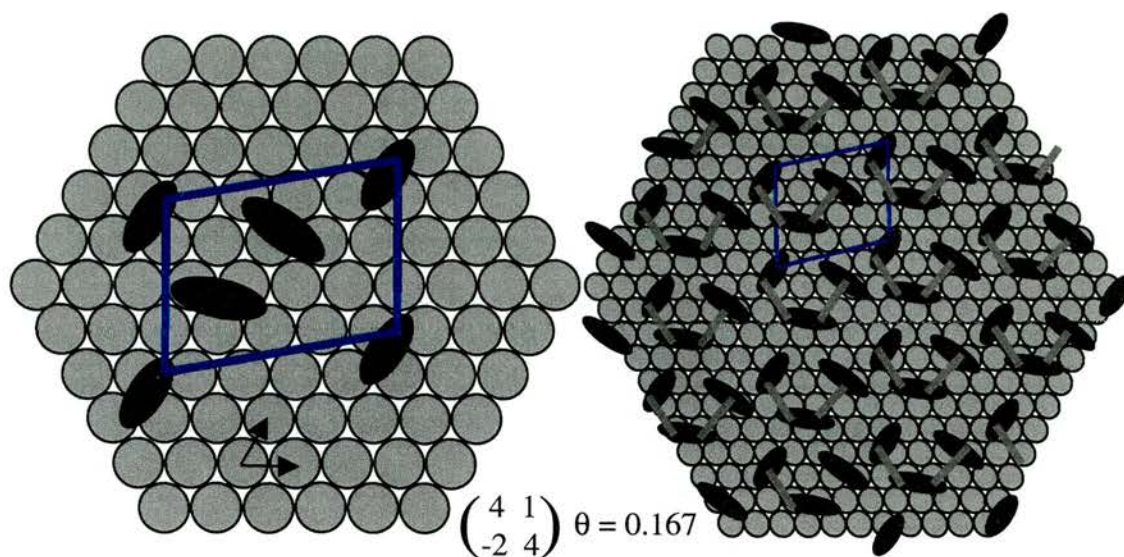


Figure 4.22. Possible model for the unit cell and overlayer structure observed in the STM image illustrated in figure 4.21.

The dimensions of the unit cell in the model have been calculated as 11.4\AA (4.6 Ni-Ni spacings) and 8.7\AA (3.5 Ni-Ni spacings) with internal angles of 102° and 78° . Taking into account for drift in the vertical direction this model appears reasonably consistent with the unit cell in the STM image in figure 4.21.

The three different orientations of individual features in the observed STM image appear to be roughly aligned along the three different close packed directions. It would be highly unlikely that these features consist purely of MAA molecules, as no order structures were observed when dosing MAA on Ni{111}. Also, it would be very doubtful if this structure consists solely of tartrate species because this ordered structure was also not observed for the adsorption of R,R-H₂TA on Ni{111}. Therefore the mostly likely explanation is that it contains MAA molecules, unfortunately without the benefit of an image having a resolution as high as that observed in figure 4.18, interpretation of this image is much less straightforward. We believe this structure

originates from adsorption of a second MAA molecules to the 0.133ML structure observed in figure 4.18 resulting in a local rearrangement of the structure already present. This suggests the formation of a local coverage of 0.167ML and a local tartrate coverage of 0.056ML. A model for this structure is illustrated in figure 4.23.

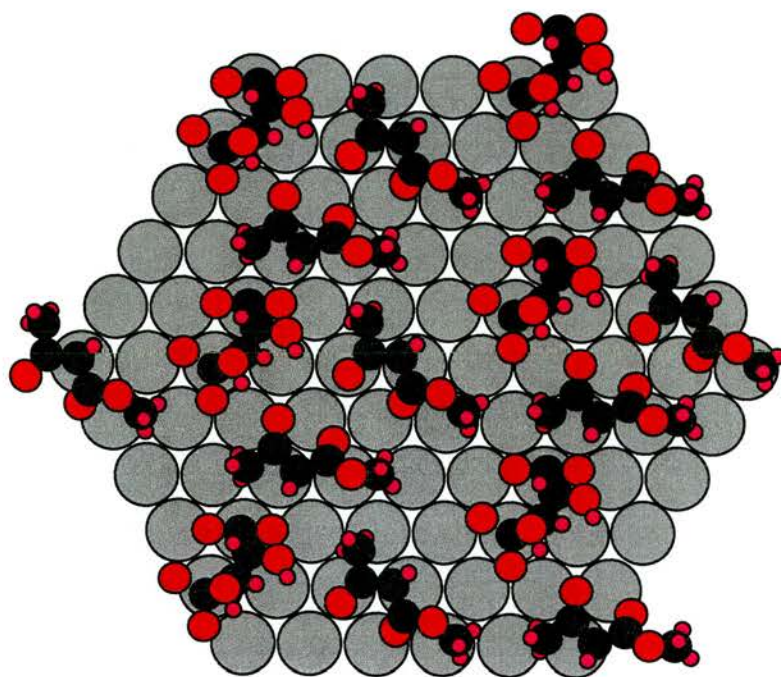


Figure 4.23. Possible model for the observed STM image in figure 4.21.

In this model, the α -hydroxy groups of the bidentate bitartrate molecule interact with the enol O-H bonds on the MAA molecule, RAIRS data confirms that at such MAA exposures, the MAA species are predominately in the enol form. The two MAA molecules would be mirror images of one another where hydrogenation of the left hand MAA molecule results in the R-form of MHB whilst hydrogenation of the right hand species would result in the production of the S-form. It would therefore appear that this site would not account for enantioselective behaviour.

4.4 Summary

The adsorption of MAA Ni{111} at 300K proceeds with a high sticking probability and the growth is characterised by a single MAA adsorption species where the MAA molecules orientate close to flat lying with respect to the surface. No ordered structures were observed at all coverages using the STM and MAA is relatively unstable on the surface, starting to decompose at about 350K. No molecular desorption is observed and the decomposition pathway yields $\text{CO}_{(g)}$, $\text{H}_{2(g)}$ and $\text{C}_{(ads)}$.

Adsorption of MAA onto a Ni{111} at 300K, precovered with a high coverage of R,R-H₂TA is observed to have a very low sticking probability that is probably very close to zero. In contrast adsorption of MAA to a lower, sub-monolayer R,R-H₂TA covered Ni{111} does proceed and the molecular orientation is characterised by a flat lying MAA species. Adsorption to the R,R-H₂TA precovered surface does not appear to occur at areas of clean surface within ordered R,R-H₂TA structure but at areas of disordered R,R-H₂TA species either at bare metal sites or by displacement of adventitious CO.

Two similar ordered structures are observed for the co-adsorption of MAA and R,R-H₂TA on Ni{111}. The first is a high, sub-molecular resolution image corresponding to a lower MAA coverage with four bidentate bitartrate species sitting at the corners of the unit cell and one MAA molecule fitting in the centre with a (31 –34) unit cell. All MAA species are present in the same orientation within this structure suggesting that hydrogenation of the MAA molecules would yield R-MHB as the dominant product. Therefore, if this structure were present on Ni nanoparticles under reaction conditions, hydrogenation of MAA would result in 100% enantioselective formation of R-MHB.

The second ordered structure is observed on a much smaller region of the surface and consists of a higher local MAA coverage. The structure consists of a (41 $\bar{2}$ 4) unit cell in which an extra MAA molecule has been inserted into the (31 $\bar{3}$ 4) structure containing two MAA molecules and one R,R-H₂TA molecule. The proposed model consists of MAA molecules adsorbed to the surface on opposite faces and hydrogenation of the MAA molecules would yield a racemic product mixture of R- and S-MHB.

This model does appear to explain certain key features of the enantioselective reaction. At high MAA coverages, the ordered structure that we observe show two MAA molecules interacting with one tartrate species such that the two MAA molecules are mirror equivalent geometries. This geometry appears to minimise the intermolecular interaction between neighbouring MAA molecules whilst allowing interactions between the tartrate species and MAA molecules. If such structures were to exist on the surface of Ni nanoparticles under reaction conditions the surface concentration of MAA would become decisive in determining enantioselectivity. If the rate of hydrogenation is fast enough to result in a relatively short surface lifetime for the molecule then one may stay in the low coverage (enantioselective) regime. Conversely, if the surface lifetime of MAA is relatively long then the catalyst would tend towards producing a racemic mixture of products.

4.5 References

- [1] MO Lorenzo; PhD thesis. University of Liverpool. 1999. Chapter 5 and 6, 163-211
- [2] JA Groenewegen and WMH Sachtler; *J. Catal* **38** (1975) 501
- [3] MA Keane; *Langmuir* **13** (1997) 41
- [4] MA Keane and G Webb; *J. Catal.* **136** (1992) 1
- [5] MA Keane; *Langmuir*. **10** (1994) 4560
- [6] Y Izumi; *Adv. Cat.* **32** (1983) 215
- [7] A Tai and T Harada; *Tailored Metal Catalysts*, Y Isawawa (ed.), D Reidel Publishing Company, 1986. 265
- [8] G Webb and PB Wells; *Cat. Today* **12** (1992) 319
- [9] A Tai, T Harada, Y Hiraki and S Murakami; *Bull. Chem. Soc. Japan* **56** (1983) 1414
- [10] MO Lorenzo, S Haq, T Bertrams, P Murray, R Raval and CJ Baddeley; *J. Phys. Chem. B* **103** (1999) 10661
- [11] MO Lorenzo, CJ Baddeley, C Muryn and R Raval; *Nature*. **404** (2000) 376
- [12] Y Nuriko, F Sekine, T Imanaka and S Teranishi; *Bull. Chem. Soc. Jpn.* **54**, 4 (1981) 980
- [13] CR Henry, C Chapon, S Giorgio and C Goyhenex; *Chemisorption and Reactivity on Supported Clusters and Thin Films*. RM Lambert and G Pacchioni (eds.), Kluwer Academic Publishers, 1997. 117
- [14] A Hoek and WMH Sachtler; *J.Catal.* **58** (1979) 276
- [15] T Burgi and A Biaker; *J. Catal.* **192**, 2 (2000) 445
- [16] KE Simons, PA Meheux, SP Griffiths, IM Sunderland, P Johnston, PB Wells, AF Carley, MK Rajumon, MW Roberts and A Ibbotson; *Recl. Trav. Chim. Pays-Bas.* **113** (1994) 465

- [17] DH Williams and I Fleming; *Spectroscopic Methods in Organic Chemistry*. Third Edition. McGraw-Hill Book Company (UK) Ltd. Chapter 2, 35-73.
- [18] FT Netzer and TE Madey; *J. Chem. Phys.* **75** (1982) 710
- [19] G Held, J Schuler, W Sklarek and HP Steinrück; *Surf. Sci.* **398** (1998) 154
- [20] A Tai and T Sugimura; *Chiral Catalyst Immobilisation and Recycling*. DE de Vos, IFJ Vanelecom and PA Jacobs (Eds), Wiley – VCH (2000) Chapter 8, 173
- [21] E Zahidi, M Castonguay and PH McBreen; *J. Phys. Chem.* **99** (1995) 17906

Chapter Five

Hydrogenation of Methyl Acetoacetate on (R,R)-Tartaric Acid Modified Ni{111}.

5.1 Introduction

Heterogeneous catalysis forms the basis of most chemical and petrochemical technologies and its importance to life sciences and environmental protection is immense ^[1]. In the 1960's before the development and application of surface science, heterogeneous catalysis was considered a 'black box' in which a mixture of reacting molecules was mysteriously converted to desirable products ^[1]. The development of UHV based surface science techniques has allowed the detailed study of structural, compositional and electronic properties at the atomic scale ^[2].

To understand heterogeneous catalysis at the atomic and molecular level is clearly very complex due to the range of parameters that control the catalyst performance such as the choice of active metal, the size and shape of the metal particles and the type of support ^[1-6]. Many of these components are determined during the catalyst preparation whilst the conditions of the catalytic reaction also play an important role. Processes that occur on the catalyst do so through a sequence of, usually poorly understood, elementary steps. The control of any one of these steps and subsequently the overall performance of the catalyst may be altered under different conditions of gas phase composition, temperature and pressure ^[3]. To fully understand how each parameter individually affects the catalytic process would take a huge length of time and is not realistically

feasible. This therefore leaves two possibilities, the first is to adopt a trial and error approach and this has worked to achieve good economical catalysts. However, there is no guarantee that the best catalyst has been realised and there still may be little or no understanding of the processes that occur on the catalyst particles. The second possibility is to dissect the catalytic events into individual components in order to obtain a fundamental understanding of these processes that occur at the liquid-solid or gas-solid interface to contribute to the advancement of heterogeneous catalysis ^[3]. The combined use of modern surface science techniques has great potential in this area.

A fundamental study requires highly idealised conditions that are hugely different to those of the real catalytic reactors. The ‘pressure gap’ means that the effect of molecular adsorption and reactivity in the presence of gas or liquid phase is ignored in UHV studies. The ‘structure gap’ means that single crystal surfaces are inadequate to model the behaviour of small metal particles, which have a high proportion of atoms at edge sites ^{[1][3-4]}. These are two of the biggest criticisms directed towards the use of surface science to investigate the interactions and processes that occur on catalyst particles as the study of single crystal surfaces under UHV conditions is too far removed from that of the real catalytic reactions ^[4].

There are several different approaches to addressing this problem. One procedure to model the structure of real catalysts more closely is to evaporate metal particles, such as Cu or Pd onto thin oxide films such as silica ^[1]. These silica films can be supported on metal substrates, such as Mo{110} and offer an interesting starting material for constructing more realistic supported-metal-particle catalysts ^[4]. Such an example is illustrated in figure 5.1.

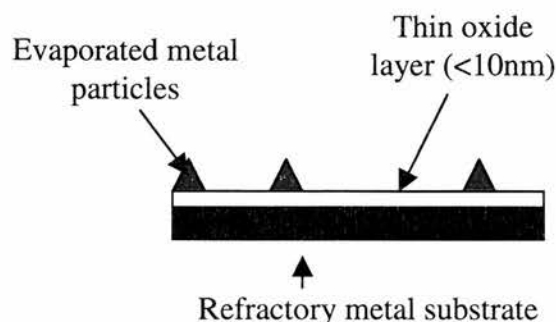


Figure 5.1. Illustration of a supported metal-particle catalysts.

This approach has been studied on several different oxide thin films, ranging in thickness from 5-100Å and has indicated that these types of model oxides exhibit bulk oxide properties but are not too thick to create insulating behaviour ^[2]. This therefore alleviates charging and referencing problems normally associated with the application of electronic spectroscopies of insulating material ^[2]. Metal-oxide interfaces can often exhibit very high activities compared to the metal alone, a phenomenon called ‘strong metal support interaction’ ^[1]. The difference in reaction rates can be in the range of orders of magnitude between the oxide and non-oxide supported systems, even though the oxide supports are often inert in the reaction ^{[1][3]}. Due to the flat and conductive nature of these thin films these model catalysts can be studied using surface science techniques such STM, AFM, XPS, AES and TPD to gain information on the particle sizes, composition and the electronic properties of the metal nanoparticles ^[2], to mention a few. Vapour deposition of metal particles onto the oxide supports serve as a useful intermediate between single crystals and high surface area supported catalysts providing information on their physical, chemical and catalytic properties as well as their function as supports for metal particles ^[2].

A second approach is to prepare model surfaces on well defined single crystal surfaces in UHV conditions, transferring the prepared sample into a reaction cell where a catalytic reaction can be performed. This type of experiment has been successfully studied previously by Somorjai and co workers^[7-9]. An experiment of this kind requires a vacuum chamber with the capability for sample transfer into a reaction cell and to ensure the vacuum chamber remains at UHV conditions whilst a reaction was running a reliable method of sealing the vacuum chamber from the cell is required. This type of approach subsequently allows direct comparison of the information gain in UHV with its activity and selectivity under real catalytic conditions and therefore serves as a useful intermediate, bridging the pressure gap that exists between catalysis and surface science.

5.2 Enantioselective Catalysis

Many catalytic studies into the hydrogenation of MAA on a variety of modified supported nickel catalysts have been reported^[10-13] giving detailed catalytic data regarding the reaction. Surface science studies have also provided an insight to the fundamental effects that occur on single crystal surfaces. Gellman and co workers^[14-16] have performed experiments of the enantiospecific properties of Cu and Ag {643} chiral single crystal surfaces and have shown that the naturally chiral step-kink sites of this crystal face adsorb opposite enantiomers with different adsorption energies. Studies by Besenbacher^[17] into the adsorption of the chiral molecule cysteine on Au{110} have shown that the molecule is capable of etching of the metal surface resulting in a chiral metal surface. These observations and the fact that modification of the nickel catalysts with R,R-H₂TA is known to be a corrosive procedure suggests the possible formation of chiral nanoparticles in which chiral step-kink sites have been created by the acid

modification. These observations appear to oppose reported catalytic data that suggest the presence of nickel nanoparticles smaller than 200Å are not conducive to the production of catalysts with good enantioselectivities^[10] and that such high Miller index planes may not always be expected for bulk termination^[15]. However, the {643} index surface is vicinal to the {111} plane^[15] and therefore the possibility that modification may lead to restructuring of the metal nanoparticle facets cannot be discounted.

In chapters 3 and 4 of this thesis it has been shown that in the 0.05-0.2ML coverage regime considerable local ordering of R,R-H₂TA occurs on Ni{111}. These coverages, in comparison to fractional coverages obtained from catalytic data in which enantioselectivity has been optimised for R,R-H₂TA coverages of 0.2^[18] and 0.3^[10]. These fractional coverages are relative to a theoretical maximum coverage of 8.8x10⁻¹⁰ mol cm⁻²^[10] which consist of 5.3x10¹⁴ atoms cm⁻². If the surface consists of Ni{111} facets the number Ni atoms in 1 cm² is

$$\frac{1}{(2.492 \times 10^{-8})^2 \times \sin 60^\circ} = 1.86 \times 10^{15} \text{ atoms}$$

and the corresponding maximum coverage of R,R-H₂TA is

$$\frac{5.3 \times 10^{14}}{1.86 \times 10^{15}} = 0.28 \text{ML}$$

This value corresponds well with the maximum R,R-H₂TA coverage observed in our studies and also Cu{110} where the highest reported coverage was 0.3ML^[19]. Due to the low sticking probability of MAA on Ni{111} with a high R,R-H₂TA coverage, this would suggest that a 1:1 interaction between the reactant and modifier would only feasibly occur at the edge of tartrate islands. The template model, as discussed in

chapter 4, is also unlikely to explain enantioselective hydrogenation due to the lack of any evidence for the interaction of MAA with ordered R,R-H₂TA islands.

A feature that has been observed in this work that may be very important is the presence of adventitious CO on Ni{111} and the observation that both R,R-H₂TA and MAA appear to displace CO from the surface. This suggests that the modifier and reactant adsorption mechanism is competitive with CO. In the modification procedure for the catalytic system, the presence of tartrate and solvent molecules in the modification solution may also compete for available sites on the metal nanoparticles. If the R,R-H₂TA coverage is below saturation coverage, the presence of solvent molecules may act to disrupt intermolecular interactions between tartrate molecules, as CO does in the model Ni{111} studies. It is highly plausible that the introduction of MAA may displace solvent molecules resulting in the formation of an ordered adlayer where the stereostructure of the incoming reactant molecule is determined by the chirality of the surrounding tartrate species. Again this effect has been observed for our model studies. Whilst this coadsorbed model is ambiguous, as there is no in-situ data to verify these suggestions it is therefore desirable to create these surfaces and investigate their activity and selectivity under realistic catalytic conditions.

This chapter shall consist of a discussion of the designing and building of the UHV system with capabilities for preparation and characterisation of chirally modified Ni{111} surfaces and with the ability to carry out the hydrogenation of MAA under realistic catalytic conditions. The effect of the presence of different solvents on the reaction shall also be analysed in this initial research. The reaction is analysed via the

use of a GC fitted with a chiral column that is able to distinguish between the two enantiomeric forms of methyl 3-hydroxybutyrate.

5.3 Chamber Design

The stainless steel chamber is based on a bell jar shape and manufactured by PSP Vacuum Technology Ltd, Macclesfield, UK. The design is very similar to any common laboratory UHV system with the addition of a section that allows the main chamber to be isolated from the sample and reaction cell. The reaction cell was based on a design successfully used by Gardin *et al* ^[7] and attaches to the chamber via a 70mm conflat flange and sealed together with a re-usable viton gasket.

The main feature in the design of the vacuum chamber is the presence of a double z-drive manipulator, the first transfers the sample into the intermediate pumping section and the second transfers the sample to the reaction cell. The building and commissioning of the UHV chamber along with the cell backing/gas lines was completed as part of this PhD by myself. An illustration of the vacuum chamber is displayed in figure 5.2.

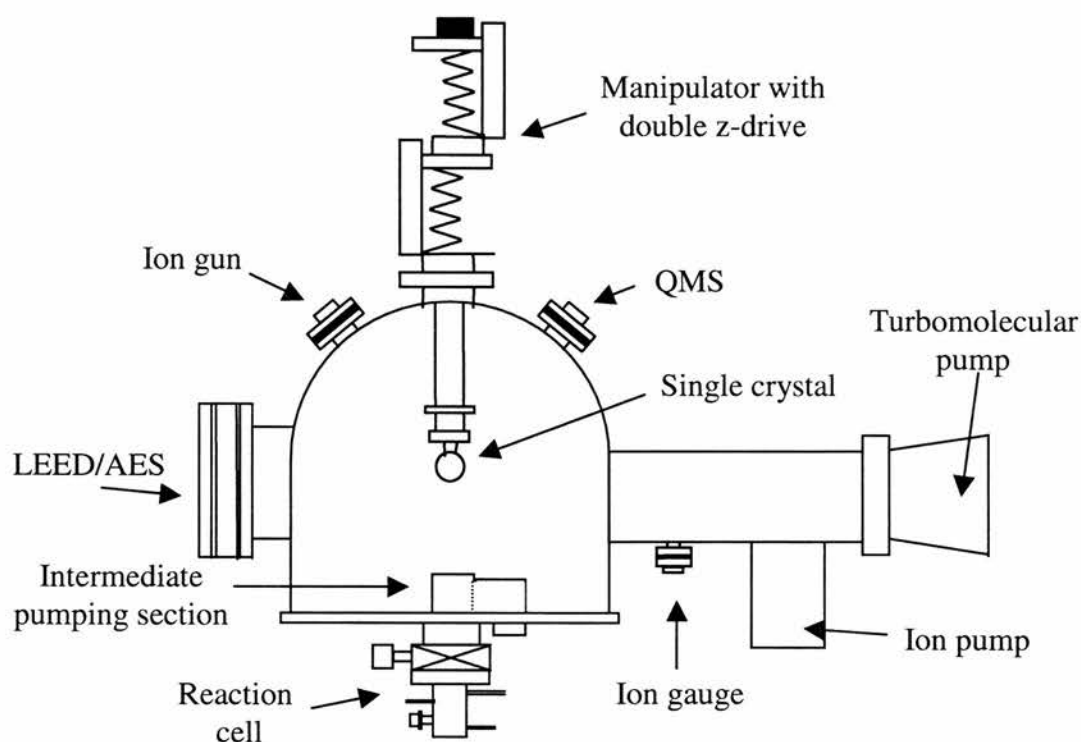


Figure 5.2. Illustration of the experimental setup including the transfer, intermediate pumping section and reaction cell.

The chamber consists of a manipulator onto which the single crystal is attached via spot welding to the power and thermocouple feedthroughs. The system is pumped from atmosphere and during dosing of R,R-H₂TA and MAA by the using of a rotary backed turbomolecular pump. The internal pressure is measured by an ion gauge whilst the integrity of the vacuum analysed by the use of a quadrupole mass spectrometer that is also a multi-mass residual gas analyser for use in TPD experiments. To accelerate the attainment of UHV conditions within a satisfactory time scale the chamber is baked to about 430K for approximately 15 hours. Once UHV conditions have been achieved ion and titanium sublimation getter pumps hold the chamber at UHV.

The sample is cleaned by Ar⁺ ion sputtering using an ion gun whilst the sample cleanliness and surface structure are characterised by AES and LEED techniques. There

are also facilities for gas and solid dosing and a sputter source for the evaporation of metals onto the sample.

The main difference with the design of this particular chamber is the presence of an intermediate pumping section. To enable ex-situ studies of the surface and eliminate the need to bake the chamber, to remove contamination that may have leaked into the main chamber after each reaction, reliable sealing between the cell and the vacuum chamber is required. Therefore, the system has a two stage sealing system, the first isolates the main chamber from the intermediate pumping section and the second seals the intermediate section from the reaction cell. The function of the intermediate pumping section ensures that if there were any leaking from the cell, this would be pumped away by an ancillary pumping device and would not enter the main chamber. For these reasons a manipulator with a double z-drive is required.

5.3.1 Sample Transfer Procedure

To transfer the sample into the intermediate stage, the first z-drive which lowers/raises the entire manipulator and sample is enabled until the manipulator is sealed over the intermediate pumping section with a viton ring. Once the seal has been made a right angled valve is opened which allows the intermediate section to be pumped by a separate rotary backed turbomolecular pump. The next step is to open a gate valve that isolates the reaction cell, pumped by a rotary pump to the intermediate pumped section. The second z-drive then enables the sample to be transferred into the reaction cell and sealed from the intermediate section by another viton ring. The final transfer setup is illustrated in figure 5.3.

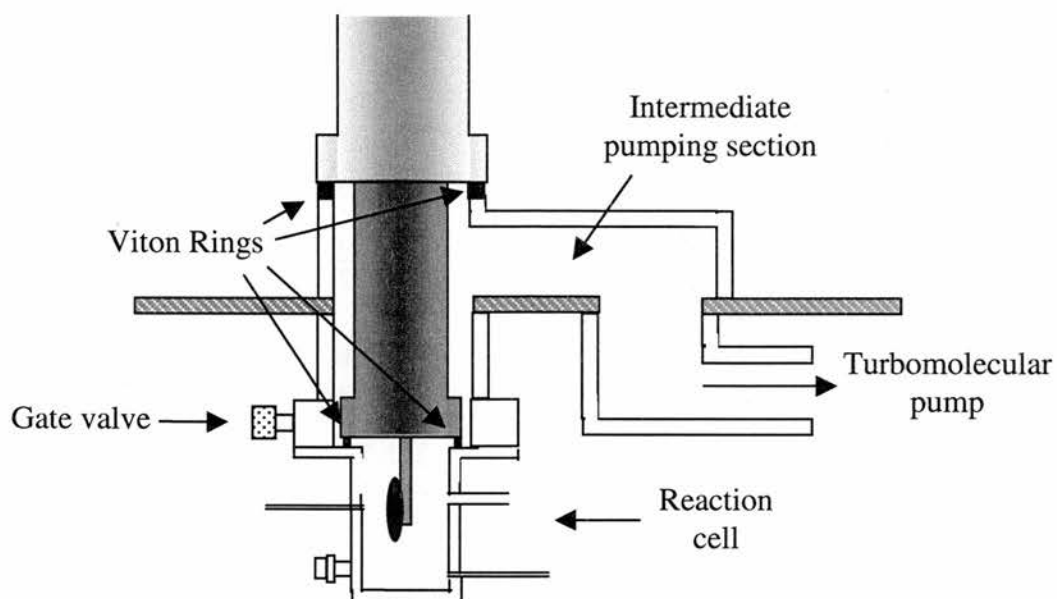


Figure 5.3. Illustration of the final positions of the sample, first and second stage sealing with relation to the reaction cell and intermediate pumping section.

In figure 5.3, the manipulator is shaded two colours, the lighter colour indicates the position that the first z-drive moves to seal on the intermediate section and the darker colour indicates that of the second z-drive to seal on the reaction cell. The sample is now in the correct position to initiate the reaction.

5.3.2 Reaction Cell

To transfer the reaction components into the reaction cell (manufactured by PSP Vacuum Technology) requires the design and building of a backing line that enables the cell to be pumped, purification of the reactant mixture and a method by which various pressures of hydrogen can be introduced accurately. This is illustrated in figure 5.4.

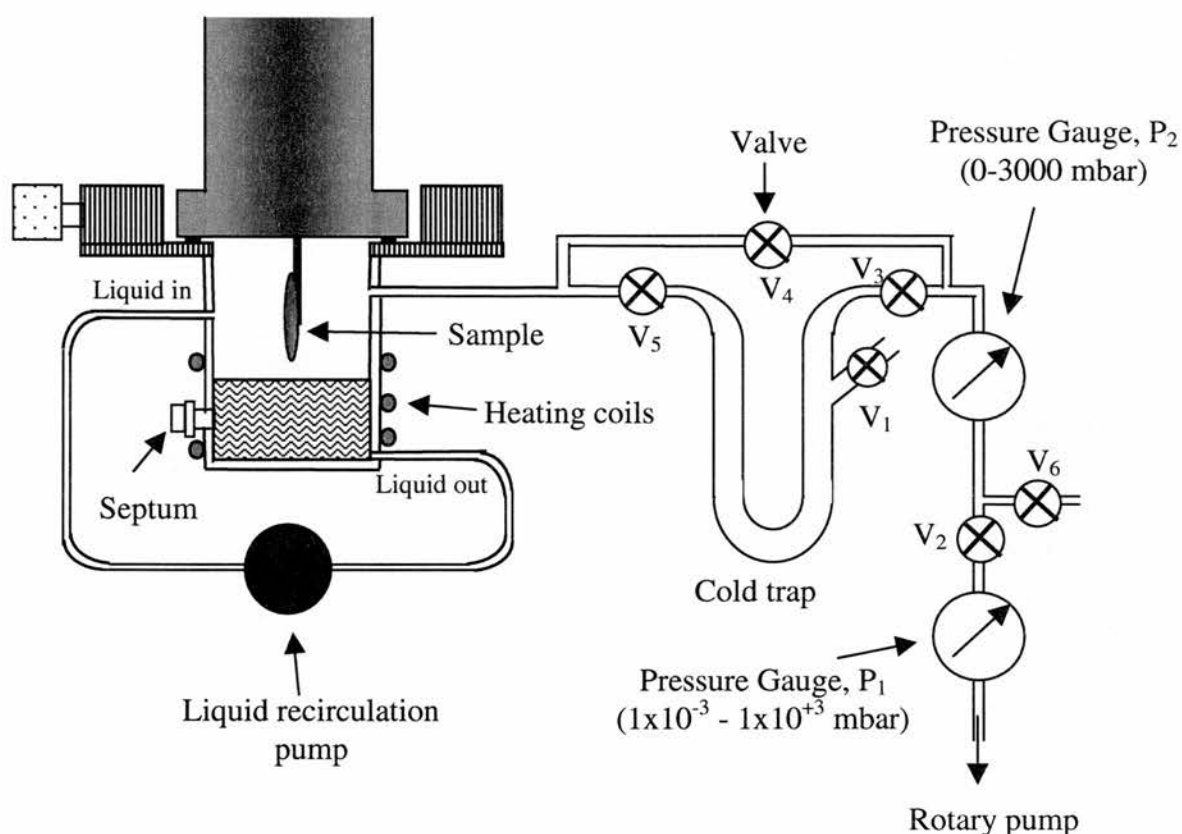


Figure 5.4. Illustration of the reaction cell and backing line for reaction component purification and transfer.

The reaction cell is gold plated to limit any side reactions that may occur on its walls because the cell is made from stainless steel that contains small amounts of Ni that may be involved in the hydrogenation reaction. Also, Fe has been tested as a hydrogenation catalyst for this reaction and has shown slight activity ^[11]. The cell has an internal volume of $\sim 15\text{cm}^3$ and is connected to a liquid recirculation pump via PTFE tubes that enables a thin jet of reaction solution to be sprayed onto the surface with varying velocities in order to obtain a good mass transport at the liquid solid interface ^[7]. The liquid that sprays onto the sample subsequently falls into the base of the cell from where the pump recirculates the liquid back to the sample. Whilst the liquid is recirculating, heating coils enable the liquid to be kept at a constant temperature, between $\sim 300\text{K}$ – 373K , for the duration of the reaction. The presence of a septum at the bottom of the

cell provides the means by which a 1 μ L aliquot of the reaction solution can be removed and analysed in a GC.

5.3.3 Purification and Transfer of the Reaction Components

The minimum volume of reaction solution required to deliver a continuous stream of liquid to the sample has been measured as $\sim 8\text{cm}^3$ and therefore $\sim 10\text{cm}^3$ of reaction solution is added to the glass cold trap via the Young's tap (V_1). With all valves closed except V_2 and V_3 , the reaction solution is purified by cycles of freeze-pump-thaw using an acetone/liquid nitrogen bath whilst pumping using the rotary pump and monitoring the pressure with the pressure gauge, P_1 . After purification, V_3 is closed and V_4 is opened to allow the cell to be pumped. The reaction mixture is heated until it is apparent that the solution is starting to evaporate at which point V_4 is shut and V_5 opened. The reaction solution subsequently transfers over to the reaction cell due to the pressure and temperature difference between the cell and trap. When the reaction mixture has transferred over to the cell, V_5 and V_2 are shut.

At this point hydrogen needs to be introduced into the cell. The source of hydrogen is a regular hydrogen gas cylinder, with a purity of $\geq 99.995\%$, that is introduced into the backing line by opening the needle valve (V_6) to the required pressure as monitored by the pressure gauge, P_2 . The hydrogen is then introduced to the cell by opening V_4 and adjusting the pressure using V_6 , up to a pressure of $\sim 2500\text{mbar}$. When the desired pressure has been attained valves V_4 and V_6 are shut.

The reaction can then be initiated by starting the recirculation pump to the desired flow rate and reaction temperature.

5.3.4 Theoretical Hydrogenation Activity

It is important to estimate accurately how fast the reaction should proceed and the amount of product that may be produced. The rate of hydrogenation of MAA over R,R-H₂TA modified nickel catalysts has been determined from catalytic studies and one such value determined by Tai *et al* ^[11] is given as 13.1mmol h⁻¹ at 1 bar hydrogen. The amount of R,R-H₂TA present on the catalyst to give this hydrogenation rate has been measured as 0.12mmol (g catalyst)⁻¹ ^[11]. This means that for 7.2x10¹⁹ molecules (g catalyst)⁻¹ of R,R-H₂TA, 7.9x10²¹ molecules of MAA are hydrogenated every hour or 110 MAA molecules are hydrogenated per tartaric acid molecule per hour. This theoretical value, for comparison, is much smaller than the experimental value of 3960 molecules per site per hour obtained by Gardin *et al* ^[7] for the liquid phase hydrogenation of cyclohexene on a 1cm² polycrystalline platinum foil.

The surface area of the single crystal used in this study is much smaller than the catalysts used in the reaction, the Ni{111} surface area is 1.3 cm² which corresponds to ~2.4x10¹⁵ atoms. Webb *et al* ^[18] have estimated the optimum fractional surface coverage of R,R-H₂TA to generate the greatest enantioselectivity is 0.2 on modified silica supported nickel catalyst ^[10]. This fractional coverage corresponds to a monolayer coverage of ~0.06ML. Assuming the same R,R-H₂TA coverage and hydrogenation rate on a single crystal, there are ~1.4x10¹⁴ R,R-H₂TA molecules present and the hydrogenation rate of MAA is ~1.6x10¹⁶ molecules h⁻¹.

If the solvent is methanol and the volume of the reaction mixture is 10cm³ this corresponds to ~2.9x10²³ molecules of solvent and the subsequent hydrogenation rate of

MAA on the Ni{111} single crystal is $\sim 0.1 \text{ ppm h}^{-1}$. This theoretical value assumes the kinetics are similar on the single crystal and indicates that after ~ 20 hours reaction time a detectable amount of reaction product would have been formed.

5.4 Experimental

The experimental procedure has been explained earlier. The reaction conditions are as illustrated in table 5.1.

Sample	MAA concentration / ppm	Solvent	Temperature / K	Flow velocity / ms^{-1}	H₂ pressure / mbar
None	100,000	Methanol	343	0	1000
None	100,000	Methanol	343	2	1000
Ni{111}	100,000	Methanol	343	2	1000
Ni{111}	10,000	Methanol	343	2	1000
R,R-H ₂ TA / Ni{111}	10,000	Methanol	343	2	1000
S,S-H ₂ TA / Ni{111}	10,000	Methanol	343	2	1000
Ni{111}	100,000	THF	343	0	1000
Ni{111}	100,000	THF	343	2	1000

Table 5.1. Illustration of the various reaction conditions employed in this study.

Several different sample conditions have been used in this study. Running the reaction with no nickel sample in the cell allows us to monitor the contribution that the cell, liquid pump and PTFE connection tubes have to the overall reaction yield. This is vital, as it is important to know from where a reaction product has been formed. Addition of the nickel sample should allow the monitoring of the racemic reaction whilst

modification of the sample with R,R- and S,S-H₂TA may produce one enantiomer as the dominant product.

The modified surfaces are prepared by dosing the surface at 300K with a source temperature of 420K, corresponding to a higher arrival rate of tartrate molecules for 60 seconds.

Two different concentrations of MAA ($\geq 99\%$ purity) were used in the reaction mixture to allow a comparison of how different amounts of MAA in the reaction solution have an effect on the hydrogenation activity, if any. Different solvents have also been studied. Both methanol ($\geq 99.5\%$ purity) and tetrahydrofuran (THF - $\geq 99.8\%$ purity) were investigated. These solvents have been shown to be good solvents in the hydrogenation reaction^[10-12].

The reactions are carried out at 343K, a temperature at which the catalytic reaction is known to proceed with good activity and selectivity^[20]. A hydrogen pressure of 1000mbar has been used to ensure a constant supply of hydrogen to the nickel surface is maintained.

The method employed in all the GC experiments is very similar to that suggested by the column supplier^[21] however they required a slight adjustment in order to improve the separation of R- and S-MHB. The method is as follows: the oven was held at a temperature of 313K, until one minute after injecting the sample. The oven was then ramped at 4Ks^{-1} until an oven temperature of 473K had been attained after which the run ended and the column allowed to cool back to 313K ready for the next injection.

5.5 Results and Discussion

The first and one of the most important experiments is to run a standard solution in the GC that consists of the reactant and the products in order to indicate their respective retention times. A solution containing 100ppm of R- and S-MHB was prepared in MAA. The solution was injected into the GC and a portion of the resulting chromatograph is displayed in figure 5.5.

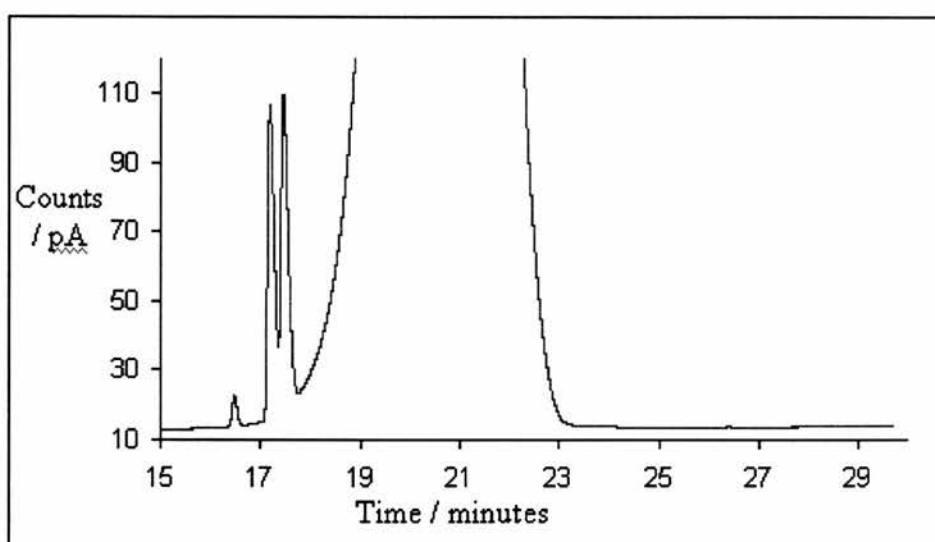


Figure 5.5. GC Chromatograph of a solution containing 100ppm of R- and S-MHB in MAA.

The chromatograph shows a large peak that starts to appear at about 17 minutes and ends at about 23 minutes that corresponds to the detection of MAA at the FID. The amount of MAA present in the solution is in massive excess to that of R- and S-MHB and therefore in order to resolve the features associated with the two enantiomers, a smaller scale is required. For this reason, a large proportion of the MAA peak is not illustrated in this, or any of the chromatographs presented in this chapter.

Along with this large feature are three others that have retention times of ~16.5, 17.1 and 17.6 minutes. The peak at lower retention time is always present in a chromatograph from MAA and it is most likely due to a slight impurity. The peak with a retention time of 17.1 minutes is a result of S-MHB whilst the feature at 17.6 minutes is that of R-MHB. Therefore, using this method it would be expected that if hydrogenation of MAA occurs in any of the reactions then as long as the enough of the product is produced, it should be detected and its selectivity determined.

In the hydrogenation reactions it is proposed to use an MAA concentration of either 100,000ppm or 10,000ppm. It is therefore advantageous to have an idea of the limits of detection for R- and S-MHB in the reaction mixture. Therefore a solution containing 10ppm R- and S-MHB in 10,000ppm of MAA in methanol was prepared and injected into the GC. The resulting chromatograph is illustrated in figure 5.6.

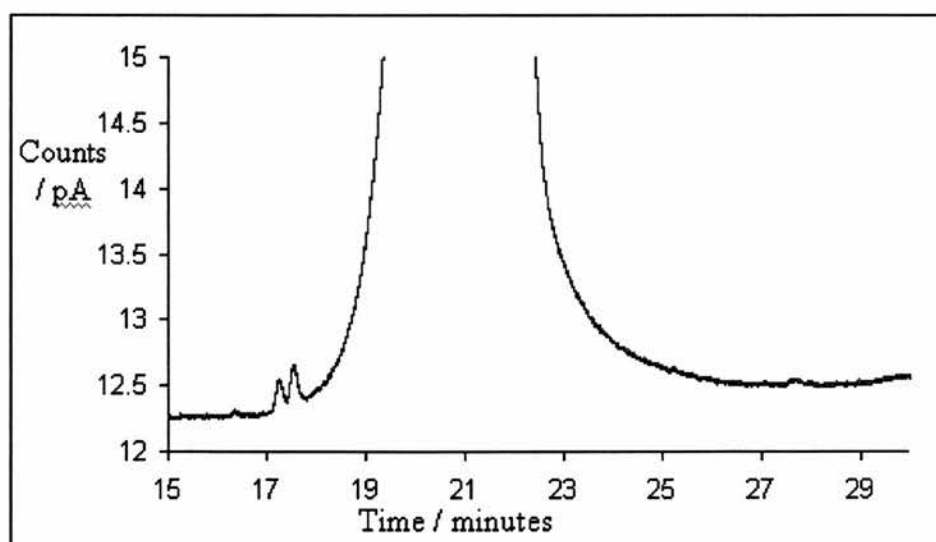


Figure 5.6. Chromatograph of a solution containing 10ppm R- and S-MHB in 10,000ppm MAA in methanol.

It can clearly be seen in figure 5.6 that both enantiomers of MHB are visible together with the larger feature associated with MAA and the small feature at ~16.5 minutes also

associated with an impurity of MAA. Therefore, one could imagine that the presence of only a couple of ppm of MHB would easily be detected using this column and GC method.

After each hydrogenation reaction the sample was transferred back into the UHV chamber where LEED and AES were employed to characterise the surface ex-situ. AES indicated that the presence of a large amount of C and O on the surface and the attenuated Ni Auger features indicated that this layer was at least 10Å thick. The lack of any visible diffraction spots and an extremely high background also backed up AES data and indicated that the overlayer structure possessed no long range order.

5.5.1 Hydrogenation Reaction in the Absence of Ni{111}

To obtain a background reaction consisting of the effect the reaction cell, recirculation pump and connecting tubing have, the hydrogenation reaction is performed in which no Ni{111} sample is present. A reaction mixture consisting of 100,000ppm MAA in methanol was transferred into the reaction cell and the reaction initiated with a hydrogen pressure of 1000mbar and a temperature of 343K. The chromatograph for the reaction where no liquid is recirculated is illustrated in figure 5.7.

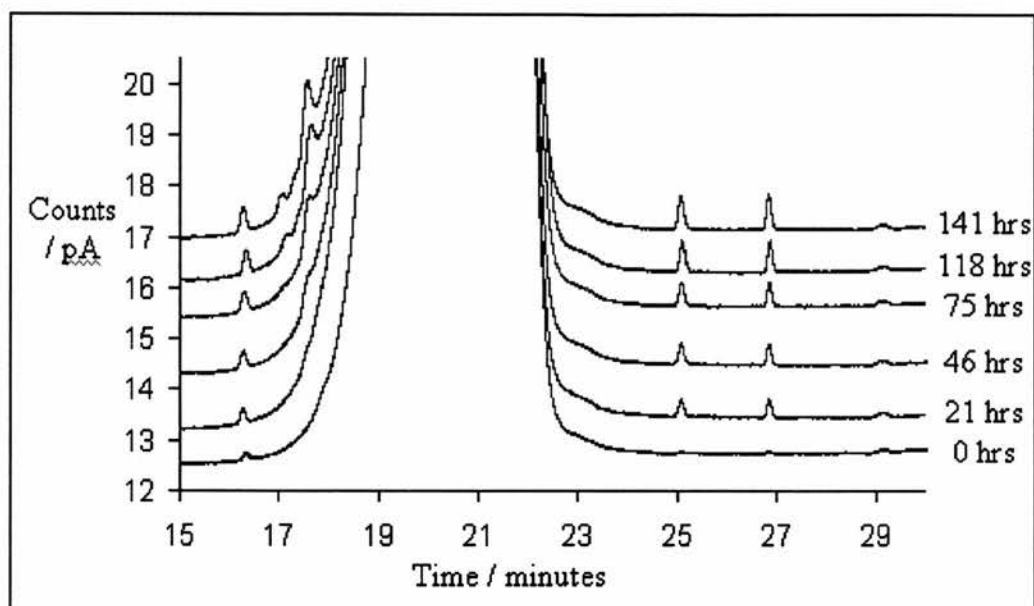


Figure 5.7. Chromatograph of the hydrogenation reaction in the absence of Ni{111} and reaction solution velocity of 0ms^{-1} . The reaction solution contains 100,000ppm MAA in methanol.

The chromatographs show a slight growth of the small feature present in MAA at 16.5 minutes after 21 hours reaction time. Also present is the growth of two small features at 25.1 and 26.9 minutes and a very small peak at ~ 29.3 minutes. As the reaction continues, a shoulder forms and grows into a feature at 17.8 minutes and is accompanied by the formation of a very small feature at ~ 17.1 minutes. The feature at 17.1 minutes coincides at the same retention time as that for S-MHB. The identities of the other features are at present unknown, however as will be shown later, they are all prominent in the chromatographs for all the reactions.

If the feature at 17.1 minutes is that of the formation of S-MHB then this implies that the reaction is occurring on the walls of the reaction cell, despite the cell being gold plated and this would then need to be taken into account in determining the overall reactivity of the Ni{111} surfaces. It is not clear either as to why the production of R-MHB is not observed, however this may suggest that coincidentally another molecule

has been formed in the reaction that has the same retention time as one of the hydrogenation product molecules.

The effect of the jet velocity has been shown to have a profound effect on the rate reaction ^[7] and therefore it is hoped that by changing the velocity in these reactions an effect on the rate of hydrogenation will result. Therefore, the same reaction has been repeated except the liquid is recirculated. This also gives an indication as to the possible effect the recirculation pump and connecting tubes have on the background reaction. The chromatographs corresponding to this reaction are illustrated in figure 5.8.

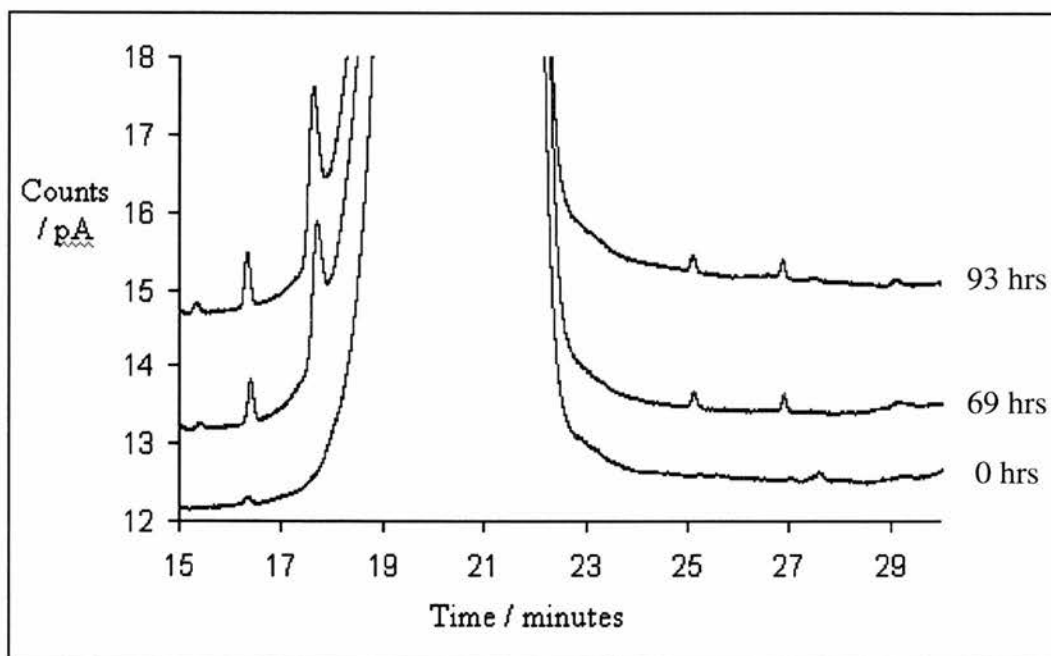


Figure 5.8. Chromatograph of the hydrogenation reaction in the absence of Ni{111} and with a reaction solution velocity of 2ms^{-1} . The reaction solution contains 100,000ppm MAA in methanol.

During the reaction the growth of the features at ~16.5, 17.8, 25.1, 26.9 and 29.3 minutes are observed. In this reaction there is no formation of any feature at 17.1 minutes but an extra feature at ~15.4 minutes is observed as the reaction occurs. These observations therefore suggest that some sort of reaction occurs on the walls of the cell.

Only when the reaction mixture is allowed to stand for some time do we observe the feature at 17.1 minutes.

It therefore appears unlikely that the hydrogenation reaction occurs when no Ni{111} is present. There is formation of other products that are so far unknown and when the reaction solution is allowed to stand in the cell the formation of a compound with the same retention time as S-MHB.

5.5.2 Hydrogenation Reaction in the Presence of Ni{111}

A series of hydrogenation reactions were carried out in the presence of Ni{111}. It would be expected that if MAA molecules are being hydrogenated, the reaction would proceed via the production of both S- and R-MHB molecules. The same reaction as presented in figure 5.8 is performed to observe the effect that Ni{111} has on the hydrogenation reaction. The chromatographs for this reaction are illustrated in figure 5.9.

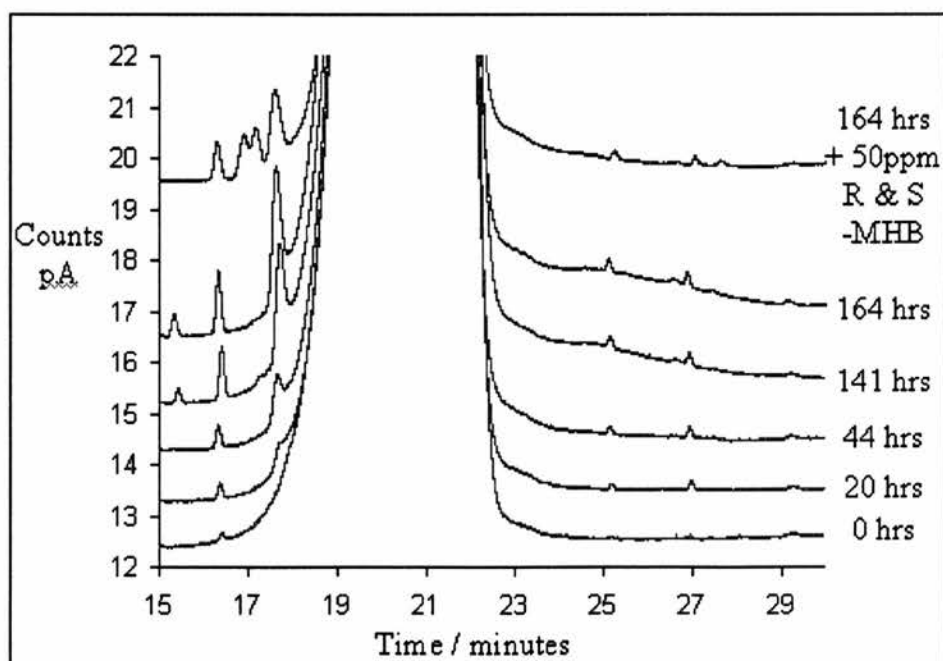


Figure 5.9. Chromatograph of the hydrogenation reaction over Ni{111} and with a reaction solution velocity of 2ms^{-1} . The reaction solution contains 100,000ppm MAA in methanol.

The same features are again observed in the chromatographs and no features are present at 17.1 and 17.6 minutes indicating that neither S- nor R-MHB have been produced. There are several possibilities that may explain why no activity is being observed. Firstly, the reaction rate is too slow and would require a longer reaction time for the amount of required product to grow. This may be reasonable to conclude, as the surface area of nickel is much smaller than that of the real catalyst. Secondly, the reaction is occurring but the retention time of the product peaks is altering so, for example, the features may be masked by the large MAA feature. 50 ppm of the two enantiomers was subsequently added to the reaction mixture after the reaction had ceased and the two enantiomers are quite clearly visible in the chromatograph in figure 5.9 Therefore, a change in retention time appears unlikely. Thirdly, the S- and R-MHB are being formed but are being further hydrogenated, forming molecules that are represented, perhaps by the feature that grows at ~17.8 minutes. Finally, the reaction may not be occurring at all due to poisoning of the Ni{111} surface or even the hydrogen transport to the surface species is too slow.

If the concentration of MAA is too high then it would appear conceivable that this may hinder the transport of hydrogen to the metal surface. Therefore a reaction is performed in which a 10,000ppm concentration of MAA is present in the reaction mixture. The reaction is illustrated in figure 5.10.

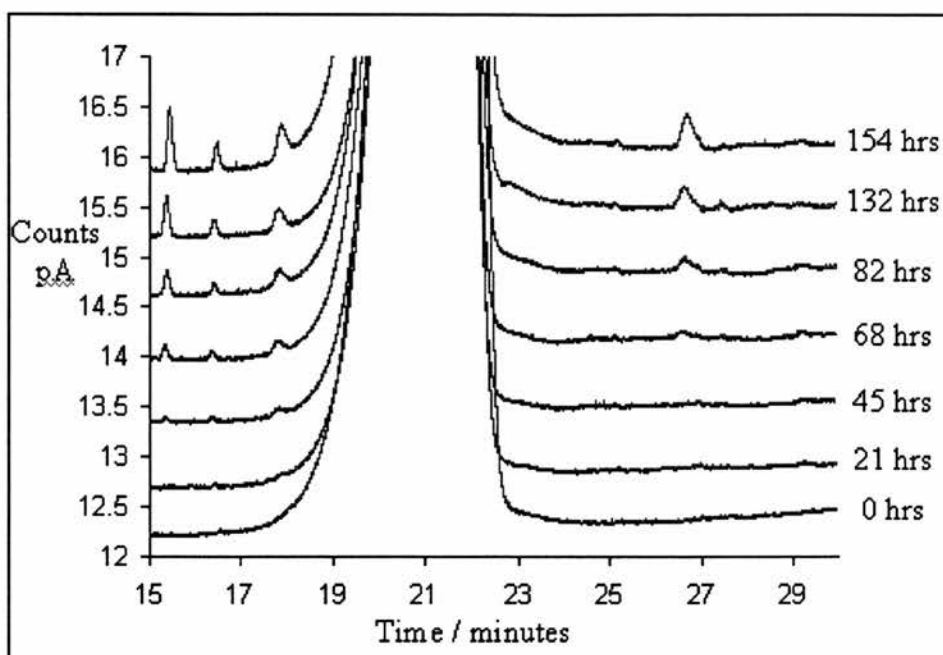


Figure 5.10. Chromatograph of the hydrogenation reaction over Ni{111} and with a reaction solution velocity of 2ms^{-1} . The reaction solution contains 10,000ppm MAA in methanol.

The reaction again proceeds in a similar way to that previously observed with two exceptions. The features at 15.4 and 26.9 minutes are much larger than before whilst the peak at 25.1 minutes is much weaker. Again there is no evidence for the hydrogenation of MAA to MHB and the change in the amounts of the three features appear to be related to the MAA concentration in some way. This may suggest that two of the previous suggestions are occurring simultaneously, the first is that for a lower MAA concentration the reaction rate is increased whilst the product is undergoing some further reaction to produce molecules that correspond to the growth of the two features. However, these are only suggestions and no evidence exist for verify them. Therefore, there is again no indication that the hydrogenation reaction is occurring.

5.5.3 Hydrogenation Reaction in the Presence of Modified Ni{111}

It would appear very unlikely that the modified surface would hydrogenate MAA when there is no evidence of the formation of a racemic product on Ni{111} however, it has been suggested in many reports that modification of metal particles results in an increased hydrogenation rate in comparison to the clean, unmodified metal surface [10-13][18].

The chromatographs illustrating the hydrogenation reaction over R,R-H₂TA modified Ni{111} is displayed in figure 5.11.

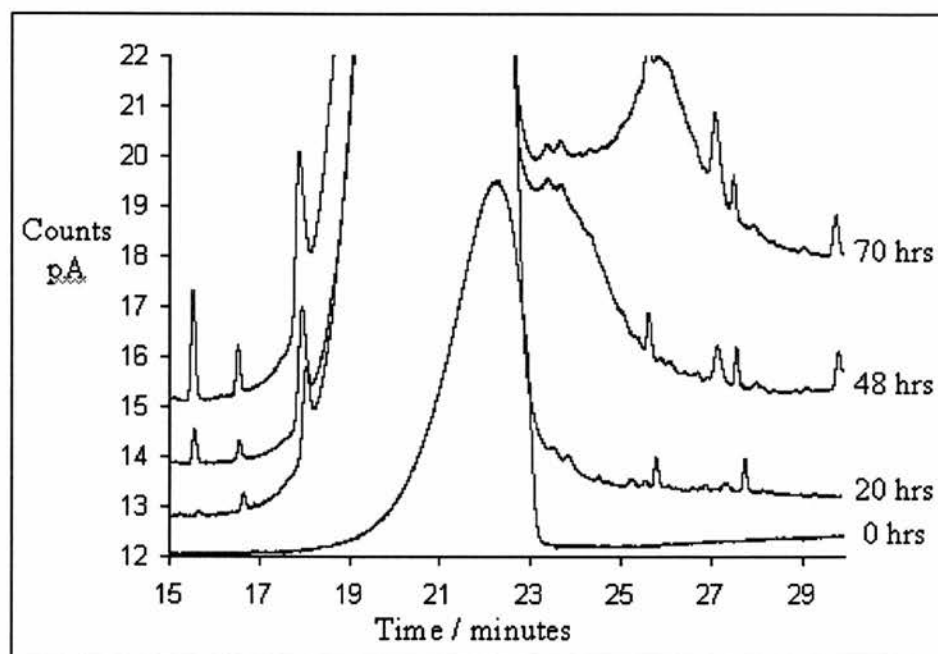


Figure 5.11. Chromatograph of the hydrogenation reaction over R,R-H₂TA modified Ni{111} with a reaction solution velocity of 2ms⁻¹. The reaction solution contains 10,000ppm MAA in methanol.

There is no evidence for the formation of any of the desired products whilst the chromatographs show a difference at the high retention side. The features that were at 25.1 and 26.9 minutes appear to have shifted to higher retention times of ~25.8 and 27.7

minutes. There is also the growth of features at 27.2 and 39.7 minutes that have not previously been observed whilst the base line does not appear to be flat between 23 and 29 minutes. Once again, there appears to be no obvious reason for these differences but if the effect is due to the modified surface the same effect would also be expected during the reaction with S,S-H₂TA modified Ni{111}.

The chromatographs for the reaction with S,S-H₂TA modified Ni{111} is illustrated in figure 5.12.

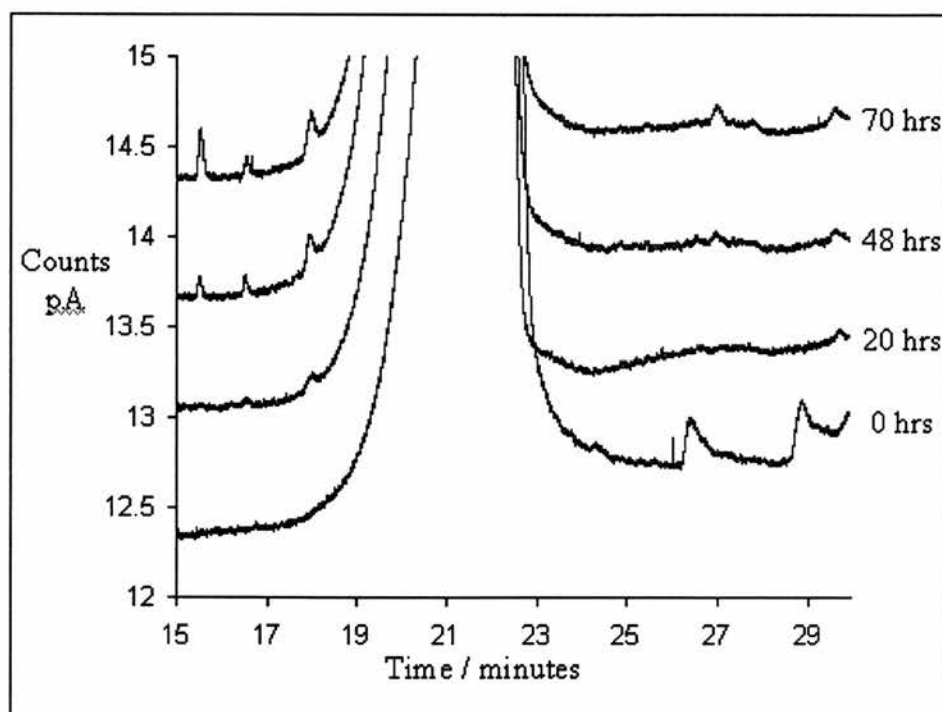


Figure 5.12. Chromatograph of the hydrogenation reaction over S,S-H₂TA modified Ni{111} with a reaction solution velocity of 2ms⁻¹. The reaction solution contains 10,000ppm MAA in methanol.

The base line for the reaction mixture before the hydrogenation reaction is initiated is different at higher retention times to that previously observed. However, we believe this

to be due to a contamination in the syringe, as this effect is not observed for the subsequent injections.

The presence of the peaks at ~27.2 and 29.7 minutes appear to match that of the R,R-H₂TA modified reaction and therefore it is possible to conclude that the presence the modifier does have an effect on the reaction, however it is not the one expected. The lack of features at 17.1 and 17.6 minutes again indicated that there is no MHB present in the reaction mixture.

5.5.4 Hydrogenation Reaction using THF as a Solvent

With the apparent unsuccessfulness of the previous experiments it was decided to change the solvent, as it may be that it is the effects of the solvent that are inhibiting the reaction. THF is another solvent that has been successfully used in catalyst reactions^[10] and therefore the reaction over Ni{111} was repeated using THF as a solvent.

The first experiment was designed to analyse the effect of the presence of solvent and reactant vapour in the reaction cell and therefore once the reaction mixture had been transferred into the cell, it was left in the base of the cell with no recirculation. The cell was pressurised to 1000mbar hydrogen and the solution was maintained at 343K.

The chromatograph is illustrated in figure 5.13.

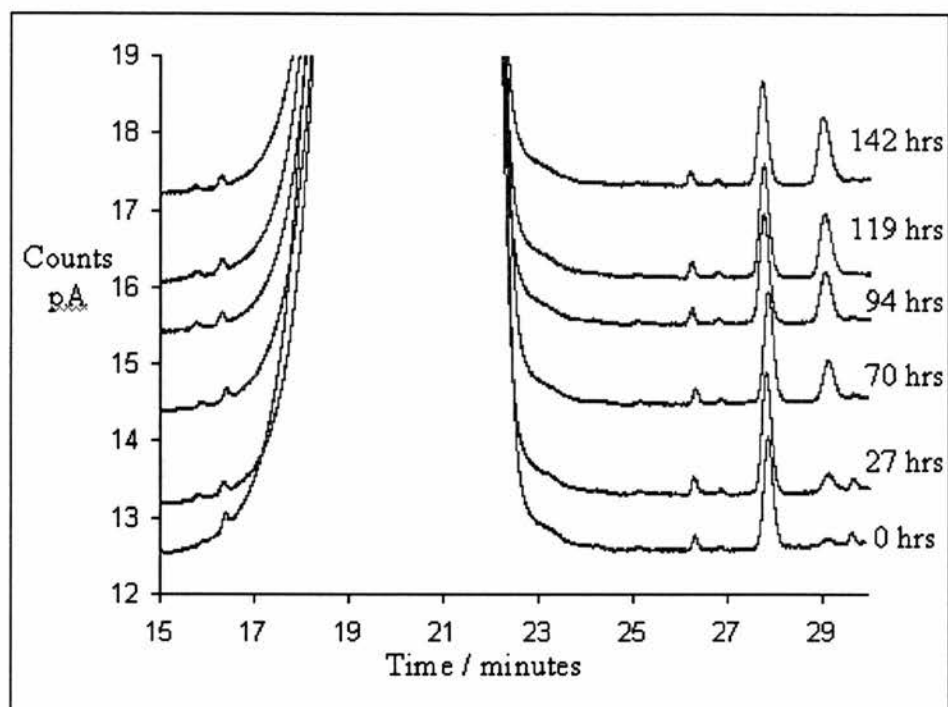


Figure 5.13. Chromatograph of the hydrogenation reaction over Ni{111} with a reaction solution velocity of 0ms^{-1} . The reaction solution contains 100,000ppm MAA in THF.

The initial chromatograph is characterised by the presence of the MAA feature between 16 and 23 minutes and the small impurity peak at 16.5. The large feature at 27.7 minutes and a smaller peak at 26.4 minutes are present in the chromatogram of THF alone and therefore probably a result as a small impurity in the solvent. Two further small features present at 29.2 and 29.7 minutes are also observed during the reactions when methanol is employed as the solvent.

With increasing reaction times the feature at 29.2 minutes increases in intensity whilst the growth of a new feature at ~16 minutes are the only observable differences in this reaction. Therefore, there is no evidence for any hydrogenation activity in this reaction.

This reaction has been repeated with a reaction liquid velocity of 2ms^{-1} and the chromatographs are illustrated in figure 5.14.

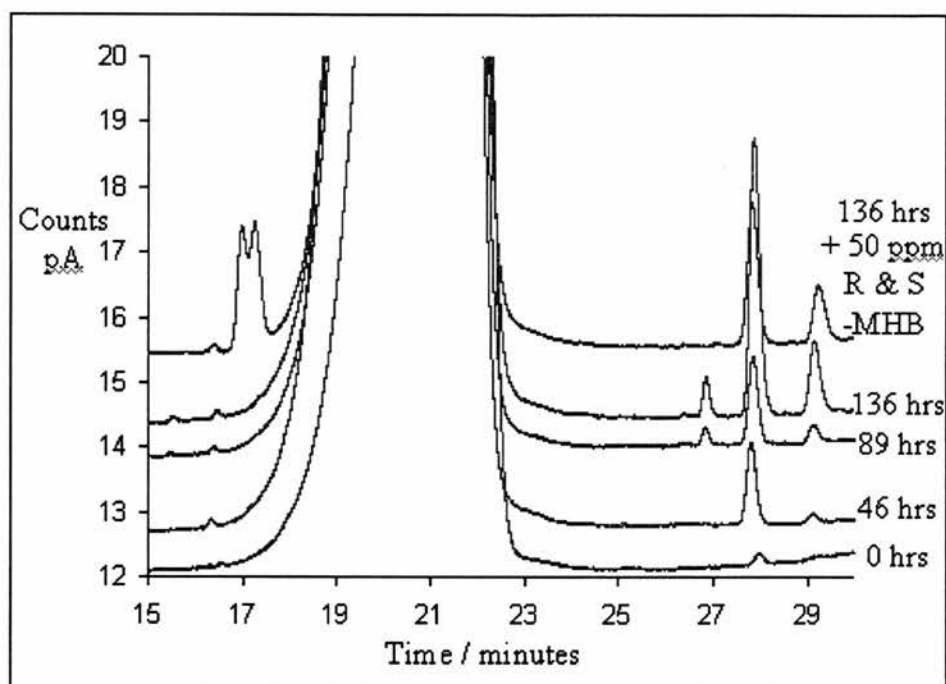


Figure 5.14. Chromatograph of the hydrogenation reaction over Ni{111} with a reaction solution velocity of 2ms^{-1} . The reaction solution contains 100,000ppm MAA in THF.

This chromatograph is very similar to that in figure 5.13 in which the reaction liquid is not recirculated around the cell and no evidence exists to indicate the formation of MHB. After the reaction had been halted, 50ppm of the S- and R-MHB GC standard was added to the reaction mixture and the GC run indicated that the enantiomers have the same retention time in THF as in methanol. The feature at ~26.9 minutes is not present after the sample was transferred out of the cell. This must be a result of the transfer process suggesting that the molecule that corresponds to this feature remains in the cell. If any of the desired products have been formed then it almost certainly should be detected.

In all of the reactions that were performed it appears as though the hydrogenation activity is zero. One of the most likely reasons for this is that surface sites have been blocked, either by the presence of solvent and reactant molecules or the sites have been

poisoned. If the sites have been poisoned it seems most likely as a result of C, due to the large amount of C present on the surface after each reaction. Therefore a test was performed in which the sample was cleaned and allowed to cool to 300K. The sample was then transferred into the reaction cell where it was left for 5 minutes then transferred back to UHV, without being in contact with any reaction mixture. This would indicate whether the surface becomes covered in C as a result of the transfer process or being in contact with the reaction mixture. The Auger spectrum of this surface indicate the presence of a large amount of C and some O. The corresponding TPD of this surface is displayed in figure 5.15.

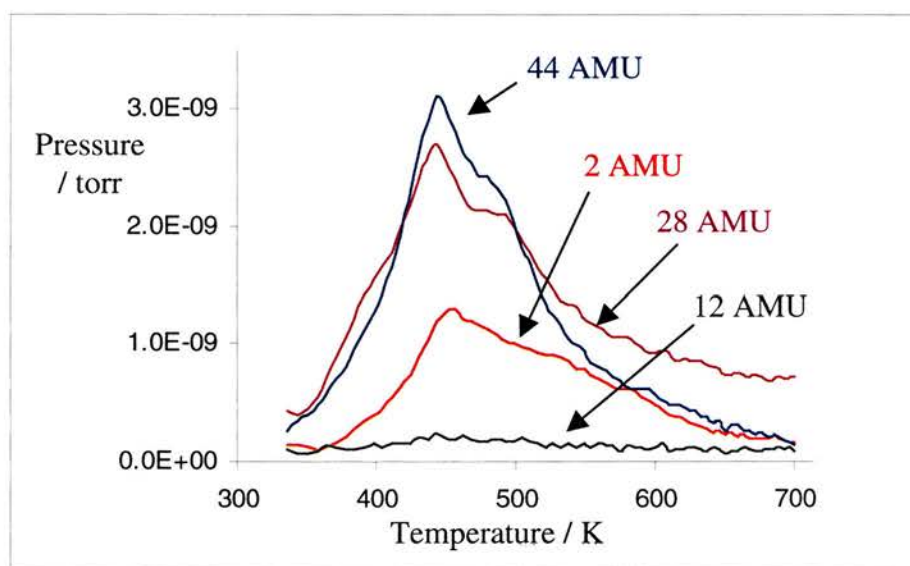


Figure 5.15. TPD of the Ni{111} surface after being transferred into the reaction cell, left for 5 minutes then returning to UHV.

The presence of CO_2 alone indicates that there is an excess of $\text{CO}_{(\text{ads})}$ and $\text{O}_{(\text{ads})}$ present on the surface and that CO oxidation is occurring as CO_2 is known not to adsorb to Ni{111} at 300K^[22]. The T_{max} of the desorption features is $\sim 445\text{K}$ and is $\sim 45\text{K}$ higher than has been observed for the clean surface in chapter 3 and about 25K higher than that observed when R,R- H_2TA or MAA was dosed onto the surface. This therefore indicates that the surface is being contaminated by vapour that is present in the reaction cell.

The cell is pumped using a rotary pump and therefore an explanation is that rotary pump oil vapour is back streaming into the cell and subsequently poisoning the surface before the reaction is initiated.

5.6 Future Work

It is clear that the design of the backing line to the cell may need to be improved. The first step to remedy this problem is to fit a foreline trap above the rotary pump to filter out oil vapour and stop the back streaming into the cell. Alternatively, the use of an oil free pump could be used or to increase the base pressure of the cell, a turbomolecular pump could be interfaced to the cell.

It is very important to identify the ‘unknown’ peaks that are observed in the chromatographs. If these features are a result of MHB being involved in a further reaction then this would require changes in the conditions of the reaction to try to quench these unwanted reactions from occurring. This may be tackled by determining the molecules that may have also been formed and testing them in standard GC reactions.

It would also be advantageous to try the reaction using RNi and Ni/SiO₂ catalysts that are known to give a good hydrogenation activity in order to continue the cell testing and development. Once a hydrogenation reaction is occurring within the cell, the reaction using the Ni{111} sample can then be performed and the conditions optimised.

5.7 References

- [1] GA Somorjai; *Surf. Sci.* **299/300** (1994) 849
- [2] DR Rainer and DW Goodman; *Chemisorption and Reactivity on Supported Clusters and Thin Films*. RM Lambert and G Pacchioni (eds.), Kluwer Academic Publishers, 1997. 27
- [3] RJ Madix; *Adv. Cat.* **29** (1980) 1
- [4] DW Goodman. *Surf. Sci.* **299/300** (1994) 837
- [5] GA Somorjai; *Elementary Reaction Steps in Heterogeneous Catalysis*. RW Joyner and RA van Santen (eds.), Kluwer Academic Publishers, 1993. 3
- [6] JW Nienmantsverdriet; *Spectroscopy in Catalysis – An Introduction*. VCH, Weinheim, 1993. 1-4
- [7] DE Gardin and GA Somorjai; *Rev. Sci. Instru.* **64**, 5 (1993) 1304
- [8] SM Davis and GA Somorjai; *J. Catal.* **65** (1980) 78
- [9] DR Kahn, EE Petersen and GA Somorjai; *J. Catal.* **34** (1974) 294
- [10] A Tai and T Sugimura; *Chiral Catalyst Immobilisation and Recycling*. DE de Vos, IFJ Vankelecom and PA Jacobs (eds), Wiley – VCH, 2000. Chapter 8, 173
- [11] A Tai and T Harada; *Tailored Metal Catalysts*, Y Isawawa (ed.), D Reidel Publishing Company, 1986. 265
- [12] Y Izumi; *Adv. Cat.* **32** (1983) 215
- [13] MA Keane; *J. Chem. Soc. Faraday Trans.* **93**, 10 (1997) 2001
- [14] CF McFadden, PS Cremer and AJ Gellman; *Langmuir* **12** (1996) 2483
- [15] AJ Gellman, JD Horvath and MT Buelow; *J. Mol. Catal. A.* **167** (2001) 3
- [16] JD Horvath and AJ Gellman; *J. Am. Chem. Soc.* **123** (2001) 7953
- [17] A Kuhnle, TR Linderoth, B Hammer and F Besenbacher; *Nature*. **415** (2002) 891
- [18] MA Keane and G Webb; *J. Catal.* **136** (1992) 1

-
- [19] MO Lorenzo, S Haq, T Bertrams, P Murray, R Raval and CJ Baddeley; *J. Phys. Chem. B* **103** (1999) 10661
- [20] MA Keane and G Webb; *J. Mol. Catal.* **73** (1992) 91
- [21] <http://www.restekcorp.com/advntage/figa98-6.htm>
- [22] HJ Freund and MW Roberts; *Surf. Sci. Rep.* **25** (1996) 225
- [19] MO Lorenzo, S Haq, T Bertrams, P Murray, R Raval and CJ Baddeley; *J. Phys. Chem. B* **103** (1999) 10661

Chapter Six

A Medium Energy Ion Scattering Study of (R,R)-Tartaric Acid Modified Cu{110} Surfaces.

6.1 Medium Energy Ion Scattering

Medium energy ion scattering (MEIS) is a unique technique enabling the investigation of near surface composition and structure of a crystalline material by the use of an ion beam probe ^[1]. The ion beam consists of positively charged hydrogen or helium ions that are accelerated in the energy range of 50-500keV and the beam is focused onto the crystalline sample along a known crystallographic direction. The incident ion beam interacts strongly with the ion cores of the atoms in the surface and as a result the beam undergoes scattering ^[2]. The energy and angle of the scattered ions are analysed simultaneously using a high energy resolution electrostatic analyser that allows the discrimination of ions with subtle energy differences. This technique is also ideal for depth profiling with the ability to give a resolution of one atomic layer ^[1].

These properties come about because the ions can undergo elastic scattering with the surface layers and inelastic scattering with sub-surface layers. The energy of the elastically scattered ions from the surface region is highly dependent on the mass of the surface atoms and therefore indicative of the surface element. As an ion moves through the solid it loses energy at a rate proportional to the ion path length so detection of ions scattered from atoms deeper into the surface layers is also useful as an elemental depth profile ^{[1][3]}.

The most useful feature of the technique for the work in this chapter is the determination of surface structure. This occurs due to shadowing, blocking and channelling effects as the ion beam, with energies within this range effectively only interact with the nucleus and therefore the atoms behave as a periodic array of discrete point charges rather than close packed spheres.

When an incident ion beam is aligned along a low-index crystallographic direction on a single crystal surface only the atoms at the surface are visible to the ion beam. The target atoms subsequently cast a shadow cone over atoms deeper into the surface (figure 6.1a) whilst ions that undergo small angle collisions with surface atoms are deflected away from the atomic rows into the channels. These ions can travel deep into the solid without undergoing any collisions, known as channelling^{[1][3]}.

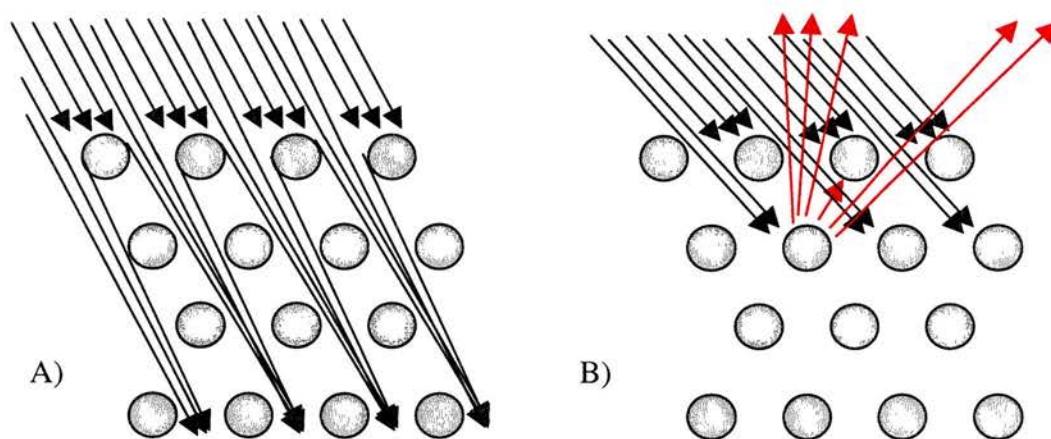


Figure 6.1. Illustration of a) shadowing and channelling and b) blocking effects on an fcc {110} surface along with $\langle 112 \rangle$ azimuth.

The shadow cone is a result of Coulombic interactions between the ion beam and the nucleus of the scattering atom. The size of the shadow cone is highly dependent on the

atomic number of both the incident and target atoms and the energy of the ion beam ^[1-2].

The radius of the shadow cone, r_s , is given by the expression ^[4]:

$$r_s = 2 \sqrt{\frac{z_1 z_2 e^2 d}{4 \pi \epsilon_0 E}}$$

where z_1 and z_2 are the atomic numbers of the incident and target atoms, d is the distance behind the target atom and E is the beam energy. ϵ_0 and e are both constant values of the vacuum permittivity and elementary charge respectively ^{[1-2][4]}.

The picture of shadowing in figure 6.1a, is only true of a sample at close to 0K. At the measurement temperature of 300K, perfect shadowing does not exist as atoms can spend a finite time outside the shadow cone ^[5] and cause the beam to be scattered from subsurface regions. This is due to three types of properties, two of which are directly related to the surface essentially being a defect.

Surface layer relaxation - The first to second layer spacing is contracted with respect to the bulk due to the surface layer having a deficient co-ordination number. This means that subsurface layers are subsequently exposed to the ion beam resulting in a contribution to the ion yield at the detector. This effect is present at 0K.

Lattice vibrations - Bulk atoms are not fixed in space but vibrate with an amplitude related to the bulk Debye temperature and the atoms can subsequently vibrate outside the shadow cone and contribute to the ion yield.

Enhanced surface vibrations - The surface atoms have enhanced vibrations with respect to the bulk increasing the effects of the two previous points.

A particularly important feature of MEIS is that of channelling. The incident ion beam encounters the first monolayer of atoms and undergoes small angle scattering to acquire the shadow cone flux distribution ^[6] causing non-backscattered ions to be deflected away from deeper lying atoms, into channels ^[7]. The important point is that many of these ions cannot get close enough to the atoms of the solid and undergo backscattering interactions. Subsequently they ‘bounce’ between the channels in an oscillatory manner and can penetrate micrometres into the bulk ^[6] until the ions are either scattered in some way or are neutralised and become buried within the bulk. Ions that are backscattered, and reach the detector do so having lost an amount of energy directly related to the distance the ion has travelled within the solid and yield information for the bulk structure. Without the channelling phenomena, bulk information would not be obtained and aligning the beam along a specific direction would be very difficult, if not impossible as only blocking features associated with scattering from the first few layers would be detected.

During data acquisition it is often desirable to obtain information of ions scattered from a particular number of surface layers. To reduce any unwanted contribution to the scattered signal from deeper lying layers and consequently increase the surface sensitivity, a ‘double alignment geometry’ is used whereby these unwanted scattered ions are blocked from reaching the detector by atoms closer to the surface. This is illustrated in figure 6.1B and if the detector is placed so that the exit blocking feature is in the middle of its angular range then only the first two surface layers are ‘visible’ to

the detector. The combination of the blocking and channelling provides a detailed picture of the surface atomic structure ^[1].

The effect of these two features can be manipulated and in favourable cases MEIS can achieve a depth resolution of one atomic layer. The entry and exit angles of the beam with respect to the surface and detector can be altered so one, two, three or more layers can be illuminated at any one time. An example of this idea is illustrated in figure 6.2, showing different illuminated layers for a fcc{110} surface along the $\langle 001 \rangle$ azimuth.

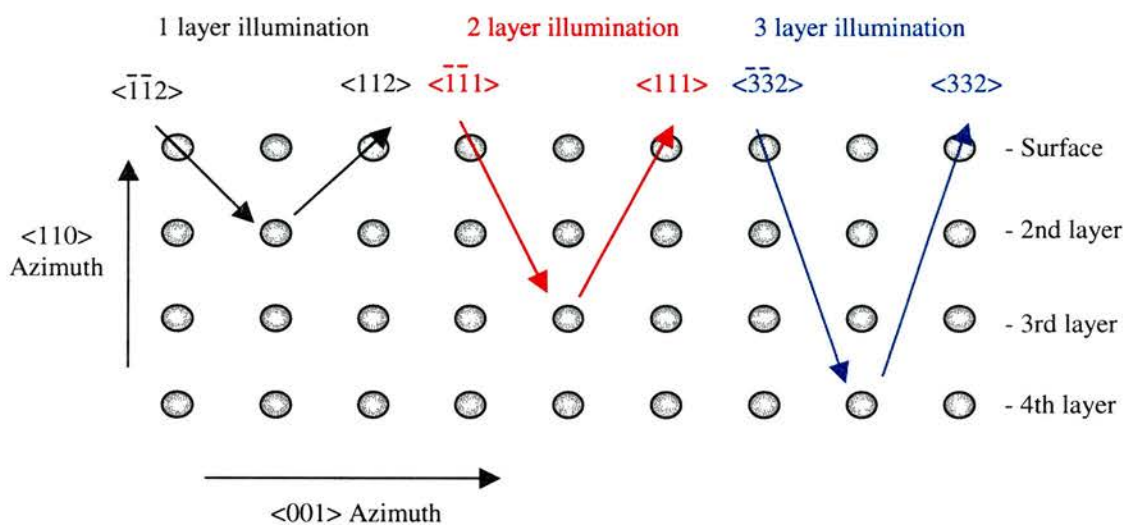


Figure 6.2. 2D Projection of 1,2 and 3 layer illumination for fcc{110} surfaces along the $\langle 001 \rangle$ azimuth.

In this example, if the beam is lined up along the $\langle -1-12 \rangle$ crystallographic direction and the detector set at an angle to monitor the $\langle 112 \rangle$ exit direction only the top layer is illuminated. Along this geometry, the beam is scattered by all surface layer atoms but the beam is blocked from the second, third etc. layer atoms by the surface layer atoms. If the in-going beam direction is $\langle -1-11 \rangle$ and exit direction $\langle 111 \rangle$ then only the top two layers are illuminated, and so on.

6.1.1 Ion Scattering

MEIS as a technique comes about because of two physical properties, elastic and inelastic scattering that occur when the ion beam collides with atoms at the surface ^[1].

6.1.1.1 Elastic Scattering

Firstly, consider an ion of mass M_1 moving with kinetic energy of E_0 that collides with an atom of mass M_2 , which is at rest. If an elastic collision occurs then the total energy and momentum must be conserved and therefore the ion of mass M_1 will be scattered over an angle θ ^[1].

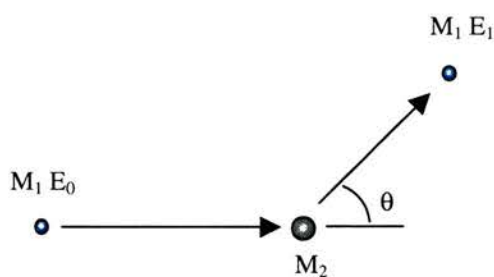


Figure 6.3. Scattering of an ion of mass M_1 travelling with a kinetic energy of E_0 by an atom of mass M_2 which is at rest.

The energy of the scattered ion is related to that of the incident ion by the kinematic factor k^2 , where

$$k^2_{M_1}(\theta) = E_1/E_0 \quad (1)$$

Considering the conservation of energy, the relationship between the scattered ion and scattering atom is given by:

$$E_0 = E_1 + E_2 \quad (2)$$

where E_2 is the energy of the recoiling target atom of mass M_2 ^[1].

Two equations can be derived to describe the conservation of momentum in the direction in which the ion has kinetic energy vectors,

$$(M_1 E_1)^{1/2} \sin \theta = (M_2 E_2)^{1/2} \cos \alpha \quad (3)$$

$$(M_1 E_0)^{1/2} = (M_1 E_1)^{1/2} \cos \theta + (M_2 E_2)^{1/2} \cos \alpha \quad (4)$$

where α is the angle of the recoiling target atom ^[1]. Combining and rearranging equations 2, 3 and 4, it can be determined that k^2 be given as:

$$k^2 = \left[\frac{(M_2^2 - M_1^2 \sin^2 \theta)^{1/2} + M_1 \cos \theta}{M_2 + M_1} \right]^2 \quad (5)$$

An important observation can be made from equation 5, the mass of the scattering atom determines the energy of the backscattered ion. If we assume a scattering angle of 90° then $\sin \theta$ becomes 1 and $\cos \theta$ is 0, therefore we can simplify equation 5 to give:

$$k_{M_2}^2(90^\circ) = \frac{(M_2 - M_1)}{(M_2 + M_1)} \quad (6)$$

The larger the value of M_2 , the mass of the scattering atom, the closer the solution to equation 6 is to 1 and it then follows by solving equation 1 that $E_0 \approx E_1$. Therefore, it can be seen that MEIS experiments are element specific ^[1].

The scattering cross-section or probability density that an ion is scattered over a certain scattering angle, is given by the equation:

$$\frac{d\sigma}{d\Omega} = F \left[\frac{z_1 z_2 e^2}{4 E \sin^2(\theta/2)} \right]^2 g(\theta, M_1, M_2) \quad (7)$$

Where z_1 and z_2 are the atomic numbers of the ion and atom, respectively. F is a screening factor emanating from the Molière approximation that takes into account the screening of the nucleus by the surrounding electrons, given by

$$F = 1 - \left[\frac{(0.0042 z_1 z_2)^{4/3}}{E} \right] \quad (8)$$

and g is given by

$$g(\theta, M_1, M_2) \approx 1 - 2 (M_1 / M_2)^2 \sin^4 \theta / 2 \quad \text{for } M_1 \ll M_2 \quad (9)$$

There are two interesting points about equation 7, firstly the cross-section is proportional to the square of the atomic numbers. This means that if the ion is changed from H^+ to He^+ there would be a fourfold increase in the scattering intensity. Secondly, the cross-section is highly dependent on the scattering angle, θ and proportional to $1/\sin^4(\theta/2)$. If the scattering angle is changed from $\theta = 180^\circ$ to $\theta = 90^\circ$ there is an accompanied fourfold increase in the scattering cross-section ^[1]. This suggests that it is advantageous to use smaller scattering angles but as mass separation is larger for larger scattering angles, it is important to think ahead and design the experiment beforehand in order to obtain the best scattering intensity over realistic scattering angles.

6.1.1.2 Inelastic Scattering

As the ion passes through into the surface it will experience small energy losses associated with the interaction of the ion and electrons in the surface atoms. The amount

of energy loss or stopping power is dependent on three factors, the ion species, its energy and the composition of the target ^[1].

The loss of energy per unit length as the ion moves through the solid is continuous but not linear. In the present studies, MEIS information of concern originates from the top 1-4 layers and the change in inelastic energy loss per unit length is so small that it is considered to be a constant value before the scattering event and another constant value after ^[1].

The inelastic energy loss normal to the surface can be illustrated in figure 6.4.

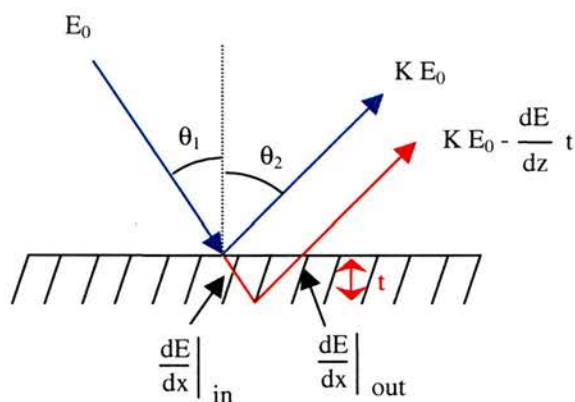


Figure 6.4. Incoming and outgoing path of an ion on a surface which is undergoing inelastic energy loss.

It can therefore be seen that the energy loss associated with interactions in the surface, i.e. the incoming and outgoing path, is given by the equation

$$\frac{dE}{dz} = \frac{K}{\cos \theta_1} \left(\frac{dE}{dx} \right)_{E_0} + \frac{1}{\cos \theta_2} \left(\frac{dE}{dx} \right)_{K E_0} \quad (10)$$

As previously stated, the value of energy loss per unit length is so small that a constant value can be assumed and therefore the energy loss of an ion scattered from depth t is given by:

$$E_{\text{loss}} = \frac{dE}{dz} t \quad (11)$$

It is this function that makes the technique suitable for depth profiling. This relationship also shows that the inelastic energy losses of the ion are also related to the atomic number of the scattering ion ^[1].

6.1.2 Facility Setup

The MEIS measurements were carried out at the MEIS facility at the CLRC laboratories, Daresbury. This consists of a duo-plasmatron ion source and accelerator with a high voltage supply delivering a beam of 100keV that is focused onto the sample sat inside the scattering chamber, inside the end station. The experimental end station includes four interconnecting UHV chambers, a scattering chamber, storage chamber, preparation chamber and load lock allow prepared samples to be transferred under UHV conditions ^[8].

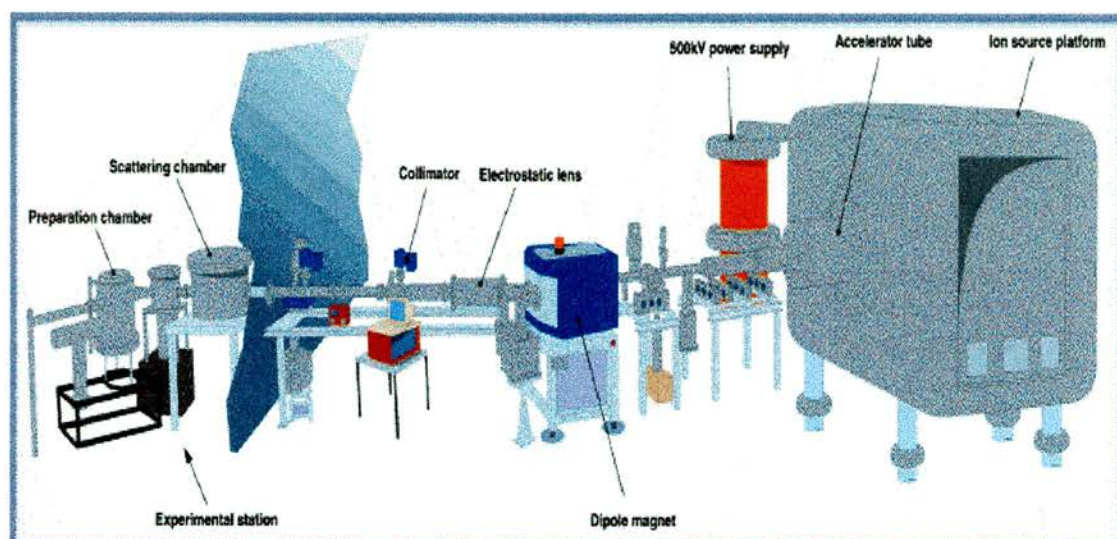


Figure 6.5. Illustration of the beamline, from the ion source to experimental end-station with its UHV setup ^[8].

The preparation chamber has facilities that include LEED, AES, argon sputter cleaning, evaporation sources and gas dosing for cleaning, dosing and characterisation of the surface ^[8]. The sample is loaded into the load lock chamber from where it can be transferred into the scattering chamber or preparation chamber via the storage chamber. The base pressure of each chamber was $\sim 1 \times 10^{-10}$ torr.

The scattering chamber houses the rotatable 2D toroidal electrostatic analyser (TEA) that detects ions over a range of $\sim 27^\circ$ and has an angular resolution of 0.3° ^[8]. Also located inside the scattering chamber is the sample goniometer, a high precision manipulator capable of lining up the sample with the beam by rotating, spinning and tilting the sample.

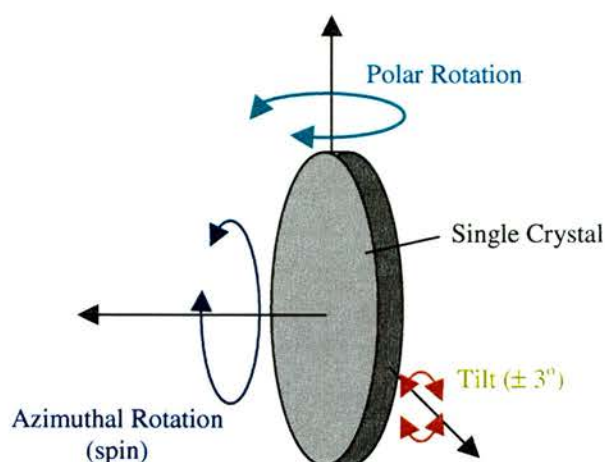


Figure 6.6. Depiction of the sample rotation, spin and tilt capabilities in the goniometer.

6.1.2.1 Sample Alignment and Data Collection

In this study, the crystallographic face of interest is that of an fcc {110} surface. Bulk alignment is begun by finding a large blocking channel such as the $\langle 10\bar{1} \rangle$ channel that is situated 60° from the surface normal along the $\langle \bar{1}12 \rangle$ azimuth, as illustrated in the stereographic projection in figure 6.7^[9].

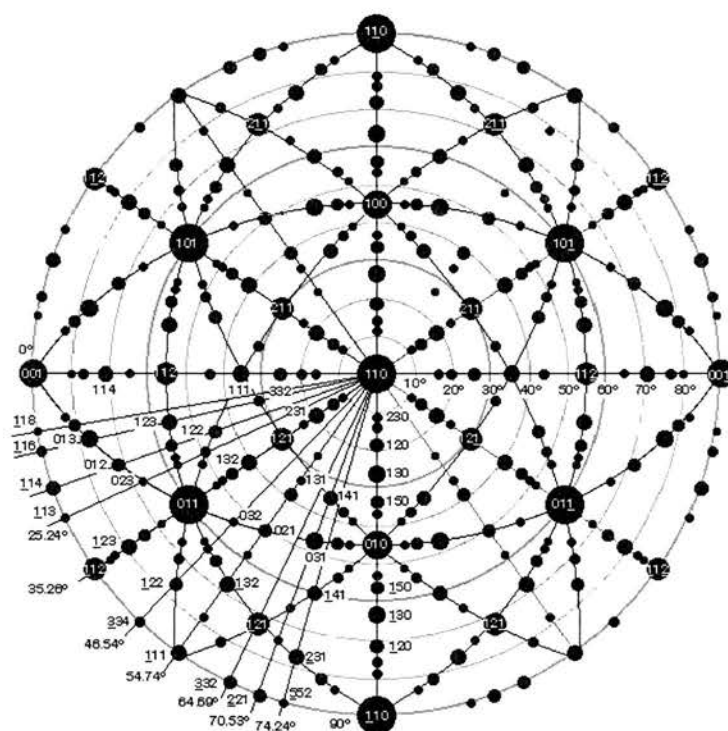


Figure 6.7. Stereographic projection of an fcc {110} surface pre-determined by P Bailey at Daresbury Laboratory^[9].

The size of the blocking channels represented in the stereographic projection are indicated by the size of the black circles. The alignment consists of a series of scans through each rotational axis of the goniometer in turn, to produce a plot of integrated counts as a function of angle. The appearance of a minimum in the scan therefore indicates the presence of the blocking feature and the angle corresponding to the bottom of the minimum is the point at which the centre of the blocking feature appears. These scans are repeated until the position of the blocking feature remains constant in each axis scan indicating that the beam is aligned correctly along the $\langle 10-1 \rangle$ incident direction. The stereographic projection can be used to assist alignment of the beam along certain crystallographic directions and with interpretation of data from the resultant data spectra.

Data is collected as a function of a pre-set integrated ion dose and ensures that all data sets are comparable. The data is obtained as a series of energy against scattering angle scans that can be tiled together to produce a full 2D profile of the surface and near surface regions.

The alignment and experimental data acquisition procedures are all controlled by a computer using the Multi Instance Data Acquisition System (MIDAS) computer software present on the computers in the end station.

6.1.3 Data Analysis

An example of the primary data that has been tiled together to give an energy v scattering angle tile, is illustrated in figure 6.8.

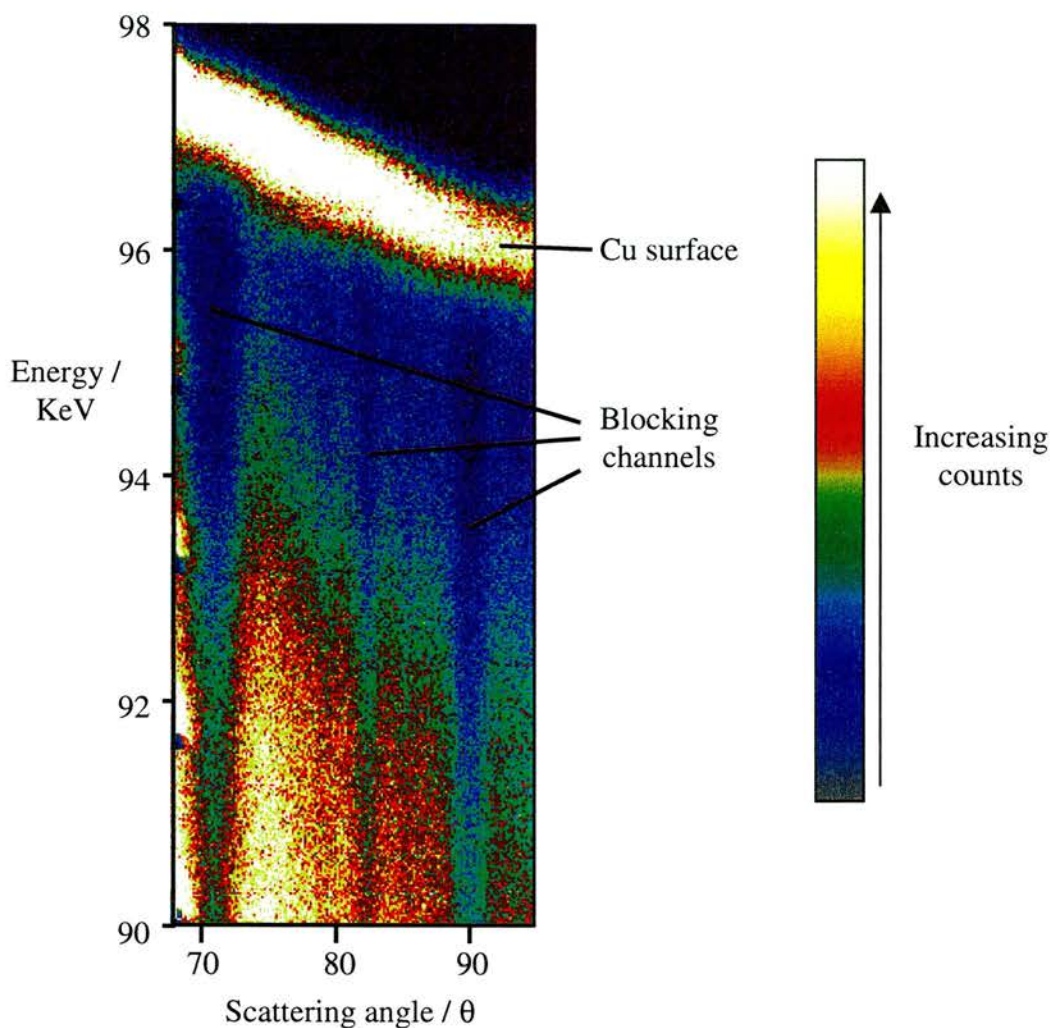


Figure 6.8. Energy v scattering angle, tiled data for a 1 layer geometry of a Cu{110} surface taken along the $\langle 001 \rangle$ azimuth. Lighter colours correspond to a larger number of scattered ions detected.

The tile in figure 6.8 illustrates a 1 layer illumination for a Cu{110} surface. The ion beam is aligned in the $\langle -1-12 \rangle$ direction situated 54.74° from the surface normal along the $\langle 001 \rangle$ azimuth, as illustrated in figure 6.2. The tile consists of a yellow/white band of decreasing intensity as a function of scattering angle arising from ions scattered by Cu atoms in the surface region. The sloping behaviour is rationalised by the kinematic factor, k^2 , that relates the energy dependency of the scattered ion with that of the scattering angle and is illustrated in equation 5^[10]. The intensity below the surface peak, with decreasing energy results from ions scattered from subsurface Cu atoms and

appears at lower energy as these ions have experienced inelastic energy losses as they move through the surface region.

There are at least three vertical channels of lower intensity in the subsurface region that represent scattered ions being blocked from reaching the detector by atoms closer to the surface. These channels appear at scattering angles of 70.53° , 81.95° and 90.00° corresponding to exit blocking directions in the 1, 3 and 2 layer geometries respectively.

Analysis of the tile is dependent on the type of information required, whether structural or elemental. Structural information is obtained by taking a cross-section of the surface and bulk regions and integrating the intensity within the cross-section to obtain a plot of scattering angle ν intensity. The cross-sections are obtained by superimposing calculated polygons onto the tile and projecting the intensity within the polygon onto a scattering angle ν intensity spectrum. The polygons used for this function are produced using a polygon creator in the Igor Pro software package by calculating the energy loss the ion beam experiences as it travels through 6 atomic layers. The corresponding polygon for the example in figure 6.8 is illustrated in figure 6.9.

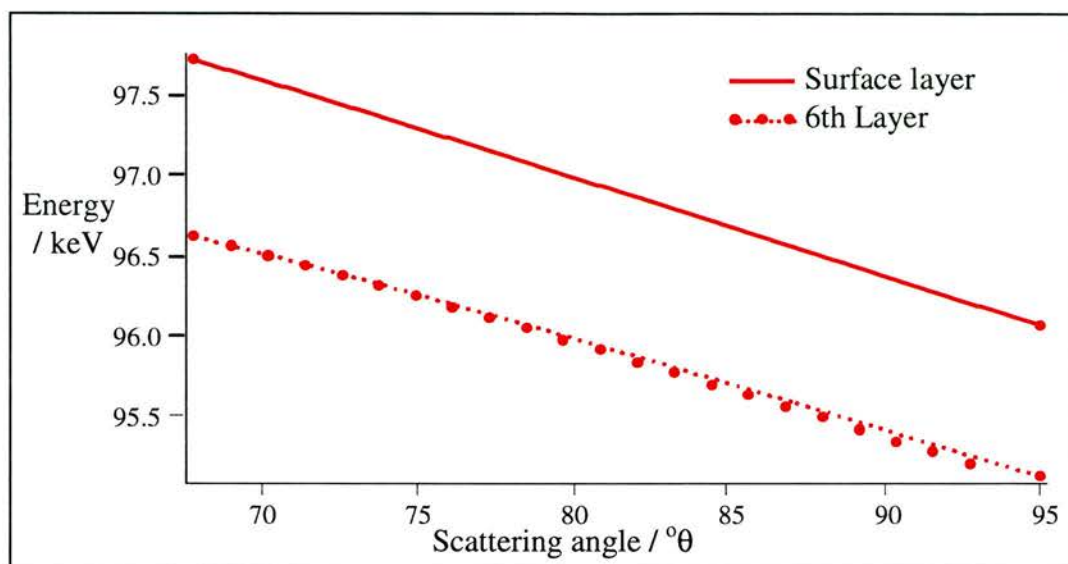


Figure 6.9. Calculated polygon representing the first 6 layers for the 1 layer illumination along the $\langle 001 \rangle$ azimuth of Cu{110}.

The calculation utilises the mass of the ion and target atom, the beam incident angle and the stopping power of the ion beam in the Cu surface using the SRIM code ^[2]. The obtained plots are corrected for the energy, angle dependency by applying a k^2 correction (equation 5). Such a plot of the surface and bulk projections for the data in figure 8 is illustrated in figure 6.10.

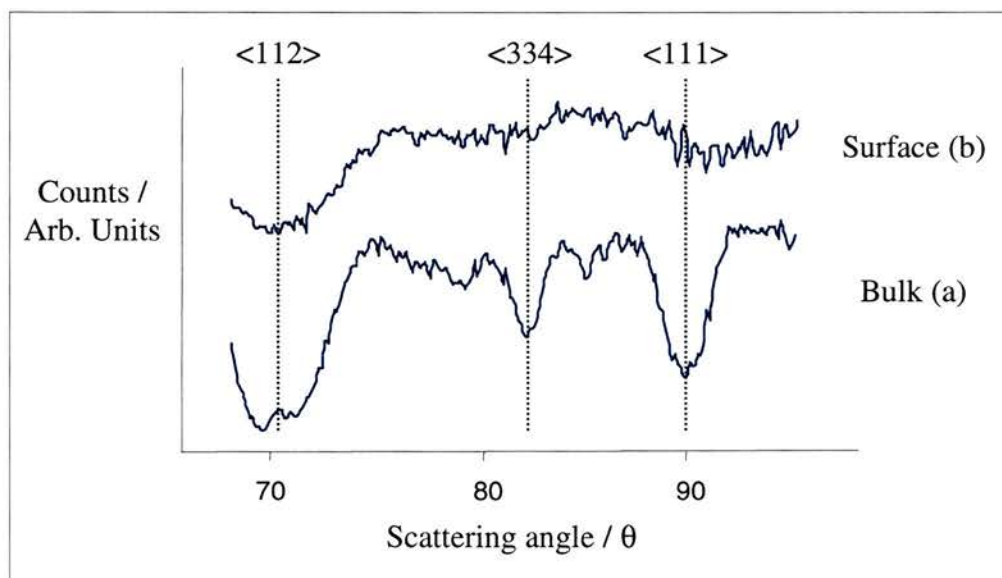


Figure 6.10. Scattering angle ν intensity plot contrasting the blocking features for cross-section taken through a) the bulk Cu and b) the surface Cu.

The plot in figure 6.10a, illustrates the position and size of the bulk blocking features and are used to confirm the correct alignment of the beam with the surface from the angles at which the blocking dips appear. The spectrum indicates the presence of the $\langle 112 \rangle$ blocking dip, corresponding to a 1 layer exit geometry at a scattering angle of 70.53° . A smaller feature at is also visible at 81.95° associated with a 3 layer exit geometry of the $\langle 334 \rangle$ blocking direction and a 2 layer exit geometry of the $\langle 111 \rangle$ blocking feature at 90.00° . Comparison of the bulk features with that of the surface, in figure 6.10b also show the presence of the 1 layer blocking feature at 70.53° and a very small dip corresponding to the 2 layer blocking channel at 90.00° . There is no obvious shift in angle of any of the surface blocking features compared to that in the bulk indicating that the surface does not appear to have been reconstructed. Also, the lack of extra features in the surface spectrum compared to those present in the bulk indicates that the surface layer is essentially unchanged.

The blocking features for a variety of surfaces can be obtained and comparison can yield interesting information. For example, a reconstruction of the surface Cu atoms may alter the positions of the blocking features or change their shape. This idea is illustrated in figure 6.11.

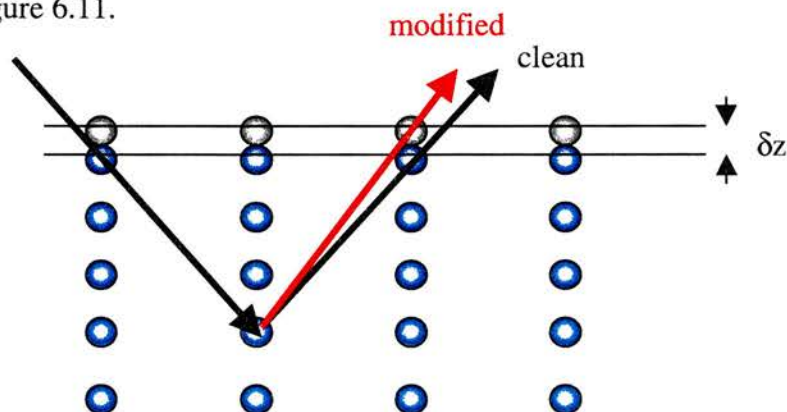


Figure 6.11. Illustration of the idea behind the effect of reconstruction of surface Cu atoms.

On the clean Cu surface, the double alignment geometry ensures that the position of the surface atoms can easily be determined using MEIS. If modification of surface Cu atoms occurs perhaps resulting in a shifting of these atoms or possibly the addition of adatoms, it would be expected that even for small values of δz the scattering angle of the blocking feature would alter noticeably (figure 6.11). There are several types of effect that should be discernible with this technique. If there is any alteration of the surface relaxation then this would result in a change in the surface blocking peak positions. If Cu adatoms are fixed in position due to the chiral adlayer the blocking patterns in the mirror equivalent direction should be different. If there is a real reconstruction of the top layer, this should be obvious in MEIS and should result in a change in the number of visible surface atoms. Therefore comparison of the clean and modified surfaces may yield important information concerning the structure of the metal surface. However observations of this type are dependent on several factors such as the proportion of surface atoms involved in the reconstruction, the sites that the reconstructed atoms occupy, the azimuth that the beam is aligned along and the number of layers illuminated.

A qualitative and quantitative elemental analysis can also be performed by analysis of the tiled spectrum in figure 6.8, using a similar methodology as that used in structural analysis. Blocking channels are regions of low scattered ion intensity and therefore by summing the ion intensity over a narrow angular range at the base of the blocking feature a plot of intensity v energy can be obtained ^[11]. This essentially consists of the number of ions scattered from Cu atoms in their respective layer as the number of ions present in the plot is dependent on the number of atoms that the ions have been

scattered from. Therefore it is possible to obtain a relative value for the number of atoms present in a required layer illumination. As the energy of the scattered ions is dependent on the atomic number of the scattering atoms, this technique can be used as a qualitative and quantitative analytical tool.

An example of the elemental analysis is illustrated in figure 6.12, a cross section for the 1 layer illumination taken down the centre of the 70.53° blocking feature in figure 6.8.

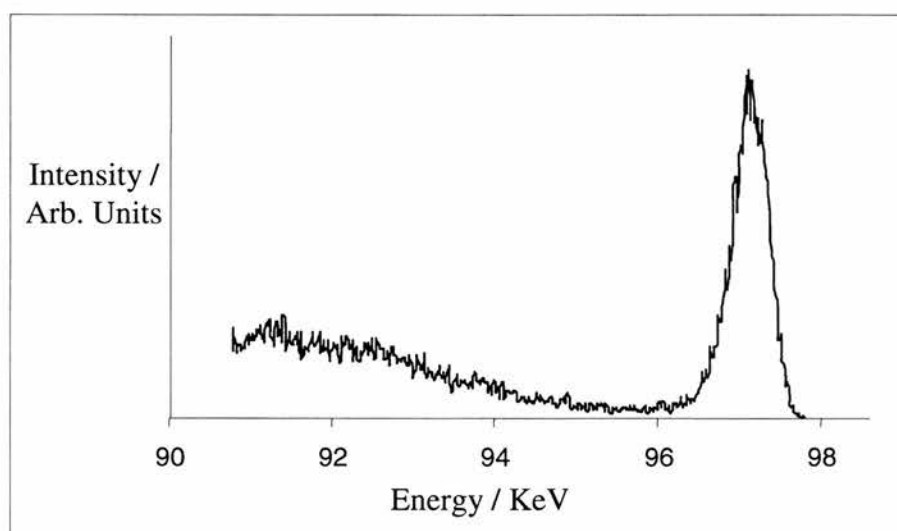


Figure 6.12. Intensity v energy plot of a 1 layered geometry for a Cu{110} surface.

The large peak with a maximum at ~ 97 KeV is due to ions scattered from Cu atoms in the surface region. The intensity at lower ion energy arise from ions scattered from sub-surface regions of the Cu{110} surface.

To allow comparison between data sets it is necessary to normalise the data due to the dependency of z^2 (the square of the atomic number), $\sin^4\theta/2$ (the θ dependence of the cross-section) and $\cos\phi$ (where ϕ is the angle between the beam and surface normal - known as the footprint correction) ^[4]. This enables a direct comparison between the

intensity of the Cu peak and the number of Cu atoms illuminated in each experimental geometry. This technique is therefore ideal for observing effects such as adsorbate induced segregation or adsorbate induced chiral faceting on metal surfaces.

6.1.3.1 VEGAS – Monte Carlo Simulations

It is possible to simulate experimental data by computer calculations, the probability densities that ions will be backscattered to the detector ^[1] using the Sincalc Xvegas MEIS simulation software. The software allows the construction of a crystal with an assumed surface geometry and by averaging over a large number of incident ions to determine a calculated surface blocking minimum over a range of scattering angles ^[1]. This is accomplished by calculating complicated expressions for the number of atoms per visible layer to the ion beam and detector and results in quantitative information that is directly comparable to the experimental data ^{[1][10]}. The code takes into account the crystal structure, the atomic number of the scattering atoms, lattice and surface vibration parameters, amongst others. The VEGAS model allows for the enhanced isotropic vibration of the surface atoms whilst sub-surface atoms vibrate with their characteristic bulk Debye temperature ^[4].

However, the computer simulation assumes the surface vibrations are isotropic, i.e. surface vibrations perpendicular to the surface are the same as those in the plane and this is not the case. Although lateral vibrations for surface atoms are enhanced, the largest enhancement is perpendicular to the surface resulting in an increase in the number of illuminated layers, an effect more prominent at more grazing incident directions ^[4].

6.2 Introduction

It has long been suggested that the effect of acid modification may play a central role in the definition of enantioselective sites in the hydrogenation of MAA over chirally modified supported Ni catalysts^[12-14]. In the heterogeneous catalytic system it has been proposed that metal atoms are leached from metal particles and these may form adsorbed complexes that are involved in the catalytically active sites. Adsorption of carboxylic acids on Cu{110} are known to cause substantial reconstruction of the Cu surface^[15]. Therefore, does UHV adsorption of R,R-H₂TA (or S,S-H₂TA) on Cu{110} cause restructuring of metal atoms and subsequently are these experiments investigating the initial stage of corrosion.

The adsorption of R,R-H₂TA on Cu{110} has been studied extensively by Lorenzo *et al*^[16]. The observation of an ordered overlayer with a (90 12) unit cell after the adsorption of R,R-H₂TA (figure 6.13) is contrasted to the formation of a mirror image overlayer with a (90 -12) unit cell when S,S-H₂TA is adsorbed.

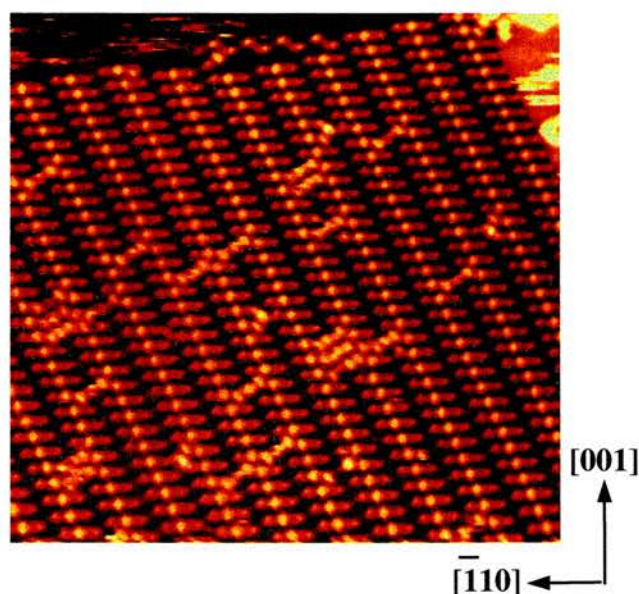


Figure 6.13. STM image (200Å x 200Å) of the (90 12) ordered array after depositing R,R-H₂TA on Cu{110} at 373K^[16].

A major point of debate regarding the adsorption of R,R-H₂TA (and S,S-H₂TA) on Cu{110} is whether the features observed in the STM are simply adsorbed tartrate species or is Cu included in the overlayer structure, possibly in the form of copper tartrate. It is not apparent from the STM data, which of the cases is correct, as it is difficult without a detailed theoretical calculation to unequivocally interpret the STM data. If Cu adatoms are included in the overlayer structure, what is the structure of the overlayer? Such effects have been observed by Chen *et al* ^[17] in which adsorption of p-aminobenzoic acid on Cu{110} causes a significant amount of mass transport modifying the morphology of the atomically flat surface into highly faceted domains. A second point of debate also relating to the STM image is why does the centre feature of the trio appear brighter than that of the outer pair? Lorenzo *et al* ^[16] have stated in their discussion concerning this surface that the carboxylate groups have a strong preference for bridged sites in the close packed rows and the body of the TA subsequently straddles the Cu row, illustrated in figure 6.14.

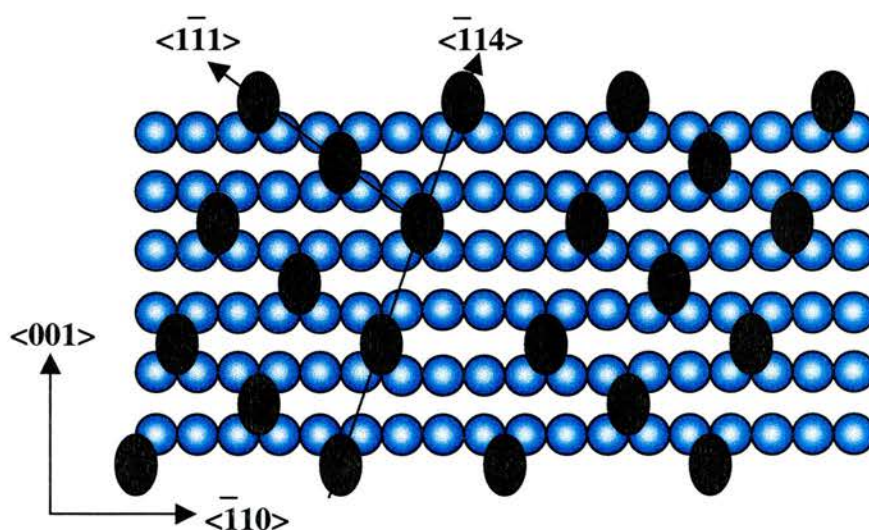


Figure 6.14. Illustration of the molecular direction in the chiral R,R-TA covered Cu(110) ^[16].

The model proposed relies on the three features in the STM images being in equivalent adsorption sites and it therefore seems doubtful that this model is 100% correct. A possible interpretation of this difference is that the centre features are not in equivalent sites to the two outer features. Simple trigonometry confirms that the $\langle -114 \rangle$ direction is 19.47° from the $\langle 001 \rangle$ direction, as suggested in the model and also that the groups of three features appear along the $\langle 1-11 \rangle$ direction, at an angle of 74.21° from the $\langle -114 \rangle$ directions. This angle, measured from the STM image is approximately 67° suggesting that the units of three atoms may not be aligned along the $\langle 1-11 \rangle$ direction however this difference can be accounted for by distortion of the image due to thermal drift.

We propose an alternative model that may explain these angles more thoroughly and this is illustrated in figure 6.15.

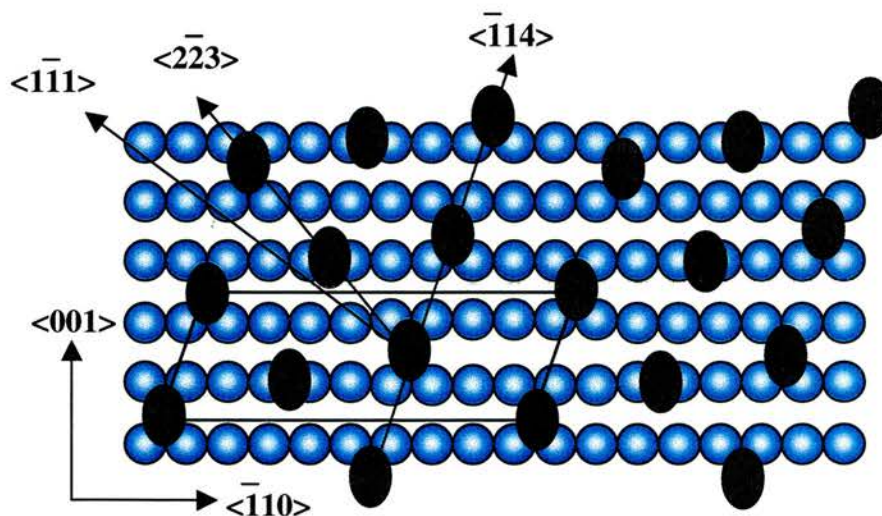


Figure 6.15. Illustration of an alternative model to describe the (90 12) overlayer structure.

In this model, the rows of atoms are again aligned along the $\langle -114 \rangle$ direction, however the units of three are now aligned along the $\langle 2-23 \rangle$ direction with an angle of 62.78° from the $\langle -114 \rangle$ direction, an angle closer to that observed in the STM image. Whilst

this model is speculative, it does appear to agree with the STM image and demonstrates a reason for the observed brighter centre feature that, in this model is a two fold bridge site. The unit cell for this model is still (90 12) and the outer two features remain in bridge sites straddling the $\langle 001 \rangle$ Cu row, both proposed in Lorenzo's ^{[16][18-19]} original model. However one of the terminal features now sits in the next equivalent site further along the $\langle 001 \rangle$ direction. The central feature therefore sits in a site further elevated from the surface compared to the outer two. If the STM image is reflecting the presence of Cu adatoms, our model places the Cu adatoms in 4-fold and 2-fold sites, similar to those proposed by Chen *et al* ^[20] for benzoic acid on Cu{110}.

The third point, in contrast to Lorenzo's model, concerns the size of the bare Cu channel in that the distance between the rows of three molecules appears much smaller in the STM image than the corresponding distance in the model proposed by Lorenzo.

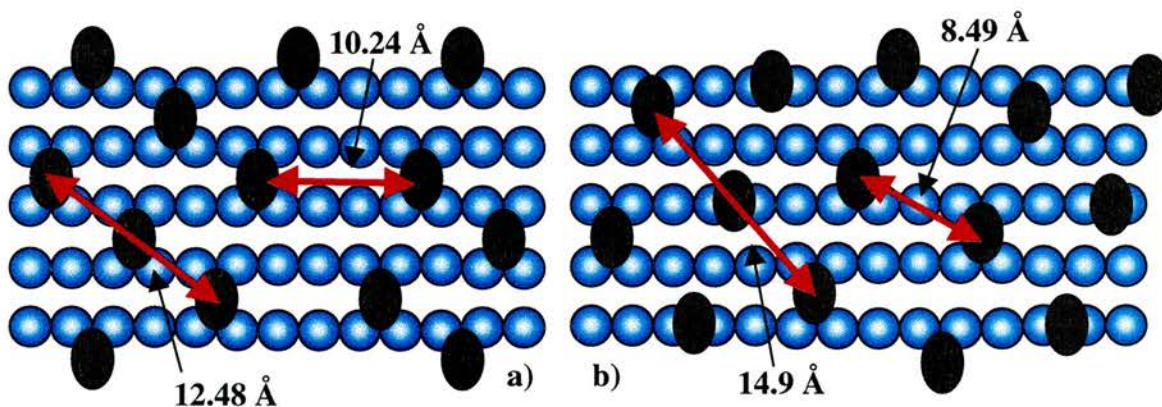


Figure 6.16. Illustration of the differences in dimensions in Lorenzo's model, a) and our alternative model, b) for the R,R-TA chiral Cu{110}.

Using this model the distance across the bare Cu channels between the nearest groups of three features is 10.24Å, as illustrated in figure 16a. This distance is ~82% of the distance across the units of three features. Comparing visually this distance with that in the STM image, it appears as though the bare Cu channels in the STM image are much

smaller and the overlayer structure much closer packed than that presented in the model. The distance across the bare Cu channel in the alternative model (figure 6.16b) is calculated as 8.49Å, whilst the distance across the units of three is 14.9Å making the gap about 57% of the distance across the units of three. This distance appears to be in better agreement with the STM images. Lorenzo's model relies on the molecules being stabilised by a hydrogen bonding network, along the <-114> direction. However, this distance is at least 4Å and it is very unlikely that a hydrogen bond will extend much more than 3Å and therefore it appears doubtful that if these features are molecules, then there is any sort of lateral stabilising hydrogen bond. This therefore provokes the question of why do the molecules align as they do and in particular is Cu involved in the structure?

Adsorption of benzoic acid on Cu{111}, as discussed in chapter 1 has been shown to adopt an upright species for all coverages whilst adsorption on Cu{110} show a coverage dependent orientation ^[21-22]. The reason given for this difference has been attributed to the higher equilibrium concentration of metal adatoms present on the {110} surface with the benzoate species 'soaking up' metal adatoms forming copper benzoate. In the catalytic system, modification of the metal catalyst is known to corrode the surface and leach metal atoms into the modification solution. This corrosive chemisorption effect of the modification procedure infers that there may be a greater number of metal adatoms present on the modified surface. If the observed STM features are those of metal atoms then perhaps the adatoms are 'pinned' into position by some sort of template, perhaps a copper tartrate type species.

Assuming the STM features are related to Cu atoms/ions and using the alternative model, the central 2-fold bridge site would sit $\sim 0.93\text{\AA}$ higher than the outside pair. The corresponding distance between the centre and outside spots in this new model is 7.51\AA .

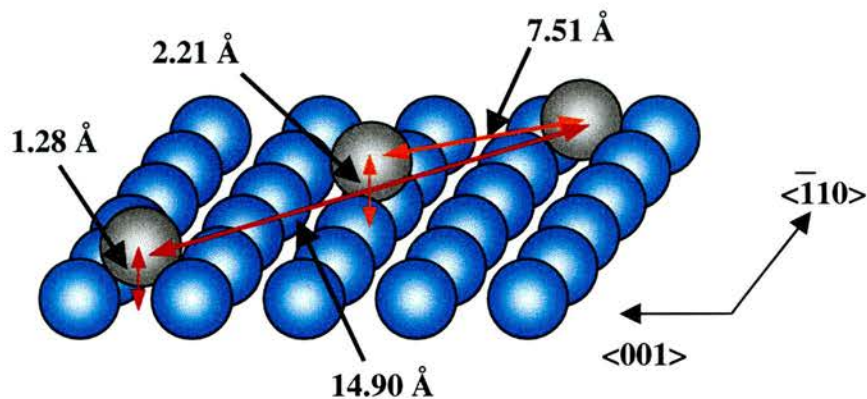


Figure 6.17. Illustration of the dimensions along the unit of three Cu atoms.

Literature values of the Cu-Cu spacing determined from the crystal structure of copper S,S-tartrate is stated as 7.875\AA in which the Cu ions are connected by tartrate dimers [23]. This distance, perhaps coincidentally, is very similar to the distance between the two adjacent features in the alternative model. This distance is much longer than that calculated for Lorenzo's model, however, it is believed that the distance across the three features in the original STM image is actually closer to 15\AA than 12.48\AA [24].

It is difficult to determine if this alternative model is correct without repeating the STM studies. It therefore becomes very important to determine if the observed STM features are those of the R,R-H₂TA or metal atoms. A model that successfully explains the observations is likely to be the crucial factor in the understanding the formation of this chiral overlayer and perhaps the enantioselective sites themselves.

To our knowledge, the MEIS technique has never been used before to study this type of effect but it is ideally suited as the technique is very sensitive to the position of surface Cu atoms in mirror image azimuthal directions. If the features observed in the STM are those of Cu atoms or ions then there are two possible types of effects that may occur, both being potentially observable using MEIS. The first is if the adatoms are included in the adlayer then one would expect that additional blocking features may be observed or a change in the intensity of features with respect to those observed from the clean surface. The second effect is if the surface Cu atoms are reconstructed then it might be expected to observe extra features or features shifting slightly from the angle that they are observed at in the clean surface blocking spectra. The position of surface blocking dips provide a sensitive measure of surface atom displacements and a shift in the position of a blocking dip away from the bulk crystal blocking direction is a direct indicator of layer relaxation or reconstruction ^[7]. Therefore, any changes observed in the blocking spectra, once confirming the beam is aligned correctly, have almost certainly arisen due to the effects of Cu rather than the adsorbate because of the weak scattering effects of C, H and O. Analysing and comparing specific directions in the clean surface with that of the modified surfaces possessing the (90 12) and (90 -12) unit cell structure, may yield effects of possible Cu rearrangement.

6.3 Experimental

The Cu{110} single crystal was mounted onto its holder, which had capabilities for electron beam heating and transferred into the load lock chamber where it was pumped down using a turbomolecular pump, transferred into the storage chamber and the sample and holder outgassed at ~700K for about half an hour.

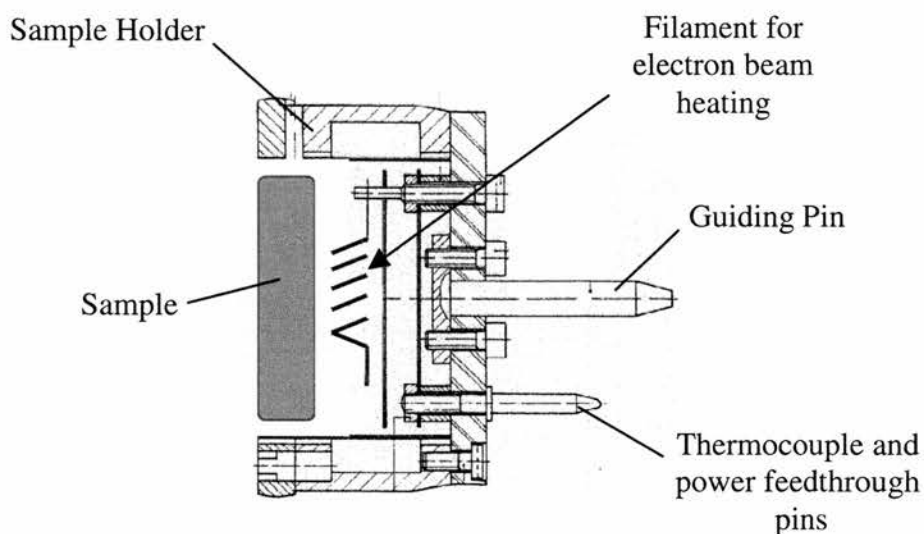


Figure 6.18. Diagram of the sample holder used in the MEIS experiments ^[25].

The sample sits into the holder and is secured by three metal clips. The holder is inserted into the goniometer via the use of transfer arms into a specific orientation that is directed by the guiding pin and ensures the thermocouple and power feedthroughs connect with their respective contacts. After the sample was transferring into the preparation chamber and the Cu{110} cleaned by cycles of Ar⁺ ion sputtering with a beam energy of 0.5keV and annealing to ~700K. The cleanliness was determined by the lack of impurity peaks in AES and by a (1x1) LEED pattern.

The prepared surfaces consisted on the (90 12) and (90 -12) overlayer unit cell for dosing of R,R-H₂TA and S,S-H₂TA respectively. The R,R-H₂TA and S,S-H₂TA sources were outgassed at 373K for 30 minutes prior to dosing whilst the surface was dosed at 373K with a source temperature of 420K. The prepared surface structures were verified using LEED to ensure the correct diffraction pattern was obtained then the sample was transferred into the scattering chamber where it was allowed to cool to room

temperature before beginning data collection. An ion beam consisting of 100KeV, H⁺ or He⁺ ions were focused onto the sample in all experiments.

The choice of azimuth that the beam is aligned along and the number of layers illuminated may have an important effect on the quality of the data produced. This specific type of experiment is very problematic mainly because any changes between the spectra are likely to be small and therefore it is important that the beam is aligned correctly. The MEIS technique is very sensitive to the position of Cu atoms but relatively insensitive to the presence of C, H and O atoms. Therefore if the features observed in the STM are not those of Cu atoms but tartrate species then the resulting spectra are unlikely to provide any helpful information to elucidate the fate of the corroded Cu atoms. The azimuths were chosen, firstly so that a structural study of the surface layers could be undertaken to observe how the surface layers behaved when R,R-H₂TA and S,S-H₂TA are adsorbed onto the Cu{110}. The results from the surface layers can then be compared with those in the bulk. Also, to understand the possible role of corrosive chemisorption a relative amount of the amount of copper in the surface layers can also be sort.

The directions that were analysed are illustrated in figure 6.19, for R,R-H₂TA on Cu{110} using the two models discussed in this chapter.

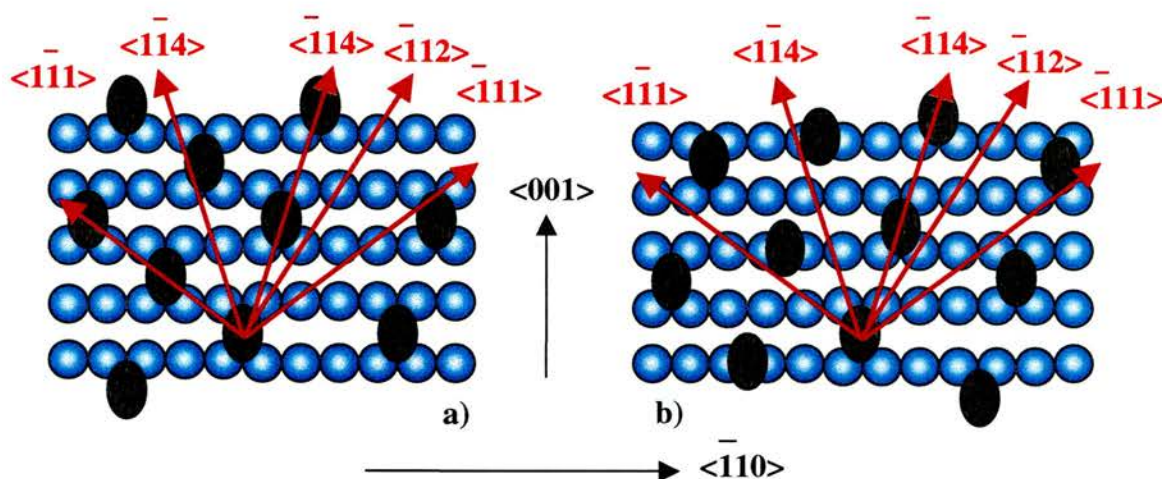


Figure 6.19. Illustration of the azimuth scan directions employed in this MEIS study for a) Lorenzo's model and b) our alternative model.

It is possible to see for both models that when R,R-H₂TA is adsorbed and the beam aligned along the $\bar{114}$ direction, ions that are scattered from subsurface regions and detected may have been blocked by the 'extra' surface atoms. When the beam is aligned along the same incident geometry, in the mirror equivalent $\langle 114 \rangle$ direction, the blocking spectrum of ions scattered should show changes that differ from those of the $\bar{114}$ direction because there is a small proportion surface blocking atoms. This is the principle behind these experiments and any effects that are observed should therefore be reversed when adsorbing S,S-H₂TA.

Another important direction in the model proposed by Lorenzo *et al* ^[16] is that of the $\langle 111 \rangle$ direction because the groups of three features also aligned along this direction. Therefore, comparison of this direction with that of the mirror equivalent $\bar{111}$ direction again should result in slight changes in the obtained blocking spectra. Ideally, aligning the beam along the $\langle 223 \rangle$ and its mirror equivalent direction and obtaining the blocking spectra would be sort but these azimuth directions lie $\pm 43.31^\circ$ from the $\langle 001 \rangle$ azimuth and relating this angle to the fcc{110} stereographic projection in figure 6.7, it

can be seen that there are no blocking features along this direction and therefore it is not possible to reproducibly align the beam.

The $\langle -112 \rangle$ direction has been chosen as there are large 1 layer entry and exit blocking channels that enable a double alignment geometry to be achieved. This allows a value for the proportion of Cu atoms present to be obtained and comparison with that of the clean surface may indicate whether extra Cu atoms are visible to the beam after the surface has been modified. Subsequently this may result in a possible indication of leaching of metal atoms or a reconstruction involving metal atoms.

A summary of the experimental set-up is illustrated in table 6.1.

Azimuth	Entry direction	Beam angle (w.r.t. surface normal)	Entry layer illumination
$\langle -112 \rangle$	$\langle -101 \rangle$	60°	1
$\langle -114 \rangle$	$\langle -2-12 \rangle$	45°	3
$\langle 1-14 \rangle$	$\langle -1-22 \rangle$	45°	3
$\langle 1-11 \rangle$	$\langle 0-21 \rangle$	50.77°	2
$\langle -111 \rangle$	$\langle -201 \rangle$	50.77°	2

Table 6.1. Summary of beam alignment positions.

6.3.1 VEGAS Simulations

Computer simulations based on the VEGAS code consist of two input sections, those of the beam and crystal parameters.

The crystal parameter requires the input of the atom positions. This usually takes the form of the smallest repeating unit cell from which the crystal can be ‘grown’ to the

desired depth. This task is trivial for an unreconstructed fcc{110} in which the unit cell consists of only two atoms, one from the surface layer and another from the second layer, from which all other atom positions can be obtained. However, the (90 12) and (90 -12) overlayer unit cell structures contain 18 surface layer Cu atoms and the sides of the unit cell are not perpendicular to one another. This causes problems with the crystal input parameters as the VEGAS software require the unit cell to be of a regular square or rectangle shape. The unit cell that fulfils this requirement for the (90 12) surface consists of 162 surface Cu atoms and corresponds to an 18 x 9 surface Cu lattice, illustrated by the black grid in figure 6.18. The x and y directions in the unit cell correspond to the $\langle 001 \rangle$ and $\langle -110 \rangle$ azimuths respectively and the points where the vertical and horizontal line cross are where surface Cu atoms exist.

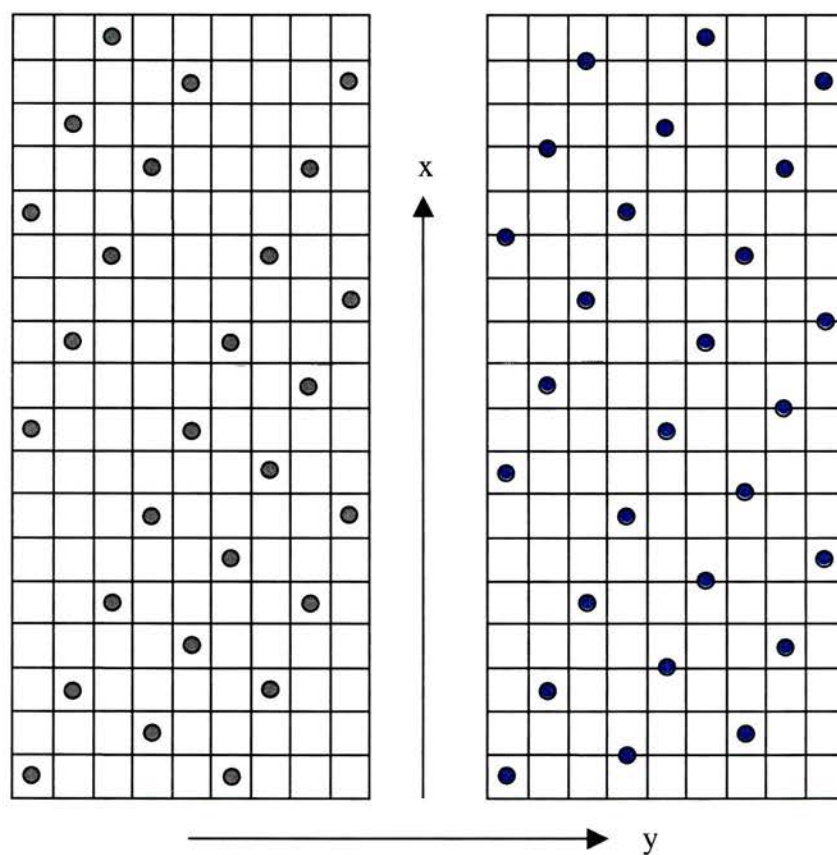


Figure 6.20. Models that describe the VEGAS input parameters for, a) crystal structure based on Lorenzo's model except consisting of Cu atoms and b) our alternative model.

The crystal was then grown in the z direction (into the plane of the page) corresponding to a depth of 6 layers. Once the crystal has been formed, it is a simple case of adding individual atoms into their respective positions above the surface layer. The grey and blue atoms indicate the position of Cu adatoms for the model based on Lorenzo's original model except consisting of Cu atoms and our alternative model respectively.

The beam parameters are subsequently added so that the beam is aligned along the required azimuth, at the specific entry direction with respect to the surface normal and blocking data simulated between the required scattering angles.

The clean surface is also simulated for comparison by removing the adatoms from the surface layer. It should be noted that in none of the simulated data was the surface layer relaxed and therefore the presented surface simulations for the clean surface are for comparison between the obtained blocking features and not an indication of their exact position.

On first inspection of the simulated surface blocking spectra along the $\langle -114 \rangle$ and $\langle 1-14 \rangle$ azimuths, all the spectra look identical, as illustrated in figures 6.21 and 6.22.

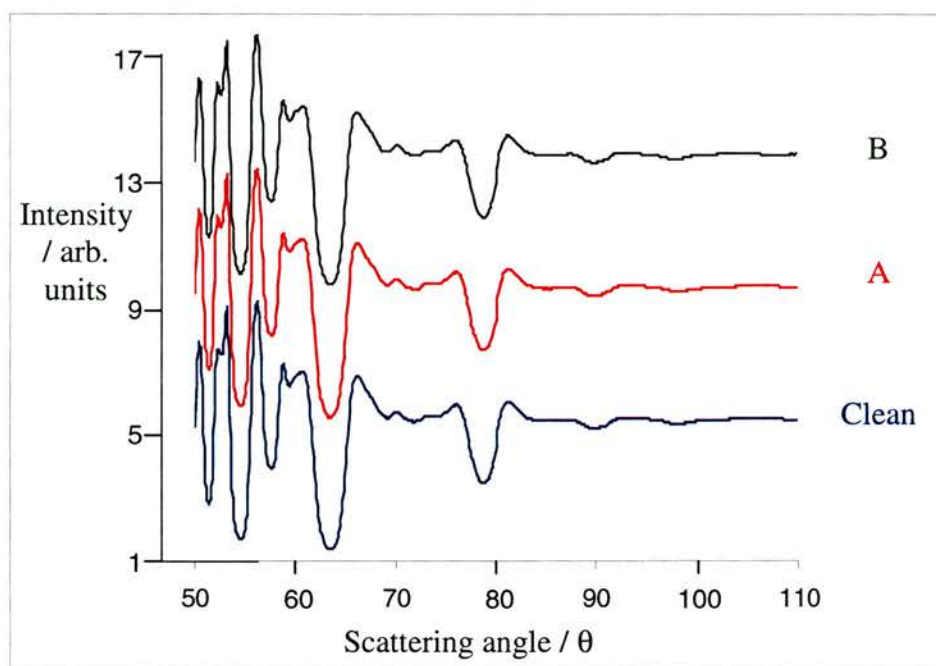


Figure 6.21. Simulated surface spectra along the $\langle -114 \rangle$ azimuthal direction comparing the clean surface, the model based on Lorenzo's structure, A and our alternative model, B.

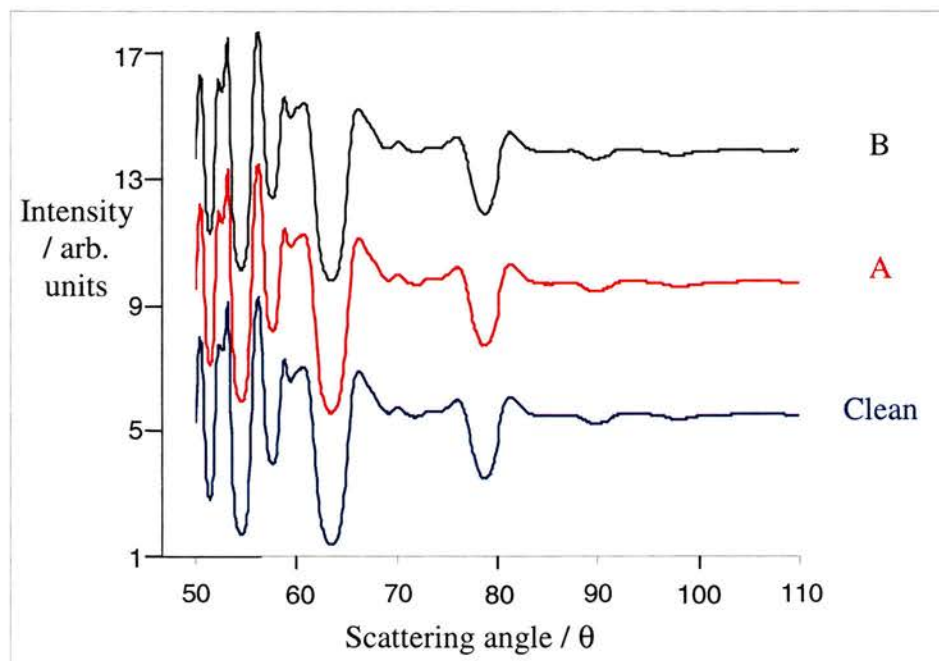


Figure 6.22. Simulated surface spectra along the $\langle 1-14 \rangle$ azimuthal direction comparing the clean surface, the model based on Lorenzo's structure, A and our alternative model, B.

However, upon subtraction of the blocking spectra for the $\langle 1-14 \rangle$ azimuth from the $\langle -114 \rangle$ azimuth for the clean surface and the two adatoms models, subtle differences in the blocking spectra did exist and are illustrated in figure 6.23.

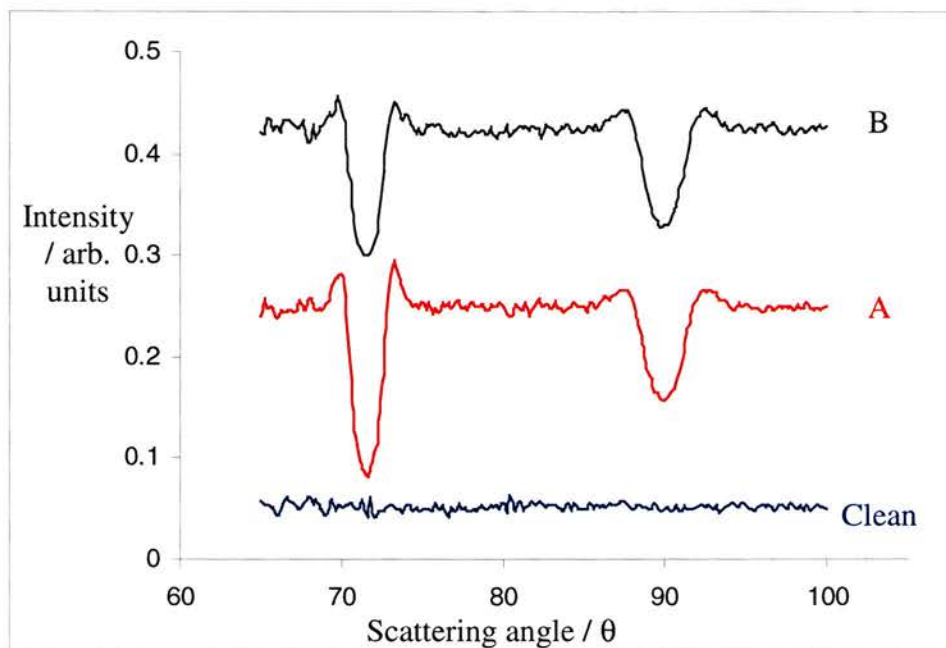


Figure 6.23. Graph of the difference in simulated surface spectra between the $\langle -114 \rangle$ and $\langle 1-14 \rangle$ azimuthal directions comparing the clean surface, the model based on Lorenzo's structure, A and our alternative model, B.

This suggests that if the features observed in the STM image are those of Cu adatoms then there should be a detectable difference in the intensity of the blocking channels at 71.57° and 90.00° between mirror equivalent azimuthal directions. However, there do not appear to be any additional blocking features in either of the adatom models.

It is also important to determine any differences between the clean blocking spectra and those of the two adatom models for both of the azimuthal directions. This was accomplished by subtracting the simulated blocking spectra for the two adatom models

from the clean blocking spectra. The differences in the $\langle -114 \rangle$ azimuth are illustrated in figure 6.24.

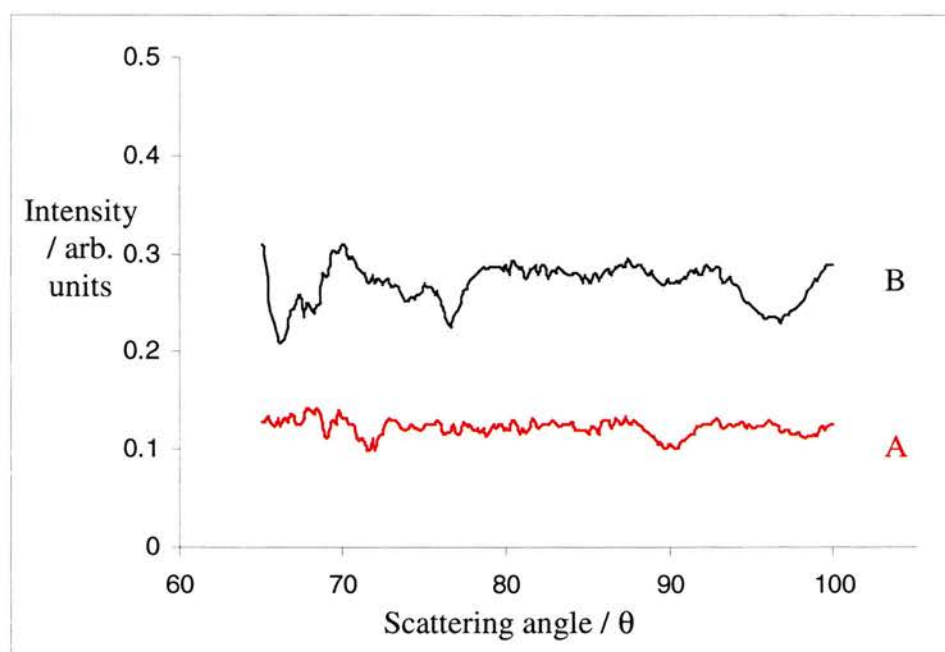


Figure 6.24. Subtracted surface blocking spectra along the $\langle -114 \rangle$ azimuth comparing the difference in the clean surface to the models based on Lorenzo's structure, A and our alternative model, B.

The subtracted blocking spectra show that there are also small differences between the data collected along the same azimuth. Whilst these changes are smaller than the spectra subtracted from the mirror equivalent azimuths in figure 6.21, it is still possible to see that there are changes in the blocking spectra and if these effects occurred on the metal surface it should be possible to observe them.

Comparison of the difference between the two adatoms models and the clean surface along the $\langle -114 \rangle$ azimuth are illustrated in figure 6.25.

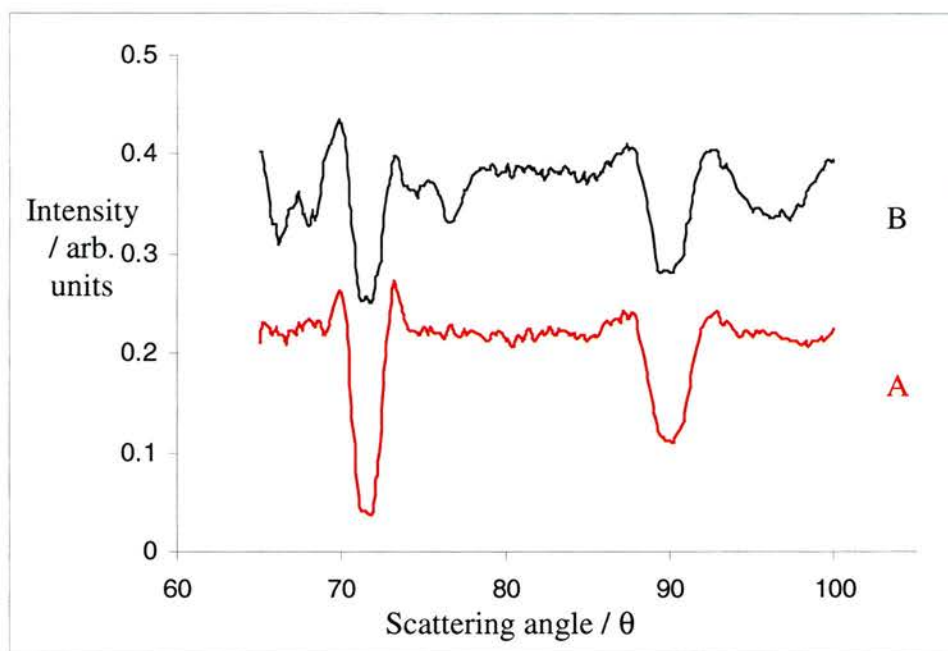


Figure 6.25. Subtracted surface blocking spectra along the $\langle 1-14 \rangle$ azimuth comparing the difference in the clean surface to the models based on Lorenzo's structure, A and our alternative model, B.

Figure 6.25 clearly indicates that the changes in blocking spectra are most prominent along the $\langle 1-14 \rangle$ azimuth. This effect is opposite to what one would expect as the $\langle 1-14 \rangle$ azimuthal direction is not the direction that the features in the STM images appear to align along. However, whilst this result was not expected it still confirms that there are differences in the intensity of the blocking features between the two mirror equivalent directions. The differences appear to be the largest along the blocking channels situated at scattering angles of 71.57° and 90.00° . If Cu atoms have arranged in a chiral manner on the surface, similar to either of the models then this technique should be able to detect these differences.

6.4 Results and Discussion

The simulated spectra indicate that if the features observed in the STM image are those of Cu adatoms then aligning the beam along the $\langle -114 \rangle$ and $\langle 1-14 \rangle$ azimuths would yield results that are most likely to reveal the largest changes to the blocking spectra.

It can be seen in figure 6.26 that when the beam is aligned 45° with respect to the surface normal, in the $\langle -114 \rangle$ or $\langle 1-14 \rangle$ azimuthal directions, the beam is aligned along the $\langle -1-22 \rangle$ or $\langle -2-12 \rangle$ crystallographic directions respectively. This crystallographic direction corresponds to a three layer entry geometry.

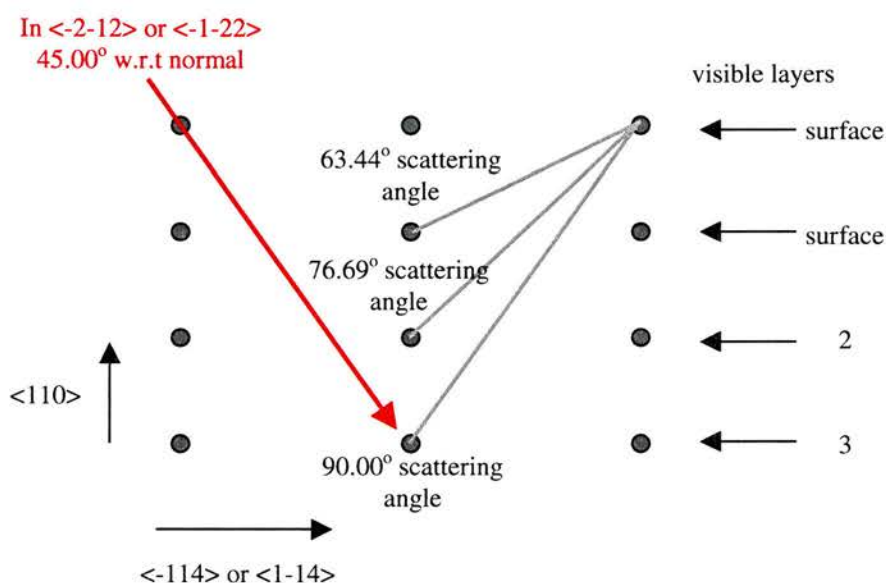


Figure 6.26. Cross section along the $\langle -114 \rangle$ and $\langle 1-14 \rangle$ azimuths illustrating the atomic arrangement as a function of depth into the $\{110\}$ surface.

If the detector is positioned so it detects ions scattered over a range of $\sim 50-110^\circ$, it can be seen that in this range blocking features associated with 1, 2 and 3 layer illuminations should be observed along with other features arising from ions scattered

from deeper lying Cu atoms. Any lateral or perpendicular movement of the Cu atoms should result in changes to the positions of the blocking dips.

Similarly, if the beam is aligned 45° with respect to the surface normal in the $\langle 1-11 \rangle$ or $\langle -111 \rangle$ azimuth, the beam is aligned with the $\langle 0-21 \rangle$ and $\langle -201 \rangle$ crystallographic directions respectively. The crystallographic direction corresponds to a two layer entry geometry.

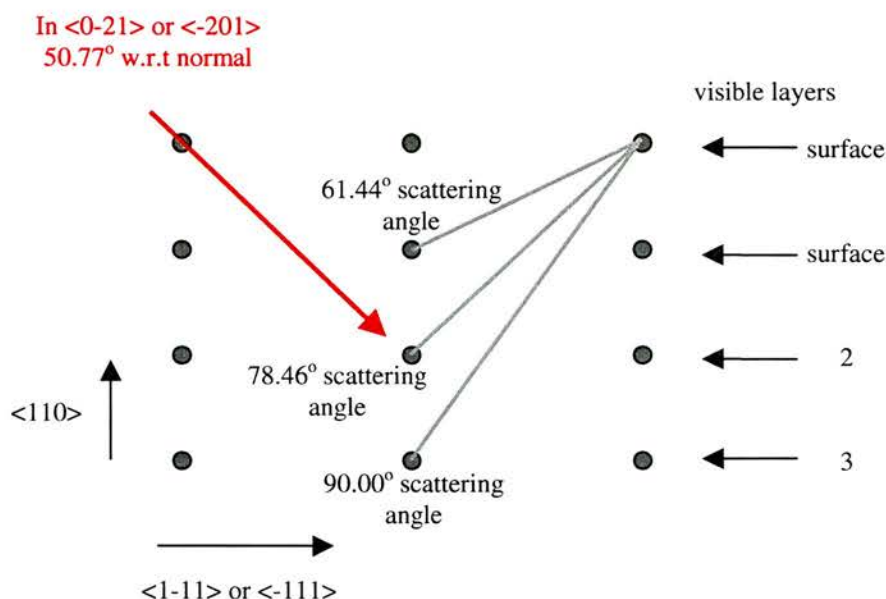


Figure 6.27. Cross section along the $\langle 1-11 \rangle$ and $\langle -111 \rangle$ azimuths illustrating the atomic arrangement as a function of depth into the $\{110\}$ surface.

Positioning the detector so that scattered ions are analysed over an area of $\sim 50-110^\circ$, then information concerning the blocking features of 1, 2 and 3 layer blocking features will be obtained.

During the course of data analysis it was found that all the data obtained from the $\langle 1-11 \rangle$ and $\langle -111 \rangle$ azimuthal directions were misaligned. The reason for this has been found to be that the motor that drives the tilt mechanism on the goniometer was defective, an important illustration of how crucial the alignment procedure is to obtain

reliable results. Therefore no data are presented for these scans but the idea has been included because it was deemed a valid and important addition to this work.

6.4.1 Structural Analysis of Cu{110}

The blocking spectra for scattering from a clean Cu{110} surface along the $\langle -114 \rangle$ and $\langle 1-14 \rangle$ direction are illustrated in figures 6.28 and 6.29 along with the simulated spectra of the clean surface.

6.4.1.1 $\langle -114 \rangle$ Azimuth

Comparison of the bulk blocking features, in figure 6.28 for the experimental and simulated data indicate the beam is aligned correctly along the $\langle -2-12 \rangle$ channel. At low and high scattering angles there are several blocking dips that do not appear at the same scattering angle as those in the simulated data, a feature that has been observed on many occasions in this study. This is peculiar as the majority of the blocking features are at the correct scattering angle and the shape of all the features looks correct. Therefore simulations were performed to try to model this behaviour in which the beam was purposely misaligned along both the spin and rotation axis, however, none of the output spectra mimicked the observed effect. It is believed, with a high degree of confidence, that the beam is aligned correctly with the required crystallographic direction and the effect has therefore been attributed to distortion of the detector at the edges of the detector channel plates.

The intensity of the experimental blocking features are not directly comparable with those of the simulation due to limitations in the simulation package. The simulation does not take into account the anisotropic surface vibrations present for the single

crystal and therefore the experimental yields are subject to slight variance from the simulated data.

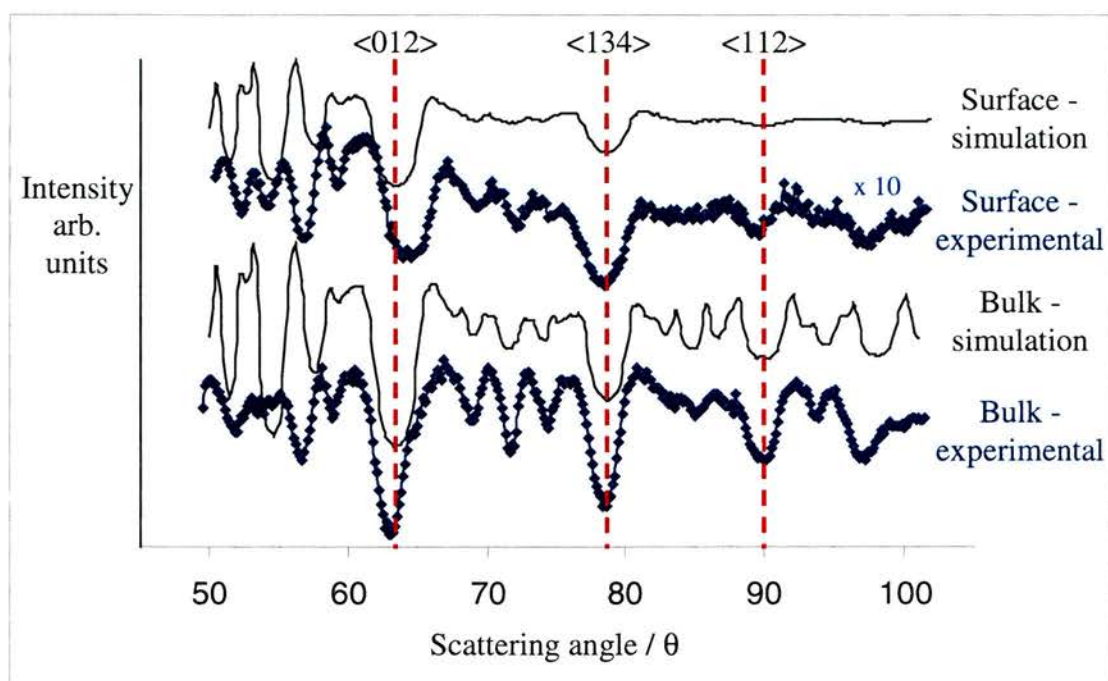


Figure 6.28. Clean Cu{110} along the $\langle -114 \rangle$ azimuth and in the $\langle -2-12 \rangle$ blocking channel obtained with a H^+ ion beam.

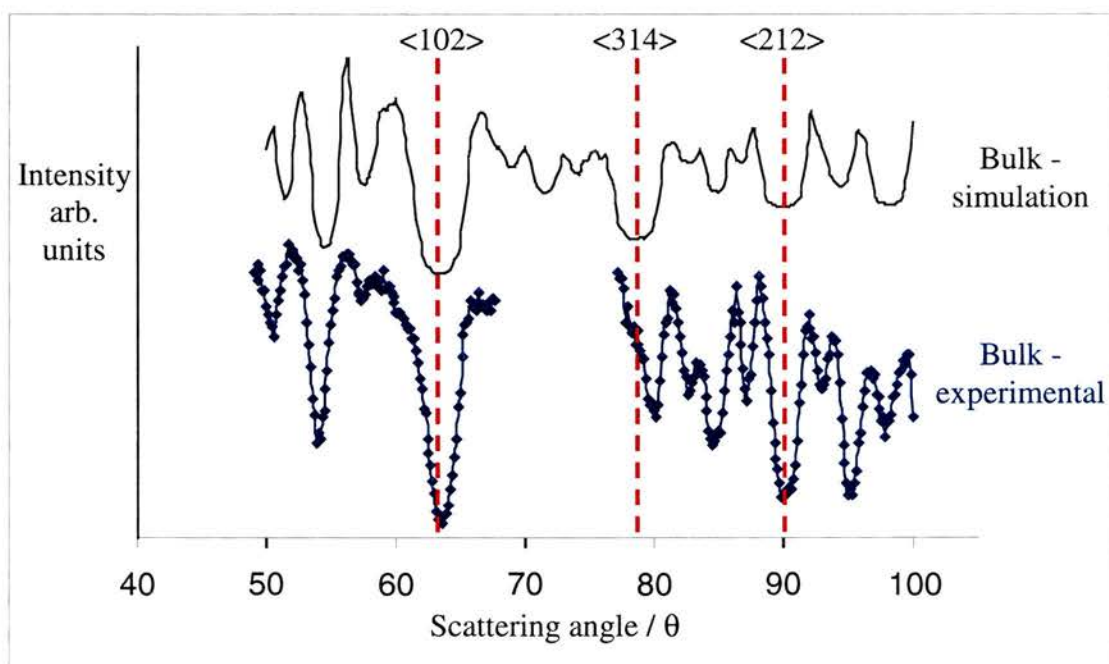


Figure 6.29. Clean Cu{110} along the $\langle -1-14 \rangle$ azimuth and in the $\langle -1-22 \rangle$ blocking channel obtained with a He^+ ion beam.

The experimental surface blocking features appear essentially identical to those of the bulk with the strongest features corresponding to the 1 (63.44°), 2 (78.69°) and 3 (71.57° , 78.69°) layer geometries. However, a glance at the feature corresponding to the 1 layer illumination at 63.44° , it is possible to see that the feature is shifted to about 64.4° . This is attributed to relaxation of the surface Cu{110} layer and the distance between the first two surface layers calculated to be $\sim 2.408\text{\AA}$. This correspond to a surface layer relaxation of $\sim 6.1\%$, consistent with literature values for the surface layer relaxation of Cu{110} [26-27].

6.4.1.2 <1-14> Azimuth

It is clear to see from the bulk experimental data (figure 6.29), that the beam is misaligned as the bulk blocking features do not match those of the simulated data. This type of problem has been encountered on many occasions, especially when aligning along the $\langle -114 \rangle$ and $\langle 1-14 \rangle$ directions. This is due to several reasons, firstly, the $\langle -1-22 \rangle$ and $\langle -2-12 \rangle$ blocking channels are very narrow and correct alignment of the beam can often depend on the conditions, more precisely the stability of the beam that may fluctuate on a day to day basis. Secondly, there are several different channels in this area of the sample that are separated only by a couple of degrees. It can then become difficult to decide whether the beam is aligned along the centre of the required channel or even where adjacent blocking dips overlap. A subtle change in the position of the single crystal, by a degree or so can make the difference between the beam being correctly aligned and misaligned. The conditions of the beam play an important role in the ability to correctly align the beam and the consistency of data obtained.

It is often difficult to determine during data collection if the beam is aligned correctly and the problem often realised after the beam time when an in depth analysis of the data is completed. Therefore the data obtained from this scan is essentially useless but illustrates an important point showing the potential difficulties that have been encountered. To try to cut down on these errors it is not unusual for a single alignment procedure to take in excess of several hours.

6.4.2 Structural Analysis of R,R-H₂TA Modified Cu{110}

The Cu{110} surface modified with R,R-H₂TA having a corresponding (90 12) LEED pattern was prepared and transferred into the scattering chamber. The blocking spectra obtained after aligning the beam along the <-114> and <1-14> azimuths are illustrated in figures 6.30 and 6.31 respectively.

6.4.2.1 <-114> Azimuth

The bulk experimental data show that the beam is aligned correctly with a slight contraction of the blocking dips associated with the distortion on the channel plates. The main difference between the surface and bulk blocking features in comparison with that of the clean surface is that the surface relaxation has been lifted, most likely due to the presence of the adsorbate on the surface. There is no evidence for any 'extra' features or shifting in position of those already present.

Comparison of the surface blocking spectra for the clean and R,R-H₂TA modified Cu{110} surface shows subtle changes in that fewer blocking dips are observed after modification with the chiral molecule. The extra blocking dips, arising from scattering of fourth, fifth and lower layers is almost certainly due to the lifting of the surface layer

relaxation. As the surface Cu atoms are in more bulk-like positions, they are able to block subsurface atoms more effectively resulting in fewer dips observed from deeper layers.

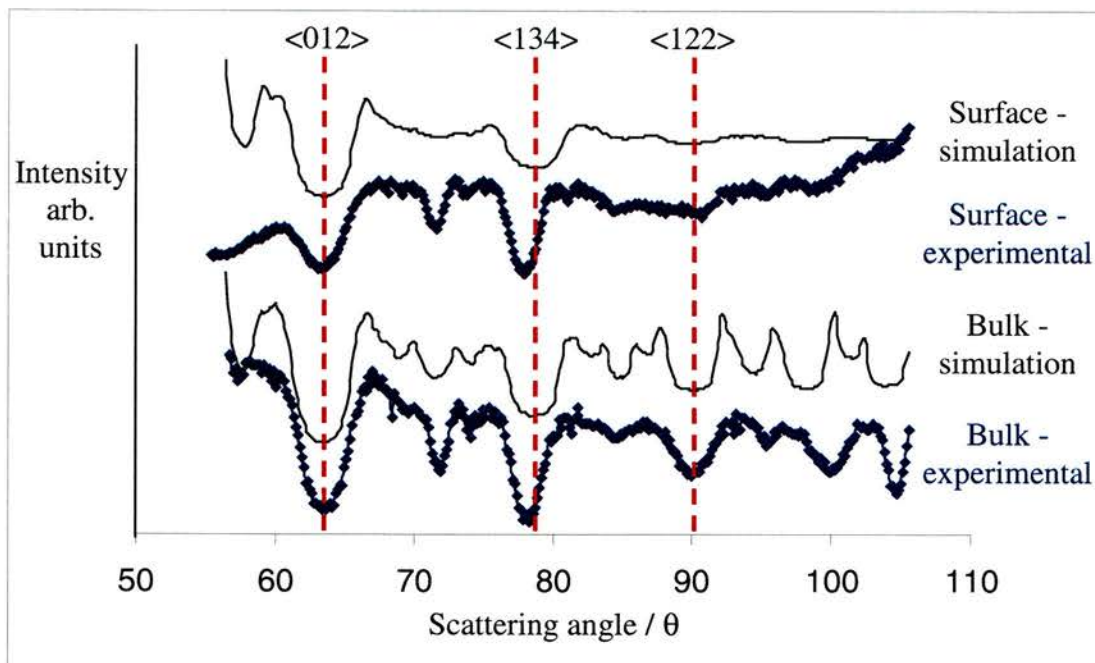


Figure 6.30. R,R-H₂TA on Cu{110} with a (90 12) unit cell, along the <-114> azimuth and in the <-2-12> blocking channel obtained with a He⁺ ion beam.

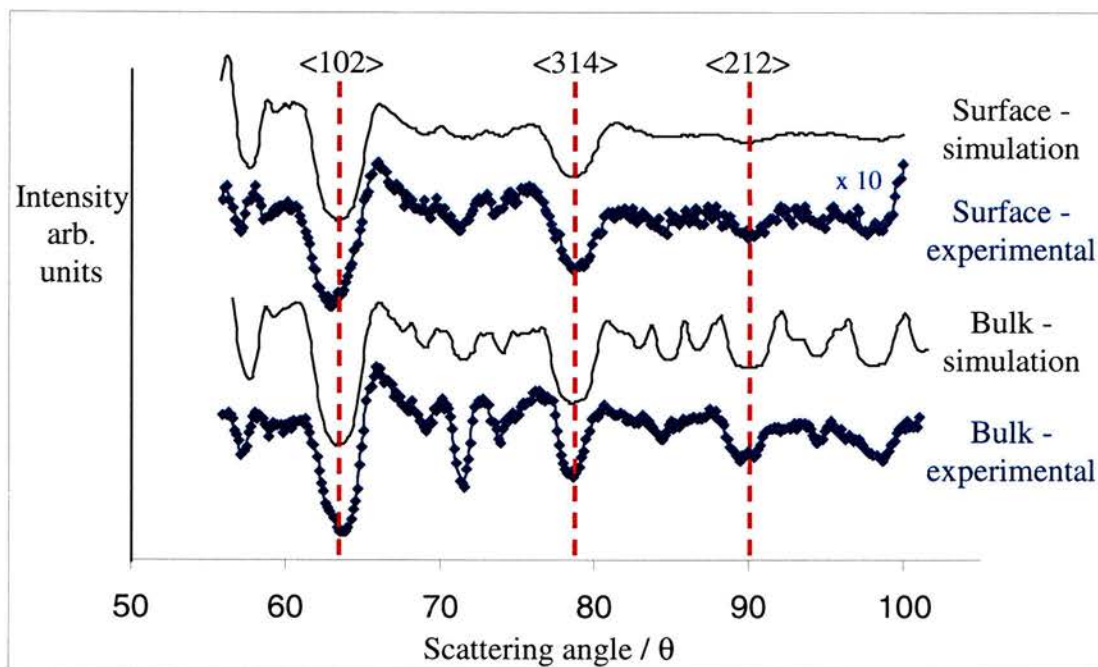


Figure 6.31. R,R-H₂TA on Cu{110} with a (90 12) unit cell, along the <-1-14> azimuth and in the <-1-22> blocking channel obtained with a H⁺ ion beam.

6.4.2.2 <1-14> Azimuth

The blocking spectra for aligning the beam along the <1-14>, mirror equivalent direction to the <-114> is illustrated in figure 6.31. It would be expected that if any changes do occur on the R,R-H₂TA modified surface then the obtained blocking spectrum along this direction should be subtly different to that of the spectrum obtained when the beam is aligned along the <-114> direction.

Comparison of the bulk experimental and simulation data again suggest that the beam is aligned correctly. The surface data shows the presence of blocking dips associated with 1, 2 and 3 layer blocking features and the lack of any extra features indicates the surface structure appears very similar to that observed along the <-114> direction. The only difference that does appear to have occurred is associated with the 1 layer blocking feature. The surface feature appears to have shifted by about 0.5° to a lower scattering angle with respect to the bulk feature.

This observation is opposite to what has been expected in the sense that any changes would most likely be observed in the <-114> azimuth however the simulated data also indicates that the largest changes should occur along the <1-14> direction. If this is a result of vertical displacement of Cu atoms then this corresponds to a surface layer expansion of ~3% however, the presence of lateral displacement or a combination of both cannot be discounted. If this effect is caused by the presence of R,R-H₂TA then preparing a (90 –12) surface structure with S,S-H₂TA should show mirror the effect.

Comparison of the intensities of the surface features at 71.57° and 90.00° in figure 6.30 and 6.31 with those of the clean surface in figure 6.26 indicate that along the $\langle -114 \rangle$ azimuth the 71.57° surface blocking channel is more intense than for the clean surface along the $\langle -114 \rangle$ direction or the R,R-H₂TA modified surface along the $\langle -1-14 \rangle$ direction. This therefore may indicate the presence of additional atoms in the surface layer of the R,R-H₂TA modified surface. However, the 90° channel appears most intense for the clean surface. It therefore appears as though there are changes between the azimuthal directions but on the basis of the simulated data, the suggested models are not able to explain the manner of these differences.

6.4.3 Structural Analysis of S,S-H₂TA Modified Cu{110}

S,S-H₂TA was adsorbed onto Cu{110} surface with a LEED pattern consistent with the presence of a (90 –12) adsorbate structure and the ion beam aligned along the $\langle -114 \rangle$ and $\langle -1-14 \rangle$ azimuthal directions. The blocking spectra are illustrated in figures 6.32 and 6.33.

6.4.3.1 $\langle -114 \rangle$ Azimuth

The bulk blocking spectra show that the beam is aligned correctly and that once again there is some contraction of the spectrum indicating the distortion of the channel plates. Although the beam appears to be aligned correctly, the position of the detector is not as it should be. The detector has an angular range of $\sim 27^\circ$ and therefore to obtain a wider scan range the detector is first positioned to a scattering angle of 65° . This means that it measures the intensity from over a range of $51.5-78.5^\circ$. Therefore to obtain a scan at higher scattering angle, the detector is moved to a second position of 90° and subsequently a scan in the range of $76.5-103.5^\circ$ is obtained. As the ion dose for each

scan is the same, the two spectra can simply be added together to get a single scan over the whole range. However, it appears as though the detector has not been positioned in the correct place, probably due to referencing problems with the detector, for either scan. This has resulted in a section where no data has been obtained and also at a scattering angle that is too high to acquire the position of the 1 layer blocking dip. Therefore no comparison can be made concerning the possible surface layer reconstruction that may have been observed when R,R-H₂TA was adsorbed on the surface.

The surface data indicates that there are no discernible differences in the position of the blocking features with that of the bulk data however, the intensity of the 90.00° and 98.13° features do appear to be bigger than has been observed in previous scans. An explanation for this may lie in the fact that these features are also strong in the bulk data.

6.4.3.2 <1-14> Azimuth

The scan along the <1-14> azimuthal direction for the (90 -12) unit cell structure is illustrated in figure 6.33.

Bulk data again shows that the beam is aligned correctly, whilst the surface spectra indicates that there is no growth of any extra features and the intensity of the features that are present are consist with what is expected. The only observable difference is the position of the 1 layer blocking feature, which again is shifted to a lower scattering angle by ~0.5°. The similarity of this effect with that observed after R,R-H₂TA was

adsorbed on the Cu{110} therefore suggests that this feature is an artifact of scanning along the $\langle 1-14 \rangle$ direction.

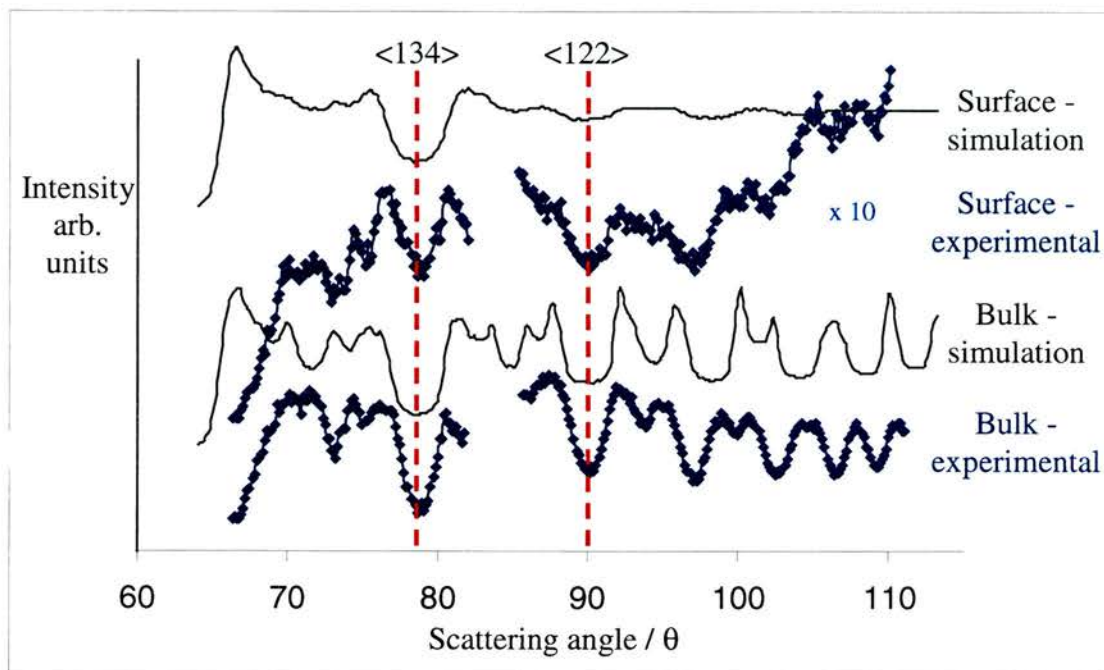


Figure 6.32. S,S-H₂TA on Cu{110} with a (90 -12) unit cell, along the $\langle -114 \rangle$ azimuth and in the $\langle -2-12 \rangle$ blocking channel obtained with a He⁺ ion beam.

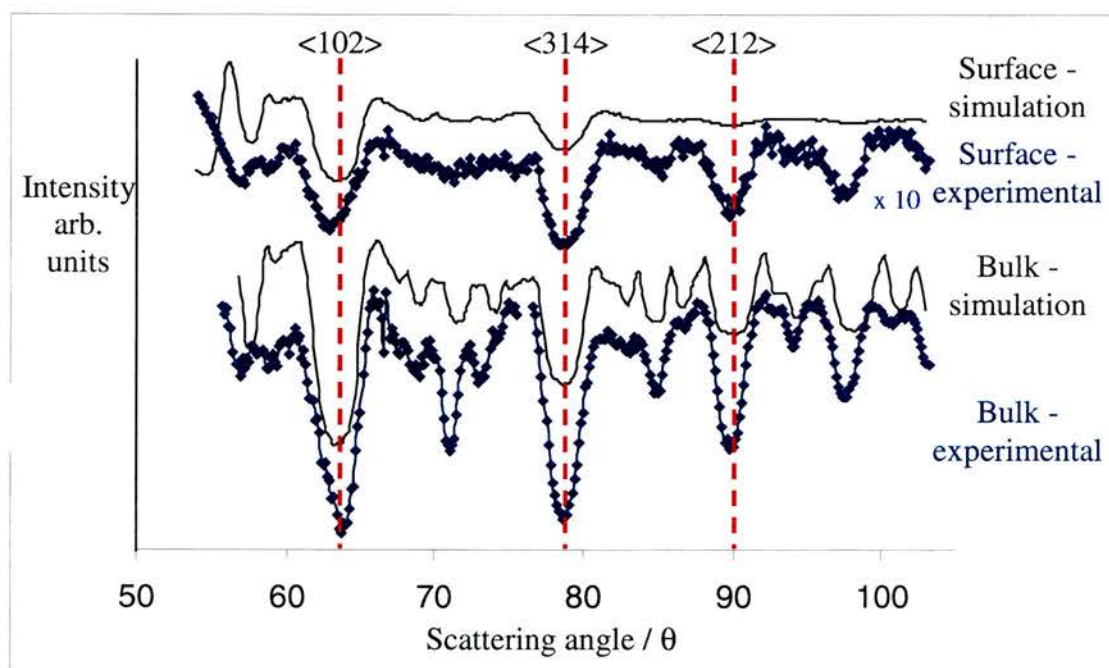


Figure 6.33. S,S-H₂TA on Cu{110} with a (90 -12) unit cell, along the $\langle 1-14 \rangle$ azimuth and in the $\langle -1-22 \rangle$ blocking channel obtained with a H⁺ ion beam.

In figure 6.33 it is noticeable that there is a very weak intensity feature at 71.57° along the $\langle 1-14 \rangle$ azimuth in comparison to the same feature along the $\langle -114 \rangle$ azimuth in figure 6.32. This effect is similar to that observed when R,R-H₂TA is adsorbed on Cu{110} along the same azimuthal directions. This suggests that this is an artifact of the $\langle 1-14 \rangle$ direction of this single crystal and may be a result of the off cut of the crystal. If the single crystal is slightly off its desired {110} plane, then the exposed crystal plane is almost certainly chiral. This may cause differences to be observed in the MEIS experiments between apparently mirror equivalent directions.

6.4.4 Quantitative Elemental Analysis

One of the beneficial features of MEIS is its ability to effectively count the number of metal atoms present in a particular layer and obtain quantitative information into its composition e.g. in bimetallic samples.

The corrosive effect of adsorption of R,R-H₂TA onto supported metal catalysts is well documented^[28] having shown that depending on modification conditions, the amount of nickel leached into the modification solution can be up to 60% of nickel initially present on the catalyst. If the features observed in the STM image (figure 6.13) for the adsorption of R,R-H₂TA on Cu{110} are those of reconstructed Cu atoms, rather than tartrate molecules, then there should be an accompanied change in the amount of Cu present in the adlayer of the modified surface in comparison to that of the clean Cu{110} surface. Lorenzo *et al*^[16] have stated that large areas of the surface are covered in the chiral surface structure and therefore any change in the amount of Cu present in the surface layer is likely to be observable using MEIS.

The ion beam is aligned along the $\langle -101 \rangle$ blocking channel, in the $\langle -112 \rangle$ azimuth for the clean, R,R-H₂TA modified and S,S-H₂TA modified Cu{110}. This is illustrated in figure 6.34.

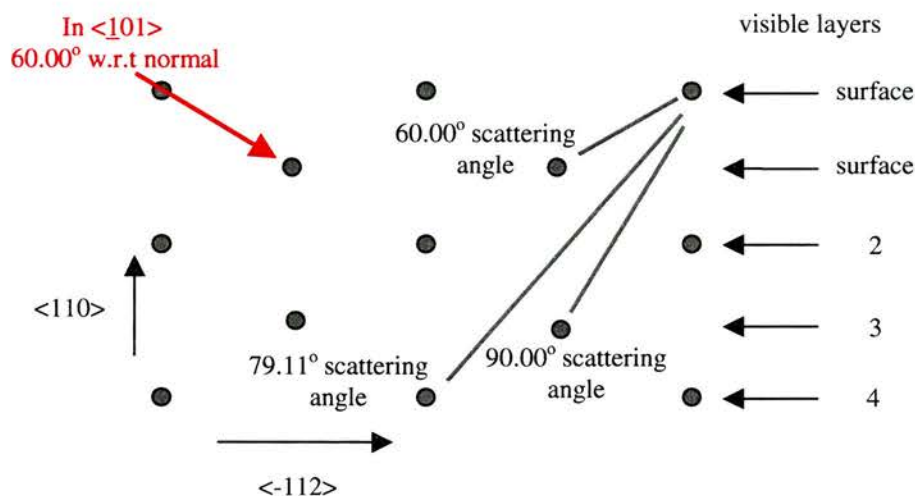


Figure 6.34. Cross section along the $\langle -112 \rangle$ azimuth illustrating the atomic arrangement as a function of depth into the {110} surface.

It can be seen that there is a large, 1 layer exit geometry with a scattering angle of 60.00° along the $\langle 011 \rangle$ direction. These large entry and exit channels ensure that alignment of the beam is straight forward and a double alignment geometry enables the amount of Cu visible to the beam in the first layer can be obtained.

Scans are taken along this direction for the three prepared surfaces and the bulk blocking features analysed to ensure the correct beam alignment. The blocking spectra are illustrated in figure 6.35.

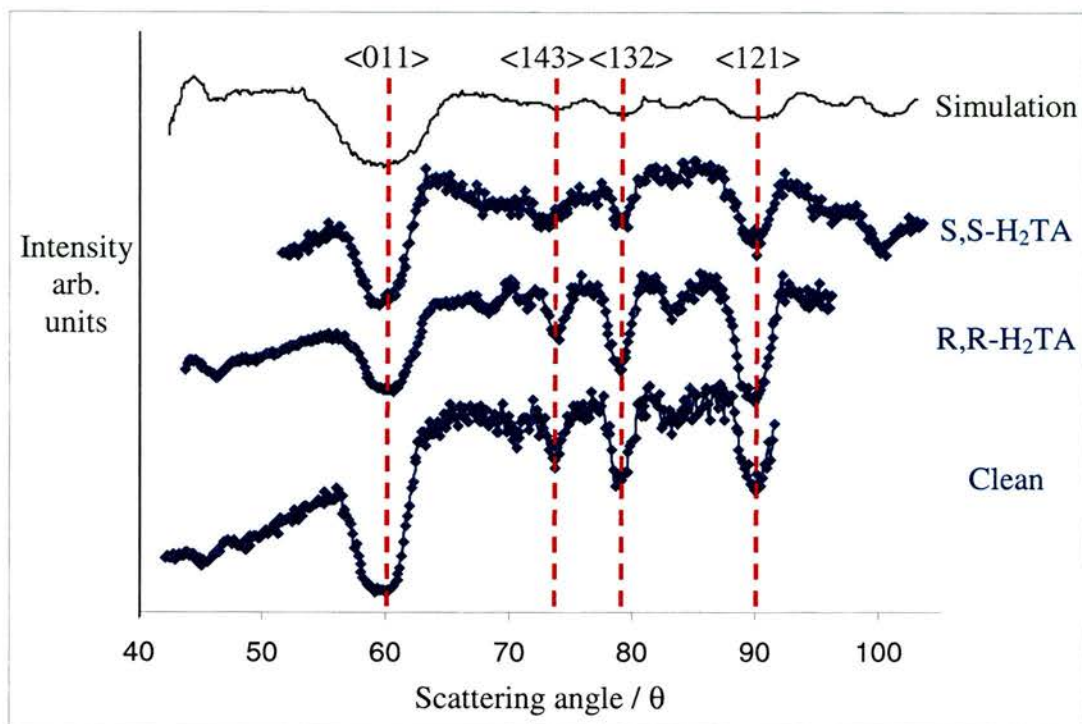


Figure 6.35. Blocking spectra taken along the $\langle -112 \rangle$ azimuth, in the $\langle -101 \rangle$ blocking channel for the clean, R,R- H_2TA modified and S,S- H_2TA modified Cu{110} and with the simulated spectrum for comparison. The spectra have been obtained with a H^+ ion beam.

The bulk data show that all of the surfaces are aligned correctly and the position of the blocking dips agree with the experimental data. The amount of Cu visible to the beam was obtained by summing the intensity at the base of the $\langle 011 \rangle$ blocking channel to obtain an intensity v energy spectrum, similar to that illustrated in figure 6.12. The amount of Cu in the surface is given by the area under the Cu peak and after applying the corrections, as described earlier, the ratio of Cu present in the surface layer is summarised in table 6.2.

SURFACE	RATIO
Clean Cu{110}	1
R,R-H ₂ TA modified Cu{110}	0.82
S,S-H ₂ TA modified Cu{110}	1.06

Table 6.2. Summary of the ratio of Cu in the first layer of clean Cu{110}, R,R-H₂TA and S,S-H₂TA modified Cu{110}.

These figures suggest that upon modification with R,R-H₂TA there is a slight decrease in the relative amount of Cu present in the first layer in comparison to the clean surface, whilst when the surface is modified with S,S-H₂TA there is a slight increase. These results do not appear to be consistent, as it would be highly unlikely that one of the two enantiomers would reconstruct the surface in an opposite manner. It would be more likely that these slight differences are a result of experimental error and subsequently the adsorption of R,R-H₂TA and S,S-H₂TA onto Cu{110} either does not cause a reconstruction of the surface layer or the effect is negligible.

6.5 Summary

In this chapter, the surface structure of R,R- and S,S-H₂TA modified Cu{110} has been investigated using MEIS in order to elucidate whether chiral arrays of surface metal adatoms exists as the surface layer should be subtly reconstructed surface to incorporate the additional Cu atoms. Despite an extensive study there does not appear to be any unambiguous evidence for the existence of a chiral array of Cu atoms or a large surface reconstruction.

The structure of the top most layers has been studied and a value for the surface relaxation of a clean Cu{110} has been extracted but there appears to be little change between the two azimuthal directions for R,R-H₂TA, S,S-H₂TA and the clean surface. Simulated data indicates that if adatoms are incorporated into the surface layer then changes should be observable, especially since the chiral adlayer is observed to exist over a large proportion of the surface. However, there are many reasons to why no effects have been observed.

Firstly, the alignment has been difficult due to the size of the crystallographic direction the beam is aligned along, referencing problems with the analyser and a defective tilt motor in the goniometer. Secondly, the crystal may be off cut slightly in which case the crystal may already be chiral resulting in blocking features being slightly different along apparently mirror equivalent directions. Thirdly, it may be that any changes that occur do so on such a small proportion of surface atoms that it is effectively below the limits of detection. Finally, if the features observed in the STM image are those of tartrate species then such a result would be expected. Therefore, at this time we are unable to determine the precise nature of these surface species.

Whilst the simulated blocking spectra show that there are no changes in the position of the blocking feature, the intensity of certain features do show very small changes between the two different adatom models and that of the clean surface. MEIS investigations tend to look for small changes and it appears unlikely that this technique would be capable of observing such subtle effects. Whilst this technique has so far not shed any light on the problem in hand, it would be very useful to observe systems in

which bigger changes occur such as the adsorption of aminobenzoic acid on Cu{110}

[17].

6.6 References

- [1] RM Tromp; *Practical Surface Analysis, Volume 2: Ion and Neutron Spectroscopy*.
2nd edition D Briggs MP Seah (eds), John Wiley and Sons Ltd, 1992. 577
- [2] P Bailey, TCQ Noakes, CJ Baddeley, SP Tear and DP Woodruff; *Nuc. Ins. Meth. B*.
183 (2001) 62
- [3] www.dl.ac.uk/MEIS/techniques/index.htm
- [4] CJ Baddeley, LH Bloxham, SC Laroze, R Raval, TCQ Noakes and P Bailey; *J. Phys. Chem. B* **105** (2001) 2766
- [5] CJ Baddeley, LH Bloxham, SC Laroze, R Raval, TCQ Noakes and P Bailey; *Surf. Sci.* **433-435** (1999) 827
- [6] LC Feldman; *Methods of Surface Characterisation, Volume 2 – Ion Spectroscopies for Surface Analysis*. AW Czanderna and DM Hercules (eds.), Plenum Press, New York, 1991. 334
- [7] BW Busch and T Gustafsson; *Surf. Sci.* **425** (1998) L1074
- [8] www.dl.ac.uk/MEIS/facility/index.htm
- [9] www.dl.ac.uk/ENG/MEIS/stereographs/sp.fcc.110.html
- [10] DP Woodruff and TA Delchar; *Modern Techniques of Surface Science* 2nd Edition.
EA Davis, IM Ward and DR Clarke (eds), Cambridge University Press. 387-391
- [11] LH Bloxham; PhD thesis. University of Liverpool. 2001. Chapter 2, 73
- [12] A Tai and T Harada; *Tailored Metal Catalysts*, Y Isawawa (ed.), D Reidel Publishing Company, 1986. 265
- [13] Y Izumi; *Adv. Cat.* **32** (1983) 215
- [14] A Hoek and WMH Sachtler; *J. Catal.* **58** (1979) 276
- [15] FM Leibsle, S Haq, BG Frederick, M Bowker and NV Richardson; *Surf. Sci.* **343**
(1995) L1175

-
- [16] MO Lorenzo, S Haq, T Bertrams, P Murray, R Raval and CJ Baddeley; *J. Phys. Chem. B* **103** (1999) 10661
- [17] Q Chen, DJ Frankel and NV Richardson; *Langmuir*. **17** (2001) 8276
- [18] MO Lorenzo, CJ Baddeley, C Muryn and R Raval; *Nature*. **404** (2000) 376
- [19] MO Lorenzo; PhD thesis. University of Liverpool. 1999. Chapter 6, 190
- [20] Q Chen, CC Perry, BG Frederick, PW Murray, S Haq and NV Richardson; *Surf. Sci.* **446** (2000) 63
- [21] CC Perry, S Haq, BG Frederick, Q Chen and NV Richardson; *Surf. Sci.* **409**, 3 (1998) 512
- [22] PDA Pudney, BG Frederick and NV Richardson; *Surf. Sci.* **307-309** (1994) 46
- [23] CK Prout, JR Carruthers and FJC Rossotti; *J. Chem. Soc. A* (1971) 3336
- [24] Personal communication with CJ Baddeley
- [25] www.dl.ac.uk/MEIS/documents/user_manual.doc
- [26] PR Watson; *J. Phys. Chem. Ref. Data*. **19**, 1 (1990) 85
- [27] JC Zheng, HQ Wang, ATS Wee and CHA Huan; *Surf. Rev. Lett.* **8**, 5 (2001) 541
- [28] G Webb and PB Wells; *J. Chem. Soc., Chem. Commun.* (1991) 1619

Chapter Seven

Summary.

7.1 Summary of Results

In chapter three the adsorption of R,R-H₂TA on Ni{111} has been studied in which two distinct ordered adlayer structures have been produced at sub-monolayer coverages whose stability is dependent on adsorption temperature. R,R-H₂TA can chemisorb to the surface either as a monotartrate or bitartrate species that are stabilised by intermolecular hydrogen bonding interactions. In the latter case the individual carboxylate groups are able to bond to the surface either in a monodentate or bidentate manner. At 300K, ordered monotartrate surface species are observed whilst at 350K, only ordered bitartrate species are observed. It is apparent that at 300K the intermolecular hydrogen bonding kinetically hinders the conversion to the bitartrate but at 350K this conversion occurs readily on the surface. The presence of adventitious CO disrupts the formation of intermolecular hydrogen bonding at lower R,R-H₂TA coverage resulting in less stable surface species than at the higher coverage structure. With increasing R,R-H₂TA adsorption, CO is displaced from the surface, coincident with the increase in stability of the surface species. After a saturation coverage of R,R-H₂TA the surface is essentially free of CO.

In chapter four the adsorption of MAA on Ni{111} and R,R-H₂TA modified Ni{111} surfaces have studied. MAA adsorbs on the surface at 300K with a relatively high sticking probability and the molecule is orientated with the molecular plane close to

parallel to the surface. No ordered MAA structures are observed for all MAA coverages. The sticking probability of MAA on a Ni{111} precovered with a high coverage of R,R-H₂TA is negligible in contrast to adsorption to a surface consisting of a moderate coverage of R,R-H₂TA and adventitious CO. MAA adsorption therefore occurs either at areas of clean Ni or by displacement of CO. Two different ordered structures are observed that are different to those formed when R,R-H₂TA alone is adsorbed on the surface. The first structure, possessing a local coverage of 0.133ML consists of one bitartrate and one MAA molecule per unit cell. The orientation of all of the MAA molecules is identical and there is evidence for interaction between the α -hydroxy group of the tartrate molecule and the keto group of the MAA. If this structure were to be observed on Ni nanoparticles under reaction conditions, hydrogenation would result in 100% enantioselective formation of R-MHB. The second, 0.167ML local coverage structure consists of one tartrate and two MAA molecules per unit cell. If hydrogenation were to occur to this structure under reaction conditions a racemic product would be produced.

In chapter five the design and building of a UHV chamber equipped with the ability to transfer the sample into a reaction cell and take part in a heterogeneous catalytic hydrogenation reaction is discussed. The apparatus was commissioned using the hydrogenation reaction of MAA over Ni{111} and R,R- and S,S-H₂TA modified Ni{111}. In these initial test reactions the conditions were altered along with the reaction solvent, however so far no hydrogenation activity has been observed.

In chapter six the effect of chiral modification under UHV conditions for the Cu{110} system is analysed using MEIS with the aim of determining whether Cu atoms are

arranged in a chiral manner on the surface. This technique potentially has the ability to detect small changes in the structure of the surface layer and such changes have been proposed as a result of the acid modification procedure. However, no unambiguous effect on the surface layer has been detected after adsorption of either R,R- or S,S-H₂TA on the Cu{110} surface.

7.2 Additional Experiments

Bimetallic catalysts have been shown to display enhanced selectivity over those of their monometallic counterparts ^[1-3] and the study of the interface has important implications as these systems are widely used in a variety of technologies.

The Mo-Ni bimetallic system has attracted recent research as a result of its interesting magnetic ^[4] and catalytic properties ^[5-6]. Mo-Ni bimetallic surfaces have been synthesised and characterised using STM, LEED, AES, MEIS and TPD in which two distinct Ni rich surface alloys have been prepared with a (3x3) and (5x5) surface alloy that are isostructural with the fcc Ni. Compositional analysis using MEIS indicates that one Mo atom is present per adlayer unit cell giving compositions of 11.1% Mo for (3x3) alloy and 4% Mo for the (5x5) alloy ^[7].

There are many studies detailing the presence of adsorbed molecules on bimetallic surfaces inducing segregation of one element so that the composition of the topmost layers differ from that of the bulk ^[8-10]. This has led to the proposal in the R,R-H₂TA modified Ni system that if it were possible to selectively quench the racemic sites, the achievement of 100% enantioselective catalysts would be extremely beneficial to the

Pharmaceutical and Chemical Industries. For this reason it is proposed that Au-Ni bimetallic surfaces will be less active towards the β -ketoester hydrogenation than pure Ni surfaces. It is anticipated that due to the stronger interaction of carboxylic acids with Ni compared with Au, R,R-H₂TA will form ordered islands and these islands will be enriched in Ni in the surface layer. The islands should be separated by bimetallic regions that have a significantly quenched activity for the racemic reaction and therefore selectivity of the system would be enhanced.

The bimetallic surfaces have been prepared and characterised using LEED, AES and MEIS. R,R-H₂TA has been adsorbed onto the surfaces and again characterised using LEED, AES, MEIS, STM, RAIRS and TPD to determine the extent of surface segregation and the effect the alloyed surface has on the adsorption of R,R-H₂TA. This work is at present on going and it is anticipated that these surfaces shall be tested for activity and selectivity under real catalytic conditions in the reaction cell attached to the UHV chamber.

7.3 References

- [1] JA Rodriguez, RA Campbell and DW Goodman; *Surf. Sci.* **307-309** (1994) 377
- [2] PM Holmblad, JH Larsen, I Chorkendorff, LP Nielsen, F Bessenbacher, I Stensaard, E Laegsgaard, P Kratzer, B Hammer and JK Norskov; *Cat. Let.* **40** (1996) 131
- [3] CJ Baddeley, M Tikhov, C Hardacre, JR Lomas and RM Lambert; *J. Phys. Chem.* **100** (1996) 2189
- [4] JW Cable, MR Khan, GP Felcher and JK Schuller; *Phys. Rev. B.* **34** (1986) 1643
- [5] A Calafat, J Laine, A Lopez-Agudo, JM Palacios; *J. Catal.* **162** (1996) 20
- [6] WRAM Robinson, JNM van Gestel, TI Koranyi, S Eijsbouts, AM van der Krann, JAR van Veen and VHJ de Beer; *J. Catal.* **161** (1996) 539
- [7] TE Jones, TCQ Noakes, P Bailey and CJ Baddeley; Submitted to *Surface Science*.
- [8] CJ Baddeley, LH Bloxham, SC Laroze, R Raval, TCQ Noakes and P Bailey; *Surf. Sci.* **433-435** (1999) 827
- [9] TCQ Noakes, P Bailey, SC Laroze, LH Bloxham, R Raval and CJ Baddeley; *Surf. Inter. Anal.* **30** (2000) 81
- [10] CJ Baddeley, LH Bloxham, SC Laroze, R Raval, TCQ Noakes and P Bailey; *J. Phys. Chem. B.* **105** (2001) 2766